

**PERFORMANCE-BASED SEISMIC DESIGN AND ASSESSMENT OF CONCRETE BRIDGE
PIERS REINFORCED WITH HIGH-STRENGTH STEEL REBAR**

by

Saif Maad Aldabagh

M.Sc., American University of Sharjah, 2016

B.Sc., American University of Sharjah, 2014

A THESIS SUBMITTED IN PARTIAL FULFILLMENT OF
THE REQUIREMENTS FOR THE DEGREE OF

DOCTOR OF PHILOSOPHY

in

THE COLLEGE OF GRADUATE STUDIES

(Civil Engineering)

THE UNIVERSITY OF BRITISH COLUMBIA

(Okanagan)

May 2021

© Saif Maad Aldabagh, 2021

The following individuals certify that they have read, and recommend to the College of Graduate Studies for acceptance, a thesis/dissertation entitled:

Performance-Based Seismic Design and Assessment of Concrete Bridge Piers Reinforced with High-Strength Steel Rebar

submitted by Saif Maad Aldabagh in partial fulfillment of the requirements of the degree of Doctor of Philosophy.

Dr. M. Shahria Alam, School of Engineering

Supervisor

Dr. Ahmad Rteil, School of Engineering

Supervisory Committee Member

Dr. Abbas Milani, School of Engineering

Supervisory Committee Member

Dr. Sina Kheirkhah, School of Engineering

University Examiner

Dr. Marc O. Eberhard, University of Washington

External Examiner

ABSTRACT

Utilizing high-strength steel (HSS) rebars in concrete bridge columns in seismic applications is greatly restricted primarily due to the lack of appropriate seismic design guidelines. The purpose of this study is to use a combination of analytical and experimental methods to evaluate the seismic performance of concrete bridge columns reinforced with HSS rebars, and thereby make appropriate design recommendations. ASTM A1035 Grade 690 steel was the primary focus of this study, however, other types of HSS were also considered in a number of assessments for comparison purposes.

In this study, a comprehensive analytical program with an overarching objective of proposing simplified expressions to predict drift ratio limit states for circular concrete columns reinforced with HSS was first carried out. A machine learning-based symbolic regression was used to fit the resulting data into simplified numerical expressions. The proposed simplified expression provided adequate predictions of the drift ratio limit states obtained from the numerical analysis as well as those measured in previous experimental programs. In addition, a comprehensive experimental study was carried out to examine the low-cycle fatigue performance of ASTM A1035 Grade 690 rebars under cyclic-strain reversals. Existing strain and energy-based fatigue-life models' constants were calibrated using the generated experimental fatigue data. Previously established low-cycle fatigue life models of HSS rebars were utilized as a part of an analytical program to identify conditions under which such rebars can achieve adequate performance in comparison to that of benchmark ASTM A706 Grade 420 steel bars in concrete bridge columns. Irrespective of the spacing-to-bar diameter ratio, ASTM A1035 Grade 690 rebars demonstrated adequate low-cycle fatigue performance for crustal earthquakes up to a displacement ductility level of 2. Design codes were found overly restrictive in not permitting the use of HSS in seismic applications based on their low-cycle fatigue performance. Lastly, analytical seismic fragility curves were developed for a concrete bridge pier alternately reinforced with HSS and conventional normal-strength steel. Comparisons between fragility curves were made to evaluate the applicability of certain clauses of the *Canadian Highway Bridge Design Code* to bridge piers reinforced with HSS.

LAY SUMMARY

High-strength steel (HSS) rebars are stronger than conventional normal-strength steel rebars and therefore, if utilized in concrete structures, can promote a reduction in the required steel reinforcement. However, the lack of appropriate design guidelines restricts the use of HSS rebars in members resisting earthquake loading such as columns in bridges. In this study, analytical and experimental programs were executed to evaluate the performance of HSS rebars in concrete bridge columns subjected to earthquake loading. The findings from those programs revealed that design codes' requirements were overly conservative. As a result, design recommendations promoting the safe and efficient use of HSS were proposed.

PREFACE

The work presented in this thesis was conducted by Saif Maad Aldabagh under the supervision of Dr. M. Shahria Alam at the University of British Columbia. Several portions of this dissertation have been either published or submitted for publication, as indicated in the following list:

1. Part of the material presented in Chapter 2 and corresponding appendices have been published [Aldabagh, S., and Alam, M. S. (2020). High-strength steel reinforcement (ASTM A1035/A1035M Grade 690): state-of-the-art-review. *Journal of Structural Engineering*, 146(80), 03120003]. S. Aldabagh was the lead investigator, responsible for conceptualization, data collection and preparation, formal analysis, visualization, writing, and manuscript composition. Dr. M. S. Alam supervised the research and reviewed/edited the manuscript.
2. Part of the material presented in Chapter 3 and corresponding appendices have been submitted [Aldabagh, S., and Alam, M. S. (Submitted in Dec. 2020). Drift ratio limit states for circular concrete columns reinforced with different types of high-strength steel reinforcing bars. *Journal of Bridge Engineering*. S. Aldabagh was the lead investigator, responsible for conceptualization, data collection and preparation, formal analysis, visualization, writing, and manuscript composition. Dr. M. S. Alam supervised the research and reviewed/edited the manuscript.
3. Part of the material presented in Chapter 4 and corresponding appendices have been published [Aldabagh, S., and Alam, M. S. (2021). Low-cycle fatigue performance of high-strength steel reinforcing bars considering the effect of inelastic buckling. *Engineering Structures*, 235, 112114. S. Aldabagh was the lead investigator, responsible for conceptualization, executing the laboratory testing, analyzing the gathered data, writing, and manuscript composition. Dr. M. Shahria Alam supervised the research and reviewed/edited the manuscript.
4. Part of the material presented in Chapter 5 and corresponding appendices have been submitted [Aldabagh, S., Rodríguez, J. and Alam, M. S. (Submitted in July 2021). Low-cycle fatigue performance of high-strength steel rebars in concrete bridge columns, *Earthquake Engineering &*

Structural Dynamics. S. Aldabagh was the lead investigator, responsible for conceptualization, data collection and preparation, formal analysis, visualization, writing, and manuscript composition. J. Rodríguez assisted in data analysis and edited the manuscript. Dr. M. S. Alam supervised the research and reviewed/edited the manuscript.

5. Part of the material presented in Chapter 6 and corresponding appendices have been published [Aldabagh, S., Khan, S., and Alam, M. S. (2020). Seismic fragility assessment of bridge piers incorporating high-strength steel reinforcement and concrete under near-fault ground motions. *Canadian Journal of Civil Engineering*]. S. Aldabagh was the lead investigator, responsible for conceptualization, data collection and preparation, formal analysis, visualization, writing, and manuscript composition. Dr. M. S. Alam and S. Khan supervised the research and reviewed/edited the manuscript.

TABLE OF CONTENTS

ABSTRACT	iii
LAY SUMMARY	iv
PREFACE	v
TABLE OF CONTENTS	vii
LIST OF TABLES	xi
LIST OF FIGURES	xiii
ACKNOWLEDGEMENTS	xvi
DEDICATION	xvii
CHAPTER 1: INTRODUCTION	1
1.1 General	1
1.2 Objectives	6
1.3 Thesis Organization.....	7
CHAPTER 2: HIGH-STRENGTH STEEL REINFORCEMENT IN STRUCTURAL CONCRETE: STATE-OF-THE-ART REVIEW	9
2.1 General	9
2.2 Production of High-Strength Steel	12
2.3 Mechanical Properties of ASTM A1035 Reinforcement	14
2.4 Corrosion Performance of ASTM A1035 Reinforcement.....	16
2.5 ASTM A1035 Reinforcing Steel in Flexural Members.....	19
2.5.1 <i>Longitudinal Reinforcement</i>	19
2.5.2 <i>Transverse Reinforcement</i>	21
2.6 Serviceability Considerations.....	24
2.6.1 <i>Deflections</i>	24
2.6.1 <i>Crack Control</i>	26

2.4	ASTM A1035 Reinforcing Steel in Compression Members.....	28
2.7	Bond Strength Characteristics of ASTM A1035 Reinforcing Steel.....	30
2.8	Seismic Performance of ASTM A1035 Reinforcing Steel.....	32
2.9	Summary	34

CHAPTER 3: DRIFT RATIO LIMIT STATES FOR CIRCULAR CONCRETE COLUMNS

REINFORCED WITH DIFFERENT TYPES OF HIGH-STRENGTH STEEL REINFORCING

BARS.....		36
3.1	General	36
3.2	High-Strength Steel Types	39
3.3	Definition of Damage States	42
3.4	Numerical Model Evaluation and Validation.....	44
3.5	Factorial Analysis.....	48
3.5.1	<i>Parameters Affecting Drift Ratios at DS-1</i>	49
3.5.2	<i>Parameters Affecting Drift Ratios at DS-2</i>	50
3.5.3	<i>Parameters affecting drift ratios at DS-3 and DS-4_{cu}</i>	50
3.5.4	<i>Parameters affecting drift ratios at DS-4_{sb}</i>	51
3.6	Drift Ratio Limit States of Concrete Columns Reinforced with HSS	54
3.7	Simplified Expressions for the Drift Ratio Limits	57
3.8	Summary	64

CHAPTER 4: LOW-CYCLE FATIGUE PERFORMANCE OF HIGH-STRENGTH STEEL

REINFORCING BARS CONSIDERING THE EFFECT OF INELASTIC BUCKLING 66

4.1	General	66
4.2	Material and Experimental Procedure	69
4.3	Low-Cycle Fatigue Test Results	74
4.3.1	<i>Effects of Strain Amplitude</i>	78
4.3.2	<i>Effects of Buckling Length</i>	79

4.3.3	<i>Effects of Rebar Diameter</i>	81
4.4	Fatigue Life Relationships for ASTM A1035 Grade 690 Reinforcing Bars	82
4.4.1	<i>Relationship between Fatigue Life and Total Strain Amplitude ϵ_a</i>	82
4.4.2	<i>Relationship between Fatigue life and Total Energy Dissipation WFT</i>	90
4.5	Summary	93

CHAPTER 5: LOW-CYCLE FATIGUE PERFORMANCE OF HIGH-STRENGTH STEEL

REBARS IN CONCRETE BRIDGE COLUMNS	95	
5.1	General	95
5.2	High-Strength Steel	98
5.3	Evaluation of Low-Cycle Fatigue Damage	101
5.4	Numerical Model and Validation	105
5.5	Selectin of Ground Motions	108
5.6	Characteristics of Bridge Columns.....	110
5.7	Results of Low-Cycle Fatigue Damage Analysis.....	112
5.8	Cumulative Damage	116
5.9	Summary	119

CHAPTER 6: SEISMIC FRAGILITY ASSESSMENT OF BRIDGE PIERS INCORPORATING

HIGH-STRENGTH STEEL AND CONCRETE UNDER NEAR-FAULT GROUND MOTIONS 122

6.1	General	122
6.2	Geometry and Design of Prototype Bridge	126
6.3	Finite Element Modeling and Model Verification	130
6.4	Fragility Function Methodology	133
6.5	Selection of Ground Motions	136
6.6	Results	138
6.6.1	<i>Static-push Over Analysis</i>	138
6.6.2	<i>Seismic Fragility Curves</i>	142

6.7	Assessment of Members Inelastic Rotation and Ductility Capacity	146
6.8	Summary	148
CHAPTER 7: SUMMARY, CONCLUSIONS AND FUTURE WORK		150
7.1	Summary and Conclusions	150
7.2	Limitations of This Study.....	154
7.3	Recommendations for Future Research.....	155
BIBLIOGRAPHY		157
APPENDICES		175
	Appendix A	175
	Appendix B	187

LIST OF TABLES

Table 1: Quantitative Measures of Corrosion Performance of ASTM A1035 Steel.	18
Table 2: Summary of Tensile Mechanical Properties of ASTM A706 Grade 550, ASTM A615 Grade 690, and ASTM A1035 Grade 690 steel.....	41
Table 3: Selected Performance Levels and the Associated Damage States.	44
Table 4: Parameters Considered in the Factorial Analysis.	52
Table 5: Percent Contributions of the Parameters Considered.	53
Table 6: Proposed Simplified Expressions of Drift Ratios at the Damage States of Concrete Columns Reinforced with different types of HSS.....	58
Table 7: Comparisons Between the Experimentally Measured Drift Ratios at Different Damage States and those Predicted Using Numerical Expressions.	63
Table 8: Summary of Mechanical Properties Derived from Monotonic Tension Tests.	72
Table 9: Low-Cycle Fatigue Results for 12.7 mm Diameter Reinforcing Bars.....	75
Table 10: Low-Cycle Fatigue Results for 15.88 mm Diameter Reinforcing Bars.....	76
Table 11: Results of Regression Analysis to Calibrate Koh-Stephens Model’s Constants.	84
Table 12: Results of Regression Analysis to Calibrate Tong et al. (1989) Model’s Constants.	92
Table 13: Reported Means and Coefficients of Variation of Key Tensile Mechanical Properties by Overby et al. (2017) and Shahrooz et al. (2011) for ASTM A706 Grade 550 and ASTM A1035 Grade 690 steel, Respectively.....	101
Table 14: Equations Correlating Material Constant, M and m , with the Spacing-to-Bar Diameter Ratio.	101
Table 15: Summary Details of the Ground Motion Sets.....	110
Table 16: Effective Yield drift Ratios (In Percent) of Bridge Columns with s/db of 4.....	112
Table 17: Comparison Between Tensile Properties of ASTM A706 Grade 420 Reinforcement and ASTM A1035 Grade 690 and 830 Reinforcement (ASTM 2016; ASTM 2020b).....	126

Table 18: Summary of the Force-Based Design Results.	130
Table 19: Properties of the Validated Experimental Tests.....	132
Table 20: Performance Criteria (CSA 2019b).	136
Table 21: Characteristics of the Selected Ground Motion Records.....	137
Table 22: Summary of the Static Pushover Analysis Results.	142
Table 23: Drift Ratio Corresponding to Minimal, Repairable, Extensive, and Probable replacement Damage States.....	145
Table 24: Percent Difference in Fragility Medians PGA for All Sections Relative to the Reference Sections.....	145
Table 25: Measured Properties Based on Approach Proposed by Priestley et al. (1996).....	148

LIST OF FIGURES

Figure 1: Stress-strain curves for ASTM A1035 and ASTM A615 reinforcing steel.....	15
Figure 2: Different methods to establish the yield strength of ASTM A1035 reinforcing steel.	15
Figure 3: Comparison of strain limits for ASTM A1035 Grade 690 (Shahrooz et al. 2014; Mast et al. 2008) and ASTM A615 Grade 420.....	20
Figure 4: Bar spacing versus clear cover for crack control for reinforcing steel with f_s of 250 and 460 MPa. (note: 1 in. = 25 mm; 1 ksi = 6.9 MPa)	28
Figure 5: Comparison of typical stress-strain curves for different types of HSS and conventional normal-strength ASTM A706 Grade 420 reinforcing bars.....	41
Figure 6: Discretization of the reinforced concrete column.....	46
Figure 7: Comparisons of global and local responses from the fiber model and test data for: (a) Test 1 (Barcley and Kowalsky 2020); (b) CH100 (Sokoli 2018); and (c) Unit 2 (Restrepo et al. 2006).	47
Figure 8: Empirical and fitted CDFs of drift ratio limit states for concrete columns reinforced	56
Figure 9: Comparison between drift ratios obtained from numerical analysis (measured) and those predicted from the proposed expressions for concrete columns reinforced with: (a) ASTM A706 Grade 550; (b) ASTM A615 Grade 690; (c) ASTM A1035 Grade 690.	59
Figure 10: Effective flexural stiffness of cracked reinforced concrete sections reinforced with: (a) ASTM A706 Grade 550; (b) ASTM A615 Grade 690; and (c) ASTM A1035 Grade 690.....	64
Figure 11: Stress-stain relations for rebars with d_b of 12.7 and 15.88 mm from monotonic tension tests..	72
Figure 12: Comparison of stress-strain relations generated using extensometer and LVDT.....	72
Figure 13: Sinusoidal loading waveform.	74
Figure 14: Typical stress-strain hysteresis relations of 15.88 mm diameter rebars gripped at $6d_b$ subjected to sinusoidal loading protocols with strain amplitudes, ϵ_a of: (a) 0.01; (b) 0.02; (c) 0.03; and (d) 0.04....	77
Figure 15: Typical stress-strain hysteresis relations of 15.88 mm diameter rebars gripped at: (a) $6d_b$; (b) $9d_b$; (c) $12d_b$; and (d) $15d_b$ subjected to sinusoidal loading protocol with a strain amplitude, ϵ_a of 0.01	77

Figure 16: Typical fracture patterns of bars: (a) typical pattern across the barrel of the rebar; and (b) typical pattern along the base of the transverse rib.	82
Figure 17: Fatigue life relationship based on half cycles to failure for ASTM A1035 Grade 690 reinforcing bars as well as those calibrated with results of other types of reinforcing steel.	84
Figure 18: Comparison between the predicted and measured fatigue life.	84
Figure 19: Relationship between β and λ	89
Figure 20: Relationship between a and λ	89
Figure 21: Comparison between the fatigue life predictions of the proposed model and those proposed by Kashani et al. (2015) and Tripathi et al. (2018) and the measured fatigue life of ASTM A1035 Grade 690 at buckling lengths of (a) $6d_b$; (b) $9d_b$; (c) $12d_b$; and (d) $15d_b$	90
Figure 22: Relationships between cyclic hysteresis energy and the number of cycles for specimens 15.88- $6d_b$ -0.01 (2) and 15.88- $15d_b$ -0.01 (2).	91
Figure 23: Fatigue life relationships for ASTM A1035 Grade 690 reinforcing bars based on total energy.	93
Figure 24: Relationship between $C1$ and λ	93
Figure 25: Comparison of tensile stress-strain responses of ASTM A706 Grade 550 (Overby et al. 2017), ASTM A1035 Grade 690 (Aldabagh and Alam 2021), and ASTM A706 Grade 420 (Overby et al. 2017).	99
Figure 26: Proposed procedure for low-cycle fatigue damage prediction analysis.	104
Figure 27: Discretization of the concrete bridge column.	107
Figure 28: (a) Measured and predicted responses at member level; (b) Measured and predicted responses at section level; (c) Predicted damage index versus $2Nf$ plots; and (d) load histories applied to the columns.	108
Figure 29: Bar fracture index versus ductility demand for bridge columns reinforced with: (a) ASTM A706 Grade 420; (b) ASTM A706 Grade 550; and (c) ASTM A1035 Grade 690.	116

Figure 30: Computed damage indices for rebars in concrete columns reinforced with ASTM A706 Grade 550 and subjected to: (a) crustal earthquakes, and (b) subduction earthquakes at μ_d level of 4.	119
Figure 31: Computed damage indices for rebars in concrete columns reinforced with ASTM A1035 Grade 690 and subjected to: (a) crustal earthquakes, and (b) subduction earthquakes at μ_d level of 2.	119
Figure 32: Stress-strain response of ASTM A1035 Grade 690 reinforcing bar.....	126
Figure 33: Selected bridge configuration (dimensions are in mm) (reproduced with permission from the project team).	129
Figure 34: Finite element modeling of the bridge pier.	132
Figure 35: Comparison of experimental and numerical responses of column reinforced with (a) conventional steel, and (b) ASTM A1035 Grade 690 steel.	133
Figure 36: Response spectra, mean response spectra, and mean response spectra \pm one standard deviation of response spectra of (a) original ground motions and (b) spectrally matched ground motions	138
Figure 37: Static pushover curves of all sections.....	141
Figure 38: Fragility curves of all sections.....	144
Figure 39: Moment-curvature relationships of bridge pier sections with diameter of (a) 1220 mm and (b) 914 mm.	147

ACKNOWLEDGEMENTS

First of all, I would like to express my deepest gratitude to my supervisor, Dr. M. Shahria Alam, who provided outstanding guidance, support and encouragement throughout the course of my studies. I feel truly honoured to have the opportunity of being his student. The completion of this thesis would not have been possible without his knowledge and dedication to which I will always feel indebted.

I offer my enduring gratitude to my supervisory committee, Dr. Ahmad Rtiel and Dr. Abbas Milani, whose constructive comments and thoughtful questions greatly helped shaping and refining my research.

I was very fortunate to work with an exceptional team of graduate students with whom I have had many discussions on the work presented in this dissertation. I am deeply grateful for their friendship, help, and support. Special thanks go to Sherif Osman, Anas Issa, Faroque Hossain, Jhordy Rodríguez, Saqib Khan, Maher Al Hawarneh, Ahmad Rahmzadeh, and Charles Rockson for making my doctoral endeavor a pleasant and rewarding experience.

I would like to acknowledge the funding received from the University of British Columbia through the University Graduate Fellowship and the Eminence Program. I would also like to acknowledge the funding received from Mitacs and associated partner organization, McElhanney, through the Mitacs Accelerate Fellowship. The support of MMFX Technologies Corporation through the generous donation of the high-strength ASTM A1035 reinforcing steel is gratefully acknowledged.

I extend my deepest gratitude to my parents whose support, sacrifice, and encouragement made this achievement and others a reality to me.

Last but not least, I would like to express by deepest and most heartfelt gratitude to my wife for her love, patience, and support that got me through the trials of this daunting enterprise.

To my parents,

Maad Al Dabagh & Taghrid Hadad,

and to my wife,

Zainab Al Rikabi

CHAPTER 1: INTRODUCTION

1.1 General

As technology advances, new types of alloys are being introduced by steel reinforcement manufactures to produce reinforcing bars exhibiting certain desirable characteristics. This is normally achieved by altering the chemical composition whose effect on the properties of the alloy is well understood. High-strength steel (HSS) reinforcement offering higher strength and enhanced corrosion resistance is one of the common alternatives to conventional steel in the concrete construction industry. Steel reinforcing bars are generally identified as HSS bars when exhibiting a yield strength in excess of 550 MPa. Several mills in the United States and worldwide have started producing different types of HSS, allowing the structural engineering community to make use of their potential benefits. Examples of HSS rebar types available in the North American steel rebar market include Grade 550 rebars conforming to ASTM A706 (ASTM 2016) and ASTM A615 (ASTM 2020a); Grade 690 conforming to ASTM A615 (ASTM 2020a) and ASTM A1035 (ASTM 2020b); and Grade 500W conforming to CSA-G30.18-M92 (CSA 2007). The stress-strain response varies among the different types and is not necessarily similar to that of the conventional normal-strength steel. The stress-strain curve of ASTM A1035 reinforcement, for instance, lacks a well-defined yield plateau, hence establishing its yield strength requires further attention when compared to other types of HSS reinforcement, as will be illustrated in subsequent sections of this study.

Practicing structural engineers in the construction industry are facing different challenges such as congestion of reinforcing steel in concrete sections possibly due to stringent architectural requirements, and corrosion of steel reinforcing bars in concrete members due to the corrosive surrounding environment. ASTM A1035 steel, with its enhanced strength and corrosion resistance, is an effective tool to address these challenges. Clearly, higher yield strength relieves the rebar congestion by reducing the amount of required reinforcement. Due to this reduction, the placement productivity of reinforcement and concrete is improved, thereby promoting reinforced concrete (RC) members of higher quality. Also, the reduction in

the amount of reinforcement leads to bringing down the overall cost through savings associated with labor cost which is a function of the material weight. In addition, ASTM A1035 steel with its enhanced corrosion resistance property promotes enhanced long-term durability in concrete structures exposed to severe environmental conditions. Examples of previous projects benefited from the implementation of HSS rebars are provided in a subsequent section.

In order to allow designers to make use of the potential benefits of ASTM A1035 and HSS in general, design codes, particularly in the United States, have been evolving to provide guidelines to design concrete structures reinforced with HSS reinforcement. In 2010, the American Concrete Institute (ACI) published the *Design Guide for the Use of ASTM A1035/A1035M Grade 100 (690) Steel Bars for Structural Concrete* (ACI ITG-6R) (ACI 2010). The recommendations provided in that guide were mainly addressing those requirements of ACI 318 (2008) that limit the efficient use of the HSS in structural concrete. Just recently, ACI Committee 439 released ACI 439.6R which is an updated version of the ACI ITG-6R, hence superseding it (ACI 2019a). In addition, in 2007, NCHRP project 12-77 was initiated to evaluate and propose appropriate guidelines to the AASHTO LRFD Bridge Design Specifications to design concrete structures reinforced with ASTM A1035 reinforcement as well as other types of steel reinforcement lacking discernable yield plateau (Shahrooz et al. 2011). The project recommendations were first incorporated into the 2013 interim revisions of the AASHTO LRFD Bridge Design Specifications, and are currently presented in the eighth edition of the AASHTO LRFD Bridge Design Specifications (AASHTO 2017). In addition, some DOTs released ASTM A0135 rebar-specific documents such as the *Structural Design Guidelines for Concrete Bridge Decks Reinforced with Corrosion-Resistant Reinforcing Bars* which was released by VDOT in 2014 (Salomon and Moen 2014). On the contrary, design codes in Canada lag behind the US standards where the CSA A23.3 and the CSA S6 do not provide guidelines specifically addressing HSS reinforcement (CSA 2019a; CSA 2019b). These design codes do not prevent the use of HSS reinforcement but impose strict limitations on the value of the design strength of reinforcement, consequently making it less efficient. However, despite the current strength limitations in Canada, to make use of the superior corrosion resistance of ASTM A1035 steel, the Ministry of Transportation in Alberta

has recently updated its Bridge Structure Design Criteria Version 7.0 (BSDC) to reflect that ASTM A1035 reinforcement or solid stainless steel are the only two acceptable types of steel to be used in bridge decks with Class 2 exposure (BSDC 2018). Similarly, The Ministry of Transportation and Infrastructure in British Columbia has introduced ASTM A1035 reinforcement into its bridge standards and procedures manual as alternative corrosion-resistant reinforcing steel (BC MoTI 2016).

The vast majority of the revisions introduced in design codes permitted the use of HSS rebars as main reinforcement only in capacity-protected elements, i.e. not part of the seismic-force-resisting system. The only exception is in the ACI 318 (2019b) where the use of HSS reinforcement conforming to ASTM 706 Grade 550 and 690 is permitted in special moment frames and structural walls resisting seismic loads, respectively. Concerns related to the performance of HSS in seismic applications stem from the known fact that the increase in yield strength is often associated with a reduction in inelastic strain capacity, the ratio of tensile to yield strength, and length of the yield plateau. This would lead to an undesirable seismic performance by limiting the spread of plasticity in the potential plastic hinge region, and potentially decreasing ductility capacity. To alleviate the concerns over the performance of HSS in seismic applications, much research has been conducted to evaluate the cyclic performance of concrete columns reinforced with HSS (Restrepo et al. 2006; Rautenberg et al. 2013; Trejo et al. 2016; Barbosa et al. 2016; Li et al. 2018; Sokoli 2018 Barclay and Kowalsky 2020). The results indicate that, other than dissipating less energy, concrete columns reinforced with HSS could exhibit comparable performance in terms of drift and flexural strength capacities to similar columns reinforced with conventional steel. Despite these findings, design code committees are still reluctant to permit the use of HSS in seismic applications. According to the *ATC-98 Project on Seismic Design of Concrete Structures with High-Strength Reinforcement* (Kelly et al. 2017), there is a need for additional research on the seismic performance of HSS before complete design recommendations for the use of HSS in seismic applications can be made.

To promote the use of HSS in seismic applications in bridges, and to further alleviate design code committees' concerns, design guidelines on the use of different types of HSS in RC columns need to be established. In the last decade, seismic design provisions in several design codes such as the *Canadian*

Highway Bridge Design Code (CHBDC) (CSA 2019b) and *New Zealand Bridge Manual (NZT 2018)* have been incorporating performance-based design (PBD) as an alternative to the classical force-based design (FBD). Unlike the FBD where structures are primarily designed to achieve only the traditional life-safety performance level, in PBD, structures are designed to achieve multiple performance levels when subjected to different levels of seismic hazards. Each performance level (sometimes referred to as “service level”) needs to be explicitly described and associated with a damage state. For instance, in the CHBDC, immediate, service limited, service disruption, and life safety performance levels are associated with minimal, repairable, extensive, and probable replacement damage states, respectively (CSA 2019b). An integral component of the PBD is the quantification of the damage states by means of engineering limit states which may be expressed as limiting values of material strains, deformations, drifts, curvatures, or damage indices. For this reason, in the past two decades, several experimental programs have been executed to relate damage states of concrete columns reinforced with conventional steel to material strains (Kowalsky 2000; Lehman et al. 2004; Goodnight et al. 2016), drifts (Berry 2006), and ductility capacities (Hwang et al. 2001). In addition, relating the damage states of concrete columns reinforced with conventional steel to engineering parameters has been achieved by experimentally verified numerical models. Babazadeh et al. (2015) employed a three-dimensional (3D) continuum-based finite element model to predict the intermediate damage states in RC bridge columns. Also, Billah and Alam (2016) utilized fiber element-based nonlinear models to develop performance-based damage states for concrete columns reinforced with different types of shape memory alloys.

Due to the significant differences between the mechanical properties of HSS and that of conventional normal-strength steel, the question of whether the engineering limit states developed for concrete columns reinforced with conventional steel would apply to those reinforced with HSS arises. Sokoli et al. (2017) demonstrated through cyclic tests that HSS rebars in columns with lower longitudinal reinforcement ratios experience larger strain demands than conventional normal-strength rebars at all drifts. This implies that the engineering limit states, which have been originally developed for normal-strength steel, found in literature, and design codes may not be applicable to bridge columns reinforced with HSS.

Research work establishing engineering limits states specifically applicable to concrete columns reinforced with different types of HSS is very limited. Barclay and Kowalsky (2020) executed an experimental program to establish strain limit states for concrete columns reinforced with ASTM A706 Grade 550. However, in Barclay and Kowalsky (2020), only four columns were tested and one type of HSS was considered. As a consequence, the established strain limits were limited and not applicable to concrete columns reinforced with different types of HSS having a wider range of geometrical and material properties. Billah and Kabir (2020) employed incremental dynamic analysis to develop predictive analytical expressions of the drift ratios at the inception of rebar yielding, concrete cover spalling, and longitudinal rebar buckling for high-strength concrete bridge columns reinforced with HSS. The proposed expressions by Billah and Kabir (2020) are applicable to concrete columns reinforced with all types of HSS with yield strength ranging between 550 and 750 MPa (i.e., irrespective of the ASTM standard to which they conform). This implies that despite their significance, the differences in mechanical properties of HSS conforming to different ASTM standards were not considered in the expressions proposed by Billah and Kabir (2020). Nevertheless, those expressions were considered in this study for comparison purposes.

Another critical aspect of the design that must be considered before design recommendation can be made is the low-cycle fatigue performance of HSS rebars. In a seismic event, the longitudinal reinforcing bars at critical sections such as those falling within the potential plastic hinge regions undergo large inelastic tension-compression strain reversals to accommodate the significant inelastic deformations caused by the earthquake loading. Due to these strain reversals, damage accumulates in the reinforcement and eventually leads to fracture. This type of failure is called low-cycle fatigue. The number of cycles to fatigue failure, or the so-called fatigue life, in reinforcing bars typically does not exceed 1000 when large strains beyond the elastic limit are applied (Ghannoum and Slavin 2016). Limited experimental studies have investigated the low-cycle fatigue performance of high-strength steel reinforcing bars where the vast majority of fatigue tests in the past were conducted on ordinary regular-strength steel reinforcing bars. Examples of ordinary reinforcing bars include ASTM A615 Grade 420 (ASTM 2020a) and ASTM A706 Grade 420 (ASTM 2016), for which the yield strength generally does not exceed 500 MPa. Ghannoum and Slavin (2016)

evaluated the low-cycle fatigue performance of other types of HSS reinforcing bars conforming to ASTM A615 (2020a) and ASTM A706 (2016) with minimum yield strengths of 690 and 550 MPa which are designated as ASTM A615 Grade 690 and ASTM 706 Grade 550, respectively. Variables considered in the investigation included production method, bar size, loading protocols, and bar unsupported length. Test results indicated that the low-cycle fatigue performance of HSS is marginally poorer than that of regular-strength steel. One of the most influencing parameters on the low-cycle fatigue performance was the bar unsupported length. Decreasing the bar unsupported length reduces the buckling amplitude and strain concentrations in the bar, and consequently substantially improves the low-cycle fatigue performance. However, experimental low-cycle fatigue test data for ASTM A1035 steel do not seem to exist. The only reported fatigue tests undertaken using ASTM A1035 steel reinforcing bars are high-cycle fatigue tests by DeJong et al. (2006). However, in such tests, the strain amplitude rarely exceeds 0.01, hence making them inappropriate to understand the fatigue characteristics of reinforcing bars for seismic applications.

1.2 Objectives

The overarching objective of this study is to propose performance-based design recommendations on the use of high-strength steel bars in concrete bridge columns. The specific tasks that will be completed as part of this research are as follows:

1. Develop expressions to predict the drift ratio limit states of concrete bridge columns reinforced with HSS.
2. Experimentally evaluate the low-cycle fatigue performance of ASTM A1035 Grade 690 bars.
3. Identify conditions under which HSS bars can achieve low-cycle fatigue performance comparable to that of the conventional normal-strength steel in concrete bridge piers.
4. Develop seismic fragility curves for a bridge pier alternately reinforced with HSS and conventional normal-strength steel.

1.3 Thesis Organization

This thesis is organized into seven chapters including this chapter which provides a brief background and motivation for this research. The general and specific objectives of this study are also outlined in this chapter. The remaining chapters describe the research as follows:

In Chapter 2, much of the knowledge generated from experimental and analytical research programs performed on HSS reinforcement is compiled and presented. First, an overview of the common methods adopted by steel manufactures to produce HSS reinforcement is provided. Then, the main characteristics of different grades of HSS reinforcement from a material perspective are presented. After that, the performance of HSS as corrosion resistant reinforcement, along with several serviceability considerations are explored. The behavior of beams, slabs, and columns reinforced with HSS rebars when subjected to shear, bending moment, and/or axial load is evaluated. The relevant clauses (if found) in available design guides are also discussed. Lastly, existing challenges limiting the applications of HSS reinforcement as well as future recommendations allowing for more efficient use of such reinforcement are provided.

Chapter 3 develops simplified expressions of the drift ratio limit states for circular concrete columns reinforced with different types of HSS bars. The effects of geometry-, section-, and material-related parameters on the drift ratio limit states are first examined by means of factorial analysis. This chapter also demonstrates how the Monte Carlo Sampling technique was employed to generate sufficient data for the development of the drift ratio limit states expressions. The procedure of fitting the generated data to simplified expressions through machine learning-based symbolic regression analysis is described. Lastly, comparisons are made between the predications of the proposed expressions and those obtained from numerical analysis as well as experimental results.

To ensure that HSS rebars in RC bridge columns designed using the drift ratio limit states proposed in Chapter 3 do not experience premature fracture under earthquake loading, low-cycle fatigue performance of HSS needs to be examined. Chapter 4 presents an experimental program designed to evaluate the low-cycle fatigue performance of ASTM A1035 Grade 690 steel. This chapter evaluates the effect of bar

diameter, strain amplitude, and buckling length on the fatigue life of ASTM A1035 Grade 690 bars. This chapter demonstrates how the experimentally generated data were employed to calibrate existing fatigue life models. Comparisons between the proposed fatigue life models and those found in the literature were made.

In Chapter 5, by utilizing the results from the previous chapter, conditions under which HSS rebars can achieve adequate low-cycle fatigue performance in comparison to that of benchmark ASTM A706 Grade 420 steel bars in concrete bridge columns are identified. This chapter adopts a fatigue-based damage model to evaluate the low-cycle fatigue performance of HSS in concrete bridge columns under different conditions of displacement ductility level (2, 4, and 6), earthquake type (crustal and subduction earthquakes), and ratio of hoop spacing to longitudinal bar diameter ratio (4 and 6). Appropriate design recommendations are made based on comparisons between the low-cycle fatigue performance of HSS and that of the benchmark ASTM A706 Grade 420.

Chapter 6 develops seismic fragility curves for a concrete bridge pier alternately reinforced with conventional normal-strength steel and HSS. The generated fragility curves are employed in this chapter to assess the vulnerability of the bridge pier to a seismic hazard representative of the seismicity in Vancouver, British Columbia. Based on such assessment, the adequacy of certain clauses of applicable design codes is evaluated.

Finally, Chapter 7 summarizes major findings and conclusions drawn from this dissertation. Future research needs are also outlined in this chapter.

CHAPTER 2: HIGH-STRENGTH STEEL REINFORCEMENT IN STRUCTURAL CONCRETE: STATE-OF-THE-ART REVIEW

2.1 General

As technology advances, new types of alloys are being introduced by steel reinforcement manufactures to produce reinforcing bars exhibiting certain desirable characteristics. This is normally achieved by altering the chemical composition whose effect on the properties of the alloy is well understood. Steel reinforcing bars are generally classified as HSS bars when exhibiting a yield strength of more than 550 MPa. Such types of reinforcement are being produced in several countries and are designated based on the material standards adopted by each country. ASTM A1035 steel offering higher strength and enhanced corrosion resistance is one of the common alternatives to conventional steel in the concrete construction industry. Its stress-strain curve lacks a well-defined yield plateau, hence establishing the yield strength requires further attention when compared to other types of HSS reinforcement, as will be illustrated in subsequent sections of this study.

Practicing structural engineers in the construction industry are facing different challenges such as congestion of reinforcing steel in concrete sections possibly due to stringent architectural requirements, and corrosion of steel reinforcing bars in concrete members due to the corrosive surrounding environment. ASTM A1035 steel, with its enhanced strength and corrosion resistance, is an effective tool to address these challenges. Clearly, higher yield strength relieves the rebar congestion by reducing the amount of required reinforcement. Due to this reduction, the placement productivity of reinforcement is improved, thereby promoting reinforced concrete members of higher quality. Besides improving concrete quality, the reduction in the amount of reinforcement leads to bringing down the overall cost through savings associated with labor cost which is a function of the material weight. In addition, ASTM A1035 steel reinforcement with its enhanced corrosion resistance property promotes enhanced long-term durability in concrete structures exposed to severe environmental conditions. Thomas et al. (2013) assessed the impact of using ASTM 1035 Grade 690 versus ASTM A615 Grade 420 steel reinforcement on the construction productivity

by developing two different designs of a hospital using the two types of reinforcement. ASTM A1035 steel was found to be effective in reducing the weight of reinforcement in beams but not in slabs, post-tensioned girders, and columns. This was due to certain code limitations related to minimum reinforcement requirement preventing significant reduction in the required steel area. The study recommended replacing conventional steel with ASTM A1035 steel in expensive labor markets where weight reduction in reinforcement can lead to substantial savings in the labor cost. In Virginia, as part of the Innovative Bridge Research and Construction Program (IBRCP), two separate bridge decks were built to compare the placement costs of epoxy-coated reinforcing (ECR) steel and ASTM A1035 steel (Sharp and Moruza 2009). Crack sealing operation was required for the bridge deck reinforced with ECR which resulted in a significant increase in the unit cost of ECR, making it less cost-effective compared to ASTM A1035 steel. Shen et al. (2019) implemented Monte Carlo simulation to quantify the probabilistic life-cycle cost of bridge decks reinforced with conventional steel and ASTM A1035 Steel. ASTM A1035 steel was found to have lower lifecycle costs in bridge decks compared to conventional steel. Over the past two decades, several state departments of transportation (DOTs) across the United States such as Virginia (VDOT), Michigan (MDOT), and Utah (UDOT), among others, have been studying the applicability of replacing ECR with ASTM A1035 steel to achieve a service life of 75 years. ASTM A1035 steel with its superior corrosion resistance compared to ECR allows for extending the useful life of highway structures. Demonstration projects, with some involving the construction of full-scale bridge decks, indicated that, with proper detailing, bridge decks reinforced with ASTM A1035 steel are characterized with satisfactory in-service performance, lower lifecycle cost, and extended anticipated service life compared to bridge decks reinforced with conventional steel (Kahl 2007; Barr and Wixom 2009; Salomon and Moen 2017). Rebars conforming to ASTM A1035 are listed as an alternative corrosion-resistant reinforcement in bridge design manuals of 11 DOTs in the United States. These DOTs are Washington, Oregon, California, Montana, Idaho, Texas, Mississippi, Florida, Virginia, Maryland, and Maine DOTs.

In order to allow designers to make use of the potential benefits of ASTM A1035 and HSS in general, design codes, particularly in the United States, have been evolving to provide guidelines to design

concrete structures reinforced with HSS reinforcement. In 2010, the American Concrete Institute (ACI) published the *Design Guide for the Use of ASTM A1035/A1035M Grade 100 (690) Steel Bars for Structural Concrete* (ITG-6R-10) (ACI 2010). The recommendations provided in that guide were mainly addressing those requirements of ACI 318 (2008) that limit the efficient use of the HSS in structural concrete. Just recently, ACI Committee 439 released ACI 439.6R (2019a) which is an updated version of the ACI ITG-6R, hence superseding it (ACI 2019a). In addition, in 2007, NCHRP project 12-77 was initiated to evaluate and propose appropriate guidelines to the AASHTO LRFD Bridge Design Specifications to design concrete structures reinforced with ASTM A1035 reinforcement as well as other types of steel reinforcement lacking discernable yield plateau (Shahrooz et al. 2011). The project recommendations were first incorporated into the 2013 interim revisions of the AASHTO LRFD Bridge Design Specifications, and are currently presented in the eighth edition of the AASHTO LRFD Bridge Design Specifications (AASHTO 2017). In addition, some DOTs released ASTM A0135 rebar-specific documents such as the *Structural Design Guidelines for Concrete Bridge Decks Reinforced with Corrosion-Resistant Reinforcing Bars* which was released by VDOT in 2014 (Salomon and Moen 2014). On the contrary, design codes in Canada lag behind the US standards where the CSA A23.3 and the CSA S6 do not provide guidelines specifically addressing HSS reinforcement (CSA 2019a; CSA 2019b). These design codes do not prevent the use of HSS reinforcement but impose strict limitations on the value of the design strength of reinforcement, consequently making it less efficient. However, despite the current strength limitations in Canada, to make use of the superior corrosion resistance of ASTM A1035 steel, the Ministry of Transportation in Alberta has recently updated its Bridge Structure Design Criteria Version 7.0 (BSDC) to reflect that ASTM A1035 reinforcement or solid stainless steel are the only two acceptable types of steel to be used in bridge decks with Class 2 exposure (BSDC 2018). Similarly, The Ministry of Transportation and Infrastructure in British Columbia has introduced ASTM A1035 reinforcement into its bridge standards and procedures manual as alternative corrosion-resistant reinforcing steel (BC MoTI 2016). The imposed limitations on design strength are primarily arising from the uncertainty associated with the behavior of members reinforced with HSS rebars when subjected to different types of loads.

This chapter attempts to compile and present much of the knowledge generated from experimental and analytical research programs involving HSS with emphasis on ASTM A1035 which is the focus of this study. First, an overview of the common methods adopted by steel manufactures to produce HSS reinforcement is provided. Then, the main characteristics of different grades of HSS reinforcement from a material perspective are presented. After that, the performance of HSS as corrosion resistant reinforcement, along with several serviceability considerations are explored. The behavior of beams, slabs, and columns reinforced with HSS rebars when subjected to shear, bending moment, and/or axial load is evaluated. The relevant clauses (if found) in available design guides are also discussed. The bond characteristics between HSS reinforcement and concrete, and the applicability of the current splice and development length related design procedures to HSS rebars are examined. The seismic performance of concrete structures reinforced with HSS rebars is evaluated. Lastly, existing challenges limiting the applications of HSS reinforcement as well as future recommendations allowing for more efficient use of such reinforcement are provided.

2.2 Production of High-Strength Steel

Three common methods are generally used to produce HSS, namely: (1) cold working, (2) micro-alloying, and (3) quenching and tempering. These three methods are described next. Cold working, or so-called cold rolling, is considered one of the earliest methods developed to produce HSS rebars (Caifu 2010). This method is normally performed at temperature levels below the steel recrystallization temperature. At the recrystallization temperature, dislocation and movement of particles are generated, hence forming crystallographic defects or irregularities within the crystal structure. The formation of these defects strongly influences the yield strength and ductility of the reinforcement. The final product using this production method tends to be harder than conventional steel but lacks a clear yielding plateau. In addition, with this method, the ductility is adversely affected, and therefore, it is not recommended to adopt the cold working method to produce steel reinforcement used in earthquake-resistant concrete structures (NIST 2014).

In micro-alloying, small percentages (ranging from 0.02 to 0.15%) of titanium (Ti), niobium (Nb), or vanadium (V) are added to produce the HSS (Caifu 2010). This method utilizes two mechanisms which

are fine-grain strengthening and precipitation strengthening. In fine-grain strengthening, the thermo-mechanical process is adopted to form very fine grains in the steel product through the pinning of grain boundaries, i.e. the area between the grains. According to the Hall-Petch relationship, reducing the grain size increases the strength of the steel, hence maintaining fine grain size is essential to produce steel of higher yield strength (Pande and Cooper 2009). After the fine-grain strengthening, the precipitation strengthening is initiated when the intermetallic carbides are dispersed through the grains, and therefore pinning line defects (dislocations) are formed, causing more increase in the yield strength. Titanium micro-alloying is very effective in precipitation strengthening, but the titanium tends to react and combine with oxygen, sulfur, and nitrogen making it difficult to control the properties of the strengthened product. Niobium micro-alloying requires relatively low temperature and high deformation at the end of production making it unsuitable to produce HSS which normally involves high rolling temperatures and less deformation (Gervasyev et al. 2019). This method is commonly used in the production of steel sheets and strips. Vanadium micro-alloying is widely used in the production of high-strength weldable reinforcement. The increase in yield strength in vanadium micro-alloying is primarily due to the precipitation of carbides and nitrides (Hamed et al. 2018). In this process, only 35.5% of the vanadium forms carbides and nitrides, while 56.3% of the vanadium does not contribute to the yield strength since it turns into a solid solution dissolved in the matrix. A higher percentage (up to 70%) of vanadium forming carbides and nitrides can be achieved by the addition of nitrogen (Caifu, 2010). The negative impact of stain aging on the steel properties is eliminated due to the ability of vanadium to pin the soluble nitrogen.

Quenching and tempering is a two-stage heat-treatment process used to produce steel reinforcement with higher strength and toughness. The first step is quenching which involves rapid cooling of metals in water, oil, forced air, or inert gases after heating them to the austenitic phase, i.e. when the solid steel starts to crystallize. The second step is tempering in which the quenched steel is heated to modify the microstructure leading to a decrease in toughness and an increase in ductility (Yan et al. 2014).

2.3 Mechanical Properties of ASTM A1035 Reinforcement

Typical stress-strain relationships of ASTM A1035 Grade 690 reinforcing steel, along with that of ASTM A615 Grade 420 are presented in Figure 1 for comparison. ASTM A1035 reinforcing steel exhibits higher tensile strength, yet it lacks a well-defined yield point and yield plateau. The stress-strain curve of HSS is characterized by a linear portion up to a proportional limit (at stress from 420 to 550 MPa), followed by a nonlinear relationship up to a tensile strength of 1125 MPa. The strain at maximum tensile strength ranges from 0.04 to 0.06. The elongation in the gauge length of 200 mm across the fracture for the bar ranges from 0.08 to 0.13 (ACI 2019a). Others have reported elongation in 200 mm across the fracture in the range of 0.08 to 0.10 (WJE 2008). The reason for the noticeable variation in the rupture strain among different studies is the inaccuracy associated with the strain gauge and extensometer measurements when capturing the ultimate behavior (Shahrooz et al. 2011). By comparison, the elongation in the 200 mm gauge length across the fracture for ASTM A615 Grade 420 ranges from 0.09 to 0.12, and that for ASTM A706 Grade 420 ranges from 0.14 to 0.20 (ACI 2019a). The initial modulus of elasticity is 200 GPa, which decreases slowly as the stress approaches the proportional limit, and decreases more rapidly thereafter as evident in Figure 1. Due to the absence of clearly defined yield plateau, the yield strength can be established by several methods: (1) 0.35% extension under load (EUL) method; (2) 0.5% EUL method; and (3) 0.2% offset method being the most common. In the 0.2% offset method, the yield strength is the stress on the engineering stress-strain curve at its intersection with a line having a slope equal to the modulus of elasticity of steel and starting from a strain of 0.2%. In the 0.35% and 0.5% EUL methods, the yield strength is the stress corresponding to a strain of 0.0035 and 0.005, respectively. Figure 2 illustrates how these methods are used to establish the yield strength of ASTM A1035 reinforcing steel. Yield strength values determined based on the 0.2% offset method are characterized with the most variability (COV = 10.3%), while those determined based on absolute strain approaches are found to be consistent at each strain level considered (COV = 7%). According to the NCHRP report 679, regardless of the method used to determine the yield strength, the condition that $f_u > 1.25f_y$ is always stratified (Shahrooz et al. 2011). ASTM A1035/A1035M

Standard specifies two minimum yield strength levels based on the 0.2% offset method which are 690 and 830 MPa. Rebars meeting the minimum yield strength requirement of 690 and 830 are designated as Grade 690 and Grade 830, respectively (ASTM 2019). The measured yield strength of ASTM A1035 Grade 690 steel, based on the 0.2% offset method, normally exceeds 830 MPa, i.e. minimum yield strength for Grade 830, hence steel manufacturers are mainly focusing on producing only Grade 690 (WJE 2008).

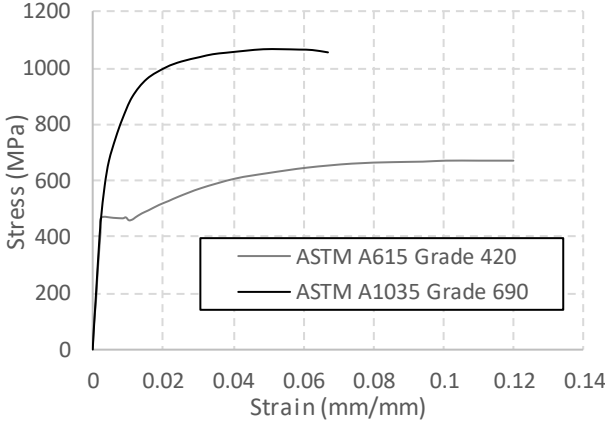


Figure 1: Stress-strain curves for ASTM A1035 and ASTM A615 reinforcing steel.

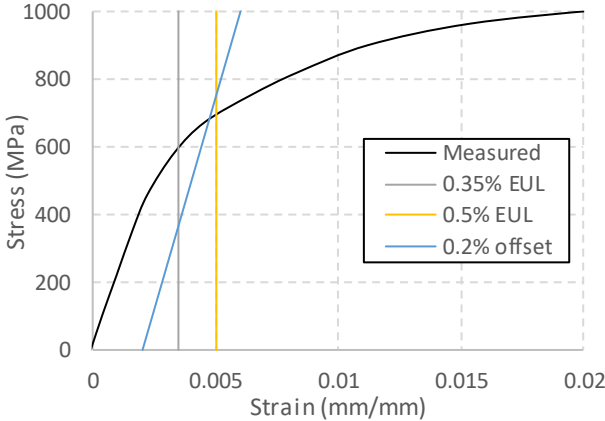


Figure 2: Different methods to establish the yield strength of ASTM A1035 reinforcing steel.

Two functions have been proposed to accurately capture the stress-strain relationship of ASTM A1035 reinforcing steel including Ramberg-Osgood (R-O) function (Ramberg and Osgood 1943) and the PCI stress-strain equation for prestressing steel. The constants in both equations were calibrated to closely match the measured stress-strain response of the ASTM A1035 reinforcing steel (Shahrooz et al. 2014;

Mast et al. 2008). The final calibrated version of the PCI stress-strain equation to predict the stress in steel (f_s) beyond the proportional limit is as follows:

$$f_s = \left\{ 1172 - \frac{2.379}{\varepsilon_s + 0.00104} \right\} \quad (1)$$

where ε_s is the corresponding reinforcing steel tensile strain ranging from 0.00241 to 0.060. The final version of the R-O function, which was calibrated using U.S. customary units to fit the experimentally measured stress-strain response of #8 bar size, is given in Eq. 2 (Shahrooz et al. 2014).

$$f_s = 29000\varepsilon_s \left\{ 0.0145 + \frac{1 - 0.0145}{[1 + (200\varepsilon_s)^{2.4}]^{1/2.4}} \right\} \leq f_{pu} \quad (2)$$

where f_s is the stress in the steel in ksi; ε_s is the corresponding strain; and f_{pu} is the ultimate strength in ksi. DeJong et al. (2006) reported that the high-cycle fatigue performance of HSS is superior to that of conventional Grade 420 steel. Their tests demonstrated that HSS rebars exhibit a fatigue strength (at $N = 1$ million cycle) of 310 MPa, while that of Grade 420 steel is 165 MPa. Extending the applicability of fatigue or endurance limit of conventional steel found in the AASHTO LRFD Bridge Design Specifications to reinforcing steel for higher-strength steel yields conservative results (Soltani et al. 2012). High-cycle fatigue considerations are expected to have little to no effect on the design of concrete structures reinforced with steel having $f_y \leq 690$ MPa (Soltani et al. 2012).

2.4 Corrosion Performance of ASTM A1035 Reinforcement

ASTM A1035 reinforcing steel is a micro-composite Fe-C-Cr-Mn alloy furnished to three different chemical compositions, designated as Alloy Type CL, CM, and CS. Table A.1 in Appendix A provides a comparison between the chemical composition of ASTM A1035 Grade 690 and other types of reinforcing steel bars available in the market. The chromium content ranges from 2 to 10.9% in these alloys, with an average value of 9% (ASTM 2019). The 9% chromium content is too low for the ASTM A1035 reinforcing steel to be classified as stainless steel ($\text{Cr} > 10.5\%$) but sufficiently high to generate corrosion resistance superior to that of conventional steel, i.e. ASTM A615 or A706 (Shahrooz et al. 2011). A significant amount

of research has been carried out to evaluate the corrosion performance of ASTM A1035 steel reinforcement and compare it to that of other common alternatives such as ASTM A615 steel, LN316 stainless steel, epoxy-coated conventional steel, and ASTM A767 (Galvanized) steel. Table 1 provides a summary of the selected research works quantifying the corrosion performance of these types of reinforcement (the reader may refer to the cited work for further details). It is evident from Table 1 that ASTM A1035 reinforcement exhibit 2 to 10 times more corrosion resistance than the ASTM A615 steel. This is attributed to the formation of a dense chromium oxyhydroxide-based film which is more corrosion-resistant than the passive layer formed on carbon steel. ASTM A1035 steel exhibits lower corrosion resistance performance than the epoxy-coated A615 steel. Darwin et al. (2002) reported that bridge decks incorporating ASTM A1035 reinforcement are less cost-effective than the decks reinforced with epoxy-coated steel. However, their conclusion was based on a life cycle cost analysis that did not consider material savings resulting from the use of ASTM A1035 reinforcement, possibly due to design code restrictions on the design yield strength of ASTM A1035 reinforcement at that time. In addition, ASTM A1035 steel was found to be substantially less corrosion-resistant than LN316 stainless steel. Ji et al. (2005) reported that bridge decks containing LN316 stainless steel are characterized by lower total life-cycle cost when compared to ASTM A1035 and A615 epoxy-coated steel. However, it is well-established that, due to its high initial cost, utilizing LN316 stainless steel can only be justified in parts of the structure exposed to chlorides or other severe environments. ASTM A1035 steel reinforcement offers an intermediate corrosion performance, between that of ASTM A615 and LN316 stainless steel, at a cost cheaper than that of LN316 stainless steel, making it more suitable for a wider range of structural applications when compared to the other corrosion-resistant reinforcement alternatives.

Table 1: Quantitative Measures of Corrosion Performance of ASTM A1035 Steel.

Performance measure	Test	Units	ASTM A615	ASTM A1035	316LN Stainless	Epoxy-Coated A615	Galvanized A767	Citation
Time to corrosion initiation	Accelerated corrosion	days	92	245	>1082	-	-	(Clemena and Virmani 2004)
Time to corrosion initiation	Rapid macrocell	weeks	-	21.4	-	-	-	(Farshadfar 2017)
Time to corrosion initiation	Modified version of ASTM G109	years	2.3	15	-	-	4.8	(Darwin et al. 2007)
Critical chloride threshold		lb/yd ³	1.63	6.34	19.14	-	2.57	
Critical chloride threshold	Accelerated chloride threshold (ACT)	kg/m ³	0.5	4.6	10.8	-	-	(Trejo and Pillai 2004)
Critical chloride threshold	Tests include rapid macrocell tests, corrosion potential tests, bench-scale tests (the Southern Exposure and cracked beam tests), and two modified versions of the Southern Exposure test	kg/m ³	0.91 to 1.22	3.70 to 4.07	-	-	-	(Ji et al., 2005)
Weight loss	Accelerated corrosion (after 56 weeks)	%	19.21	2.43	-	-	-	(Seliem 2007)
Corrosion rate	Pore solution (after 26 weeks)	mA/m ²	43-50	10	-	-	-	(Fahim et al. 2019)
	Cracked-beam test (after 420 days)	µm/year	4-8	2.3	-	-	-	
Corrosion rate	Macrocell	µm/year	35.64	12	-	4.2	-	(Gong et al. 2002)
	Bench-scale (Southern Exposure test)		5.6	1.56	-	0.31	-	
	Bench-scale (Cracked-beam test)		4.84	2.7	-	0.92	-	
Corrosion rate	ASTM B117	µm/year	914.7	625	1.2	-	1190.2	(WJE 2006)

2.5 ASTM A1035 Reinforcing Steel in Flexural Members

2.5.1 *Longitudinal Reinforcement*

The use of HSS bars as an alternative to ASTM A615 Grade 420 bars in flexural members would not be effective in reducing reinforcement quantities or possibly member cross-section sizes if there are limitations on the design yield strength. Hence, Mast et al. (2008) and Shahrooz et al. (2014) evaluated ACI 318 and AASHTO provisions related to the use of high-strength reinforcing steel in flexural members, respectively. Prior to and including the ACI 318 (2011), reinforcement yield strength used for the design (defined as the stress corresponding to the strain of 0.0035) must not exceed 552 MPa (ACI 2011). Similarly, prior to and including the AASHTO (2012) edition of the AASHTO LRFD Bridge Design specifications, adopting a design yield strength value greater than 517 MPa was not permitted (AASHTO 2012). These limits prevented designers from taking full advantage of HSS reinforcement in flexural members. Mast et al. (2008) carried out numerical analysis on a rectangular singly reinforced concrete section having different reinforcement ratios to assess the adequacy of using a proposed idealized elastic-perfectly plastic stress-strain curve (similar to that used for ASTM A615 Grade 420) for ASTM A1035 Grade 690 steel in section analysis satisfying equilibrium and strain compatibility. The idealized elastic-plastic stress-strain relationship consists of an elastic portion with a modulus of elasticity of 200 GPa followed by a perfectly plastic behavior when $f_y = 690$ MPa. Mast et al. (2008) established the appropriate tension- and compression-controlled strain limits for the proposed simplified material model. Tensile strains in the reinforcement closest to the bottom surface greater than 0.009 are required to ensure tension-controlled behavior. Compression-controlled behavior occurs when these tensile strains are less than 0.004 (Mast et al. 2008). Simple beams reinforced with ASTM A1035 Grade 690 reinforcing steel and designed at tension-controlled strain limit of 0.009 exhibited similar ductility behavior when compared to those of the beams reinforced with ASTM 615 Grade 420 at tension-controlled strain limit of 0.005 (Mast et al. 2008). On the other hand, Shahrooz et al. (2014) carried out a similar analysis but considered sections having different concrete compressive strengths, and tension and compression longitudinal reinforcement

ratios. Their recommendations were similar to that of Mast et al. (2008) except for the following: (1) the yield point in the idealized elastic-perfectly plastic stress-strain curve is taken as the stress corresponding to strain equal to 0.0035 or 0.005 rather than 690 MPa (fixed value); and (2) the tension-controlled strain limit is 0.008 instead of 0.009. Flexural strength reduction factor ϕ versus extreme tensile strain, ϵ_t , relationships proposed by Mast et al. (2008) and Shahrooz et al. (2014) are presented and compared against that of ASTM A615 Grade 420 in Figure 3.

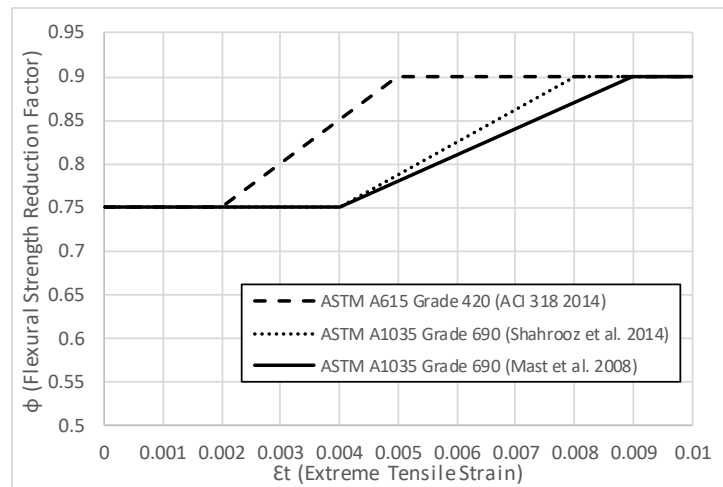


Figure 3: Comparison of strain limits for ASTM A1035 Grade 690 (Shahrooz et al. 2014; Mast et al. 2008) and ASTM A615 Grade 420.

The recommendations of Mast et al. (2008) on computing the flexural resistance of concrete beams reinforced with ASTM A1035 were incorporated into the ACI ITG-6R-10 (2010) (Currently referred to as ACI 439.6R-19). The ACI 318 (2019) permits the use of ASTM A1035 steel as longitudinal reinforcement in flexural members not designated as part of the seismic-force-resisting system. Shahrooz et al. (2014)'s recommendations are currently presented in the eighth edition of the AASHTO LRFD Bridge Design Specifications which permits the use of ASTM A1035 Grade 690 in flexural elements in Seismic Zone 1 (AASHTO 2017). According to AASHTO (2017), the value of f_y used in the design of concrete beams reinforced with HSS is equal to the specified minimum yield strength defined in the material standards. Consequently, for ASTM A1035 Grade 690, a design f_y of 690 MPa is appropriate since it is the specified minimum yield strength in the ASTM A1035 (2019) for ASTM A1035 Grade 690. Both the CSA A23.3

(2019a) and CSA S6 (2019b) do not permit the use of ASTM A1035 reinforcing bars and limit the design yield strength value to 500 MPa for other applicable types (such as CSA G30.18 Grade 500) of deformed reinforcement with a yield strength greater than 400 MPa. To prevent compression-controlled failure in flexural members reinforced with ASTM A1035 bars, Mast et al. (2008) suggested using compression reinforcement with $f_y = 550$ MPa. Aldabagh et al. (2018) demonstrated that compression reinforcement had little to no effect in controlling the concrete compression failure of concrete beams reinforced with ASTM A1035 Grade 690 bars. In addition, they reported that fiber-reinforced concrete is more effective in enhancing the flexural characteristics of such beams than compression steel.

A minimum amount of longitudinal reinforcement computed in accordance with ACI 318 requirements using $f_y = 690$ MPa must be provided at every section where tension reinforcement is required (ACI 2019a). Puranam (2018) confirmed that reducing the minimum longitudinal reinforcement ratio in slabs reinforced with HSS in inverse proportion to the increase in the yield strength is acceptable. Experimental tests of one-way slabs reinforced with HSS having a longitudinal reinforcement ratio as small as 0.09% exhibited rotational capacity greater than 4% (Puranam 2018). Moment redistribution is inapplicable to members containing ASTM A1035 bars until further research data becomes available (ACI 2019a). However, Puranam (2018) reported that beams designed to have a target tensile strain of 0.005 exhibited sufficient rotational capacity for moment redistribution.

2.5.2 Transverse Reinforcement

The performance of ASTM A1035 steel as transverse reinforcement in flexural members was first evaluated by Sumpter et al. (2009). The main two variables considered in their work were the stirrup spacing (152, 102, and 76.2 mm) and type of longitudinal and transverse steel reinforcement (ASTM A1035 and ASTM A615). Their main focus was the shear behavior under overload conditions in which the steel is subjected to high stress levels. Direct replacement of ASTM A615 stirrups with ASTM A1035 stirrups resulted in a small increase in the shear-carrying capacity and improved serviceability in terms of crack distribution and crack width. They demonstrated that with $f_y = 552$ MPa, the use of ACI, CSA, and

AASHTO design codes leads to conservative estimates of the shear strength, with the CSA being the most accurate. Since the failure of the test beams was governed by concrete crushing, the maximum stress developed in ASTM A1035 stirrups was 552 MPa. It was recommended to limit the design yield strength to 552 MPa to ensure the conservativeness of shear strength predictions (Sumpter et al. 2009). In 2011, Munikrishna et al. (2011) assessed the shear behavior of large-sized concrete beams reinforced with ASTM A1035 Grade 690 steel and designed to induce stresses of 550 and 690 MPa in the stirrups. They reported that it is feasible to reduce the transverse reinforcement ratio in concrete beams by using ASTM A1035 steel while maintaining shear strength similar to that of beams with higher transverse reinforcement ratio but reinforced with ASTM A615 Grade 420 steel. At ultimate, prior to the crushing of the concrete strut, the measured strains in the ASTM A1035 stirrups were equal to or greater than 0.0035 which corresponds to the stress of 690 MPa. Using a design yield strength value of 690 MPa to predict the shear strength of concrete beams transversely reinforced with ASTM A1035 steel was found to be acceptable if 135-degree hooks are provided (Munikrishna et al. 2011). The measured shear crack widths were within limits in the two research programs (Sumpter et al. 2009; Munikrishna et al. 2011). Shahrooz et al. (2017) conducted full-scale testing to examine the performance of ASTM A1035 steel stirrups in flexural members. Their findings were in conformity with Munikrishna et al. (2011). They recommended modifying AASHTO provisions to permit using $f_y = 690$ MPa when computing the shear strength if ASTM A1035 Grade 690 steel stirrups are used (Shahrooz et al. 2017). The ACI 439.6R (2019) considers Sections 11.1, 11.2, 11.4 and 11.5 of ACI 318 (2008) to be applicable when designing for shear and torsion in flexural members reinforced with ASTM A1035 bars (ACI 2019a). The ACI 439.6R (2019a) permits using $f_y = 552$ MPa in Eq. (11-2), (11-3), and (11-15) of ACI 318-08 to compute the shear capacity based on the recommendations of Sumpter et al. (2009). However, spacing and minimum quantity requirements of ACI 318-08, sections 11.4.5 and 11.4.6 must be satisfied. If shear cracking is a critical design consideration, f_y in the above equations must be limited to 410 MPa. In addition, due to the lack of research data, the value of f_y must be limited to 410 MPa in stirrups designed for torsion (ACI 439.6R 2019). The ACI 318 (2019b) permits the

use of ASTM A1035 to resist shear provided that its design yield strength is limited to 420 MPa. Shahrooz et al (2017)'s recommendations were incorporated into Article 5.7.2.5, 5.7.2.6, 5.7.2.7, and 5.7.3.3 of the AASHTO (2017) edition of the AASHTO LRFD Bridge Design Specifications. In these articles, which are related to the design of transverse reinforcement in flexural members, a design f_y of 690 MPa can be used when ASTM A1035 steel is used.

In lightly reinforced elements (with ρ less than 1%) containing longitudinal ASTM A1035 rebars, the use of ACI 318 provisions to compute the shear strength provided by the concrete leads to unsafe predictions (ACI 2019a). Consequently, ACI 439.6R requires that all lightly reinforced beams should contain minimum shear reinforcement. Desalegne and Lubell (2010) proposed a simplification to Hoult et al. (2008) model to predict the shear strength provided by the concrete, V_c , in lightly reinforced flexural members (beams and one-way slabs) containing only longitudinal ASTM A1035 rebars (without shear reinforcement) and subjected to insignificant axial load as follows:

$$V_c = \left(\frac{154}{1000+2.1d} \right) \sqrt{f'_c} b_w d \quad (3)$$

where d is the effective depth of longitudinal tension reinforcement, b_w is the web width, and f'_c is the concrete compressive strength. The proposed simplified model assumes a longitudinal reinforcement strain of 0.0042, which corresponds to a stress of 690 MPa.

The punching shear behavior of two-way slabs longitudinally reinforced with ASTM A1035 rebars was evaluated by Yang et al. (2010). Direct replacement of conventional steel bars with ASTM A1035 rebars resulted in a 27% increase in the punching shear resistance. Two-way slabs longitudinally reinforced with ASTM A1035 steel exhibited similar punching shear resistance, but lower stiffness and larger cracks, when compared to their ASTM A615-bar reinforced counterparts with higher longitudinal reinforcements ratio. The use of ACI 318 (2008) and CSA A23.3 (2004) leads to conservative estimates of the punching shear resistance of two-way slabs reinforced with ASTM A1035 bars (Yang et al. 2011).

Utilizing ASTM A1035 Grade 690 rebars to resist the shear-friction mechanism, which is generated when shear is transferred across a concrete interface subject to Mode II (sliding mode) displacement, is not

recommended. Harries et al. (2012b) tested push-off specimens simulating the connection between an AASHTO girder and a slab to assess the performance of shear-friction interfaces containing ASTM A1035 Grade 690. It was observed that large values of crack opening on the order of 2.5 mm were required to generate sufficient strains, and consequently stresses, in the ASTM A1035 rebars to fully engage them. For this reason, it was found that reducing the amount of reinforcement in inverse proportion to the increase in the yield strength at the shear interface is inapplicable. Based on the findings of Harries et al. (2012b), AASHTO (2017) limits the design yield strength of ASTM A1035 steel to 410 MPa in shear-friction interfaces.

2.6 Serviceability Considerations

2.6.1 Deflections

A fundamental issue associated with the use of ASTM A1035 steel reinforcement is that these reinforcing bars will experience higher stresses, and consequently strains compared to those of conventional bars (ASTM A615/A615M) at service load levels. Concrete members reinforced with HSS and designed to have comparable strength relative to those reinforced with conventional steel (ASTM A615/A615M) are likely characterized by a reduced amount of longitudinal reinforcement. This reduction in the amount of reinforcement, while maintaining the same nominal dimensions, induces higher stresses and strains in ASTM A1035 steel when compared to ASTM A615/A615M Steel. The reinforcement stress at service load conditions, f_s , is normally approximated to be on the order of $0.6f_y$. Therefore, longitudinal reinforcing bar stresses of 248, 414, and 496 MPa at service load would be appropriate for steel reinforcement having a yield strength of 414, 690, and 827 MPa, respectively. These noticeable differences in reinforcing bar stresses between conventional steel and different grades of HSS at service load levels greatly impact deflection calculations and crack control parameters. In one-way members, the ACI 439.6R adopts similar deflection control provisions to that in the ACI 318. These provisions suggest two methods to control the deflection at service load level: (1) implicitly control deflection through minimum thicknesses; and (2) direct deflection calculations. In the first approach, Table 7.3.1.1 in ACI 318, depending on the member

type (for example, solid one-way slab or beam) and support configuration (for example, simply supported or continuous), gives minimum member thickness h for span L (ACI 318 2014). This approach is not applicable to members supporting or attached to partitions and other construction likely to be damaged by large deflections. Footnote (b) of Table 9.5(a) requires that the expressions presented in the table be multiplied by an adjustment coefficient $(0.4 + f_y/690)$ to increase h when reinforcing steel with yield strength other than 414 MPa and ranges between 280 and 550 MPa is used. However, although this range does not cover the yield strength of ASTM A1035 Grade 690 steel (with $f_y = 690$ MPa), the ACI 439.6R (2019a) still confirms the applicability of the multiplier to members reinforced with ASTM A1035 Grade 690 steel based on the findings of Mast (2006). When the yield strength value of 690 MPa is used, the adjustment coefficient will be 1.4. Mast (2006) reported that the deflection of members reinforced with ASTM A1035 Grade 690 steel at service load is 1.4 times of those reinforced with ASTM A615 Grade 414 MPa (Mast 2006). Puranam (2018) reported that the extrapolation of the expressions presented in Table 9.5(a) to members reinforced with HSS reinforcement would lead to acceptable immediate and long-term deflections.

In the other method, direct deflection calculations are based on an effective moment of inertia I_e which accounts for variable cracks at different sections along the member length. The I_e provides a transition between the upper and lower bounds of the gross moment of inertia I_g and cracked moment of inertia I_{cr} as a function of the ratio M_{cr}/M_a , where M_{cr} is the cracking moment and M_a is the maximum service moment. Both ACI (2019b) and AASHTO (2017) prescribe Branson's (Branson, 1977) equation to compute I_e of cracked concrete section as follows:

$$I_e = \left(\frac{M_{cr}}{M_a}\right)^3 I_g + \left[1 - \left(\frac{M_{cr}}{M_a}\right)^3\right] I_{cr} \leq I_g \quad (4)$$

However, Bischoff (2005) proposed a modified version of Branson's equation considering the effect of tension stiffening especially for "soft" sections having a low reinforcement ratio as follows:

$$I_e = \frac{I_{cr}}{1 - \left(1 - \frac{I_{cr}}{I_g}\right)\left(\frac{M_{cr}}{M_a}\right)^2} \leq I_g \quad (5)$$

Although the ACI 439.6R and the NCHRP report provide the two equations to compute I_e , it is generally recommended to use Bischoff's equation since members reinforced with HSS are normally characterized by sections having a low reinforcement ratio (ACI 2019a; Shahrooz et al. 2011). Additionally, Bischoff's approach is based on fundamental mechanics, whereas Branson's formulation is empirical and calibrated for conventional steel, hence the earlier is more suitable for any type of elastic reinforcing material such as HSS. Soltani (2010) reported that for specimens reinforced with HSS and having a low reinforcement ratio (0.007), short-term deflections were underestimated when Branson's equation was used. Similarly, Puranam (2018) reported that the deflection estimation based on I_e using Branson's equation was smaller than those obtained from Bischoff's equation and the actual measured values for elements having low reinforcement ratios.

Designers can choose to use either the implicit deflection provisions or carry out direct deflection calculations when checking deflections; however, they are encouraged to consider the latter approach, especially for detailed design. Desalegne and Lubell (2013) recommend the use of direct deflection calculations instead of implicit deflection provisions when checking deflections of slabs longitudinally reinforced with ASTM A1035 steel since the implicit deflection provisions can lead to uneconomic estimates of the minimum required slab thickness. The use of implicit deflection provisions is not permitted in lightly reinforced members (ACI 2019a).

2.6.1 Crack Control

One of the main factors affecting the crack width in normal size beams and one-way slabs is the strain in the tension steel. As mentioned earlier, the strains in the tension steel are expected to be greater in flexural members reinforced with HSS than those in conventional steel, consequently generating wider cracks. ACI 439.6R (2019a) considers equation Eq. (10-4) of ACI 318-08 (2008) for crack control to be applicable to flexural members reinforced with HSS. Eq. (10-4) of ACI 318-08, which is a modified version of Frosch equation (Frosch, 1999), provides the maximum longitudinal bar spacing s for adequate crack control as follows:

$$s \leq 15 \left(\frac{40000}{f_s} \right) - 2.5c_c \leq 12 \left(\frac{40000}{f_s} \right) \quad (6)$$

where c_c is the minimum concrete cover measured to the center of the reinforcing bar closest to the extreme tension face in inches and f_s is the service load stress in the reinforcing bar in psi. Although Eq. 6 is only valid for service load steel stresses ranging from 170 to 330 MPa (24,000 to 48,000 psi), ACI 439.6R (2019a) permits taking f_s as 460 MPa (67,000 psi) which corresponds to two-thirds of the specified minimum f_y of HSS. A bilinear relationship is generated when the above equation is used as illustrated in Figure 4. It can be seen from the figure that when f_s of 460 MPa is used, Eq. 6 gives conservative results when compared to the case where f_s is taken as 250 MPa. For example, 160 mm spacing s would be required for ASTM A1035 Grade 690 reinforcement (i.e. with $f_s = 460$ MPa) to limit crack widths to 0.41 mm at 25 mm cover, whereas 340 mm spacing would be required to meet the same crack width criterion for ASTM A615 Grade 420 (i.e. with $f_s = 250$ MPa). The ACI 439.6R (2019a) recommends using the above equation not only for beams but also for members with minimal cover such as slabs and walls given that they are designed based on $f_s = 460$ MPa and $f_y = 690$ MPa.

On the other hand, the NCHRP report 679 (2011) recommended adopting AASHTO (2007) provisions for crack control which takes a similar form of ACI equation as follows:

$$s \leq \frac{700\gamma_d}{\beta_s f_s} - 2d_c \quad (7)$$

where d_c is the minimum concrete cover measured to the center of the reinforcing bar in inches, γ_d is a coefficient to calibrate the required spacing depending on the exposure class, f_s is the service load stress in reinforcing bar in ksi, and

$$\beta = 1 + \frac{d_c}{0.7(h-d_c)} \quad (8)$$

where h is the depth of the concrete section in inches. The AASHTO (2017) de facto crack width limits for Class 1 and Class 2 exposure are 0.43 and 0.33 mm, respectively. Soltani et al. (2013) carried out a detailed analytical assessment of expected crack widths in concrete prisms reinforced longitudinally with HSS rebars of different sizes in which nonlinear stress transfer between rebars and surrounding concrete and

nonlinear bar slip functions associated with the stress transfer were considered. Except for the prism reinforced with the largest bar considered (#10), all other prisms were characterized with crack widths below 0.43 mm up to reinforcing bar stress of 496 MPa. Harries et al. (2012a) demonstrated through flexural tests on concrete beam having longitudinal reinforcement ratio ranging from 0.007 to 0.023 that the measured average crack widths on beams reinforced with HSS remain below AASHTO de facto limits for Class 1 and Class 2 exposure up to a reinforcing bar stress of 496 MPa. Aldabagh et al. (2018) reported that the crack widths and the deep propagation of cracks in beams reinforced with ASTM A1035 reinforcement can be greatly restrained when fiber-reinforced concrete is used. Nevertheless, it is evident from the previous discussion that the ACI and AASHTO crack control provisions exhibit sufficient inherent conservativeness to extend their applicability to concrete elements reinforced with HSS.

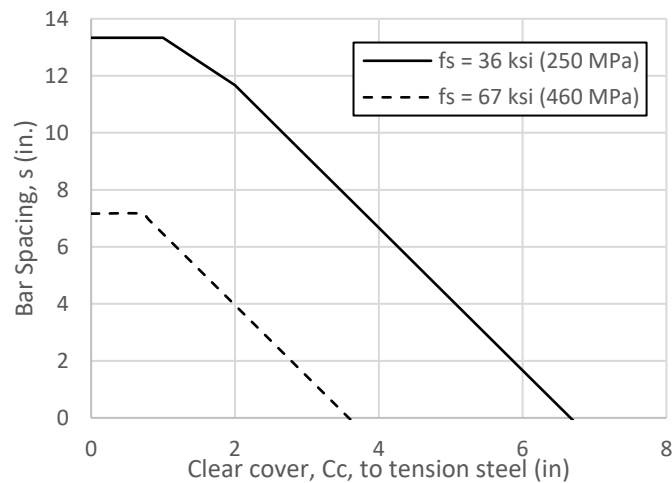


Figure 4: Bar spacing versus clear cover for crack control for reinforcing steel with f_s of 250 and 460 MPa. (note: 1 in. = 25 mm; 1 ksi = 6.9 MPa)

2.4 ASTM A1035 Reinforcing Steel in Compression Members

Ward (2009) carried out a parametric study to determine whether columns reinforced with A1035 longitudinal and transverse reinforcement will reveal any unexpected results compared to columns reinforced with commonly used A615 steel. The variables in the parametric study included: (1) reinforcement grade; (2) column type; (2) column size; (4) transverse reinforcement bar size; and (5)

concrete compressive strength. The moment-curvature responses were analytically generated for an axial load corresponding to $0.1A_gf'_c$, where A_g is the column gross section area. The stress-strain response of the ASTM A1035 steel was modeled using the Ramberg-Osgood function described earlier in this study. Columns reinforced with ASTM A1035 steel had a longitudinal reinforcement ratio of 2%, whereas those reinforced with ASTM A615 had a longitudinal reinforcement ratio of 4%. Because of this, columns reinforced with ASTM A615 were stiffer than the columns reinforced with ASTM A1035. This needs to be considered when designing columns to resist seismic loading. Detailed discussion regarding the performance of ASTM A1035 in the seismic application is provided in the subsequent section of this study. Other than reduced stiffness, no unusual or unexpected trends were reported in the response of columns reinforced with ASTM A1035 when compared to the response of those reinforced with ASTM A615. As a result, Article 5.6.4.4 in AASHTO (2017) permits using a design f_y of 690 MPa in Eq. (5.6.4.4-2) and (5.6.4.4-3) to compute the nominal axial resistance of columns reinforced with longitudinal ASTM A1035 reinforcement and located in Seismic Zone 1. On the other hand, the ACI 439.6R (2019a) imposes a limitation of 550 MPa on f_y for the longitudinal reinforcement when using Eq. (10-1) and (10-2) of ACI 318-08 (2008) to compute the axial load capacity of columns longitudinally reinforced with ASTM A1035 Grade 690. Steel strain corresponding to this stress is 0.0028 which is almost equal to the maximum usable concrete compression strain (0.003) assumed by the ACI 318-08. For members subjected to combined axial load and moment, f_y shall be taken as 690 MPa for the longitudinal rebars in tension, whereas f_y shall be taken as 550 MPa for longitudinal rebars in compression (ACI 2019a).

Another parametric study was carried out by Ward (2009) to assess the adequacy of AASHTO (2007) §5.7.4.6, Eq. 5.7.4.6-1 in determining the required volumetric ratio of spiral reinforcement in non-seismic applications. The use of $f_{yh} = 690$ MPa in AASHTO (2007) Eq. 5.7.4.6-1 was found to be justified only for Seismic Zone 1. For this reason, Article 5.6.4.6 in AASHTO (2017) permits using $f_{yh} = 690$ MPa in Eq. 5.6.4.6-1 (which is identical to Eq. 5.7.4.6-1 in AASHTO 2007) to compute the volumetric ratio of spiral reinforcement in compression members whose design is not controlled by seismic requirements.

Similarly, ACI 439.6R (2019a) permits using $f_y = 690$ MPa in Eq. (10-5) in Section 10.9.3 of ACI 318-08 to determine the required volumetric ratio in compression members reinforced with ASTM A1035 spirals. Also, when ASTM A1035 bars are used in columns as transverse reinforcement, minimum size and maximum tie spacing requirements of section 7.10.5 of ACI 318-08 must be satisfied, irrespective of the yield strength of reinforcement (ACI 2019a). The previous discussion related to computing the shear capacity in flexural members is applicable to compression members designed to resist shear forces (ACI 2019a).

2.7 Bond Strength Characteristics of ASTM A1035 Reinforcing Steel

Because of the higher tensile strength and the unique nonlinear stress-strain response of ASTM A1035 steel, bond characteristics of ASTM A1035 reinforcing bars are different than those of ASTM A615 steel rebars. The equations for development and splice lengths found in design codes such as ACI 318-08 (2008) and ACI 408R-03 (2003) are empirical and were developed based on research work performed using steel having a maximum yield strength of 555 MPa. The applicability of these equations to determine the development and splice lengths of ASTM A1035 steel bars was initially evaluated by Seliem et al. (2009). Sixty-nine large-scale beam-splice specimens containing ASTM A1035 steel rebars were tested. The results indicated that substantially higher stress levels can be achieved in the rebars if confining transverse reinforcement is provided. The presence of transverse reinforcement allowed for splitting cracks to be distributed along the spliced rebars and thereby promoted higher strength and greater deformation before failure. Stresses of up to 1035 MPa were recorded in 25 and 36 mm spliced rebars with transverse reinforcement confinement. Section 12.2 of ACI 318 (2008) was found to be applicable to calculate the development and splice lengths of only ASTM A1035/A1035M confined rebars. Nevertheless, Seliem et al. (2009) proposed adopting a revised strength reduction factor of 0.80, instead of 0.82, in the ACI 408R-03 (2003) equation 4-11a to reasonably estimate the development and splice lengths for both confined and unconfined spliced ASTM A1035 rebars (Seliem et al. 2009). Similar recommendations were proposed by Hassan et al. (2012) but with a strength reduction factor of 0.92. The recommendations of Seliem et al.

(2009) are presented in the ACI 439.6R (2019a) and are applicable to ASTM A1035 spliced rebars in tension. However, for ASTM A1035 rebars in compression, with unavailable test data, the ACI 439.6R suggests using Section 12.3 of ACI 318-08 but with specified yield strength limited to 550 MPa (ACI 2019a). Article 5.10.8.2 of AASHTO (2017) permits the use of f_y up to 690 MPa in Equation 5.10.8.2.1 a-1 to determine the development length of ASTM A1035 bars based on the findings of Harries et al. (2010). However, this is only applicable when the ASTM A1035 spliced rebars are confined and the design concrete compressive strength does not exceed 100 MPa.

Substituting f_y of 690 MPa in the above equations would require long development or splice lengths. Since these lengths may be uneconomical or impractical, designers are encouraged to consider mechanical splices (couplers) or spliced T-headed rebars (ACI 2019a). Mechanical splices used to connect ASTM A1035 rebars must be capable of developing the actual tensile strength and actual elongation of the spliced rebars (ACI 2019a). The reason for this stringent requirement is to ensure that adequate ductility is provided in the connected bars. Excessive heating of the reinforcing bars when installing the mechanical splices must be avoided so that it does not cause unfavorable alterations to the microstructure of the ASTM A1035 steel. Reinforced concrete beams containing ASTM A1035 rebars which are lap spliced using mechanical couplers exhibit ductile flexural failure (i.e. rebars yield in tension and concrete crushes in compression) when transverse reinforcement is provided (Berna et al. 2018). In the case of spliced T-headed rebars, although the ACI 318 provides the requirements of developing such rebars, it is limited to reinforcing bars with f_y not exceeding 410 MPa, thereby cannot be extended to ASTM A1035 steel. Consequently, The ACI 439.6R (2019a) requires that when T-headed rebars are used, experimental results showing the adequacy of such mechanically attached heads need to be provided. Berna et al. (2008) demonstrated that transverse reinforcement within the lap splice of T-headed ASTM A1035 bars promotes ductile flexural failure by changing the force-transfer mechanism between adjacent bars and increasing stresses along with the splice and member deformation capacity. From the above discussion, it is evident

that transverse confinement along the lap splice region of ASTM A1035 rebars is crucial and must always be provided to avoid sudden and brittle failure irrespective of the type of splices.

The anchorage strength of ASTM A1035 hooked bars was evaluated by Harries et al. (2010), Sperry et al. (2017), and Sperry et al. (2018). If adequate cover and confinement are provided, the development length of ASTM A1035 hooked bars prescribed by AASHTO (2007) Section 5.11.2.5 (2) was found to be adequate to develop tensile stress up to 860 MPa (Harries et al. 2010). Development lengths of ASTM A1035 hooked bars calculated based on Section 25.3 of ACI 318-14 are very conservative for No. 16 bars and become gradually less conservative with the increase in bar size and concrete compressive strength (Sperry et al. 2017). The change in bend angle (90 or 180 degrees) and side concrete cover (between 65 and 80 mm) had no impact on the anchorage strength of ASTM A1035 hooked bars (Sperry et al. 2018). Anchorage strength of ASTM A1035 180-degree hooked rebars noticeably increases when confining reinforcement with parallel or perpendicular orientation is provided. However, for ASTM A1035 90-degree hooked rebars, confining reinforcement oriented parallel to the development length is more effective in increasing the anchorage strength than reinforcement oriented perpendicular to the development length (Sperry et al. 2018).

2.8 Seismic Performance of ASTM A1035 Reinforcing Steel

Several researchers have evaluated the seismic performance of high-strength transverse reinforcement as column confinement (Muguruma and Watanabe 1990; Muguruma et al. 1991; Sugano et al. 1990; Budek et al. 2002). Concrete columns confined with high strength reinforcement (f_{yt} up to and beyond 827 MPa) exhibited satisfactory performance when compared to those confined with conventional steel. Moreover, the seismic performance of high-strength longitudinal reinforcement in columns was assessed by Stephan et al. (2003), Restrepo et al. (2006), Lepage et al. (2008), Rautenberg et al. (2013), Trejo et al. (2016), Barbosa et al. (2016), and Barclay and Kowalsky (2020). Columns reinforced with longitudinal high-strength steel rebars (Grade 550 to 830) had drift capacities ranging from 4 to 8%, indicating a satisfactory performance when compared to similar columns reinforced with conventional steel.

However, columns reinforced longitudinally with ASTM A1035 Grade 690 steel were characterized by a limited ductility capacity and reduced energy dissipation. The lower energy dissipation is attributed to the reduction in post-cracking stiffness (Rautenberg et al. 2013). Since columns designed with ASTM A1035 Grade 690 steel contain less longitudinal reinforcement than columns designed with conventional steel, they are characterized with smaller initial stiffness and hence greater yield displacements. This, along with relatively small ultimate lateral deformation, lead to limited ductility response (Restrepo et al. 2006). While reviewing the findings of the previous research work, it is evident that greater concerns related to ductility capacity and energy dissipation arise when ASTM A1035 Grade 690 steel is incorporated as longitudinal than transverse (confining) steel in plastic hinge regions. In addition to the previous seismic applications, the performance of ASTM A1035 Grade 690 in beam-column joints subjected to pure flexural monotonic and cyclic quasi-static loading protocols was evaluated by Ibarra and Bishaw (2016). The use of ASTM A1035 Grade 690 steel increased the flexural capacity of the beam-column joints by more than 60% but reduced the ductility and energy dissipation capacity. In order to overcome the aforementioned deficiencies resulting from the use of ASTM A1035 Grade 690 in seismic applications, Lepage et al. (2012) and Ibarra and Bishaw (2016) considered introducing steel fibers. The presence of these fibers increased the peak strength and greatly reduced the cracking and spalling of concrete but had an insignificant impact on the energy dissipation capacity. A number of studies (Rautenberg et al. 2013; Rautenberg and Pujol 2013; Billah and Alam 2013; Bishaw 2016) numerically evaluated the seismic performance of concrete columns reinforced with ASTM A1035 Grade 690 steel. Rautenberg et al. (2013) and Rautenberg and Pujol (2013) reported that the roof drifts of frame buildings having columns longitudinally reinforced with ASTM Grade 830 steel were not consistently larger than the roof drifts of buildings having columns longitudinally reinforced with twice as much conventional steel. Columns in high-rise buildings incorporating high-strength concrete and reinforcement were found to be less vulnerable to far-field ground motions than those incorporating normal strength materials (Billah and Alam 2013). On the contrary, Bishaw (2016) reported that, in moment-resisting frames, elements reinforced with high-strength steel exhibited reduced ductile characteristics, and hence lower collapse capacities when compared to elements with conventional steel.

The reason for the contradicting conclusions drawn from Billah and Alam (2013) and Bishaw (2016) could be due to the variability in adopted material models and selected ground motions in their numerical simulations.

The applicability of the ACI 439.6R (2019a) recommendations is limited to structures assigned to Seismic Design Category (SDC) A, B, and C. For structures assigned to SDC D, E, or F, the application of the ACI 439.6R recommendations is limited to slab systems, foundations, and other components which are expected to remain elastic during a seismic event. The only exception is when ASTM A1035 steel is used as transverse reinforcement in columns for concrete confinement. In this case, the ACI 439.6R permits using $f_{yt} = 690$ MPa for confinement but limits f_{yt} to 410 MPa for shear strength (ACI 2019a). Similarly, ACI 318-19 permits using a yield strength of up to 690 MPa when ASTM A1035 Grade 690 is used for confinement (ACI 2019b). In AASHTO (2017), the NCHRP Report 679 recommendations are considered applicable only for elements and connections in Seismic Zone 1 (Shahrooz et al. 2011). This means that, in Seismic Zone 2, 3 and 4, the yield strength of ASTM A1035 Grade 690 reinforcement would be limited to 500 MPa in most applications. Russell et al. (2011) examined the applicability of the NCHRP Report 679 guidelines to bridges located in Seismic Zone 3 and 4. They recommended extending the applicability of the NCHRP Report 679 guidelines to capacity protected members (such as footings, bent cap beams, joints, and superstructure) in Seismic Zone 3 and 4 since these elements are designed to remain essentially elastic. In addition, they provided several examples of bridges reinforced with ASTM A1035 Grade 690 steel and constructed in Seismic Zone 3 and 4 with documented satisfactory performance. Nevertheless, their recommendations were not incorporated into the AASHTO (2017).

2.9 Summary

Over the last two decades, there has been a significant amount of research work carried out on ASTM A1035 and other types of HSS to assess their performance in structural concrete. ASTM A1035 steel bars exhibit higher strength and corrosion resistance in comparison to conventional ASTM A615 Grade 420 steel. One of the most unique properties of the ASTM A1035 Grade is the lack of distinct yield

point and yielding plateau. The high-strength steel, and ASTM A1035 steel, in particular, is normally produced through cold working, micro-alloying, or quenching and tempering with micro-alloying being the most common. The ASTM A1035 steel exhibits superior corrosion resistance to that of conventional ASTM A615 Grade 420 steel. ASTM A1035 steel can be two to ten times more corrosion resistant than conventional steel depending on the type of alloy, i.e. chromium content. ASTM A1035 steel demonstrated satisfactory performance in various structural elements such beams, slabs, and columns whether used as longitudinal or transverse reinforcement.

However, the vast majority of the recent research work evaluating the performance of concrete members containing HSS rebars has focused on those designated not part of the seismic-force-resisting system (ACI 2019a; Shahrooz et al. 2011). This is because of concerns related to the limited ductility capacity of concrete members reinforced with HSS under lateral cyclic loading. Those concerns stem from the known fact that the increase in yield strength is often associated with a reduction in inelastic strain capacity, the ratio of tensile to yield strength, and length of the yield plateau, which could lead to an undesirable seismic performance by limiting the spread of plasticity in the potential plastic hinge region. However, the ability of HSS to reduce rebar congestion makes it an attractive alternative to regular-strength reinforcing steel bars in members forming plastic hinges which often contain heavily reinforced sections, especially in highly seismic regions. There is a need for design guidelines and further assessments on the performance of different types of HSS in RC columns to promote the use of HSS in seismic applications. With more revisions accommodating ASTM A1035 steel in design codes and systematic and well-designed future research programs, designers, engineers, and practitioners would have a greater chance of utilizing ASTM A1035 steel and making use of its potential benefits in various applications.

CHAPTER 3: DRIFT RATIO LIMIT STATES FOR CIRCULAR CONCRETE COLUMNS REINFORCED WITH DIFFERENT TYPES OF HIGH-STRENGTH STEEL REINFORCING BARS

3.1 General

As technologies advance, different types of reinforcing steel with higher yield strength than conventional carbon steel are becoming commercially available in North America and worldwide. Such types of reinforcing steel are characterized by a yield strength greater than 550 MPa and are often referred to as high-strength steel (HSS) rebars. Utilizing such rebars would significantly reduce the required cross-sectional area of reinforcement, and subsequently improves reinforcement and concrete placement productivity (Aldabagh and Alam 2020). In addition, much of the interest in HSS as an attractive alternative to conventional steel in reinforced concrete (RC) structures is driven by the fact that steel reinforcing bars with higher yield strength are often characterized by enhanced corrosion resistance. For instance, the ASTM A1035 Grade 690 steel, which is one of the common types of HSS available in the North American markets, can be between two and ten times more corrosion resistant than conventional ASTM A615 “black” steel (Clemena and Virmani 2004). Design codes, especially in the United States, such as the ACI 318 (ACI 2019) and the AASHTO LRFD *Bridge Design Specifications* (AASHTO 2017) have been evolving to accommodate the HSS reinforcement, hence allowing designers to make use of its potential benefits. However, the vast majority of the revisions introduced in the two design codes permitted the use of HSS rebars as main reinforcement only in capacity-protected elements, i.e. not part of the seismic-force-resisting system. The only exception is in the ACI 318 (2019b) where the use of HSS reinforcement conforming to ASTM 706 Grade 550 and 690 is permitted in special moment frames and structural walls resisting seismic loads, respectively. In Canada, design codes lag as the use of HSS rebars is not permitted for both non-seismic and seismic applications (CSA 2019a and CSA 2019b). Concerns related to the performance of HSS in seismic applications stem from the known fact that the increase in yield strength is often associated with a reduction in inelastic strain capacity, the ratio of tensile to yield strength and length of the yield

plateau. This would lead to an undesirable seismic performance by limiting the spread of plasticity in the potential plastic hinge region, and potentially decreasing ductility capacity. To alleviate the concerns over the performance of HSS in seismic applications, much research has been conducted to evaluate the cyclic performance of concrete columns reinforced with HSS (Restrepo et al. 2006; Rautenberg et al. 2013; Trejo et al. 2016; Barbosa et al. 2016; Li et al. 2018; Sokoli 2018 Barclay and Kowalsky 2020). The results indicate that, other than dissipating less energy, concrete columns reinforced with HSS could exhibit comparable performance in terms of drift and flexural strength capacities to similar columns reinforced with conventional steel. Despite these findings, design code committees are still reluctant to permit the use of HSS in seismic applications. According to the *ATC-98 Project on Seismic Design of Concrete Structures with High-Strength Reinforcement* (Kelly et al. 2017), there is a need for additional research on the seismic performance of HSS before complete design recommendations for the use of HSS in seismic applications can be made.

To promote the use of HSS in seismic applications in bridges, and to further alleviate design code committees' concerns, design guidelines on the use of different types of HSS in RC columns need to be established. In the last decade, seismic design provisions in several design codes such as the *Canadian Highway Bridge Design Code* (CHBDC) (CSA 2019b) and *New Zealand Bridge Manual* (NZT 2018) have been incorporating performance-based design (PBD) as an alternative to the classical force-based design (FBD). Unlike the FBD where structures are primarily designed to achieve only the traditional life-safety performance level, in PBD, structures are designed to achieve multiple performance levels when subjected to different levels of seismic hazards. Each performance level (sometimes referred to as "service level") needs to be explicitly described and associated with a damage state. For instance, in the CHBDC, immediate, service limited, service disruption, and life safety performance levels are associated with minimal, repairable, extensive, and probable replacement damage states, respectively (CSA 2019b). An integral component of the PBD is the quantification of the damage states by means of engineering limit states which may be expressed as limiting values of material strains, deformations, drifts, curvatures, or damage indices. For this reason, in the past two decades, several experimental programs have been executed

to relate damage states of concrete columns reinforced with conventional steel to material strains (Kowalsky 2000; Lehman et al. 2004; Goodnight et al. 2016), drifts (Berry 2006), and ductility capacities (Hwang et al. 2001). In addition, relating the damage states of concrete columns reinforced with conventional steel to engineering parameters has been achieved by experimentally verified numerical models. Babazedeh et al. (2015) employed a three-dimensional (3D) continuum-based finite element model to predict the intermediate damage states in RC bridge columns. Also, Billah and Alam (2016) utilized fiber element-based nonlinear models to develop performance-based damage states for concrete columns reinforced with different types of shape memory alloys.

Due to the significant differences between the mechanical properties of HSS and that of conventional normal-strength steel, the question of whether the engineering limit states developed for concrete columns reinforced with conventional steel would apply to those reinforced with HSS arises. Sokoli et al. (2017) demonstrated through cyclic tests that HSS rebars in columns with lower longitudinal reinforcement ratios experience larger strain demands than conventional normal-strength rebars at all drifts. This implies that the engineering limits states, which have been originally developed for normal-strength steel, found in literature, and design codes may not be applicable to bridge columns reinforced with HSS. Research work establishing engineering limits states specifically applicable to concrete columns reinforced with different types of HSS is very limited. Barclay and Kowalsky (2020) executed an experimental program to establish strain limit states for concrete columns reinforced with ASTM A706 Grade 550. However, in Barclay and Kowalsky (2020), only four columns were tested and one type of HSS was considered. As a consequence, the established strain limits were limited and not applicable to concrete columns reinforced with different types of HSS having a wider range of geometrical and material properties. Billah and Kabir (2020) employed incremental dynamic analysis to develop predictive analytical expressions of the drift ratios at the inception of rebar yielding, concrete cover spalling, and longitudinal rebar buckling for high-strength concrete bridge columns reinforced with HSS. The proposed expressions by Billah and Kabir (2020) are applicable to concrete columns reinforced with all types of HSS with yield strength ranging between 550 and 750 MPa (i.e., irrespective of the ASTM standard to which they conform).

This implies that despite their significance, the differences in mechanical properties of HSS conforming to different ASTM standards were not considered in the expressions proposed by Billah and Kabir (2020). Nevertheless, those expressions were considered in this study for comparison purposes.

The objective of this chapter is the development of empirical expressions capable of predicting the drift ratio limit states of circular concrete columns reinforced with different types of HSS. Given the fact that developing such expressions requires a large amount of data, developing them as part of an experimental program would be very costly, and often infeasible. As a result, in this study, as an alternative approach, the limited available experimental data on the cyclic performance of concrete columns reinforced with HSS were employed to validate fiber-based finite element models. Quasi-static analyses were performed to apply displacement-based cyclic loading to the columns and record the drift ratio limits corresponding to predetermined material strains. The material strains were determined using well-established definitions reflecting different levels of damage. Uncertainties in material, geometric, and section properties of the concrete columns were considered employing the Monte Carlo sampling technique. State-of-the-art machine learning-based symbolic regression was used to develop the predictive expressions of drift ratio limit states. Due to the large number of variables considered and to limit the complexity of the proposed expressions, prior to the regression analysis, the full factorial analysis was performed to identify the most contributing variables to each drift limit state.

3.2 High-Strength Steel Types

In this study, three types of HSS, namely ASTM A706 Grade 550 (ASTM 2016), ASTM A615 Grade 690 (ASTM 2020a), and ASTM A1035 Grade 690 (ASTM 2020b), were considered. Selected representative tensile stress-strain responses of these types, as well as conventional ASTM A706 Grade 420, are given in Figure 5. The stress-strain curves of ASTM A706 Grade 550 and ASTM A615 Grade 690 consist of an initial linearly elastic portion up to the yield strength, followed by a yield plateau and subsequent strain hardening region. These are also the characteristics of the stress-strain response of ASTM A706 Grade 420 rebars which exhibit the most desirable properties for seismic applications. However, as

seen in Figure 5, the ASTM A1035 Grade 690 steel exhibit a unique stress-strain response when compared to the other types of reinforcing steel. Its stress-strain curve lacks a distinct yield plateau and is characterized by an initial elastic portion, followed by a nonlinear relationship up to the ultimate strength. Therefore, to establish the yield strength for ASTM A1035 Grade 690, one of the following methods need to be used: (1) 0.35% extension under load (EUL) method, (2) 0.5% EUL, and 0.2% offset method, with the last being the most common. In the 0.2% offset method, the yield strength is defined at the intersection of the stress-strain curve with a line having a slope equal to the Young's modulus and starting from 0.2% strain. The 0.2% offset method is also applicable to steel types with well-defined yield points. As is evident in Figure 5 that the increase in yield strength generally decreases the uniform and fracture strains, and the tensile to yield strength ratios. Table 2 provides a summary of the results of statistical evaluations of the tensile mechanical properties of the three types of HSS. The statistical evaluations of mechanical properties of ASTM A706 Grade 550 and ASTM A1035 Grade 690 steel were performed by Overby et al. (2017) and Shahrooz et al. (2011), respectively. As for the ASTM A615 Grade 690, such evaluations do not seem to exist. As a result, in this study, the mechanical properties of ASTM A615 Grade 690 were established on a statistical basis by reviewing available tensile test data of ASTM A615 Grade 690 (Slavin 2015; Glucksman 2018; Casanova et al. 2018; Sokoli 2018). Defining the mechanical properties on a statistical basis was critical to account for the uncertainty in the material properties of the HSS reinforcing bars in subsequent analyses. The mean tensile-to-yield ratios of the ASTM A706 Grade 550 and ASTM A1035 Grade 690 exceed 1.25, which is a standard characteristic of reinforcing steel used in seismic applications. According to Shahrooz et al. (2011), regardless of the method by which the yield strength of ASTM A1035 Grade 690 is established, the condition that tensile strength is not less than 1.25 times the yield strength is satisfied. On the other hand, the mean tensile-to-yield strength ratio of the ASTM A615 Grade 690 steel is not greater than, but almost equals 1.25. The tensile-to-yield strength ratio of the ASTM A615 Grade 690 is largely dependent on the manufacturing process. ASTM A615 Grade 690 steel produced by quenching and tempering process exhibits tensile-to-yield strength ratio on the order of 1.15, whereas that produced by micro-alloying process exhibits tensile-to-yield strength ratio on the order of 1.25 (Ghannoum and Slavin

2016). For the statistical evaluations of the mechanical properties of the ASTM A615 Grade 690 steel, tensile test data for rebars produced by the two processes were considered. By reviewing the values of the standard deviations given in Table 1, ASTM A706 Grade 550 steel appears to have the least variability in the mechanical properties when compared to the other two types. Also, its mechanical properties are the closest to those specified by the *AASHTO Guide Specifications for LRFD Seismic Bridge Design (2014)* for ASTM A706 Grade 420.

Table 2: Summary of Tensile Mechanical Properties of ASTM A706 Grade 550, ASTM A615 Grade 690, and ASTM A1035 Grade 690 steel.

Property	ASTM A706 Grade 550		ASTM A615 Grade 690		ASTM A1035 Grade 690	
	Mean	St. Dev.	Mean	St. Dev.	Mean	St. Dev.
Elastic Modulus (MPa)	192281	11039	196197	15461	193996	13851
Yield Strength* (MPa)	586.7	20.2	708.2	42.2	834.3	86.2
Tensile Strength (MPa)	775.7	25.2	878.4	70.5	1172.1	52.7
Tensile-to-Yield Strength Ratio	1.32	0.03	1.24	0.06	1.39	0.13
Strain at Onset of Strain Hardening	0.0074	0.0019	0.008	0.001	-	-
Uniform Strain	0.095	0.0055	0.080	0.0083	0.049	0.0055

* Based on 0.2% offset method

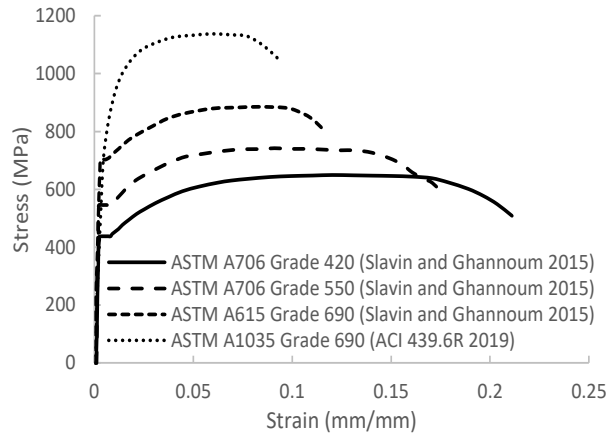


Figure 5: Comparison of typical stress-strain curves for different types of HSS and conventional normal-strength ASTM A706 Grade 420 reinforcing bars.

3.3 Definition of Damage States

Fundamental to the PBD methodology is the establishment of performance levels and their associated damage states. Unfortunately, there is a lack of consensus among researchers, code committees, and practitioners on the definitions of performance levels and corresponding qualitative and quantitative assessment parameters. In this study, the performance levels and associated damage states were established based on the multi-level performance evaluation approach proposed by Hose et al. (2000). This approach was introduced by Hose and Seible (1999) and later adopted by Caltrans in their Visual Catalog of Reinforced Concrete Bridge Damage (2006). Table 3 lists the selected performance levels and corresponding damage states. Since damage is intrinsically related to material strains, the onsets of the damage states were related to tensile strains in longitudinal steel rebars and compressive strains in concrete. The onset of DS-1, which is associated with the “yielding” performance level, was established when the tensile strain in any of the longitudinal rebars at the two cross-section extremes in the loading direction reaches the yield strain. In defining the yield strain for the three types of HSS, the yield point was established following the 0.2% offset method. The yield strain was considered as a variable as it depends on the yield strength and the modulus of elasticity of steel. At DS-1, cracks would be clearly visible but do not likely require repair (Hose et al. 2000). DS-2 is initiated when the concrete cover begins to spall off. Concrete spalling is a good indicator of local damage and would require more expensive, time-consuming, and possibly disruptive repairs (Lehman et al. 2004). Compressive strain in the concrete cover at the onset of spalling in reinforced concrete columns cannot be directly measured during experiments, and hence it is often either back-calculated or determined using numerical predictive analysis. This has led to a considerable spread in the reported strains at the onset of spalling, with values ranging from 0.002 to 0.018 for circular reinforced concrete columns (Lehman et al 2004; Hose et al. 2000). In this study, a reasonable conservative estimate of 0.004 was considered as the strain limit at which concrete cover begins spalling, as recommended by Paulay and Priestley (1992). The damage at DS-3 is characterized by very wide cracks and extensive concrete spalling. Extensive spalling was identified when compressive strains in the concrete

core reach 80% of the ultimate compression strain of the confined concrete, ϵ_{cu} (CSA 2019b). Extensive concrete spalling signals a point at which significant repairs are required. Paulay and Priestley (1992) proposed a conservative estimate of ϵ_{cu} as follows:

$$\epsilon_{cu} = 0.004 + 1.4\rho_s f_{yh} \epsilon_{sm} / f_{cc}' \quad (9)$$

where ρ_s = volumetric ratio of confining steel; f_{yh} = yield strength of transverse steel; ϵ_{sm} = steel strain at maximum tensile stress; f_{cc}' = confined concrete compressive strength. The last damage state, DS-4, occurs when either concrete core crushes or longitudinal rebars buckle. DS-4 with subscripts *cu* and *sb* denote DS-4 associated with concrete core crushing and longitudinal rebar buckling hereafter, respectively. The level of damage at DS-4 causes a significant rapid loss of lateral-load strength. Consequently, at DS-4, repairs become infeasible, and the component or structure often needs to be replaced. The initiation of core concrete crushing was determined when the compressive strains in the concrete core reach ϵ_{cu} . To predict the peak tensile strains in the longitudinal rebars prior to buckling, ϵ_{sb} , the following empirical expression proposed by Goodnight et al. (2016) was considered:

$$\epsilon_{sb} = 0.03 + 700\rho_s \frac{f_{yhe}}{E_s} - 0.1 \frac{P}{f_{ce}' A_g} \quad (10)$$

where ρ_s is the transverse volumetric steel ratio; f_{yhe} is the expected yield strength of reinforcement; E_s is the modulus of elasticity of steel; P is the applied axial load; f_{ce}' is the concrete compressive strength; and A_g is the gross cross-sectional area. Barclay and Kowalsky (2020) demonstrated experimentally that Eq. (10) well-predicts the peak tensile strains prior to buckling in concrete columns reinforced with ASTM A706 Grade 550 steel. Nevertheless, the adequacy of the proposed strain limits in identifying the onset of damage states in concrete columns reinforced with HSS was evaluated in the next section.

Table 3: Selected Performance Levels and the Associated Damage States.

Level	Performance level	Damage classification	Damage state	Description of damage
I	Yielding	Minor	DS-1	- Yielding of main reinforcement
II	Initiation of local mechanism	Moderate	DS-2	- Open cracks - Onset of spalling
III	Full development of local mechanism	Major	DS-3	- Very wide cracks - Extended concrete spalling
IV	Strength degradation	Local failure/collapse	DS-4	- Crushing of core concrete - Buckling of main reinforcement

3.4 Numerical Model Evaluation and Validation

Fiber-based models of the reinforced concrete columns were developed using *OpenSees* (McKenna et al. 2000). Figure 6 shows the discretization of the reinforced concrete column. The length of the column (L) is discretized into six displacement-based beam-column elements. The first element has 10 integration points and extends from the bottom of the column to the end of the plastic hinge length (L_p). The remaining length of the column (i.e. $L - L_p$) constitutes of five equal-in-length elements with 5 integration points. In this study, the L_p was computed using the probabilistic plastic hinge length model proposed by (Ning and Li 2016). According to their model, the plastic hinge length in reinforced concrete columns can be computed using the following expression:

$$L_p = L \left(0.042 + 0.072 \frac{P}{P_o} \right) + 0.298H + 6.407d \quad (11)$$

where L is the column length; P/P_o is the axial load ratio; H is the column sectional height; d is the diameter of longitudinal reinforcement. Ning and Li (2016) reported that Eq. (11) predicts the plastic hinge length with greater accuracy than the modified Priestley and Park (1987) formula developed by Lu et al. (2005) and the expression proposed by Paulay and Priestley (1992). The reinforced concrete section was discretized into three materials, namely, reinforcing steel, unconfined concrete, and confined concrete. OpenSees *Concrete01* material model was used to simulate the uniaxial stress-strain response of the unconfined and confined concrete. The properties of the confined concrete were determined based on the

theoretical stress-strain model proposed by Mander et al. (1988) for confined concrete. Since, as previously mentioned, ASTM A706 Grade 550 and ASTM A615 Grade 690 exhibit stress-strain responses similar to that of ASTM A706 Grade 420, their responses were incorporated using the OpenSees *ReinforcingSteel* material model (Dodd and Restrepo-Posada 1995). Such a model requires defining several parameters such as the tangent at initial strain hardening and strain corresponding to initial strain hardening which makes it appropriate for reinforcing steel types with well-defined yield point and yield plateau. On the other hand, due to the unique stress-strain response of the ASTM A1035 Grade 690 steel, its response was incorporated using the *Steel02* OpenSees material model (i.e. Giuffré-Menegotto-Pinto Model) (Filippou et al. 1983). Such a model can capture the “roundhouse” stress-strain curve of the ASTM A1035 Grade 690 by specifying several shape parameters (i.e. R0, cR1, and cR2) controlling the transition from elastic to plastic branches. To account for strain penetration effects, the hysteretic model developed by Zhao and Sritharan (2007) (known as *Bond SP01* in OpenSees) was integrated into the analysis using a zero-length section element, as shown in Figure 6.

To validate the numerical models for concrete columns reinforced with ASTM A706 Grade 550, ASTM A615 Grade 690, and ASTM A1035 Grade 690, their predicted responses were compared against those measured experimentally of specimens Test 1, CH100, and Unit 2 from Barclay and Kowalsky (2020), Sokoli (2018), and Restrepo et al. (2006), respectively. Since material strain responses are critical in this study for the identification of the onset of the damage states, the experimentally measured and numerically predicted responses were compared not only at the global but also at the local/sectional level. Figure 6 provides a comparison of global and local responses from the fiber model and test data for: (a) Test 1 (Barclay and Kowalsky 2020); (b) CH100 (Sokoli 2018); and (c) Unit 2 (Restrepo et al. 2006). Detailed descriptions of the constitutive models used for numerical model validations are given in Appendix A. The parameters defining each of the constitutive models were determined using the reported material properties in Barclay and Kowalsky (2020), Sokoli (2018), and Restrepo et al. (2006).

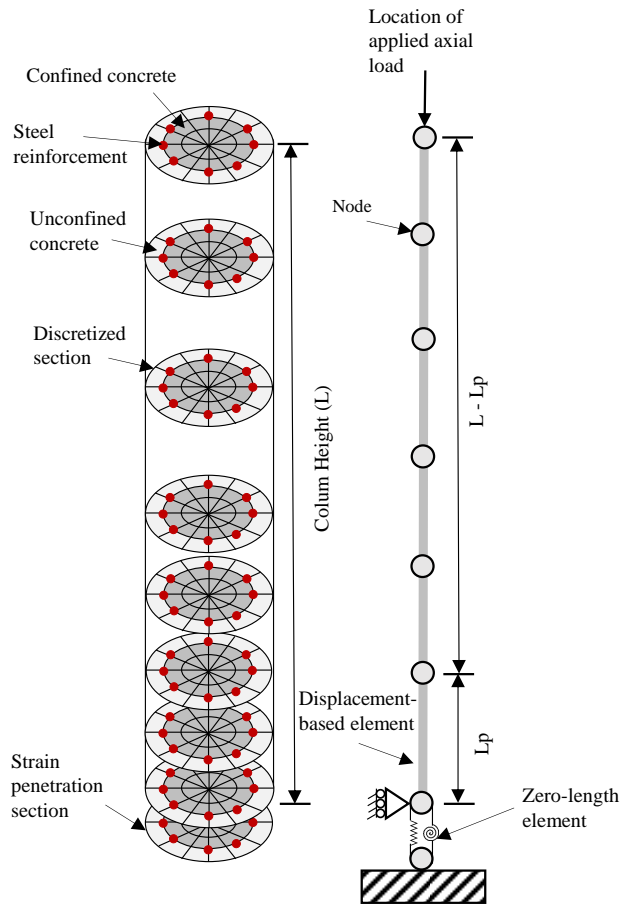


Figure 6: Discretization of the reinforced concrete column.

At the global level, as evident in Figure 7, the numerical models for the three types of HSS generated hysteretic force-drift relationships that closely follow those from the experimental data. In addition, at the local level, the numerical models well-predicted the hysteretic strains in the longitudinal rebars at sections of the maximum moment in Test 1 and CH100, and the profile of the longitudinal rebar strains in Unit 2 prior to failure. For Test 1, the predicted drift ratios from the fiber model at DS-1 and DS-4_{sb} were 0.88% and 5.5%, respectively. Barclay and Kowalsky (2020) reported the first longitudinal rebar yielding and buckling at 0.81% and 6.6% drifts for Test 1, respectively. For instrumentation purposes, the concrete cover was removed before testing, and therefore the drift ratios at concrete spalling and crushing were not reported for Test 1 by Barclay and Kowalsky (2020). For CH100, the fiber model drift ratio predictions at DS-1, DS-2, and DS-4_{sb} were 0.98%, 1%, and 4.4%, respectively. According to Sokoli

(2018), the first longitudinal rebar yielding and cover concrete spalling occurred at 1.01% and 1.5%, respectively, whereas the first longitudinal rebar buckling occurred in the second half cycle to a drift of 5.5%. Lastly, for Unit 2, the fiber model predicated the initiation of DS-1, DS-2, DS-4_{cu} and DS-4_{sb} at 1.3%, 1.3%, 3.1%, and 3.5%, respectively. Restrepo et al. (2006) reported yield and cover concrete spalling drifts of 1.64% and 2.8% for Unit 2, respectively. In addition, according to Restrepo et al. (2006), the fracture of the hoop at 3.1% drift led to both concrete core crushing and longitudinal rebar buckling. It is evident that from the previous findings that the generated fiber model is generally capable of conservatively predicting the onset of different types of damage states in concrete columns reinforced with different types of HSS.

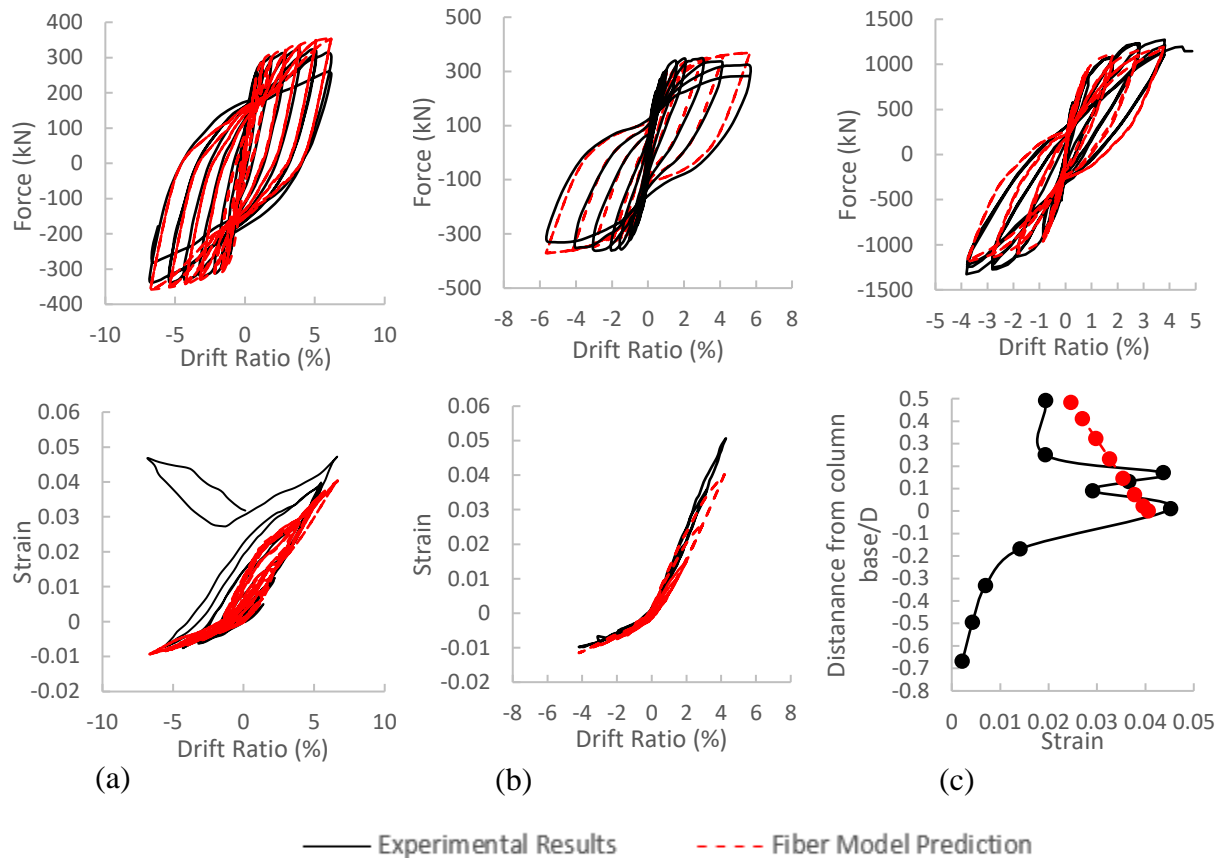


Figure 7: Comparisons of global and local responses from the fiber model and test data for: (a) Test 1 (Barclay and Kowalsky 2020); (b) CH100 (Sokoli 2018); and (c) Unit 2 (Restrepo et al. 2006).

3.5 Factorial Analysis

Many parameters need to be identified to generate the fiber models of the reinforced concrete columns as part of this study. These parameters could be related to geometry (such as aspect ratio), section (such as longitudinal reinforcement ratio), or material (such as yield strength). To identify the significant parameters contributing to the initiation of the damage states, and subsequently limit the complexity of the proposed drift limits expressions, the “design of experiments” (DOE) approach (Montgomery 2013) was adopted. In a full factorial experiment, all of the possible combinations of the levels of the parameters are considered. In this study, each parameter was considered at two levels, upper and lower. For each combination of parameter levels, an experiment, or in this case a reinforced concrete column, is analyzed and the response of interest (i.e. drift corresponding to the initiation of damage states) is monitored. Therefore, for a two-level DOE, the factorial design would require 2^k runs, where k is the number of parameters. Table 4 lists the parameters considered in this study and their upper and lower levels. Upper and lower levels were determined to reflect typical details of bridge columns currently in use in the regions of high seismicity in North America. The number of parameters considered for concrete columns reinforced with ASTM A706 Grade 550 and ASTM A615 Grade 690 was 10, whereas that considered for concrete columns reinforced with ASTM A1035 Grade 690 was 8. This implies that the number of analyses required was 1024 for the former case and 256 for the latter case. Less number of parameters were considered for concrete columns reinforced with ASTM A1035 Grade 690 because of the *Steel02* material model used which does not include strain corresponding to strain hardening and tensile strength parameters. In such a model, instead of explicitly providing the value of tensile strength, the tensile strength is identified using the strain-hardening ratio which was taken as 0.01 based on the proposed representative stress-strain response of ASTM A1035 Grade 690 by Shahrooz et al. (2011). For the three types of HSS, the minimum value of aspect ratio considered was 4 to ensure flexure-dominated behavior. Upper and lower levels of the $P/A_g f'_c$, ρ_l , ρ_s , and f'_c were defined to reflect common design practices and the properties of the well-confined circular concrete columns in the PEER Structural Performance Database (Berry et al. 2013). In

addition, upper and lower levels of the reinforcing steel material-related parameters were identified based on the available tensile test data (Overby et al. 2017; Shahrooz et al. 2011; Slavin 2015; Glucksman 2018; Casanova et al. 2018; Sokoli 2018). The reinforced concrete columns in the factorial analysis were subjected to a displacement-controlled loading protocol consisting of three cycles at 1, 1.5, 2, 3, 4, 5, 6, and 7 times the equivalent yield displacement. The equivalent yield displacement is equal to the first yield displacement multiplied by the ratio of analytical nominal to first yield moments which were determined through moment-curvature analysis.

Percent contributions of the parameters considered obtained from the factorial analysis are presented in Table 5. Percent contribution is calculated as the variance component for each parameter divided by the total variation multiplied by 100. For additional details on the DOE, the reader may consult one of the textbooks that deal specifically with the design and analysis of experiments (e.g., Montgomery (2013), Hayter (2002), among others). In Table 5, significant parameters are printed in boldface. Percent contributions shown inside parentheses indicate a negative effect. The following provides a discussion on the effect of the significant parameters on drift ratios at the onset of the damage states.

3.5.1 Parameters Affecting Drift Ratios at DS-1

For concrete columns reinforced with the three types of HSS, the drift at DS-1, which is associated with the first yielding of main reinforcement, was mainly affected by the L/D and ρ_l . The average percent contribution of L/D and ρ_l to the drift at DS-1 for the three types of HSS were 81.5% and 6.8%, respectively. These observations are consistent with those reported from experimental results by others. Lehman et al. (2004) demonstrated through testing concrete columns reinforced with conventional ASTM A706 Grade 420 steel that as the aspect ratio increases, the drift ratio at yield increases drastically. A similar observation was reported by Barbosa et al. (2016) for concrete columns reinforced with high-strength ASTM A706 Grade 550 steel. On the other hand, Lehman et al. (2004) also reported that drift ratios at yield were slightly affected by ρ_l . The increase in ρ_l from 0.7% to 3.0% resulted in increasing the yield drift ratios from 0.83% to 1.0% for concrete columns reinforced with conventional ASTM A706 Grade 420

steel. Similarly, the increase in ρ_l from 0.83% to 1.58% resulted in a higher drift at yield by 4% in concrete columns reinforced with ASTM A706 Grade 550 (Trejo et al. 2016).

3.5.2 Parameters Affecting Drift Ratios at DS-2

Irrespective of the type of HSS, the significant parameters contributing to the drift limits at DS-2, which is associated with the spalling of concrete cover, were L/D and $P/A_g f'_c$, with the latter having a negative effect (see Table 5). The average percent contributions of L/D and $P/A_g f'_c$ were 80.2% and 12.9%, respectively. These results are in line with the findings of previous cyclic testing of concrete columns reinforced with conventional steel. According to Lehman et al. (2004), the spalling drift increases as the aspect ratio increases in concrete columns reinforced with conventional steel. On contrary, the $P/A_g f'_c$ caused a reduction in the drift ratios at DS-2. This is primarily attributed to the fact that the increase in $P/A_g f'_c$ generates greater concrete compressive stresses, and consequently strains, which ultimately results in concrete cover spalling at lower drifts.

3.5.3 Parameters affecting drift ratios at DS-3 and DS-4_{cu}

Significant parameters affecting the drift ratio limits at DS-3 and DS-4_{cu} for the three types of HSS were the same since both damage states were identified using the concrete ultimate compression strain, ϵ_{cu} . These parameters were L/D , $P/A_g f'_c$, ρ_s , and f'_c . Their average percent contributions to DS-3 were 50%, 7.4%, 10.6%, and 17.4%, whereas their average percent contributions to DS-4_{cu} were 48.4%, 7.4%, 11.4%, and 18.8%, respectively. Of the four parameters, $P/A_g f'_c$ and f'_c had negative effects. Similar to DS-2, the increase in $P/A_g f'_c$ increases the concrete compressive stresses and strains, and consequently makes the core concrete more susceptible to crushing at lower drifts. The positive and negative effects of the ρ_s and f'_c , respectively, on the drifts at DS-3 and DS-4_{cu} were anticipated since, as per the definition of ϵ_{cu} in Eq. (9), ϵ_{cu} is directly proportional to the former and inversely proportional to the latter (Paulay and Priestley 1992).

3.5.4 Parameters affecting drift ratios at $DS-4_{sb}$

Significant parameters contributing to the drift ratio at $DS-4_{sb}$ for concrete columns reinforced with ASTM A706 Grade 550 and ASTM A615 Grade 690 were L/D , $P/A_g f'_c$, ρ_s , and f'_c . The same parameters but excluding $P/A_g f'_c$ and f'_c were found significant in their contribution to the $DS-4_{sb}$ for concrete columns reinforced with ASTM A1035 Grade 690. It appears the effects of $P/A_g f'_c$ and f'_c on the buckling of the main rebars diminishes with the increase in the yield strength of steel. Irrespective of the type of HSS, $P/A_g f'_c$ and f'_c had negative influences on the buckling of the HSS rebars (see Table 5). The positive and negative effects of the ρ_s and $P/A_g f'_c$, respectively, were consistent with the observations from the experimental program by Barclay and Kowalsky (2020) in which concrete columns reinforced with high-strength ASTM 706 Grade 550 steel were tested under cyclic loading. In columns with ρ_s of 0.7%, the longitudinal rebars first buckled at 4.5%, whereas those with ρ_s of 1.3%, the longitudinal rebars buckled at 6.4% drift (Barclay and Kowalsky (2020)). Higher ρ_s provides greater confinement to restrain the buckling of longitudinal rebars. Also, Barclay and Kowalsky (2020) reported that ASTM A706 Grade 550 longitudinal rebars in concrete columns subjected to higher axial load ratios buckled at lower drift ratios.

Table 4: Parameters Considered in the Factorial Analysis.

Type of HSS	Parameter	Symbol	Lower Level	Upper Level	Unit
ASTM A706 Grade 550	Aspect ratio	L/D	4	10	-
	Axial load ratio	$P/A_g f'_c$	5	20	%
	Longitudinal reinforcement ratio	ρ_l	1	4	%
	Spiral reinforcement ratio	ρ_s	0.7	1.3	%
	Concrete compressive strength	f'_c	30	80	MPa
	Yield strength	f_y	566	606	MPa
	Tensile strength	f_u	750	801	MPa
	Elastic modulus	E	181243	203320	MPa
	Strain at onset of strain hardening	ε_{sh}	0.0055	0.0093	mm/mm
	Uniform strain	ε_u	0.0899	0.1009	mm/mm
ASTM A615 Grade 690	Aspect ratio	L/D	4	10	-
	Axial load ratio	$P/A_g f'_c$	5	20	%
	Longitudinal reinforcement ratio	ρ_l	1	4	%
	Spiral reinforcement ratio	ρ_s	0.7	1.3	%
	Concrete compressive strength	f'_c	30	80	MPa
	Yield strength	f_y	666	750	MPa
	Tensile strength	f_u	808	949	MPa
	Elastic modulus	E	180735	211658	MPa
	Strain at onset of strain hardening	ε_{sh}	0.007	0.009	mm/mm
	Uniform strain	ε_u	0.0713	0.0879	mm/mm
ASTM A1035 Grade 690	Aspect ratio	L/D	4	10	-
	Axial load ratio	$P/A_g f'_c$	5	20	%
	Longitudinal reinforcement ratio	ρ_l	1	4	%
	Spiral reinforcement ratio	ρ_s	0.7	1.3	%
	Concrete compressive strength	f'_c	30	80	MPa
	Yield strength	f_y	748	920	MPa
	Elastic modulus	E	180145	207847	MPa
	Uniform strain	ε_u	0.0435	0.0545	mm/mm

Table 5: Percent Contributions of the Parameters Considered.

Parameter	ASTM A706 Grade 550					ASTM A615 Grade 690					ASTM A1035 Grade 690				
	DS-1	DS-2	DS-3	DS-4 _{cu}	DS-4 _{sb}	DS-1	DS-2	DS-3	DS-4 _{cu}	DS-4 _{sb}	DS-1	DS-2	DS-3	DS-4 _{cu}	DS-4 _{sb}
L/D	85.53	78.07	41.76	39.98	54.40	81.68	80.63	47.47	46.44	61.18	77.24	81.81	60.90	58.73	64.82
$P/A_g f'_c$	0.00	(14.8)	(9.40)	(9.53)	(11.0)	0.02	(12.4)	(7.32)	(7.39)	(6.38)	0.13	(11.6)	(5.46)	(5.39)	(2.44)
ρ_l	6.39	0.06	(4.08)	(3.76)	2.53	6.82	0.34	(3.66)	3.78	2.71	7.12	0.56	(1.81)	(3.55)	2.47
ρ_s	0.02	(0.05)	12.80	12.87	16.31	0.04	(0.05)	11.38	12.29	16.64	0.05	(0.06)	7.64	9.11	17.32
f'_c	(4.20)	0.05	(21.4)	(24.5)	(7.53)	(4.94)	0.00	(18.7)	(20.5)	(5.07)	(4.96)	(0.02)	(12.2)	(11.4)	(2.29)
f_y	0.37	0.05	0.11	0.09	0.15	1.29	0.09	0.37	0.29	0.37	4.13	0.13	2.15	1.92	4.16
f_u	0.00	0.00	0.01	0.01	0.02	0.00	0.00	0.04	0.07	0.37	-	-	-	-	-
E	(0.61)	(0.15)	(0.04)	(0.02)	(0.54)	(1.34)	(0.16)	(0.13)	(0.09)	(1.24)	(1.19)	(0.06)	(0.25)	(0.20)	(1.35)
ϵ_{sh}	0.00	0.00	(0.01)	0.00	0.00	0.00	0.00	(0.00)	0.00	0.00	-	-	-	-	-
ϵ_u	0.00	0.00	0.32	0.27	(0.04)	0.00	0.00	1.11	0.93	(0.09)	0.00	0.00	1.42	1.18	(0.06)

3.6 Drift Ratio Limit States of Concrete Columns Reinforced with HSS

Drift ratios identifying the onset of damage states need to be established on a probabilistic basis, especially if employed as part of seismic fragility assessments. In such assessments, to account for the uncertainty associated with the mean values of limit states, a coefficient of variance (COV) is assigned to each limit state. If enough information is not available to determine the coefficients of variance of the limit states, they could be determined subjectively. Nielson (2005) recommended taking COV of 0.25 for slight and moderate damage states (i.e. DS-1 and DS-2), and 0.5 for extensive and complete damage states (i.e. DS-3 and DS-4) for concrete columns reinforced with conventional steel. Coefficients of variance for concrete columns reinforced with different types of HSS have not been established yet. In this study, the Monte Carlo sampling technique was adopted to generate a number of random samples based on the probability distributions of the parameters considered. The parameters considered are the same as those considered in the factorial analysis. To account for the uncertainties in the following parameters: L/D , $P/A_g f'_c$, ρ_l , ρ_s , and f'_c , they were considered to be uniformly distributed between the upper and lower levels given in Table 4. As for the uncertainties in the parameters related to the properties of the HSS, they were considered to be normally distributed with mean and standard deviation values provided in Table 2, as recommended by Overby et al. (2017) and Shahrooz et al. (2011). 1000 unique sets of data, each representing a reinforced concrete column, were generated for each type of HSS. The concrete columns were subjected to the same loading protocol in the factorial analysis, and the drift ratios corresponding to the initiation of each of the damage states were recorded. Samples of the measured drift ratios corresponding to the damage states for all columns are given in Appendix A. Empirical and fitted cumulative distribution functions (CDFs) of the computed drift ratio limit states for concrete columns reinforced with ASTM A706 Grade 550, ASTM A615 Grade 690, and ASTM A1035 Grade 690, are plotted in Figure 8. Also, Figure 8 depicts the type of the fitted CDF, mean (μ), and COV of the drift ratio limit states. A goodness-of-fit test, the Anderson-Darling test, was employed to identify the appropriate fitted CDFs. Drift ratios at DS-1 and DS-2 were fitted to a 3-parameter Weibull distribution, whereas those at DS-3, DS-4cu, DS-4sb were fitted

to a lognormal distribution. Parameters defining each of the PDFs were determined by the maximum likelihood method and are provided in Appendix A.

The average coefficients of variation for DS-1, DS-2, DS-3, and DS-4 were 0.27, 0.25, 0.29, and 0.27, respectively. This implies that Nelson's (2005) recommended values of COV are appropriate for DS-1 and DS-2, but not DS-3 and DS-4 for concrete columns reinforced with HSS. For the samples of reinforced concrete columns considered, concrete columns reinforced with ASTM A1035 Grade 690 were characterized with the highest mean drift ratio at DS-1. This is attributed to the higher yield strength of ASTM A1035 Grade 690 steel when compared to the other two types of HSS (see Table 2). Insignificant differences in the mean drift ratio at DS-2 among the three types of HSS were observed. The reason for this observation is that concrete cover spalling in a concrete column is not influenced by the properties of its reinforcing steel. The average drift limits at DS-2 for concrete columns reinforced with ASTM A706 550, ASTM A615 Grade 690, and ASTM A1035 Grade 690 was 1.9%. The evident lack of symmetry in the distributions of drift ratios at DS-1 and DS-2 is due to the noticeable effect of the uniform distribution of the aspect ratio on the responses at these two damage states. According to the factorial analysis, the averages of the percent contributions of the aspect ratio to drifts at DS-1 and DS-2 for the three types of HSS were 81.4% and 80.2%, respectively. At DS-3 and DS-4_{cu}, concrete columns reinforced with ASTM A1035 Grade 690 were characterized with the lowest mean drift ratio, as shown in Figure 8. This is owing to the limited uniform strain capacity of ASTM A1035 Grade 690 steel which influences the ϵ_{cu} , as per Eq. 9. At DS-4_{sb}, concrete columns reinforced with ASTM A706 Grade 550 exhibited the lowest mean drift ratio. The prime reason for this is the lower yield strength of ASTM A706 Grade 550 when compared to the other two types of HSS.

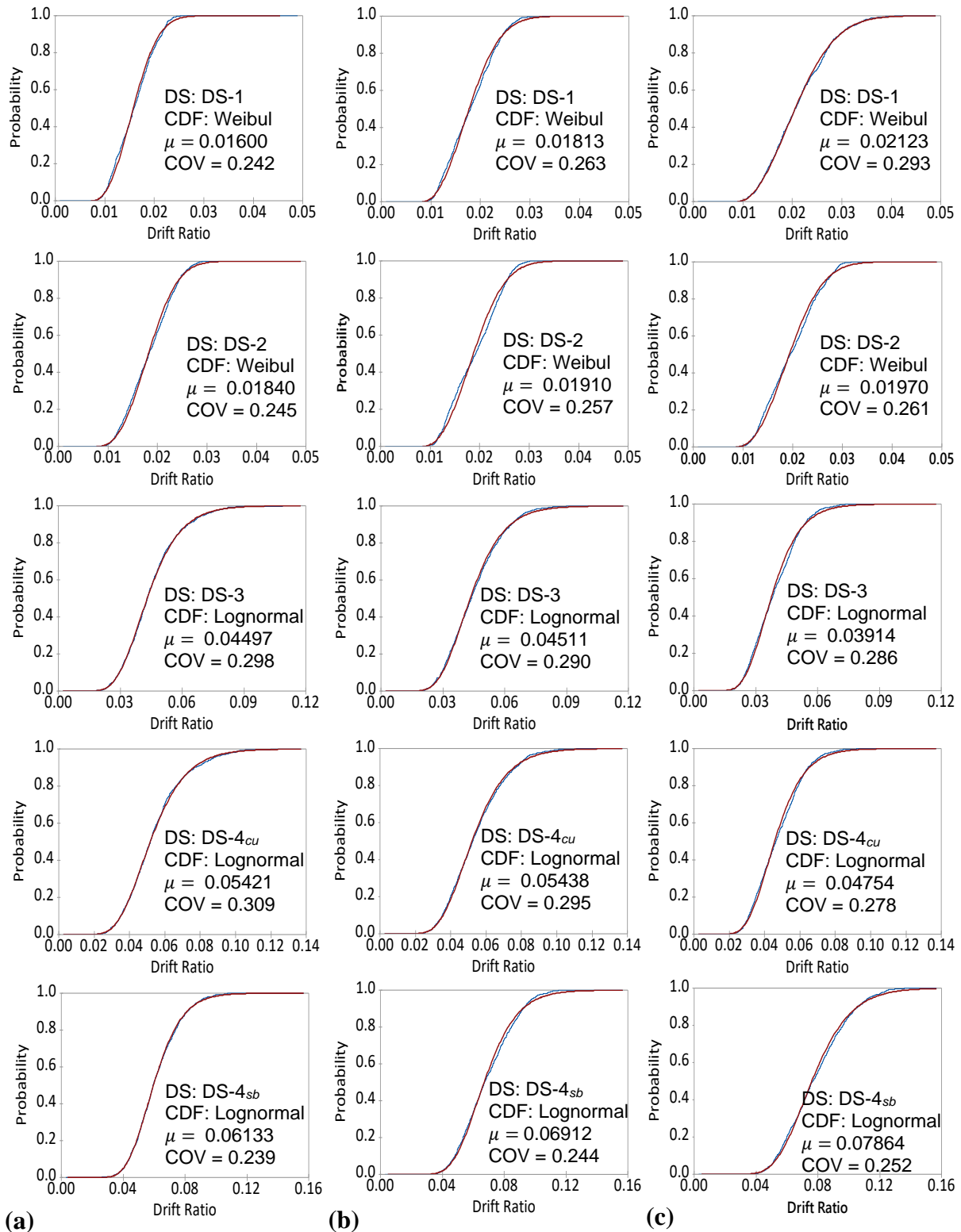


Figure 8: Empirical and fitted CDFs of drift ratio limit states for concrete columns reinforced with: (a) ASTM A706 Grade 550; (b) ASTM A615 Grade 690; and (c) ASTM A1035 Grade

690.

3.7 Simplified Expressions for the Drift Ratio Limits

The data from the previous analysis were processed through a symbolic regression tool, Eureqa (Schmidt and Lipson 2013), to generate simplified predictive expressions of the drift ratios at each damage state for the three types of HSS. Eureqa, originally developed at the Computational Synthesis Lab at Cornell University by Schmidt and Lipson (2009), is based on a machine learning model in which the genetic algorithm is developed to fit different analytical expressions to training data. The tool would keep updating the training data until best-fit expressions are found. In this study, 50% of the data were used to train the models, whereas the remaining 50% were used as validation data. Certain restrictions were imposed on the models to limit the complexity of the proposed expressions. Mathematical building blocks were limited to the following: constant, integer content, addition, subtraction, and multiplication. Also, only two-level interaction between the parameters was considered. In addition, the parameters considered for each expression were limited to only those found significant in the factorial analysis. Table 6 lists the proposed simplified expressions. Comparisons between the measured and predicted drift ratios at each damage state for concrete columns reinforced with the three types of HSS are presented in Figure 9. Also, the square of the correlation coefficient (R^2) for each of the proposed expressions is given in Figure 9. It should be noted that the expressions in Table 6 are only applicable to concrete columns having L/D , $P/A_g f'_c$, ρ_l , ρ_s , and f'_c falling within the upper and lower levels given in Table 4. As previously mentioned, these lower and upper levels bounded the properties of the concrete columns generated as part of the Monte Carlo sampling. As seen in Figure 9, the correlations between the predicted and measured drift ratios at DS-1, DS-3, DS-4_{cu}, DS-4_{sb} were higher for concrete columns reinforced with ASTM A706 Grade 550 compared to those reinforced with ASTM A615 Grade 690 and ASTM A1035 Grade 690. The prime reason for this observation is the greater variability in the mechanical properties of the latter two when compared to the former. For instance, the standard deviation of the yield strength of ASTM A706 Grade 550 was 20.2 MPa, whereas that of ASTM A615 Grade 690 and ASTM A1035 Grade 690 were 42.2 and 86.2 MPa, respectively (see Table 2). The insignificant differences in the values of R^2 at DS-2, which is not influenced by the

mechanical properties of the steel reinforcement, among the three types of concrete columns confirms the adequacy of the previous explanation. As more refined statistical data on the mechanical properties of HSS becomes available, the accuracy of proposed expressions for concrete columns reinforced with ASTM A615 Grade 690 and ASTM A1035 Grade 690 could be further improved.

Table 6: Proposed Simplified Expressions of Drift Ratios at the Damage States of Concrete Columns Reinforced with different types of HSS.

Type of HSS	Damage state	Eq. No.	Simplified expression of drift ratios
ASTM A706 Grade 550	DS-1	(12)	$0.00126 + 0.0017 (L/D) + 0.0138((L/D) (\rho_l))$
	DS-2	(13)	$0.00132 + 0.00305(L/D) - 0.00529 ((L/D)(P/A_g f'_c))$
	DS-3	(14)	$2.37(\rho_s) + 0.00855(L/D) - 0.00334 - 0.0989(P/A_g f'_c) - 0.0000623((L/D)(f'_c))$
	DS-4 _{cu}	(15)	$3.37(\rho_s) + 0.0102(L/D) - 0.00666 - 0.127(P/A_g f'_c) - 0.0000773((L/D)(f'_c))$
	DS-4 _{sb}	(16)	$3.39(\rho_s) + 0.00855 (L/D) - 0.00335 - 0.117(P/A_g f'_c) - 0.0000399((L/D)(f'_c))$
ASTM A615 Grade 690	DS-1	(17)	$0.00102 + 0.00189 (L/D) + 0.0201((L/D) (\rho_l))$
	DS-2	(18)	$0.00087 + 0.00323(L/D) - 0.00518 ((L/D)(P/A_g f'_c))$
	DS-3	(19)	$2.58(\rho_s) + 0.00855(L/D) - 0.00855 - 0.0785(P/A_g f'_c) - 0.0000576((L/D)(f'_c))$
	DS-4 _{cu}	(20)	$3.38(\rho_s) + 0.0102(L/D) - 0.0107 - 0.108(P/A_g f'_c) - 0.0000709((L/D)(f'_c))$
	DS-4 _{sb}	(21)	$4.15(\rho_s) + 0.00947(L/D) - 0.00947 - 0.115(P/A_g f'_c) - 0.0000382((L/D)(f'_c))$
ASTM A1035 Grade 690	DS-1	(22)	$0.000546 + 0.0025 (L/D) + 0.00992((L/D) (\rho_l))$
	DS-2	(23)	$0.000558 + 0.00338(L/D) - 0.00497((L/D)(P/A_g f'_c))$
	DS-3	(24)	$1.77(\rho_s) + 0.00693(L/D) - 0.00821 - 0.0422(P/A_g f'_c) - 0.0000351((L/D)(f'_c))$
	DS-4 _{cu}	(25)	$2.29(\rho_s) + 0.00814(L/D) - 0.00977 - 0.0561(P/A_g f'_c) - 0.0000404((L/D)(f'_c))$
	DS-4 _{sb}	(26)	$0.0179 + 0.00224 (L/D) + 0.65((L/D) (\rho_s))$

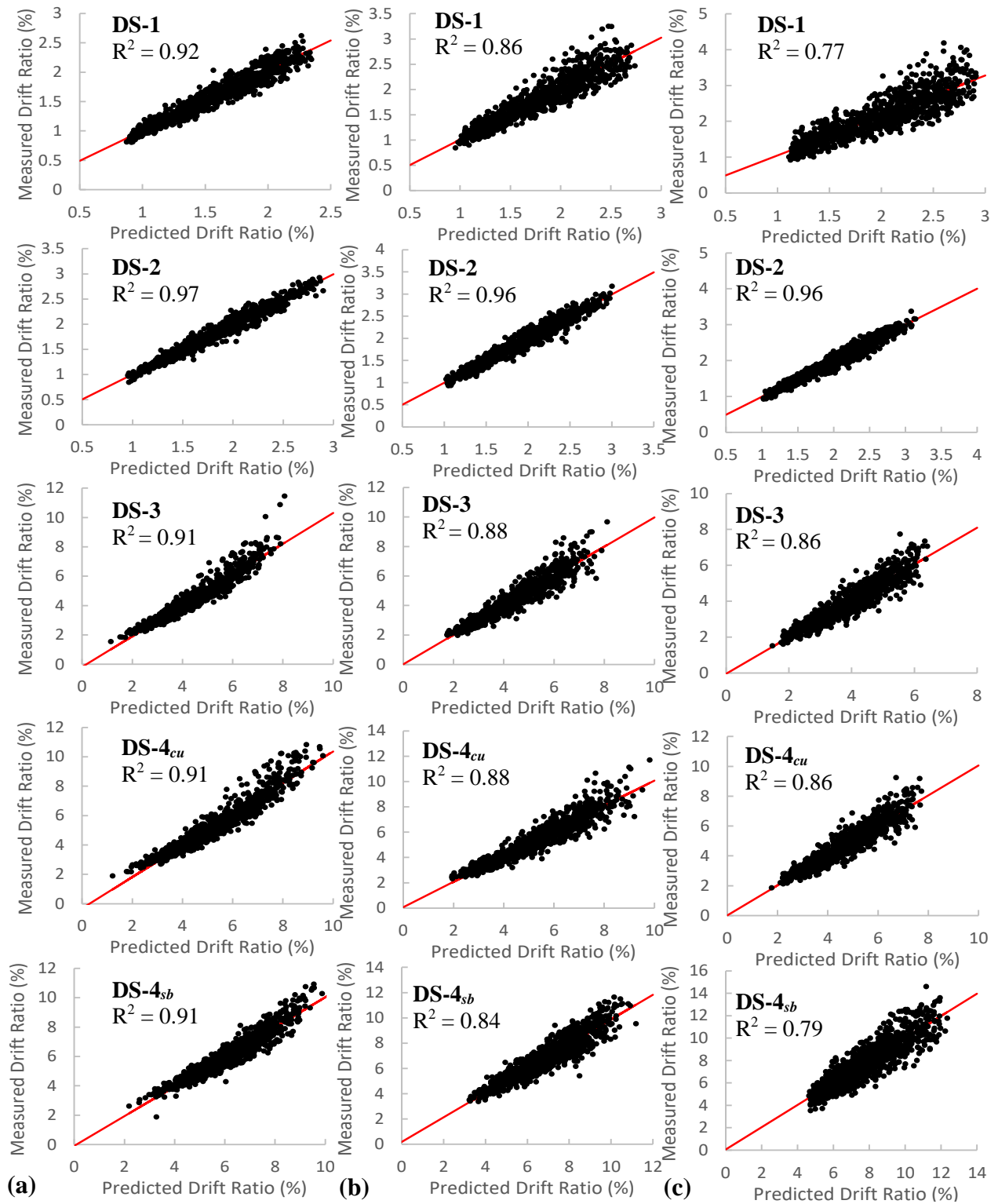


Figure 9: Comparison between drift ratios obtained from numerical analysis (measured) and those predicted from the proposed expressions for concrete columns reinforced with: (a) ASTM A706 Grade 550; (b) ASTM A615 Grade 690; (c) ASTM A1035 Grade 690.

To further evaluate the accuracy of the proposed simplified expressions, their drift ratio limit state predictions were compared against those reported from experimental programs on concrete columns reinforced with HSS, as presented in Table 7. Besides, the predictions of several equations found in the literature are also given in Table 7 for comparison purposes. The selected columns from Trejo et al. (2014) and Barclay and Kowalsky (2020) had properties satisfying the conditions of applicability of the proposed expressions. As seen in Table 7, Eq. 12 well-predicted the drift ratios at yield (i.e. DS-1) for all columns with a root-mean-square error (RMSE) of 0.001. Billah and Kabir (2020) proposed an expression to predict the yield drift ratio (Δ_y/L) for concrete bridge columns reinforced with HSS as follows:

$$\frac{\Delta_y}{L} (\%) = 0.55 + 0.1\rho_l + 180 \left(\frac{f_y}{E_s} \right) + \frac{L}{75D} \quad (27)$$

Eq. 27 predictions had an RSME of 0.002 indicating a comparable level of accuracy to that of Eq. 12. When compared to the experimentally measured drift ratios at spalling for specimens C2 and C4, Eq. 13 provided conservative predictions with an RMSE of 0.005. This is attributed to the conservative estimate of the concrete compression strain at concrete cover spalling on which the proposed expressions at DS-2 were based. Berry and Eberhard (2003) proposed an empirical expression to predict the drift ratio at concrete cover spalling (Δ_{sp}/L) for reinforced concrete columns which takes the following form:

$$\frac{\Delta_{sp}}{L} (\%) = 1.6 \left(1 - \frac{P}{f'_c A_g} \right) \left(1 + \frac{L}{10D} \right) \quad (28)$$

Billah and Kabir (2020) proposed a similar expression but for concrete bridge columns reinforced with HSS as follows:

$$\frac{\Delta_{sp}}{L} (\%) = 1.6 - 7.0 \left(\frac{P}{f'_c A_g} \right) + \frac{L}{3D} \quad (29)$$

The predictions of Eqs. 28 and 29 had an RMSE of 0.005 and 0.012, respectively, and are presented in Table 7. This indicates that the proposed expression (Eq. 13) and 28 had the same level of accuracy in predicting the drift ratios at concrete cover spalling for concrete columns reinforced with ASTM A706 Grade 550. Among the columns examined, the drift ratio at concrete core crushing was only reported for

C2 (Trejo et al. 2014) for which the percentage error of the prediction of Eq. 15 (i.e. DS-4_{cu}) was only 1.6%. Also, for the same specimen, at DS-3, the drift ratio prediction of Eq. 14 was 84% of that measured experimentally at concrete core crushing which indicates that DS-3 not only reflects extensive spalling but also provides a safety margin against the onset of concrete core crushing. Concrete cover in the plastic hinge region of the specimens tested by Barclay and Kowalsky (2020) was removed for instrumentation purposes prior to testing, and consequently drift ratios corresponding to the onset of DS-2, DS-3, and DS-4_{cu} (i.e. spalling, extensive spalling, and concrete core crushing, respectively) for specimens 1-4 were not reported. The bar buckling drift ratio predictions of Eq. 16 were comparable to those measured experimentally with an RMSE of 0.006. Several equations to predict the drift ratio at the onset of rebar buckling (Δ_{bb}/L) in reinforced concrete columns can be found in the literature. Those proposed by Berry and Eberhard (2005) and Goodnight et al. (2016) are the most widely used for concrete columns reinforced with normal-strength steel and are thus considered in this study for comparison purposes. The equation proposed by Berry and Eberhard (2005) takes the following form:

$$\frac{\Delta_{bb}}{L} (\%) = 3.25 \left(1 + k_{ebb} \rho_{\text{eff}} \frac{d_b}{D} \right) \left(1 - \frac{P}{A_g f'_c} \right) \left(1 + \frac{L}{10D} \right) \quad (30)$$

where $k_{ebb} = 150$ for spiral-reinforced concrete columns, $\rho_{\text{eff}} = \rho_s f_{yh} / f'_c$, f_{yh} is the yield strength of transverse reinforcement, d_b is the diameter of the longitudinal reinforcing steel bar. On the other hand, the equation proposed by Goodnight et al. (2016) takes the following form:

$$\frac{\Delta_{bb}}{L} (\%) = 0.9 - 3.13 \frac{P}{A_g f'_c} + 142000 \rho_s \frac{f_{yh}}{E_s} + 0.45 \frac{L}{D} \quad (31)$$

In addition, Billah and Kabir (2020) developed a similar expression specifically applicable to concrete columns reinforced with HSS as follows:

$$\frac{\Delta_{bb}}{L} (\%) = 5 + 125 \left(\frac{f_y}{E_s} \right) \rho_s - 18 \left(\frac{P}{A_g f'_c} \right) + 0.85 \left(\frac{L}{D} \right) \quad (32)$$

Drift ratio predictions of Eqs. 30, 31, and 32 for the specimens considered are presented in Table 7. Among the three expressions, Eq. 31 provided the best predictions of drift ratios at rebar buckling with an RMSE of 0.01. However, when compared to the proposed expression (i.e. Eq. 16 with RSME of 0.006), it provided poorer predictions. It must be noted that experimental results of cyclic tests on circular concrete columns reinforced with ASTM A615 Grade 690 and ASTM A1035 Grade 690 with properties falling within the ranges of applicability of the proposed expressions do not seem to exist. For this reason, comparisons between the drift ratio limit state predictions of the proposed expressions and those measured experimentally were only made for concrete columns reinforced with ASTM A706 Grade 550. As more experimental data from cyclic tests on concrete columns reinforced with different types of HSS become available, the accuracy of the proposed expressions could be further validated for concrete columns having a wider range of geometrical and material properties. Nevertheless, the proposed simplified expressions generally provide adequate predictions of the drift ratio limit states determined from the analyses of the fiber-based models as well as those measured in previous experimental programs. Therefore, the proposed expressions could be employed within the context of performance-based design to predict the drift ratio limit states of concrete columns reinforced with different types of HSS. This would be mostly useful at preliminary design stages where detailed types of analysis such as nonlinear static pushover are often unnecessary. In addition, since the predictions of the proposed expressions were validated using previous experimental data, they would serve as a benchmark for practitioners when determining the limit states of concrete columns reinforced with HSS through numerical analyses. Lastly, design aid charts in the form of elastic stiffness ratio versus axial load ratio were produced by performing a series of moment-curvature analyses on HSS bar-reinforced concrete column sections with varying axial load ratio ($P/A_g f'_c$) and longitudinal reinforcement ratio (ρ_l). $P/A_g f'_c$ was varied from 5% to 25%, while ρ_l was varied from 1% to 4%. The variation of the elastic stiffness ratio with the axial load ratio for concrete sections reinforced with HSS is plotted in Figure 10. Despite the slight differences in the elastic stiffness ratios, the trends of the curves in Figure 10 seem similar to those of concrete sections reinforced with conventional ASTM

A706 Grade 420 steel (AASHTO 2014). Within the context of PBD, the curves in Figure 10 could be employed to determine the cracked section properties of concrete columns reinforced with HSS, which are required to compute the seismic drift demands as part of the response spectrum analysis.

Table 7: Comparisons Between the Experimentally Measured Drift Ratios at Different Damage States and those Predicted Using Numerical Expressions.

Exp. program		Trejo et al. (2014)		Barcley and Kowalsky (2020)			
Specimen		C2	C4	1	2	3	4
HSS Type		ASTM A706 Grade 550					
L/D		6	6	4	4	4	4
$P/A_g f'_c$		0.05	0.05	0.05	0.1	0.05	0.05
ρ_l		0.02	0.0083	0.016	0.02	0.016	0.016
ρ_s		0.01	0.0082	0.01	0.01	0.007	0.013
f_y (MPa)		593	594	572	572	572	572
f_{yh} (MPa)		590	590	545	545	545	545
f'_c (MPa)		30	30	39.8	45.7	47	47.8
DS-1	Pred. (Eq. 12)	0.013	0.012	0.009	0.009	0.009	0.009
	Pred. (Eq. 27)	0.012	0.012	0.011	0.011	0.011	0.011
	Exp.	0.011	0.011	0.008	0.009	0.008	0.008
DS-2	Pred. (Eq. 13)	0.018	0.018	0.012	0.011	0.012	0.012
	Pred. (Eq. 28)	0.024	0.024	0.021	0.020	0.021	0.021
	Pred. (Eq. 29)	0.033	0.033	0.026	0.022	0.026	0.026
	Exp.	0.017	0.026	-	-	-	-
DS-3	Pred. (Eq. 14)	0.051	0.051	0.040	0.033	0.031	0.045
	Exp.	-	-	-	-	-	-
DS-4 _{cu}	Pred. (Eq. 15)	0.062	0.062	0.049	0.041	0.037	0.057
	Exp.	0.061	-	-	-	-	-
DS-4 _{sb}	Pred. (Eq. 16)	0.063	0.063	0.053	0.046	0.041	0.061
	Pred. (Eq. 30)	0.080	0.087	0.071	0.064	0.060	0.073
	Pred. (Eq. 31)	0.069	0.069	0.064	0.063	0.053	0.076
	Pred. (Eq. 32)	0.092	0.092	0.075	0.066	0.075	0.075
	Exp.	0.061	-	0.066	0.045	0.045	0.064

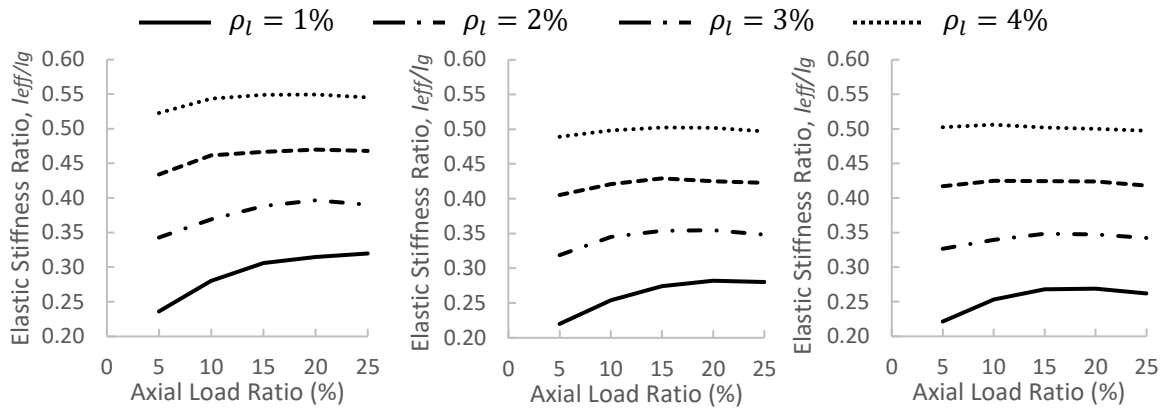


Figure 10: Effective flexural stiffness of cracked reinforced concrete sections reinforced with: (a) ASTM A706 Grade 550; (b) ASTM A615 Grade 690; and (c) ASTM A1035 Grade 690.

3.8 Summary

This study presents the results of a comprehensive analytical program with an overarching objective of proposing simplified expressions to predict drift ratios corresponding to the onset of different damage states for concrete columns reinforced with HSS. Three types of HSS, namely, ASTM A706 Grade 550, ASTM A615 Grade 690, and ASTM A1035 Grade 690, were considered. The accuracy of the fiber-based numerical models in predicting the drift limit states of concrete columns reinforced with HSS was initially verified using available previous experimental data. Full factorial analysis considering upper and lower levels of geometry-, section-, and material-related parameters was carried out. The results of the factorial analysis provided a better understanding of the effect of different parameters on the drift ratio limit states and were critical in limiting the complexity of the proposed simplified expressions since only those with significant contributions were considered. To generate sufficient data to generate the expressions, the Monte Carlo sampling technique was adopted. Three samples each consisting of 1000 unique columns, were generated for the three types of HSS. The columns were subjected to displacement-controlled quasi-static cyclic loading protocols, and the drift ratios at the onset of the damage states were recorded. The resulting data were first used to establish the drift ratio limit states on a probabilistic basis. Then, the resulting data

were processed through a symbolic regression analysis which fitted simplified numerical expressions to the data. The proposed simplified expressions for concrete columns reinforced with ASTM A706 Grade 550 had the highest square of correlation coefficients. This was owing to the lower variability in the mechanical properties of ASTM A706 Grade 550 when compared to ASTM A615 Grade 690 and ASTM A1035 Grade 690. Nevertheless, the proposed simplified expression provided adequate predictions of the drift ratio limits determined from the analyses of the fiber-based models as well as those measured in previous experimental programs. As more experimental data from cyclic tests on concrete columns reinforced with different types of HSS become available, the accuracy of the proposed expressions could be further validated for concrete columns having a wider range of geometrical and material properties. It must be noted that the proposed expressions are only applicable to concrete columns having properties falling within the upper and lower levels of the data on which the proposed expressions were based. The proposed expressions would be mostly useful at preliminary design stages where detailed types of analysis such as nonlinear static pushover are often unnecessary. Besides, since the predictions of the proposed expressions were validated using previous experimental data, they would serve as a benchmark for the bridge engineering community when determining the limit states of concrete columns reinforced with HSS through numerical analyses.

CHAPTER 4: LOW-CYCLE FATIGUE PERFORMANCE OF HIGH-STRENGTH STEEL REINFORCING BARS CONSIDERING THE EFFECT OF INELASTIC BUCKLING

4.1 General

High-strength steel (HSS) reinforcing bars conforming to ASTM A1035 (ASTM 2020b) have been gaining increasing popularity in the past two decades due to their superior strength and corrosion resistance when compared to conventional reinforcing steel grades such as ASTM A615 (ASTM 2020a). Utilizing such rebars in construction reduces rebar congestion, and hence improves concrete placement productivity (Aldabagh and Alam 2020). In addition, the use of HSS reduces the weight of reinforcement. Hence, the labor cost of placing reinforcement is significantly lower for HSS than that of conventional steel (Thomas et al. 2013). Because of the higher chromium content, ASTM A1035 steel can be between two and ten times more corrosion-resistant than the conventional ASTM A615 steel (ACI 2019a). In the United States and Canada, ASTM A1035 steel bars are currently being produced in two minimum yield strength levels, namely: 690 and 830 MPa and are designated as Grade 690 and Grade 830, respectively. The stress-strain curve of ASTM A1035 steel differs from that of ASTM A615 steel where the former lacks a well-defined yield point and yield plateau. Recently, the ACI released *Guide for the Use of ASTM A1035/A1035M Type CS Grade 100 (690) Steel Bars for Structural Concrete* (ACI 2019a) in which the ACI requirements limiting the efficient use of ASTM A1035 Grade 690 in structural concrete were revised. Besides, the *AASHTO LRFD Bridge Design Specifications* (AASHTO 2017) permits the use of ASTM A1035 steel with the design yield strength of 690 MPa in different applications based on the findings of the NCHRP Project 12-77 (Shahrooz et al. 2011). However, the two documents restrict the use of ASTM A1035 Grade 690 reinforcing bars in structural components designated as part of the seismic-force-resisting system. The only exception is when ASTM A1035 Grade 690 steel is used as lateral ties for confinement in the plastic hinge regions. One of the main drivers for such code restrictions is the lack of research work documenting the low-cycle fatigue performance of ASTM A1035 Grade 690 reinforcing bars. According to the *ATC-98 Project on*

Seismic Design of Concrete Structures with High-Strength Reinforcement, additional research work is still required before recommending the use of Grades 690 and 830 rebars as longitudinal reinforcement in seismic regions (Kelly et al. 2017).

In a seismic event, the longitudinal reinforcing bars at critical sections such as those falling within the potential plastic hinge regions undergo large inelastic tension-compression strain reversals to accommodate the significant inelastic deformations caused by the earthquake loading. Due to these strain reversals, damage accumulates in the reinforcement and eventually leads to fracture. This type of failure is called low-cycle fatigue. The number of cycles to fatigue failure, or the so-called fatigue life, in reinforcing bars typically does not exceed 1000 when large strains beyond the elastic limit are applied (Ghannoum and Slavin 2016). Buckling is often accompanied by the fracture of reinforcement in tension due to the accumulation of low-cycle fatigue damage (El-Bahy et al. 1999; Brown and Kunnath 2004; Lehman et al. 2004). The buckling and fracture of longitudinal reinforcing bars in reinforced concrete columns cause significant moment and strength degradation and thereby often adopted by design codes to signal the initiation of collapse limit state. For example, when carrying out performance-based seismic design, the *Canadian Highway Bridge Design Code* identifies the onset of the “life safety” performance level, at which the bridge is no longer usable, by rebar buckling, fracture, and/or concrete crushing (CSA 2019b). As a result, it is of critical importance to understand the fatigue characteristics of HSS reinforcing bars before utilizing them in seismic applications.

Limited experimental studies have investigated the low-cycle fatigue performance of high-strength steel reinforcing bars where the vast majority of fatigue tests in the past were conducted on ordinary regular-strength steel reinforcing bars. Examples of ordinary reinforcing bars include ASTM A615 Grade 420 (ASTM 2020a) and ASTM A706 Grade 420 (ASTM 2016), for which the yield strength generally does not exceed 500 MPa. Koh and Stephens (Koh and Stephens 1991) evaluated the fatigue performance of ASTM A723 quenched and tempered high-strength steel having yield and ultimate strengths of 1170 and 1262 MPa, respectively. The specimens were machined and tested under axial-strain-controlled reversed cyclic tests with strain ratios (R , defined later) of -2, -1, 0, 0.5, and 0.75; and strain amplitudes ranging from

0.0025 to 0.03. The fatigue life of the tested specimens ranged from 15 to 100000 cycles. The strain ratio R had a negligible effect on the cyclic stress-strain responses generated based on half-life hysteresis loop peaks. The mean stress data were best represented by the log-log linear Smith, Watson and Topper (SWT) model. A similar investigation was conducted by Mander et al. (Mander et al. 1994) but using unmachined ASTM A722 Type II hot-rolled and proof-stressed alloy-steel thread bars with a minimum ultimate tensile strength of 1083 MPa. Mander et al. (1994) reported that the commonly used strain-life models for low cycle fatigue such as Coffin-Manson models for plastic strain and total strain (Coffin 1954; Manson 1953), Koh-Stephens Model (Koh and Stephens 1991), modified SWT model (Smith et al. 1970), and Lorenzo-Laird model (Lorenzo and Laird 1984) fitted well to the experimental data. Energy-based fatigue models, which relate the total dissipated energy with the number of half-cycles to failure, were also established. The study demonstrated that both regular- and high-strength steel reinforcing bars exhibited similar modulus of toughness and low-cycle fatigue life. For this reason, design codes not permitting the use of HSS in seismic applications were considered to be overly restrictive (Mander et al. 1994). Ghannoum and Slavin (2016) evaluated the low-cycle fatigue performance of other types of HSS reinforcing bars conforming to ASTM A615 (ASTM 2020a) and ASTM A706 (ASTM 2016) with minimum yield strengths of 690 and 550 MPa which are designated as ASTM A615 Grade 690 and ASTM 706 Grade 550, respectively. Variables considered in the investigation included production method, bar size, loading protocols, and bar unsupported length. Test results indicated that the low-cycle fatigue performance of HSS is marginally poorer than that of regular-strength steel. One of the most influencing parameters on the low-cycle fatigue performance was the bar unsupported length. Decreasing the bar unsupported length reduces the buckling amplitude and strain concentrations in the bar, and consequently substantially improves the low-cycle fatigue performance. Kashani et al. (2015) and Tripathi et al. (2018) investigated the effect of inelastic buckling on the low-cycle fatigue performance of commonly used normal-strength reinforcing steel bars. Specifically, in the experimental program by Kashani et al. (2015), a total of ninety specimens were tested under axial-strain-controlled cyclic loading with strain amplitudes ranging from 1% to 5%. The influence of rebar surface condition, rebar diameter, and buckling length on the low-cycle fatigue performance of

B500B and B460 British-manufactured reinforcing bars was established. On the other hand, a similar experimental program was executed by Tripathi et al. (2018) but considering Grade 300E and 500E reinforcing bars which represent common types of normal-strength reinforcing bars used in reinforced concrete structures in New Zealand. Both studies reported that the increase in the buckling length deteriorated the low-cycle fatigue life of the reinforcing bars. Consequently, empirical models capturing such effects were proposed. Those models were considered in this study for comparison purposes.

Experimental low-cycle fatigue test data for ASTM A1035 steel do not seem to exist. The only reported fatigue tests undertaken using ASTM A1035 steel reinforcing bars are high-cycle fatigue tests by DeJong et al. (2006). However, in such tests, the strain amplitude rarely exceeds 0.01, hence making them inappropriate to understand the fatigue characteristics of reinforcing bars for seismic applications. The main objectives of this study include: (1) evaluating the low-cycle fatigue behavior of ASTM A1035 Grade 690 under axial-strain-controlled reversed cyclic tests with zero mean strain and constant total strain amplitudes ranging from 0.01 to 0.04; (2) capturing the effect of strain amplitude, inelastic buckling, rebar size on the low-cycle fatigue performance of ASTM A1035 Grade 690 steel reinforcing bars; (3) proposing models relating the fatigue life to the total strain amplitude and dissipated energy considering the effect of inelastic buckling; (4) assessing the applicability of existing predictive strain and energy-based fatigue models to ASTM A1035 Grade 690 reinforcing bars; and (5) utilizing the proposed models to make appropriate recommendations for the use of ASTM A1035 Grade 690 steel in reinforced concrete columns in seismic regions.

4.2 Material and Experimental Procedure

ASTM A1035 Grade 690 deformed rebars with nominal diameters (d_b) of 12.7 and 15.88 mm (i.e., #4 and #5) were used in this research. The chemical composition of these rebars (wt %) was 0.2 C, 1.5 Mn, 0.035 P, 0.045 S, 0.50 Si, 0.05 Ni, 4.0-7.9 Cr (ASTM 2020b). Monotonic uniaxial tension tests and axial-strain-controlled reversed cyclic tests were performed using a 500-kN MTS servo-hydraulic universal materials testing machine. This machine is capable of performing constant or variable amplitude load-

strain-, or displacement-controlled low-cycle fatigue tests. The machine consists of upper and lower independent hydraulic grips with a v-groove surface. The rebars penetrated a distance of 70 mm in each grip and were subjected to hydraulic pressure to prevent rebar slippage during the tests. This penetration length also provided sufficient rotational fixity to reflect the actual boundary conditions of longitudinal rebars restrained by stiff transverse reinforcement in concrete columns. According to Dhkal and Maekawa (2002), under such conditions, tie spacing (gripping span) is equal to the buckling length. Rebars rolled-on deformations are normally the locations where stresses are concentrated, and hence often become initiators of fatigue cracks (Brown and Kunnath 2004). For this reason, the surface of the rebars tested was not machined or altered to obtain low-cycle fatigue properties reflective of those of rebars in reinforced concrete columns as recommended by Mander et al. (1994), Hawileh et al. (2010), and Ghannoum and Slavin (2016).

Monotonic tensile tests of four bar specimens (two with d_b of 12.7 mm and two with d_b of 15.88 mm) were first performed to obtain the mechanical properties and generate tensile stress-strain curves. In these tests, the specimens were subjected to displacement-controlled loading with a constant loading rate of 1.0 mm/min. The axial strain was measured over a gauge length of 25 mm using an extensometer mounted at mid-height of the specimen. In addition to the extensometer, a Linear Variable Displacement Transducer (LVDT) was mounted to the specimen to measure the change in rebar length between the loading grips. This measurement was used to compute axial strain averaged over the unsupported reinforcing bar length. The total length of the rebar in the monotonic tension tests was 150 mm, whereas it was varied in the low-cycle fatigue tests depending on the target slenderness ratio. The material properties obtained include: modulus of elasticity (E_s), yield strength (f_y), ultimate tensile strength (f_{su}), the ratio of ultimate tensile strength to yield strength (T/Y), and strain at failure (ϵ_{sf}). Table 8 lists the measured mechanical properties for the four tested specimens. Sample stress-strain curves of the rebars with d_b of 12.7 and 15.88 mm are shown in Figure 11. These curves are characterized by a linear portion up to a proportional limit followed by a nonlinear curve up to the tensile strength. The proportional limit ranges from 420 to 550 MPa (ACI 2019a). The stress-strain curves lack a well-defined yield point and plateau. For

this reason, the yield strength is normally established using one of the following methods: (1) 0.35% extension under load (EUL) method; (2) 0.5% EUL method; and (3) 0.2% offset method with the last being the most common. In the 0.2% offset method, the yield strength is the stress on the engineering stress-strain curve at its intersection with a line having a slope equal to its modulus of elasticity and starting from the strain of 0.2%. In the 0.35% and 0.5% EUL methods, the yield strength is the stress corresponding to a strain of 0.0035 and 0.005, respectively. The average yield strength (established using the 0.2% offset method) of the four specimens was 784.8 MPa. The rebar diameter had little to no effect on the mechanical properties of the tested specimens. The T/Y , which was computed using a yield strength established based on the 0.2% offset method, ranged from 1.31 to 1.34 with an average value of 1.32. According to Shahrooz et al. (2011), irrespective of the method by which the yield strength is determined, the T/Y of ASTM A1035 Grade 690 reinforcing steel exceeds 1.25. This limit of 1.25 is the minimum specified T/Y ratio in ASTM A706 (ASTM 2016) for ASTM A706 reinforcing bars, which are commonly used in seismic applications. However, the measured average ϵ_{sf} of ASTM A1035 Grade 690 is approximately only one-third of the minimum specified ϵ_{sf} for ASTM 706 reinforcing bars. Macchi et al. (1996) reported that the strain hardening, i.e. T/Y , of reinforcing bars has a greater effect on the seismic performance of concrete columns than the ϵ_{sf} . The previous discussion indicates that, from a monotonic-tensile-properties perspective, ASTM A1035 Grade 690 reinforcing bars could have the potential to be used as vertical reinforcement in concrete beams or columns capable of developing plastic hinges, but only in regions characterized with low seismicity in which the rebars in concrete columns would be subjected to relatively low axial strain demands. Figure 12 provides a comparison of the stress-strain relationships generated using axial strain measured using the extensometer and average axial strain measured using the LVDT. It is evident from Figure 12 that, prior to the removal of the extensometer, the two curves are almost identical, indicating that the average axial strain computed using the LVDT measurement is accurate. This observation is important since the stress-strain curves in the low-cycle fatigue tests were generated using only the average axial strain measured by the LVDT. The extensometer was not used in the low-cycle fatigue tests to prevent

damaging it since the tested reinforcing bars were prone to buckling during the low-cycle fatigue tests. The same procedure was followed in low-cycle fatigue tests by Kashani et al. (2015) and Tripathi et al. (2018) in which the effect of inelastic buckling of rebar was considered.

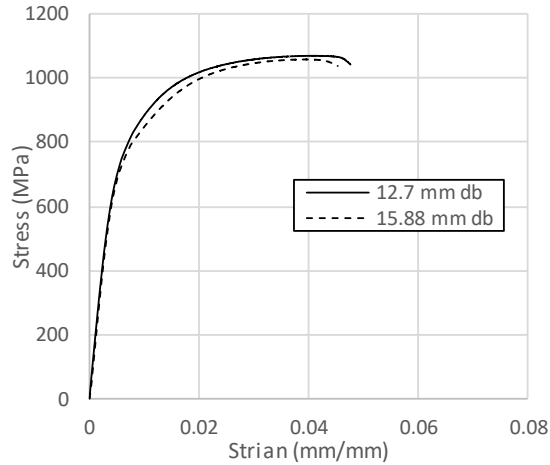


Figure 11: Stress-strain relations for rebars with d_b of 12.7 and 15.88 mm from monotonic tension tests.

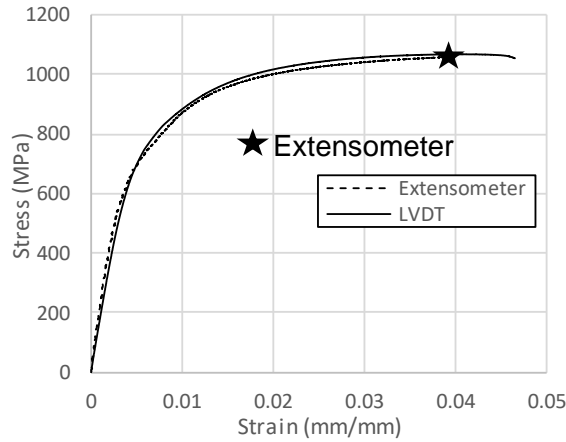


Figure 12: Comparison of stress-strain relations generated using extensometer and LVDT.

Table 8: Summary of Mechanical Properties Derived from Monotonic Tension Tests.

d_b (mm)	Specimen	E_s (GPa)	f_y (MPa)			f_{su} (MPa)	T/Y	ϵ_{sf}
			0.35% EUL	0.5% EUL	0.2% Offset			
12.7 (#4)	1	191.1	668.9	716.6	817.4	1075.1	1.32	0.044
	2	175.2	613.2	657.0	773.6	1034.2	1.34	0.047
15.88 (#5)	1	179.2	627.2	672.0	765.8	1012.2	1.32	0.045
	2	184.7	646.5	692.6	782.2	1022.4	1.31	0.044

A total of sixty-four bar specimens were tested under axial strain-controlled low-cycle fatigue. The test setup for these tests was similar to that of the monotonic tension tests described earlier except for the loading protocol and the bar unsupported length. A sinusoidal loading waveform consisting of fully reversed constant-amplitude strain cycles was applied to the bar specimens. Figure 13 shows the loading history adopted in the low-cycle fatigue tests indicating the key characteristics, where T is the time period of the loading. Frequencies (f) ranged from 0.00625 to 0.025 Hz, resulting in an average (peak-to-peak) strain rate of 0.001/s, as recommended by Ghannoum and Slavin (2016). The total strain amplitudes (ε_a) considered in this study were 0.01, 0.02, 0.03, and 0.04. The total strain amplitude is defined as the sum of the elastic and plastic portions of the strain. The considered bar unsupported length, i.e. the length between the grips, ranged from $6d_b$ to $15d_b$ in $3d_b$ increments. The low-cycle fatigue tests were carried out with a constant mean strain ratio (R) of -1, where R is defined as (Collins 1993):

$$R = \frac{\varepsilon_{s,\min}}{\varepsilon_{s,\max}} \quad \text{if } |\varepsilon_{s,\max}| \geq |\varepsilon_{s,\min}| \quad (33)$$

$$R = \frac{\varepsilon_{s,\max}}{\varepsilon_{s,\min}} \quad \text{if } |\varepsilon_{s,\max}| < |\varepsilon_{s,\min}| \quad (34)$$

where $\varepsilon_{s,\min}$ is the largest compressive strain, and $\varepsilon_{s,\max}$ is the largest tensile strain. This study considers a constant R because of the findings of Mander et al. (1994) which demonstrated that R had a negligible effect on the low-cycle fatigue life of regular- and high-strength reinforcing steel. Failure was established when the bar specimens were completely fractured. Two identical specimens were tested for each test configuration to ensure the repeatability of the results. The specimens were labeled to indicate d_b , bar unsupported length, ε_a , and specimen number. For example, 15.9-9 d_b -0.01 (1) refers to specimen 1 with d_b of 15.9 mm, 9 d_b bar unsupported length, and tested using the loading protocol with ε_a of 0.01.

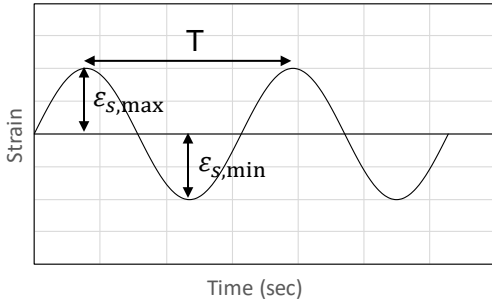


Figure 13: Sinusoidal loading waveform.

4.3 Low-Cycle Fatigue Test Results

Results of the low-cycle fatigue tests are listed in Tables 9 and 10, with Figure 14 and Figure 15 presenting certain selected stress-strain responses. Tables 9 and 10 contain several measures of low-cycle fatigue performances, which are defined as follows:

- $2Nf$ = number of half-cycles to failure, i.e. fatigue life.
- ΔW_{p1} = hysteretic energy dissipated in the first cycle.
- W_{fT} = total hysteretic energy dissipated to failure.
- $\Delta W_{p,avg}$ = average hysteretic energy dissipated per cycle, which is equal to W_{fT} divided by the number of cycles to failure (Nf).

For energy computations, the trapezoid rule was used to numerically integrate the area enclosed within the hysteresis loops. The well-accepted non-dimensional bar buckling parameter (λ) introduced by Dhakal and Maekawa (2002) was employed in this study to incorporate the effect of inelastic buckling into the proposed models. The bar buckling parameter describes the buckling behavior of a reinforcing bar based on its yield strength (f_y) and slenderness ratio (L/D) as follows:

$$\lambda = \frac{L}{D} \sqrt{\frac{f_y}{100}} \quad (35)$$

Here, L/D is the ratio of the rebar buckling length, i.e. unsupported length of the rebar between the grips, to the rebar diameter. f_y should be in MPa in Eq. 35. In this study, f_y is taken as 785 MPa which is the

average yield strength (based on the 0.2% offset method) of the four rebars tested in the monotonic tension tests. This indicates that rebars with L/D of 6, 9, 12, 15 will have λ values of 16.81, 25.33, 33.62, and 42.03, respectively.

Table 9: Low-Cycle Fatigue Results for 12.7 mm Diameter Reinforcing Bars.

Specimen	Buckling Parameter, λ	Frequency, f (Hz)	$2Nf$	ΔW_{P1} (MPa*)	W_{FT} (MPa*)	$\Delta W_{P,avg}$ (MPa*)
12.7-6 d_b -0.01 (1)	16.81	0.025	98.8	7.60	365.56	7.40
12.7-6 d_b -0.01 (2)			88.7	7.19	310.45	7.00
12.7-6 d_b -0.02 (1)		0.0125	7.6	42.81	124.54	32.77
12.7-6 d_b -0.02 (2)			8	40.71	122.97	30.74
12.7-6 d_b -0.03 (1)**		0.00833	2.4	58.80	58.72	48.93
12.7-6 d_b -0.03 (2)			4.4	62.56	110.72	50.33
12.7-6 d_b -0.04 (1)**		0.00625	2.4	73.81	73.68	61.40
12.7-6 d_b -0.04 (2)			2.2	75.62	75.57	68.70
12.7-9 d_b -0.01 (1)	25.22	0.025	60.8	9.44	225.96	7.43
12.7-9 d_b -0.01 (2)			55	9.06	205.96	7.49
12.7-9 d_b -0.02 (1)		0.0125	8.6	31.69	94.86	22.06
12.7-9 d_b -0.02 (2)			6.8	31.61	81.89	24.09
12.7-9 d_b -0.03 (1)		0.00833	4.4	50.34	84.41	38.37
12.7-9 d_b -0.03 (2)			4.5	47.88	86.69	38.53
12.7-9 d_b -0.04 (1)		0.00625	4.3	65.91	102.58	47.71
12.7-9 d_b -0.04 (2)			4.4	64.03	70.42	32.01
12.7-12 d_b -0.01 (1)	33.62	0.025	30.2	14.17	139.50	9.24
12.7-12 d_b -0.01 (2)			34.7	12.12	145.90	8.41
12.7-12 d_b -0.02 (1)		0.0125	8.5	33.20	90.07	21.19
12.7-12 d_b -0.02 (2)			8.5	34.39	93.77	22.06
12.7-12 d_b -0.03 (1)		0.00833	6.5	41.57	84.63	26.04
12.7-12 d_b -0.03 (2)			4.6	41.32	74.67	32.47
12.7-12 d_b -0.04 (1)		0.00625	4.5	46.39	70.85	31.49
12.7-12 d_b -0.04 (2)			4.5	46.76	73.46	32.65
12.7-15 d_b -0.01 (1)	42.03	0.025	29	14.03	125.72	8.67
12.7-15 d_b -0.01 (2)			28.9	14.85	131.91	9.13
12.7-15 d_b -0.02 (1)		0.0125	10.5	28.45	89.61	17.07
12.7-15 d_b -0.02 (2)			9.2	30.56	84.35	18.34
12.7-15 d_b -0.03 (1)		0.00833	6.4	38.23	77.11	24.10
12.7-15 d_b -0.03 (2)			6.5	37.37	74.11	22.80
12.7-15 d_b -0.04 (1)		0.00625	6.5	45.77	72.46	22.30
12.7-15 d_b -0.04 (2)			5.6	43.61	66.67	23.81

*It represents energy per volume (N.mm/mm³)

**Fractured at the gripping edge.

Table 10: Low-Cycle Fatigue Results for 15.88 mm Diameter Reinforcing Bars.

Specimen	Buckling Parameter, λ	Frequency, f (Hz)	$2Nf$	ΔW_{P1} (MPa*)	W_{fT} (MPa*)	$\Delta W_{P,avg}$ (MPa*)	
15.88-6 d_b -0.01 (1)	16.81	0.025	96.6	8.86	360.94	7.47	
15.88-6 d_b -0.01 (2)			62.6	9.34	237.30	7.58	
15.88-6 d_b -0.02 (1)		0.0125	6.8	37.83	115.91	34.09	
15.88-6 d_b -0.02 (2)			10.5	33.50	148.06	28.20	
15.88-6 d_b -0.03 (1)		0.00833	0.00833	4.4	61.11	116.94	53.15
15.88-6 d_b -0.03 (2)				2.5	81.48	100.71	80.57
15.88-6 d_b -0.04 (1)		0.00625	0.00625	2.4	87.24	99.19	82.66
15.88-6 d_b -0.04 (2)				2.2	77.29	77.31	70.28
15.88-9 d_b -0.01 (1)	25.22	0.025	54.8	10.19	218.64	7.98	
15.88-9 d_b -0.01 (2)			46.8	10.14	186.15	7.96	
15.88-9 d_b -0.02 (1)		0.0125	6.8	28.66	86.62	25.48	
15.88-9 d_b -0.02 (2)			8.4	29.96	97.28	23.16	
15.88-9 d_b -0.03 (1)		0.00833	0.00833	4.5	46.48	92.63	41.17
15.88-9 d_b -0.03 (2)				4	47.77	80.96	40.48
15.88-9 d_b -0.04 (1)		0.00625	0.00625	4.4	62.95	108.79	49.45
15.88-9 d_b -0.04 (2)				2.2	55.09	55.10	50.09
15.88-12 d_b -0.01 (1)	33.62	0.025	29.2	13.79	147.63	10.11	
15.88-12 d_b -0.01 (2)			33.6	13.10	152.12	9.05	
15.88-12 d_b -0.02 (1)		0.0125	11	31.07	101.97	18.54	
15.88-12 d_b -0.02 (2)			8.5	28.11	89.09	20.96	
15.88-12 d_b -0.03 (1)		0.00833	0.00833	6.5	38.97	88.26	27.16
15.88-12 d_b -0.03 (2)				4.8	39.53	78.90	32.87
15.88-12 d_b -0.04 (1)		0.00625	0.00625	4.6	40.51	73.95	32.15
15.88-12 d_b -0.04 (2)				4.5	41.99	71.67	31.85
15.88-15 d_b -0.01 (1)	42.03	0.025	28.6	12.83	123.23	8.62	
15.88-15 d_b -0.01 (2)			28.5	12.20	121.52	8.53	
15.88-15 d_b -0.02 (1)		0.0125	8.6	25.82	79.20	18.42	
15.88-15 d_b -0.02 (2)			10.5	24.04	91.73	17.47	
15.88-15 d_b -0.03 (1)		0.00833	0.00833	6.4	33.88	75.79	23.68
15.88-15 d_b -0.03 (2)				6.6	32.86	74.27	22.50
15.88-15 d_b -0.04 (1)		0.00625	0.00625	4.8	37.52	63.42	26.43
15.88-15 d_b -0.04 (2)				6	40.23	79.58	26.53

*It represents energy per volume (N.mm/mm³)

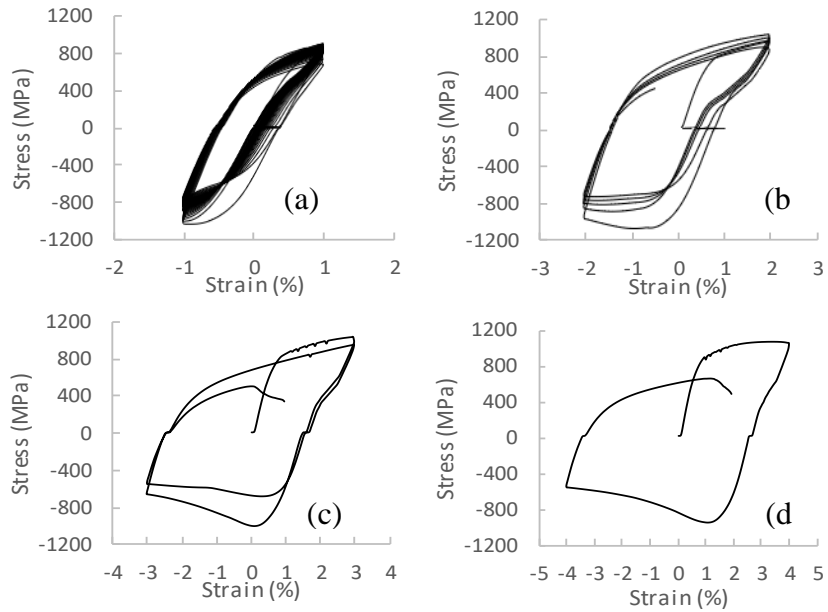


Figure 14: Typical stress-strain hysteresis relations of 15.88 mm diameter rebar gripped at $6d_b$ subjected to sinusoidal loading protocols with strain amplitudes, ϵ_a of: (a) 0.01; (b) 0.02; (c) 0.03; and (d) 0.04.

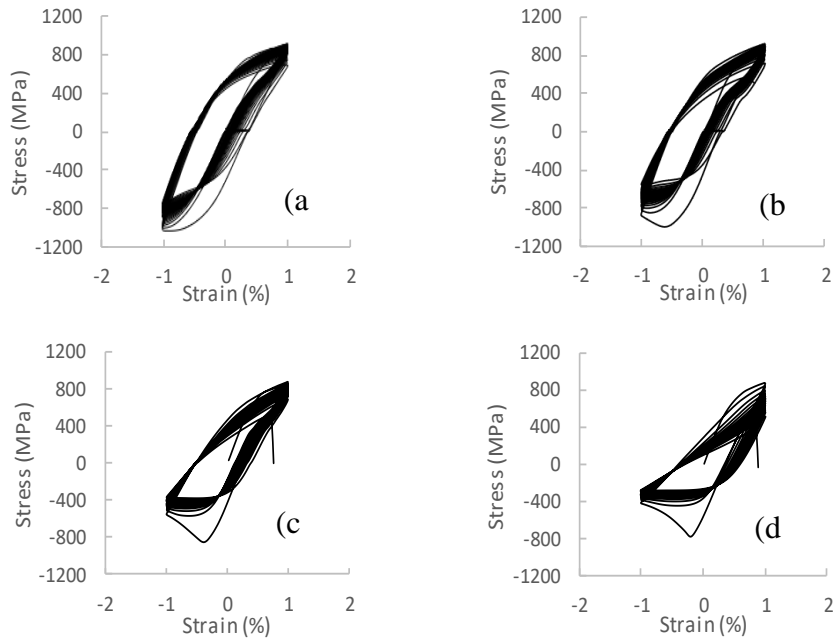


Figure 15: Typical stress-strain hysteresis relations of 15.88 mm diameter rebar gripped at: (a) $6d_b$; (b) $9d_b$; (c) $12d_b$; and (d) $15d_b$ subjected to sinusoidal loading protocol with a strain amplitude, ϵ_a of 0.01

4.3.1 Effects of Strain Amplitude

Figure 14 shows typical stress-strain curves of 15.88 mm diameter rebars gripped at $6d_b$ and subjected to loading protocols with ϵ_a of 0.01, 0.02, 0.03, and 0.04. It can be observed that an increase in ϵ_a reduces the fatigue life of the ASTM A1035 reinforcing bars. Such observation is not new and was anticipated since several other researchers have established this phenomenon for other types and grades of reinforcing steel, that higher ϵ_a results in fewer half-cycles to fracture (Brown and Kunnath 2004; Mander et al. 1994; Hawileh et al. 2010; Hawileh et al. 2016). However, $2Nf$ of ASTM A1035 Grade 690 steel is lower than that of other types and grades such as ASTM A615 Grade 420 and ASTM A716 Grade 420. For instance, at L/D of 6 and ϵ_a of 0.02, the average $2Nf$ of ASTM A1035 Grade 690 reinforcing bars was 8.2, whereas Hawileh et al. (2010) reported an average $2Nf$ of 113.2 and 128.7 for ASTM A706 Grade 420 and ASTM A615 Grade 420, respectively. It should be noted that a collar was used in the experimental program by Hawileh et al. (2010) which completely prevented rebar buckling. In this study, a gripping span as short as $6d_b$ was not sufficient to prevent buckling, as can be observed from the unsymmetrical stress-strain response of specimen 15.88- $6d_b$ -0.01 (1) (see Figure 14(a)). This could be one of the reasons for the substantial differences between the $2Nf$ of the ASTM A1035 rebars tested in this study and those of conventional ASTM A615 Grade 420 and ASTM A716 Grade 420 rebars tested by Hawileh et al. (2010). However, while comparing the $2Nf$ of the ASTM A1035 Grade 690 to that of the other types of HSS reinforcement such as ASTM 615 Grade 690, the differences are smaller. Ghannoum and Slavin (2016) reported that, at L/D of 6 and ϵ_a of 0.02, the mean number of half-cycles for No. 8 (25 mm) ASTM A615 Grade 690 produced by two manufactures ranged from 26.7 to 28.5. In addition, it can be observed from Figure 14(d) that, at $\epsilon_a = 0.04$, ASTM A1035 reinforcing bar can barely complete one full cycle. The average $2Nf$ for specimens gripped at $6d_b$ and subjected to loading protocol with ϵ_a of 0.04 was 2.3, i.e. $Nf = 1.15$. This seems in line with the observation of Restrepo et al. (2006) who reported the first longitudinal bar fracture after one cycle of generating tensile strains in the rebars exceeding 0.04 in concrete columns reinforced with ASTM A1035 Grade 690 steel rebars and tested under displacement reversals. Tables 9 and

10 indicate that increasing ϵ_a increases ΔW_{P1} and $\Delta W_{P,avg}$, but decreases W_{fT} . This is in agreement with the findings of other similar studies using ASTM A706 and A615 reinforcement (Ghannoum and Slavin 2016; Hawileh et al. 2010); and Grade 300E and 500E reinforcing bars manufactured in New Zealand (Tripathi et al. 2018). The nominalized total hysteretic energy dissipated to failure, which is obtained by dividing W_{fT} by the measured yield strength of the bars, for ASTM A1035 Grade 690 reinforcing bars seems to be lower than that of the conventional reinforcing bars such as Grade 300E and 500E. For example, at L/D of 6 and ϵ_a of 0.01, the average normalized strain energy dissipated by ASTM A1035 reinforcing bars was found to be 0.40, whereas, at similar testing conditions, Tripathi et al. (2018) reported an average normalized strain energy dissipation of 2.1 for Grade 500E reinforcing bars. However, ASTM A1035 reinforcing bars do not always dissipate less energy than the other types of HSS reinforcing bars. Ghannoum and Slavin (2016) reported that the average normalized strain energy dissipated by ASTM A615 Grade 690 rebar ranged from 0.162 to 3.63. Nevertheless, it is well-established that, although they could exhibit satisfactory seismic performance, reinforced concrete columns reinforced with high-strength steel reinforcement dissipate less energy than those reinforced with conventional reinforcing bars (Restrepo et al. 2006; Rautenberg et al. 2013; Barbosa et al. 2016; Li et al. 2018).

4.3.2 Effects of Buckling Length

Figure 15 presents typical stress-strain relations from cyclic tests of 15.88 mm diameter rebars gripped at $6d_b$, $9d_b$, $12d_b$, and $15d_b$; and subjected to loading protocol with strain amplitudes ϵ_a of 0.01. From Figure 15, it can be observed that the gripping span, i.e. buckling length, has a detrimental effect on the cyclic stress-strain hysteretic curve of ASTM A1035 Grade 690 rebars. The adverse effect of the increase in gripping span was most evident at a strain amplitude of 0.01. As seen in the results of low-cycle fatigue testing in Tables 9 and 10, the fatigue life (i.e. number of half-cycles to failure) noticeably deteriorated when buckling length increased from $6d_b$ to $15d_b$ at strain amplitude of 0.01. Fatigue cracks initiating earlier in rebars with longer gripping spans result in shorter fatigue life. This is due to the second-order effect, where the rebars would be subjected to higher strain demands at the crack initiation location

generated from the combined axial compression and bending stresses. After the crack initiation, the reduction in strength at the end of each cycle was observed at a gradually increasing rate until complete fracture (separation) of the rebar. Generally, fatigue cracks were initiated at the base of the transverse rib (rolled-on deformations) on the inside face of the buckled bar. Two distinct fatigue crack propagation patterns were observed. In the first pattern, fatigue cracks propagate horizontally across the barrel of the rebar. In the second pattern, fatigue cracks propagate along the base of the transverse rib at the intersection of the transverse rib to the barrel of the rebar. These crack propagation patterns are similar to those reported by Brown and Kunnath (2004) and Ghannoum and Slavin (2016). Figure 16 shows the surfaces of rebars fractured due to the two crack propagation patterns. The majority of the specimens either fractured at approximately mid-span or one-third of the gripping span. With the increase in the total strain amplitude, the adverse effect of the increase in buckling length on the fatigue life diminishes. Several rebars especially those subjected to strain amplitudes approaching the inelastic tensile strain capacity were characterized by shorter fatigue life despite having shorter buckling length. Similar observations have been reported by Kashani et al. (2015). Also, few rebars with relatively smaller cross-sectional area and buckling length experienced premature failure due to the rapid propagation of the fatigue cracks to the gripping region. Those rebars are highlighted in Tables 9 and 10. The proposed models reflected the previous observations as will be demonstrated in subsequent sections of this study.

The use of HSS reinforcing bars with their higher yield strengths often promotes greater center-to-center spacing between the transverse reinforcement when used in reinforced concrete columns. For this reason, “anti-buckling” requirements prescribed by design codes normally govern the design. In the ACI 318-19 (ACI 2019b) and AASHTO Guide Specifications for LRFD Seismic Bridge Design (2014), as part of “anti-buckling” requirements, the center-to-center spacing between the transverse reinforcements should not exceed eight and six times the diameter of the longitudinal reinforcement, respectively. However, in this study, rebars with unsupported length as short as $6d_b$ were susceptible to inelastic buckling as evident by the unsymmetrical stress-strain hysteresis presented in Figure 15(a). Ghannoum and Slavin (2016) reported that a transverse reinforcement spacing limit of $5d_b$ would be beneficial for ASTM A615 Grade 690 rebars.

In this study, due to geometric constraints, rebars were not tested at gripping spans less than $6d_b$. Nevertheless, to make appropriate design recommendations, the predictive model described in subsequent sections of this manuscript was used to obtain fatigue life and total strain energy dissipation of ASTM A1035 reinforcing bars with unsupported length less than $6d_b$.

When comparing the numbers of half-cycles to failure reported in this study for high-strength ASTM A1035 Grade 690 steel with those reported by Tripathi et al. (2018) for normal-strength Grade E500 steel, it appears that the increase in yield strength has pronounced adverse effect on the low-cycle fatigue performance. For example, under a similar test setup (i.e. mean strain ratio of -1 and buckling length of $6d_b$, at ϵ_a of 0.01, 0.02, 0.03, and 0.04, the averages of the number of half-cycles to failure for ASTM A1035 Grade 690 were 86, 8, 3, and 2; whereas those reported by Tripathi et al. (2018) were 542, 118, 37, and 21, respectively. This corresponds to an average percentage reduction of 90% in the number of half-cycles to failure due to the increase in the yield strength of the reinforcing steel. On the other hand, at strain amplitude of 0.01 where, as mentioned earlier, the effect of buckling length on fatigue life was most evident, the increase in the buckling length from $6d_b$ to $15d_b$ resulted in reducing the fatigue life of ASTM A1035 Grade 690 by 67%. Similarly, Tripathi et al. (2018) reported an average percentage reduction of 74% when the buckling length increased from $6d_b$ to $15d_b$ at strain amplitude of 0.01. This implies that the increase in yield strength has a greater adverse effect on the low cycle fatigue performance than the increase in buckling length. The prime reason for the noticeable reduction in the fatigue life of reinforcing steel due to the increase in yield strength is the well-established fact that the increase in yield strength is often associated with a reduction in inelastic tensile strain capacity. Reinforcing bars with lower inelastic strain capacities are susceptible to greater damage by the large cyclic-strain amplitudes, and consequently fail at a lower number of cycles.

4.3.3 Effects of Rebar Diameter

By comparing the values of $2N_f$, ΔW_{P1} , W_{fT} , and $\Delta W_{P,avg}$ of 12.7 mm-diameter rebars (presented in Table 9) to those of 15.88 mm-diameter rebars (presented in Table 10), it can be observed that the smaller

rebars generally perform better. Overall, the $2N_f$ and W_{FT} for 12.7 mm-diameter rebars was higher than those of the 15.88 mm-diameter rebars by 7% and 3.85%, respectively. Studies that have used other types and grades of reinforcing steel bars have reported similar observations (Brown and Kunnath 2004; Kashani et al. 2015).

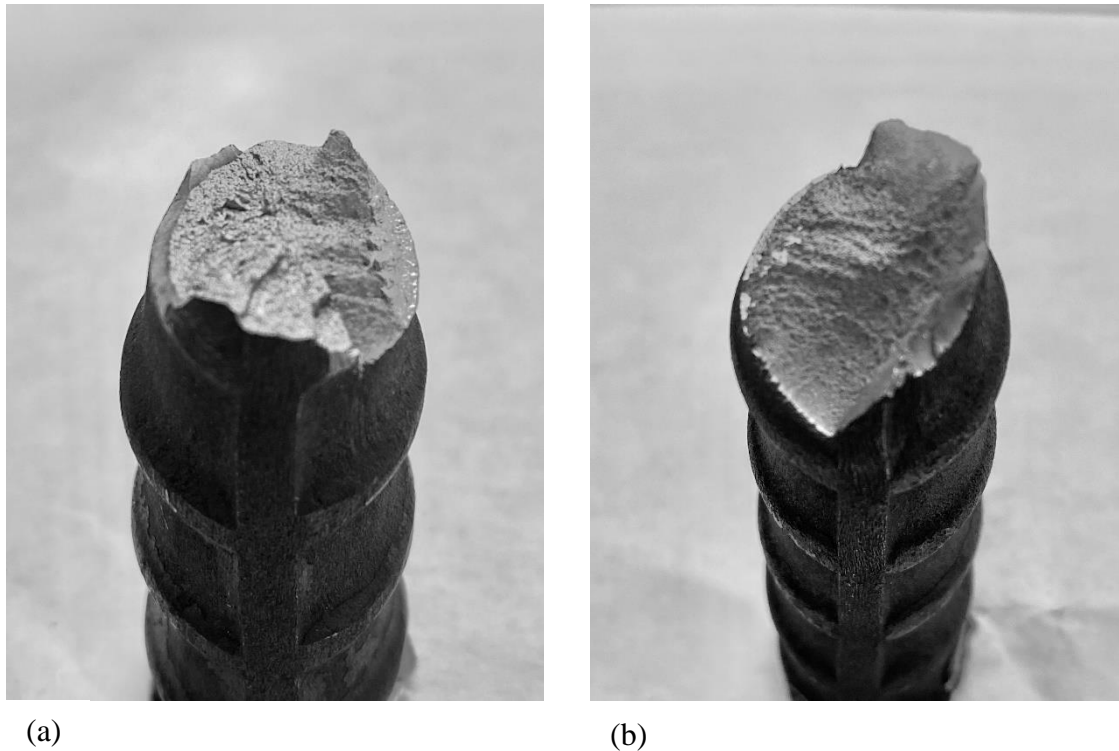


Figure 16: Typical fracture patterns of bars: (a) typical pattern across the barrel of the rebar; and (b) typical pattern along the base of the transverse rib.

4.4 Fatigue Life Relationships for ASTM A1035 Grade 690 Reinforcing Bars

4.4.1 Relationship between Fatigue Life and Total Strain Amplitude ϵ_a

Several predictive fatigue life models relating plastic and total strain amplitudes to the number of half-cycles (or strain reversals) to failure were previously established (Koh and Stephens 1991; Mander et al. 1994; Coffin 1954; Manson 1953). According to Brown and Kunnath (2004), such models generally take the following form:

$$y = a(x)^c \quad (36)$$

where y is a deformation quantity, x is the number of half or full cycles to failure, and a and c are constants derived from experimental data. The original form of the Coffin-Manson equation (Coffin 1954; Manson 1953) related the plastic strain amplitude (ε_p) to $2Nf$ in the following form:

$$\varepsilon_p = \varepsilon_f' (2Nf)^c \quad (37)$$

where ε_f' is the fatigue ductility coefficient, and c is the fatigue ductility exponent. The main shortcoming of this model is its dependency on the plastic strain amplitude, which can be difficult to define due to the Bauschinger effect (Bauschinger 1881). Koh and Stephens (1991) suggested that, for most low-cycle fatigue analyses, the effect of the elastic strain can be neglected, and hence, their proposed fatigue life model is solely based on the total strain amplitude (elastic strain + plastic strain) as follows:

$$\varepsilon_a = \beta (2Nf)^a \quad (38)$$

where β is the fatigue ductility coefficient and a is the fatigue ductility exponent. Due to its simplicity, the implementation of the Koh and Stephens (1991) model in finite element software such as in *OpenSees* (2011) is easier than the Coffin-Manson Model. Also, Brown and Kunnath (2004) reported that for materials whose yield strain is essentially constant, the accuracy of the fatigue life predictions is not influenced when Koh and Stephens (1991) model is used instead of Coffin-Manson Model. For these reasons, in this study, experimental fatigue data were only fitted to the Koh-Stephens model. To obtain β and a in Eq. (38), linear least-squares regression analysis was performed in log space. This analysis was repeated for each λ to capture the effect of λ on the β and a . For each λ , fatigue data of the two rebar sizes were considered. Experimental data fitting Koh-Stephens model for rebars with a gripping span of $6d_b$ is presented in Figure 17. β , a , and square of the correlation coefficient (r^2) obtained from the four regression analyses (i.e. for each λ) are summarized in Table 11. r^2 ranges from 0.93 to 0.97 indicating an excellent correlation between the data and the Koh-Stephens model. It must be noted that the predictions of the proposed fatigue life models are valid only for ε_a ranging from 0.01 to 0.04. Figure 18 provides a comparison between the fatigue life predictions obtained from the numerical model and those measured from the low-cycle fatigue tests. As seen in Figure 18, the proposed model well-predicted the measured low-cycle fatigue life of ASTM

A1035 Grade 690 rebars with overall r^2 of 0.94. The normality of the residuals was verified through Kolmogorov–Smirnov test where a P -value of 0.05 was adopted as the statistical significance level.

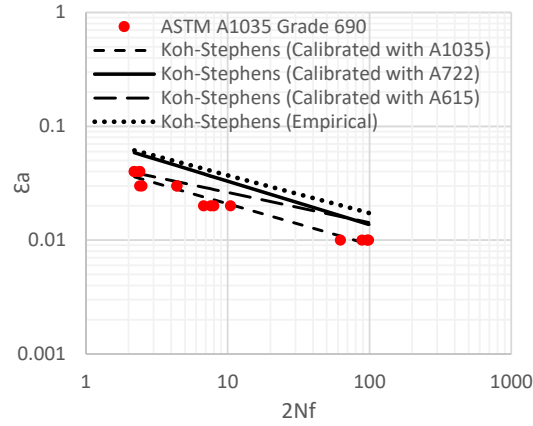


Figure 17: Fatigue life relationship based on half cycles to failure for ASTM A1035 Grade 690 reinforcing bars as well as those calibrated with results of other types of reinforcing steel.

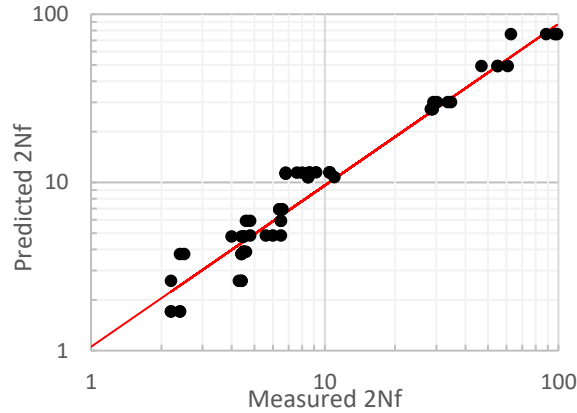


Figure 18: Comparison between the predicted and measured fatigue life.

Table 11: Results of Regression Analysis to Calibrate Koh-Stephens Model’s Constants.

Slenderness Ratio (L/D)	Buckling Parameter (λ)	Fatigue Ductility Coefficient (β)	Fatigue ductility Exponent (a)	Square of the Correlation Coefficient (r^2)
6	16.81	0.0486	-0.365	0.97
9	25.22	0.0626	-0.471	0.93
12	33.62	0.0998	-0.677	0.97
15	42.03	0.141	-0.801	0.96

Mander et al. (1994) fitted the fatigue experimental data of ASTM A722 type II hot-rolled and proof-stressed alloy-steel thread rebars tested with a gripping span of $6d_b$ to the Koh-Stephens model. These rebars were 15.88 mm in diameter and had a specified minimum ultimate tensile strength of 1083 MPa, hence were designated as HSS in Mander et al. (1994). They share many similar characteristics with ASTM A1035 Grade 690 reinforcing bars such as lack of well-defined yield plateau and yield point in their monotonic tensile stress-strain curves. For this reason, some researchers suggested considering the Koh-Stephens model calibrated with the fatigue experimental data of ASTM A722 rebars when evaluating the low-cycle fatigue performance of ASTM A1035 Grade 690 rebars (Russell et al. 2011). Using the Koh-Stephens model, Mander et al. (1994) proposed the following fatigue life expression:

$$\varepsilon_a = 0.0791(2Nf)^{-0.381} \quad (39)$$

where β and a are 0.0791 and -0.381, respectively. With these values of β and a , the fatigue experimental data of ASTM A722 rebars were well-correlated with the Koh-Stephens model with r^2 of 0.989. Besides, Ghannoum and Slavin (2016) proposed a similar expression but for high-strength ASTM A615 Grade 690 which is characterized by a minimum yield strength equal to that of ASTM A1035 Grade 690 as follows:

$$\varepsilon_a = 0.0483(2Nf)^{-0.265} \quad (40)$$

In addition, Koh and Stephens (1991) proposed a general empirical equation applicable to all types and grades of reinforcing steel, which relates ε_a to $2Nf$ as follows:

$$\varepsilon_a = 0.08 (2Nf)^{-0.333} \quad (41)$$

The three previous expressions are plotted in Figure 17 for comparison purposes. As evident from Figure 17, poor correlation between the fatigue life experimental data of ASTM A1035 Grade 690 and that obtained from the expressions in Eqs. 39-41 was observed. Utilizing these equations would result in over-estimating the fatigue life of ASTM A1035 Grade 690 rebars. For instance, at ε_a of 0.01 and gripping span of $6d_b$, $2Nf$ of ASTM A1035 Grade 690 rebars predicted using Eqs. (39), (40), and (41) would be approximately 227.7, 378, and 515.2, respectively, whereas the reported experimental $2Nf$ for ASTM A1035 Grade 690 ranged from 62.6 to 98.9. This finding indicates that, although two types of rebars could

exhibit similar mechanical properties and monotonic stress-strain characteristics, strain-fatigue life models such as the Koh-Stephens model must be developed for each rebar type separately using its fatigue experimental data. More interestingly, Ghannoum and Slavin (2016) reported different β and a when calibrating the Koh-Stephens model for rebars conforming to the same ASTM requirements but produced by two different manufactures.

Kashani et al. (2015) introduced an approach to incorporate the effect of inelastic buckling into strain-fatigue life models by making use of the non-dimensional buckling parameter λ defined in Eq. (35). In this approach, the buckling parameter is correlated with the Koh-Stephens model's exponent and coefficient through regression analyses. This approach was initially utilized by Kashani et al. (2015) to capture the effect of inelastic buckling on the low-cycle fatigue life of B500B ribbed and B460 smooth British manufactured reinforcing bars and later was successfully implemented by Tripathi et al. (2018) for New Zealand's manufactured Grade 300E and 500E reinforcing bars. In the current study, the same approach was adopted for the ASTM A1035 Grade 690 reinforcing bars. Regression analyses were performed to identify the interrelationship between β and a of the fatigue models and the parameter λ . The results of these regression analyses are presented in Figures 19 and 20. The following equations were obtained from the regression analyses:

$$\beta = \frac{9}{400} e^{\left(\frac{109}{2500}\right)\lambda} \quad (42)$$

$$a = \frac{-9}{500} \lambda - \frac{243}{5000} \quad (43)$$

The values of r^2 corresponding to the aforementioned regression fits were 0.99 and 0.98, respectively. Eqs. (42) and (43) can be utilized to obtain β and a for ASTM A1035 Grade 690 rebars with gripping spans less than $6d_b$, which, as mentioned earlier, were not tested in this study due to the geometric constraints. Kashani et al. (2015) proposed expressions relating the buckling parameter to β and a for 16-mm-diameter B500B ribbed British-manufactured rebars as follows:

$$\beta = 0.007e^{(0.045\lambda)} + 0.03 \quad (44)$$

$$a = -0.018\lambda - 0.159 \quad (45)$$

Tripathi et al. (2018) proposed similar expressions but for 500E New Zealand-manufactured rebars as follows:

$$\beta = \frac{-\lambda}{350} + 0.2 \quad (46)$$

$$a = -\left(\frac{\lambda}{1200} + 0.441\right) \quad (47)$$

Figure 21 presents a comparison between the fatigue life predictions of the proposed model and those proposed by Kashani et al. (2015) and Tripathi et al. (2018) and the measured fatigue life of ASTM A1035 Grade 690 at buckling lengths of $6d_b$, $9d_b$, $12d_b$, and $15d_b$. As can be seen from Figure 21, irrespective of the buckling length, the most accurate predictions of the low-cycle fatigue life of ASTM A1035 Grade 690 rebars were generated from the proposed model. However, it appears that as the buckling length increases, the accuracy of the model proposed by Tripathi et al. (2018) increases, especially at relatively high strain amplitudes.

To make appropriate design recommendations related to the use of ASTM A1035 reinforcing bars in concrete columns or bridge piers, strain demands along with the number of inelastic displacement/strain reversals that the ASTM 1035 reinforcing bars would be subjected to during seismic events in such elements need to be examined first. Unfortunately, shake table tests of concrete columns reinforced with ASTM A1035 reinforcing bars do not seem to exist. However, it was established by Sokoli et al. (2017) that HSS reinforcing bars with yield strength of 690 MPa are subjected to double the strains of ordinary A706 Grade 420 reinforcing bars when subjected to the same drift ratios. Schoettler et al. (2015) performed shake table tests of full-scale bridge column reinforced with ASTM A706 Grade 420 steel to assess the column performance at target displacement ductilities of 1, 2, 4, and 8. At target displacement ductility of 2, the maximum recorded tensile strain in ASTM A706 Grade 420 reinforcing bars was 0.011, and hence, if the ASTM A1035 Grade 690 was used, the maximum recorded tensile strain would be 0.022 based on the observations by Sokoli et al. (2017). Bazaez and Dusicka (2016) carried out simplified rainflow counting to compute the number of inelastic cycles imposed on reinforced concrete bridge columns subjected to strong motions of long duration from subduction megathrust earthquakes. In their analyses, a total of 262

ground motion records generated from subduction earthquakes was considered. At a target displacement ductility of 2, the average number of inelastic cycles, i.e. cycles generating strains in the longitudinal rebars exceeding yield strain, was 8 for reinforced concrete columns having elastic periods ranging from 0.2 to 4.0 seconds, and when all excursions are considered. According to the calibrated Koh-Stephens model, at ε_a of 0.022 and at the gripping span of $6d_b$, ASTM A1035 Grade 690 reinforcing bars would exhibit a fatigue life of 9 cycles, hence exceeding the number of inelastic cycles suggested by Bazaez and Dusicka [39] by only one cycle. It might seem critical but it is not since the estimates by the Koh-Stephens model and other fatigue-life models are conservative. They are based on constant strain amplitudes rather than variable strain amplitudes. In other words, when the Koh-Stephens model was used to compute the fatigue life of ASTM A1035 reinforcing bars, it was based on the assumption that the rebars would be subjected to cyclic reversals with a constant strain amplitude of 0.022, which is not true. Longitudinal rebars in reinforced concrete columns when resisting seismic forces are normally subjected to reversals with variable strain amplitude (i.e. ranging from zero to 0.022 for ASTM A1035 rebars in reinforced concrete columns at target displacement ductility of 2). Reducing the gripping span to improve the fatigue life of ASTM A1035 rebars is not recommended since the fatigue experimental data, along with the proposed fatigue life relationships, have shown that such reduction beyond $6d_b$ would have an insignificant impact on fatigue life, especially when ε_a exceeds 0.01. In addition, the authors believe that promoting “anti-buckling” requirements for ASTM A1035 Grade 690 rebars with center-to-center spacing between transverse reinforcement limited to $5d_b$ or $4d_b$ (i.e. less than $6d_b$) would greatly counteract the potential benefit of HSS, which is the reduction of the required reinforcements. Based on the previous discussion, ASTM A1035 Grade 690 rebars could exhibit satisfactory low-cycle fatigue performance in concrete columns subjected to ground motions producing a target displacement ductility of 2 provided that the center-to-center spacing between transverse reinforcement is limited to $6d_b$. Nevertheless, this finding is applicable to only the concrete column tested by Schoettler et al. (2015), and hence further investigations considering geometrical and material variability of concrete columns are deemed warranted.

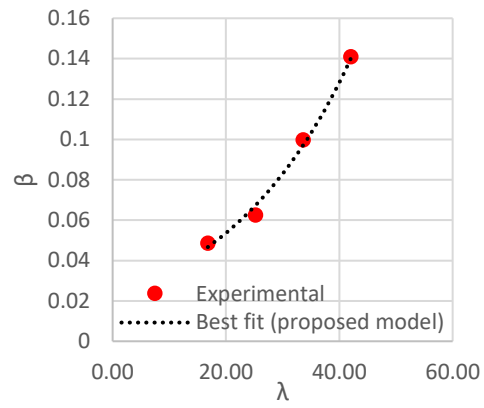


Figure 19: Relationship between β and λ .

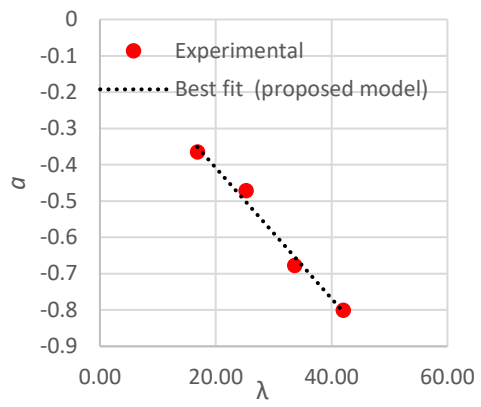


Figure 20: Relationship between α and λ .

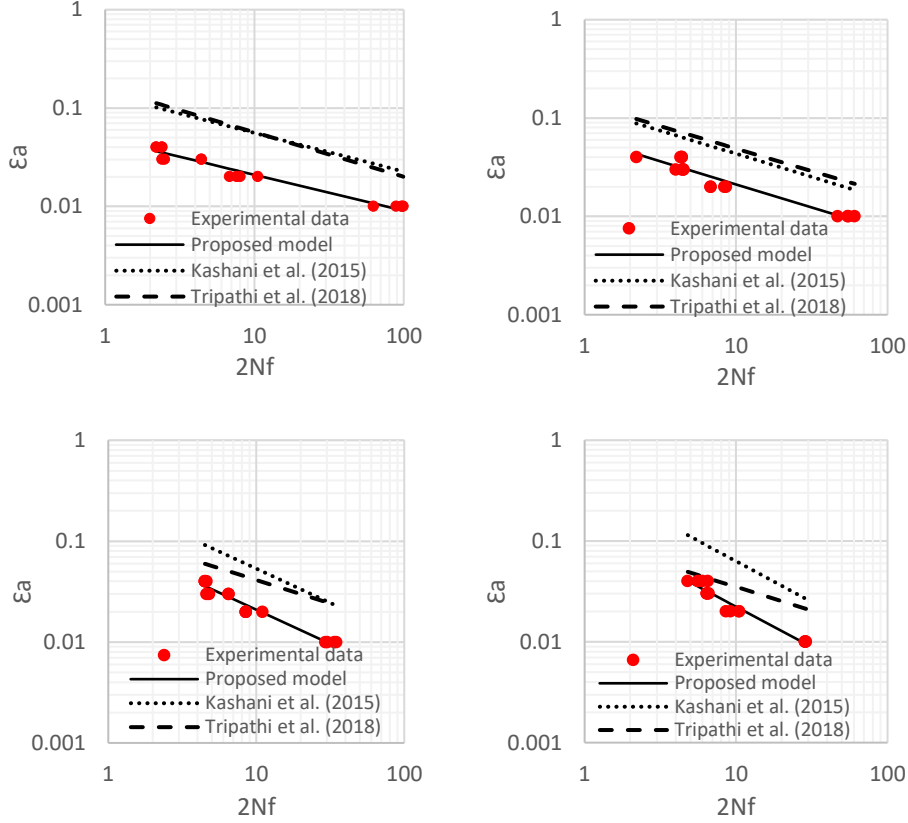


Figure 21: Comparison between the fatigue life predictions of the proposed model and those proposed by Kashani et al. (2015) and Tripathi et al. (2018) and the measured fatigue life of ASTM A1035 Grade 690 at buckling lengths of (a) $6d_b$; (b) $9d_b$; (c) $12d_b$; and (d) $15d_b$.

4.4.2 Relationship between Fatigue life and Total Energy Dissipation W_{fT}

Many researchers have developed energy-based fatigue models in which the total energy dissipated is related to either fatigue life (Hawileh et al. 2010; Tong et al. 1989) or strain amplitude and maximum stress (Brown and Kunnath 2004; Mander et al. 1994). Such formulations were most applicable when engineering demand parameters need to be expressed in a form suitable for damage calibrations. Tong et al. (1989) proposed the following relation to relate the W_{fT} to $2Nf$:

$$W_{fT} = C_1 (2Nf)^{\gamma_1} \quad (48)$$

where C_1 and γ_1 are material constants to be derived from the low-cycle fatigue experimental data. Previous studies by Tong et al. (1989) and Lefebvre and Ellyin (1984) have established that for a fully reversed

constant-strain-controlled low-cycle fatigue test, there is insignificant variation in the cyclic hysteresis energy with the number of cycles during fatigue life, and therefore W_{fT} in Eq. 48 can be taken as the product of cyclic hysteresis energy at half-life by Nf . This, however, is not applicable to ASTM A1035 Grade 690 reinforcing bars. The variations in the cyclic hysteresis energy with the number of cycles for specimens 15.88-6db-0.01 (2) and 15.88-15db-0.01 (2) are plotted in Figure 22. The trend of the curves shown in Figure 22 shows that the cyclic hysteresis energy of ASTM A1035 Grade 690 is noticeably decreased with the increase in the number of cycles due to the effect of inelastic buckling. In addition, by comparing the responses of specimens 15.88-6db-0.01 and 15.88-15db-0.01 given in Figure 22, it can be observed that the effect of inelastic buckling on the variation of the cyclic hysteresis energy with the number of cycles becomes more pronounced when the gripping span is increased. Therefore, the energy-fatigue life model of Tong et al. (1989) was calibrated using the W_{fT} measured experimentally instead of computing it using the procedure described earlier in which $W_{fT} = \text{cyclic hysteresis energy at half-life} \times Nf$.

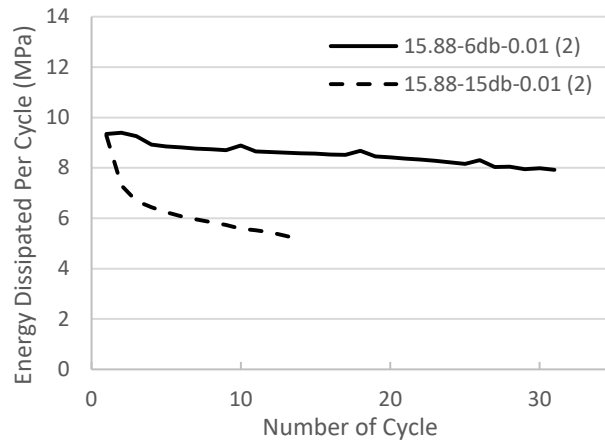


Figure 22: Relationships between cyclic hysteresis energy and the number of cycles for specimens 15.88-6db-0.01 (2) and 15.88-15db-0.01 (2).

To obtain C_1 and γ_1 in Eq. (48), linear least-squares regression analysis is performed in log space. This analysis was repeated for each λ to capture the effect of λ on C_1 and γ_1 . For each λ , fatigue data of the two rebar sizes were considered. Experimental data fitting to the model proposed by Tong et al. (1989) for

rebars with a gripping span of $6d_b$ is presented in Figure 23. C_1 , γ_1 , and the square of the correlation coefficient (r^2) obtained from the four regression analyses (i.e. for each λ) are summarized in Table 12. r^2 ranges from 0.96 to 0.99 indicating satisfactory agreement between the model and the test results. Mander et al. (1994) also calibrated Tong et al. (1989)'s model under similar testing conditions (i.e. using 15.88 mm diameter rebars with a gripping span of $6d_b$) but using ASTM A722 high-strength prestressing rebars, and proposed the following energy-based fatigue model:

$$W_{fT} = 126.2 (2Nf)^{0.486} \quad (49)$$

This expression is also plotted in Figure 23. Poor correlation between the fatigue experimental data and the energy-based fatigue model of Mander et al. (1994) can be seen in Figure 23. This indicates that even though two types of rebars exhibit nearly identical mechanical properties and stress-strain characteristics, it is critical to establish energy-based models separately for each rebar type using its fatigue experimental data. To incorporate the effect of inelastic buckling in the proposed energy-based models, non-linear regression analyses were performed to relate λ to C_1 and γ_1 . The best fit curve relating λ to C_1 is plotted in Figure 24 and can be described using the following expression:

$$C_1 = 314.49\lambda^{-0.565} \quad (50)$$

γ_1 was not influenced by the change in λ and had a constant value of 0.35. Similarly, in energy-based models incorporating the effect of inelastic buckling by Tripathi et al. (2018), γ_1 held a constant value but was equal to 0.51 for Grade 300E and 500E New Zealand's manufactured reinforcing bars.

Table 12: Results of Regression Analysis to Calibrate Tong et al. (1989) Model's Constants.

Slenderness Ratio (L/D)	Buckling Parameter (λ)	Material Constant (C_1)	Material Constant (γ_1)	Square of the Correlation Coefficient (r^2)
6	16.81	64.471	0.35	0.98
9	25.22	49.762	0.35	0.96
12	33.62	43.548	0.35	0.99
15	42.03	38.163	0.35	0.97

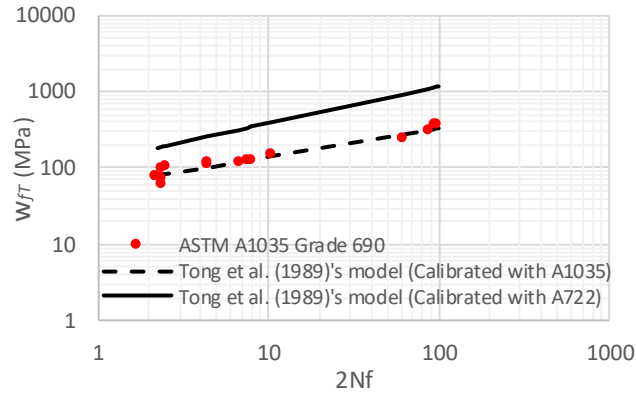


Figure 23: Fatigue life relationships for ASTM A1035 Grade 690 reinforcing bars based on total energy.

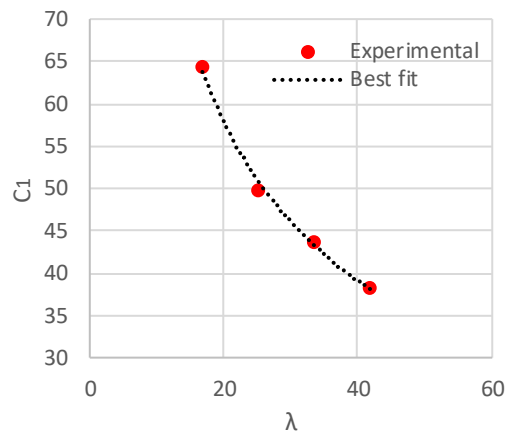


Figure 24: Relationship between C_1 and λ

4.5 Summary

In this chapter, ASTM A1035 Grade 690 rebars were tested under monotonic tension and low-cycle fatigue tests to evaluate their adequacy for structural seismic applications. Rebars with diameters of 12.7 and 15.88 mm were tested under monotonic tension to determine their mechanical properties and generate stress-strain relationships. The stress-strain curves were characterized with a linear portion up to a proportional limit followed by a nonlinear relationship up to the tensile strength, hence lacked a well-defined yield point and plateau. ASTM A1035 Grade 690 rebars satisfied the condition that the tensile-to-yield strength ratio exceeds 1.25 which is often prescribed by design codes for steel reinforcing bars used in seismic applications. However, the inelastic tensile strain capacity of ASTM A1035 Grade 690 rebars

was approximately one-third that of ASTM A706 Grade 420. In the low-cycle fatigue tests, sixty-four ASTM A1035 Grade 690 rebar specimens were tested considering the following variables: rebar size, strain amplitude, and buckling length. Rebar size had little to no effect on low-cycle fatigue performance. Increasing the strain amplitude and gripping span generally reduced fatigue life and total energy dissipated. Using fatigue experimental data, constants of existing strain, and energy-based fatigue-life models were calibrated. The results revealed that utilizing previous fatigue life models with constants calibrated using reinforcing steel exhibiting nearly identical mechanical properties to that of ASTM A1035 would lead to inaccurate fatigue life predictions. The effect of inelastic buckling was incorporated into the proposed strain and energy-based fatigue-life models by correlating their constants with a buckling parameter. While utilizing the proposed models, it was found that ASTM A1035 Grade 690 reinforcing bars in reinforced concrete columns subjected to a target displacement ductility of 2 could exhibit sufficient fatigue life provided that center-to-center transverse reinforcement is limited to six longitudinal bar diameters. Nevertheless, such a conclusion was drawn based on the experimental results of one concrete bridge column only, and hence further investigations considering geometrical and material variability of concrete columns are deemed warranted.

CHAPTER 5: LOW-CYCLE FATIGUE PERFORMANCE OF HIGH-STRENGTH STEEL REBARS IN CONCRETE BRIDGE COLUMNS

5.1 General

As technology advances, the reinforcing steel industry continues to develop by introducing different types of higher-grade steel reinforcing bars with yield strength exceeding 550 MPa. Such types of rebars are often identified as high-strength steel (HSS) rebars. Several mills in the United States and worldwide have started producing different types of HSS, allowing the structural engineering community to make use of their potential benefits. Examples of HSS rebar types available in the North American steel rebar market include Grade 550 rebars conforming to ASTM A706 (ASTM 2016) and ASTM A615 (ASTM 2020a); Grade 690 conforming to ASTM A615 (ASTM 2020a) and ASTM A1035 (ASTM 2020b); and Grade 500W conforming to CSA-G30.18-M92 (CSA 2007). HSS rebars have the potential of reducing reinforcement congestion, thereby leading to improved steel and concrete placement productivity. This would not only result in a higher quality product, but also reduce associated labor costs and construction time (Aldabagh and Alam 2020).

The vast majority of the recent research works evaluating the performance of concrete members containing HSS rebars have focused on those not part of the seismic-force-resisting system (ACI 2019a; Shahrooz et al. 2011). This is because of concerns related to limited ductility capacity of concrete members reinforced with HSS under lateral cyclic loading. Those concerns stem from the known fact that the increase in yield strength is often associated with a reduction in inelastic strain capacity, ratio of tensile to yield strength, and length of the yield plateau, which could lead to an undesirable seismic performance by limiting the spread of plasticity in the potential plastic hinge region. However, the ability of HSS to reduce rebar congestion makes it an attractive alternative to regular-strength reinforcing steel bars in members forming plastic hinges which often contain heavily reinforced sections, especially in highly seismic regions. Therefore, to alleviate such concerns, several experimental programs have been executed to evaluate the cyclic performance of concrete columns reinforced with different types of HSS (Restrepo et al. 2006;

Rautenberg et al. 2013; Trejo et al. 2016; Barbosa et al. 2016; Li et al. 2018; Sokoli 2018; Barcley and Kowalsky 2020). The results indicate that, other than dissipating less energy, concrete columns reinforced with HSS exhibited comparable performance to similar columns reinforced with conventional steel. Additional research has focused on establishing strain and drift limits identifying the onset of various damage states of concrete columns reinforced with HSS under cyclic lateral loading (Barcley and Kowalsky 2020; Billah and Kabir 2020; and Aldabagh and Alam 2021a). Such limits are key elements of the performance-based seismic design methodology, which has been adopted by several design codes as an alternative to the classical force-based design. Despite these efforts, design code committees such as that responsible for the *AASHTO Guide Specifications for LRFD Seismic Bridge Design* are still reluctant to permit the use of HSS in members forming plastic hinges. According to the *ATC-98 Project on Seismic Design of Concrete Structures with High-Strength Reinforcement* (Kelly et al. 2017), there is a need for additional research on the seismic performance of HSS before complete design recommendations for the use of HSS in seismic application can be made.

According to Article 8.4.1 of *AASHTO Guide Specifications for LRFD Seismic Bridge Design* (2014), HSS rebars can be used in seismic applications only if demonstrated through testing that their low-cycle fatigue performance is not inferior to normal-strength steel rebars. This requirement is justified in the commentary to the same article by referring to low-cycle fatigue tests by Mander et al. (1994) which have shown that ASTM A722 high-strength prestressing rebars could exhibit low-cycle fatigue life comparable to that of conventional normal-strength rebars. However, low-cycle fatigue tests on other modern types of HSS rebars conforming to typical rebar standards such as ASTM A706, ASTM A615, and ASTM A1035 have proven otherwise. Ghannoum and Slavin (2016) reported that higher-grade bars satisfying ASTM A706 and ASTM A615 showed marginally poorer low-cycle fatigue performance than the benchmark ASTM A706 Grade 420. A similar observation was reported by Aldabagh and Alam (2021b) for ASTM A1035 Grade 690 rebars. It is noteworthy that in spite of having adequate low-cycle fatigue performance, ASTM A722 rebars tested by Mander et al. (1994) are characterized by very limited inelastic tensile strain capacity, hence are unlikely to be considered as a potential alternative to conventional normal-strength

rebars in seismic applications. While the aforementioned requirement remains in place and with the recently reported low-cycle fatigue data, the implementation of modern types of HSS bars in earthquake-resistant members designed following *AASHTO Guide Specifications for LRFD Seismic Bridge Design* becomes infeasible. This raises the question of whether code restrictions on the seismic applications of modern HSS types based on their low-cycle fatigue performance are justified. Answering this question requires research work evaluating the low-cycle fatigue performance of HSS in bridge concrete columns under earthquake loading, which at the time of writing this dissertation, seems nonexistent.

A prominent failure mode in well-confined reinforced concrete bridge columns with flexure-dominated behavior is the fracture of longitudinal reinforcing steel due to low-cycle fatigue (Lehman et al. 2004). For this reason, several models based on the cumulative damage concept have been formulated to predict the low-cycle fatigue-induced deterioration and failure of longitudinal steel rebars in reinforced concrete columns subjected to lateral cyclic loading. One of which is that formulated by Krawinkler et al. (1983) where the two hypotheses of a Coffin-Manson relationship and Miner's rule are employed as a baseline. Such model and its variants are generally referred to as "fatigue-based damage models". According to Kunnath et al. (1997), when compared to other energy- and ductility-based damage models, fatigue-based damage models demonstrated better reliability in predicting the experimentally observed damage. Using a fatigue-based damage model, Sokoli (2018) also well-predicted the fracture of HSS longitudinal rebars in concrete columns tested under quasi-static cyclic loading. This study builds upon the work of Ghannoum and Slavin (2016) and Aldabagh and Alam (2021b) by utilizing their reported low-cycle fatigue data in a fatigue-based damage model to compare the low-cycle fatigue-induced deterioration and failure of HSS rebars with those of benchmark ASTM A706 Grade 420 rebars in circular concrete bridge columns. A validated numerical fiber type model was utilized to perform nonlinear time-history analysis on the bridge columns, and thereby extract the strain demands to which the longitudinal rebars would be subjected during an earthquake. Responses at displacement ductility demands of two, four, and six, from ground motions of crustal as well as subduction megathrust earthquakes were considered. Also, the following variables in the properties of the bridge columns were considered: axial load ratio,

longitudinal and spiral reinforcement ratios, and spacing-to-rebar diameter ratio. The findings of this study are expected to provide sound support for future code revisions by integrating HSS rebars into the seismic provisions of bridge design codes.

5.2 High-Strength Steel

In this study, two types of HSS, namely, ASTM A706 Grade 550 and ASTM A1035 Grade 690 were considered. Stress-strain responses obtained from tensile tests on those two types as well as ASTM A706 Grade 420 are plotted in Figure 25. As observed in Figure 25, ASTM A706 Grade 550 steel exhibits stress-strain curve similar to that of ASTM A706 Grade 420. Their stress-strain curves are characterized by an initial linearly elastic portion up to the yield strength, followed by a yield plateau and subsequent strain hardening region. ASTM A1035 Grade 690, however, exhibits a unique stress-strain curve owing to the lack of distinct yield plateau. Its stress-strain curve is characterized by a linear elastic portion up to a proportional limit at stress typically on the order of 480 MPa, followed by a nonlinear relationship up to the ultimate strength (Shahrooz et al. 2011). For this reason, determining the yield strength of ASTM A1035 Grade 690 rebars requires utilizing one of the following methods: (1) 0.35% extension under load (EUL) method, (2) 0.5% EUL, and 0.2% offset method, with the last being the most common. In the 0.2% offset method, the yield strength is defined as the stress at the intersection of the stress-strain curve with a line having a slope equal to the Young's modulus and starting from 0.2% strain at zero stress. Shahrooz et al. (2011) and Overby et al. (2017) assembled previous tensile test data for ASTM A1035 Grade 690 and ASTM A706 Grade 550, respectively to determine means and coefficients of variation (COV) of the key tensile mechanical properties. Based on their findings, Table 13 provides a comparison between key tensile mechanical properties of ASTM A706 Grade 550 and ASTM A1035 Grade 690. The reported mean mechanical properties in Table 13 were also utilized to define the reinforcing steel bars' constitutive relations within the numerical model whose details are provided in a subsequent section of this chapter. Upon examination of Table 13, it appears that between the two types of HSS, ASTM A706 Grade 550 exhibits more desirable properties for seismic applications for two reasons: first, its mechanical properties

are more tightly controlled as evidenced by the lower coefficients of variation, and second, its mechanical properties are closer to those of the benchmark ASTM A706 Grade 420. It is noteworthy that irrespective of the method by which the yield strength of ASTM A1035 Grade 690 steel is established, the tensile-to-yield ratio always exceeds the minimum specified tensile-to-yield ratio of 1.25 specified in the ASTM A706 material standard (Shahrooz et al. 2011). This is critical to ensure that concrete members reinforced with ASTM A1035 Grade 690 are characterized by sufficient flexural plasticity spread when forming plastic hinges.

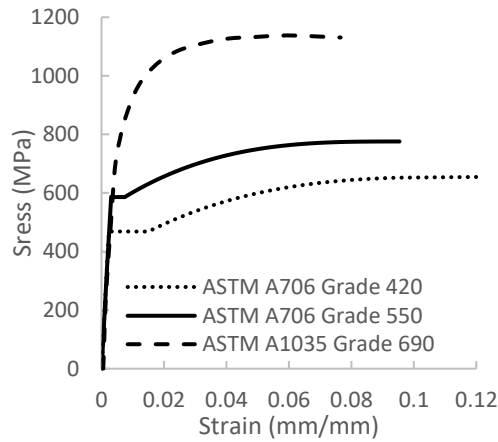


Figure 25: Comparison of tensile stress-strain responses of ASTM A706 Grade 550 (Overby et al. 2017), ASTM A1035 Grade 690 (Aldabagh and Alam 2021), and ASTM A706 Grade 420 (Overby et al. 2017).

Material-specific Coffin-Manson relationship calibrated through fatigue tests is the cornerstone of the fatigue-based damage model. One common variant of Coffin-Manson relationship is that formulated by Koh and Stephens (1991). It relates the total strain amplitude (ϵ_a) to the corresponding number of half-cycles to failure ($2N_f$) and takes the following form:

$$\epsilon_a = M(2N_f)^m \tag{51}$$

where M and m are material constants derived from low-cycle fatigue tests data. In low-cycle fatigue tests, rebars are subjected to axial-strain-controlled cycles with constant large strain amplitudes (typically ranging from yield to ultimate strain) up to fracture. Such tests were performed by Ghannoum and Slavin (2016) for ASTM A706 Grade 420 and Grade 550, and by Aldabagh and Alam (2021b) for ASTM A1035 Grade

690. In both experimental programs, specimens tested were virgin (unmachined) rebars to preserve the rolled-on deformations, and thereby appropriately simulate the seismic behavior in structural concrete members when compared to their machined counterparts (Mander et al. 1994). Besides, in low-cycle fatigue tests involving unmachined rebars, the rotational fixity generated by the hydraulic grips mimic the boundary conditions of longitudinal reinforcing bars restrained by transverse bars. As a result, the gripping span (sometimes referred to as buckling length) in such tests reflects the spacing between the transverse bars in concrete members. In the low-cycle fatigue tests by Ghannoum and Slavin (2016) and Aldabagh and Alam (2021b), the ratio of the gripping span (or spacing) to bar diameter ratio was varied to evaluate its influence on the low-cycle fatigue life of the rebar types under consideration. This allowed correlating the material constants in Eq. 51 with the spacing-to-bar diameter ratio through regression analysis. The equations correlating the material constants, M and m , with the ratio of the spacing (s) to bar diameter (d_b) for ASTM A706 Grade 420, ASTM A706 Grade 550, and ASTM A1035 Grade 690 are given in Table 14. These equations were utilized in the proposed fatigue-based damage model to account for the effect of rebar buckling, as will be illustrated in the next section. When examining the low-cycle fatigue life predictions of the proposed models by Ghannoum and Slavin (2016) and Aldabagh and Alam (2021b), it appears that among the two types of HSS under consideration, ASTM A1035 Grade 690 exhibit poorer low-cycle fatigue performance when compared to the benchmark performance of ASTM A706 Grade 420. For instance, according to the proposed models, at s/d_b of 4 and ε_a of 0.01, the benchmark fatigue life (i.e., of ASTM A706 Grade 420) is 386 half-cycles, whereas those of ASTM A706 Grade 550 and ASTM A1035 under the same conditions are 276 and 178 half-cycles, respectively.

Table 13: Reported Means and Coefficients of Variation of Key Tensile Mechanical Properties of ASTM A706 Grade 550 (Overby et al. 2017) and ASTM A1035 Grade 690 steel (Shahrooz et al. 2011).

Property	ASTM A706 Grade 550		ASTM A1035 Grade 690	
	Mean	COV	Mean	COV
Elastic Modulus (MPa)	192281	5.7%	193996	7.1%
Yield Strength (MPa)	586.7	3.5%	834.3*	10.3%
Tensile Strength (MPa)	775.7	3.2%	1172.1	4.5%
Tensile-to-Yield Ratio	1.32	2.2%	1.39	9.3%
Strain at Onset of Strain Hardening	0.0074	26.2%	-	-
Uniform Strain	0.095	5.8%	0.049	11.2%

* Based on 0.2% offset method

Table 14: Equations Correlating Material Constant, M and m , with the Spacing-to-Bar Diameter Ratio.

Rebar type	Material constant	
	M	m
ASTM A706 Grade 420	$M = -0.0012 \left(\frac{s}{d_b} \right) + 0.0847$	$m = -0.0188 \left(\frac{s}{d_b} \right) - 0.271$
ASTM A706 Grade 550	$M = -0.0015 \left(\frac{s}{d_b} \right) + 0.0723$	$m = -0.0374 \left(\frac{s}{d_b} \right) - 0.1871$
ASTM A1035 Grade 690	$M = 0.0225 e^{0.1219 \left(\frac{s}{d_b} \right)}$	$m = -0.0505 \left(\frac{s}{d_b} \right) - 0.0485$

5.3 Evaluation of Low-Cycle Fatigue Damage

Figure 26 provides a schematic depicting the low-cycle fatigue damage prediction procedure adopted in this study. The first step involves subjecting the bridge column to a seismic excitation in the transverse direction by means of nonlinear dynamic time-history analysis (see Figure 26 (a)). From such analysis, at the section of maximum moment, the strain histories of longitudinal bars whose centers are the closest to the cross-section extremes in the direction of applied earthquake loading are extracted. Those rebars are labeled as S1 and S2 in Figure 26, and among other longitudinal bars in the cross-section, typically they experience the highest strain demands. Since the proposed damage model takes into account

the effect of inelastic buckling which is unlikely to initiate at the interface between the column and the foundation, extracting strain histories at the section of maximum moment may not seem the best practice. An all-encompassing model capable of predicting the buckling location of rebars in concrete columns is, nonetheless, absent in the literature, hence to avoid additional associated uncertainty while ensuring conservatism in the damage predictions of the proposed model, strain histories were extracted at section of maximum moment. Longitudinal bar buckling is a major behavioral milestone for concrete columns tested under cyclic loading beyond which significant loss in lateral force capacity is typically observed (Lehman et al. 2004). For this reason, several models have been formulated over the past few decades to predict the onset of longitudinal bar buckling in concrete columns. Notable recent examples of such models include those formulated by Berry and Eberhard (2005), Feng et al. (2015), and Goodnight et al. (2016). Goodnight et al. (2016) demonstrated that their model's predictions were more accurate than those of the other two models, i.e., formulated by Berry and Eberhard (2005) and Feng et al. (2015), since they considered data from a large database of experimentally tested columns with a wide range of geometrical and material properties. According to Goodnight et al. (2016), longitudinal bar buckling is initiated upon reversal from peak tensile strain, ε_{bb} , which can be approximated using the following expression:

$$\varepsilon_{bb} = 0.03 + 700\rho_s \frac{f_{yh}}{E_s} - 0.1 \frac{P}{f'_c A_g} \quad (52)$$

Where ρ_s is the spiral reinforcement ratio; f_{yh} is the yield strength of spiral or hoop reinforcement, E_s is the modulus of elasticity of steel; P is the applied axial load; f'_c is the compressive strength of concrete; and A_g is the gross area of column cross-section. Eq. (52) also well-predicted the experimentally measured peak tensile strains in longitudinal HSS bars prior to buckling (Barcley and Kowalsky 2020), and was thus considered in this study to detect the onset of bar buckling in the proposed damage model. In the example given in Figure 26, bar S1 is deemed to buckle because it was subjected to tensile strains exceeding ε_{bb} , and consequently its strain history response was split into two stages: pre- and post-buckling to account for the effect of buckling in subsequent analysis (see Figure 26 (b)). In order to utilize the information from constant amplitude tests such as those performed by Ghannoum and Slavin (2016) and Aldabagh and Alam

(2021b) in irregular cyclic loading histories such as those generated from dynamic time-history analysis, cumulative damage theories need to be considered. One of the most commonly used cumulative damage theory is that propounded by Miner (1945) and originally proposed by Palmgren (1921), the so-called “Miner’s rule”. The Miner’s rule is based on an assumption of linear damage accumulation throughout the fatigue life, i.e., if it takes $2N_{fj}$ half cycles of constant amplitude ε_{aj} to cause failure, then the damage per applied cycle with the same ε_a is $1/2N_{fj}$, and the accumulated damage after N half cycles of different amplitudes ε_{ai} is given as:

$$D = \sum D_i = \sum_{i=1}^N \frac{n_i}{2N_{fi}} \quad (53)$$

where n_i is the number of half-cycles a bar is cycled to a certain strain amplitude of ε_a , and $2N_{fi}$ is the number of half-cycles to fracture to the same strain amplitude of ε_a . A value of accumulated damage, D , (hereafter referred to as damage index) of unity would constitute bar fracture. The two most commonly quoted shortcomings associated with the implementation of Miner’s rule are that the mean strain effects and sequence effects are neglected. Mean strain effects, nonetheless, were found to have a negligible effect on the low-cycle performance of ordinary and high-strength deformed bars (Mander et al. 1994). Sequence effect on the other hand was found to be of lesser importance where there is significant inelastic action such that found in low-cycle fatigue problems (Krawinkler et al. 1983). These observations justify the prevalent up-to-date implementation of Miner’s rule to predict the low-cycle fatigue failure of longitudinal bars in concrete members forming plastic hinges (e.g., Sokoli 2018; To et al. 2021; among others). Prior to computing the damage index, the irregular strain history responses need to be converted into a series of half-cycles and corresponding strain ranges. To accomplish this, Matlab function “Simple Rain Flow Counting Algorithm” developed by Gong (2012) based on ASTM E1049-85 (2017) was used, as illustrated in Figure 26. In Figure 26 (c), the range of each half cycle is equal to the strain amplitude used in Eq. 51 to determine the $2N_f$ which in turn substituted in Eq. 53 to compute the damage index. In pre-buckling stage, the material constants, M and m , of Eq. 51 were determined based on the initial pitch of spiral since prior to buckling, the circular hoop reinforcement provides sufficient rotational fixity to reflect that provided by

the grips during low-cycle fatigue tests. This hypothesis, however, does not hold true in post-buckling stage, and consequently to account for the rapid deterioration in low-cycle fatigue life after bar buckling, material constants of Eq. 51 in post-buckling stage were based on twice the initial pitch of spiral. As evident in Figure 26 (d), because of buckling, bar S1 is characterized by more rapid deterioration than bar S2 which did not buckle. As a consequence, the cumulative damage index in bar S1 exceeds 1, hence deemed to fracture under the applied ground motion. The adequacy of the proposed procedure in predicting low-cycle fatigue fracture of longitudinal bars in concrete columns under cyclic loading is demonstrated in the next section through comparisons with experimental observations.

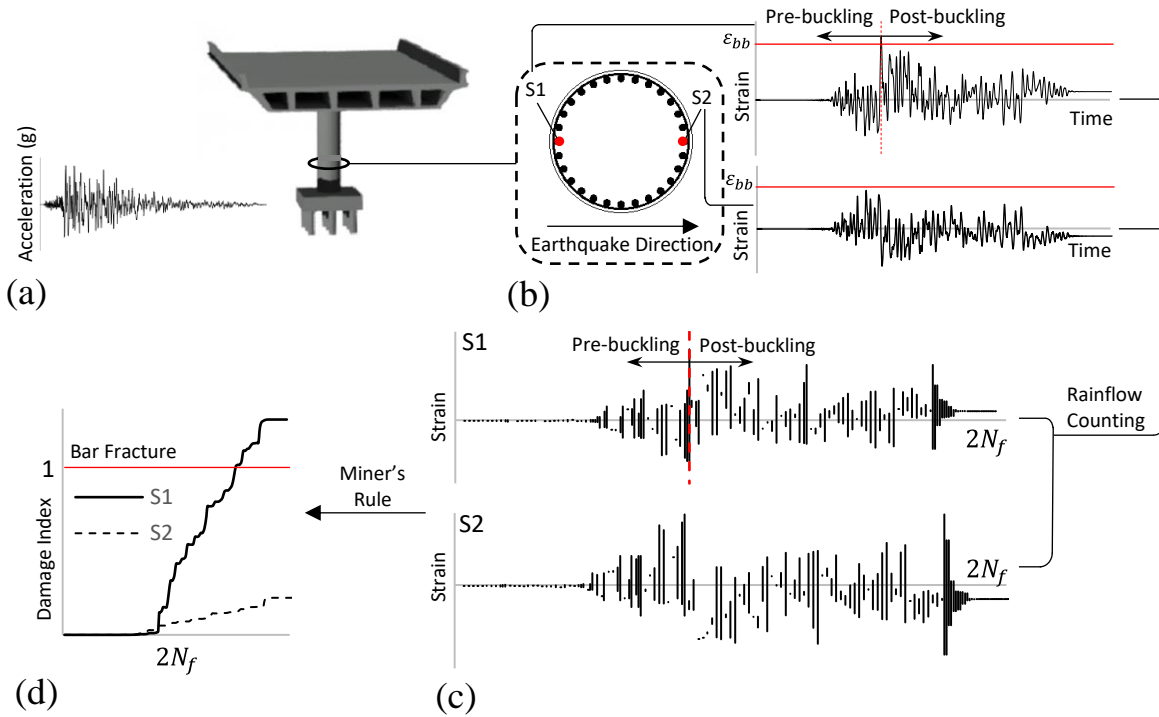


Figure 26: Proposed procedure for low-cycle fatigue damage prediction analysis.

5.4 Numerical Model and Validation

The fiber-type models of the bridge columns were generated using the structural analysis software OpenSees (Mckenna 1997). A representative discretization of the bridge column is presented in Figure 27. The column consisted of six distributed plasticity elements with the displacement-based formulation. The first element extended over the potential plastic hinge region and the remaining five elements were equal in length and constituted the remaining portion of the column (i.e. $L - L_p$). Each element had five integration points. The plastic hinge length (L_p) was computed using the equation proposed by Priestley et al. (1996) as follows:

$$L_p = 0.08L + 0.022f_{ye}d_{bl} \geq 0.044f_{ye}d_{bl} \quad (54)$$

where L is the distance from the critical section of the plastic hinge to the point of contraflexure in mm, f_{ye} is the yield strength of transverse reinforcement in MPa, and d_{bl} is the diameter of the longitudinal reinforcement. The fiber section was discretized into three types of materials namely unconfined concrete, confined concrete, and reinforcing steel. Appropriate constitutive models were selected to accurately incorporate the stress-strain responses of these materials into the numerical model. OpenSees *Concrete01* material model was used to simulate the uniaxial stress-strain response of the unconfined and confined concrete. The properties of the confined concrete were determined based on the theoretical stress-strain model proposed by Mander et al. (1988) for confined concrete. The responses of ASTM A706 Grade 420 and ASTM A706 Grade 550 steel were incorporated into the numerical model using the OpenSees *ReinforcingSteel* material model (Dodd and Restrepo-Posada 1995). Such model requires defining tangent at initial strain hardening and strain corresponding to initial strain hardening which makes it appropriate for reinforcing steel types with well-defined yield point and yield plateau such as the ASTM A706 Grade 420 and ASTM A706 Grade 550 steel. On the other hand, due to the unique shape of its stress-strain relationship, the response of ASTM A1035 Grade 690 was incorporated into the numerical model using OpenSees *Steel02* material model (i.e. Giuffré-Menegotto-Pinto Model) (Filippou et al. 1983). Such model can capture the “roundhouse” stress-strain curve of the ASTM A1035 Grade 690 by specifying several shape

parameters (i.e. R0, cR1, and cR2) controlling the transition from elastic to plastic branches. To account for strain penetration effects, the hysteretic model developed by Zhao and Sritharan (2007) (known as *Bond SP01* in OpenSees) was integrated into the analysis using a zero-length section element, as shown in Figure 27. Second-order P-Delta effects were treated in the numerical model.

Experimentally reported data were utilized to assess the accuracy of the proposed procedure in predicting the low-cycle fatigue failure of HSS as well as ordinary steel rebars. Test 15, Test 3, and Unit 2 from experimental programs executed by Goodnight et al. (2015), Barclay and Kowalsky (2020) and Restrepo et al. (2006) were considered. The former was reinforced with conventional ASTM A706 Grade 420, while the latter two were reinforced with high-strength ASTM A706 Grade 550 and ASTM A1035 Grade 690 steel, respectively. The parameters defining all of the constitutive models used to construct the numerical models of the three columns were based on the reported material properties and are given in Appendix B. Since a critical output of the numerical model, as part of the proposed procedure, is the resultant strain history, the numerical model accuracy needs to be validated not only at the global (or member), but also at the local (or sectional) level. While evaluating the accuracy of the model at the global level, the force-displacement hysteretic response was considered, whereas at the local level, either strain-displacement hysteretic response at the section of maximum moment or strain profile in plastic hinge region prior to failure was considered. Figs. 28 (a and b) provide a comparison between measured and predicted responses at global and local levels, respectively. As clearly evident in Figs. 28 (a and b), the measured responses at both levels for all three columns were well predicted. Following the proposed damage prediction procedure, the damage indices were computed and plotted against $2N_f$ in Figure 28 (c). Also, Figure 28 (c) shows the pre- and post-buckling regions defined based on peak tensile strains in bars prior to buckling, ϵ_{bb} , which were equal to 0.036, 0.039, and 0.042 for Test 15, Test 3, and Unit 2, respectively. Based on the computed damage indices, the points at which longitudinal bars were deemed to buckle and fracture were determined and are indicated with un-filled markers on the loading histories of the three columns in Figure 28 (d). Besides, the same milestones observed experimentally are indicated with filled markers in Figure 28 (d) for comparison purposes. Slight discrepancies between the predicted half-cycles at first longitudinal bar

buckling and fracture and those reported experimentally can be observed in Figure 28 (d). This level of discrepancy was anticipated and is likely owing to the simplifying assumptions within the proposed procedure. The bar buckling prediction model, for example, accounts for only the axial load ratio, spiral reinforcement ratio, and steel strength amongst many other potentially contributing parameters. In addition, the low-cycle fatigue properties reported by Ghannoum and Slavin (2016) and Aldabagh and Alam (2021b) are not necessarily reflective of those of the rebars used in the three columns. In fact, Ghannoum and Slavin (2016) reported that HSS bars produced by two different manufacturing processes could exhibit different low-cycle fatigue performance despite conforming to the same ASTM standard. Nevertheless, the proposed procedure yielded predictions with reasonable accuracy, which was deemed fairly adequate compared to the experimental results, and was therefore adopted in subsequent analyses in this study.

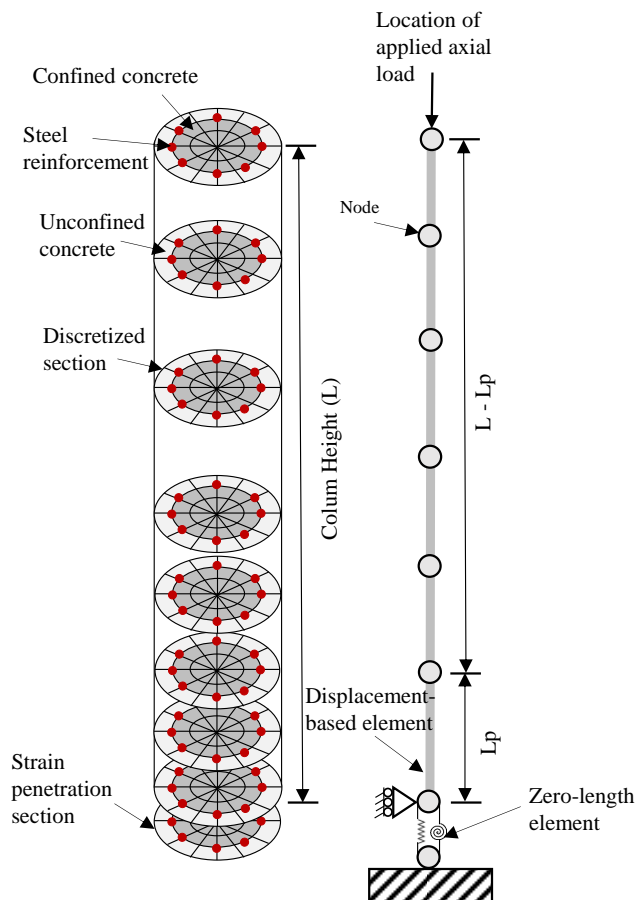


Figure 27: Discretization of the concrete bridge column.

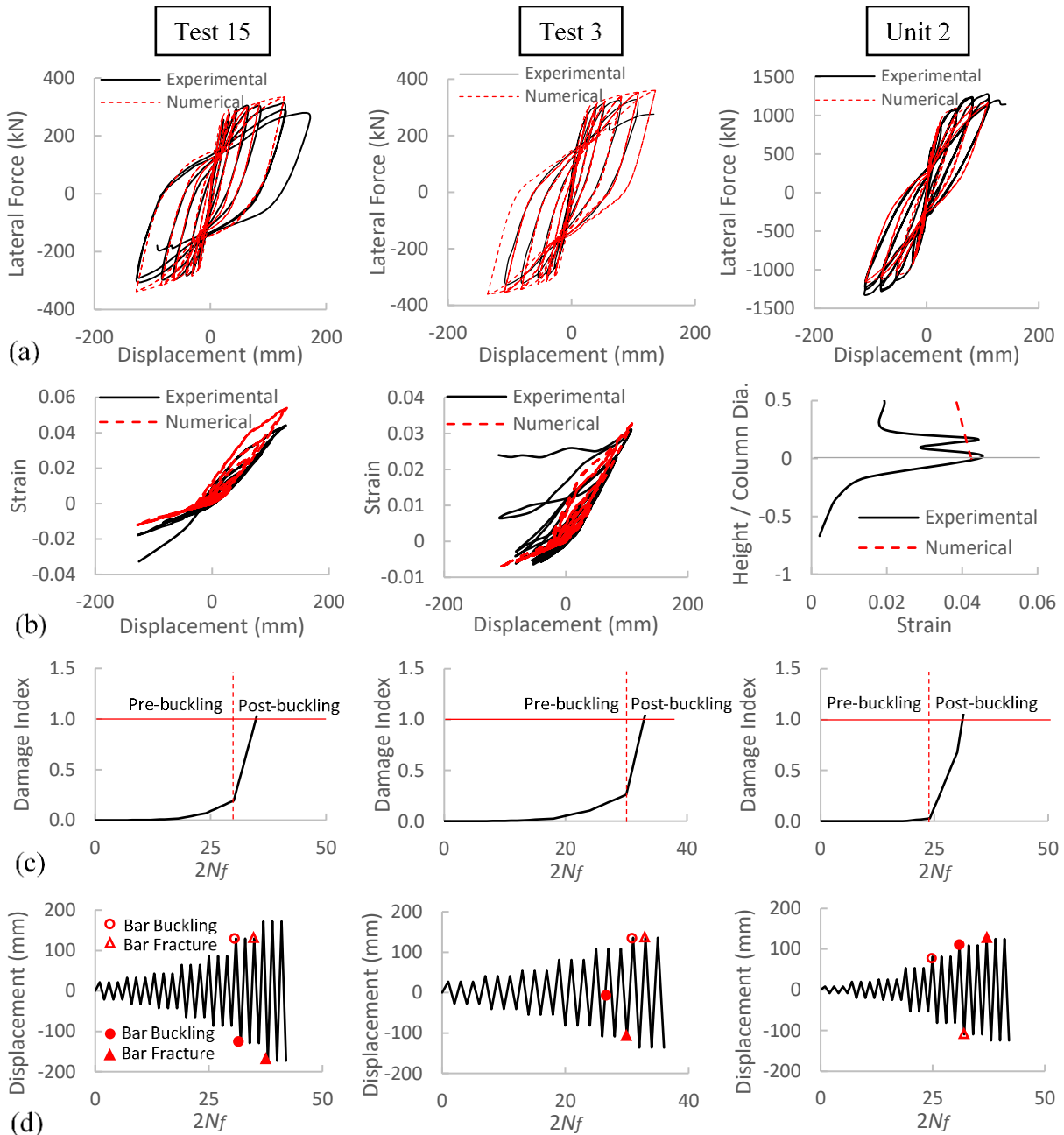


Figure 28: (a) Measured and predicted responses at member level; (b) Measured and predicted responses at section level; (c) Predicted damage index versus $2N_f$ plots; and (d) load histories applied to the columns.

5.5 Selectin of Ground Motions

In this study, ground motions generated from two types of earthquakes, namely, crustal and subduction earthquakes were considered. Crustal shallow earthquakes are normally generated by active

faults within the crust with focal depths of about 30 km or less. This type of earthquakes is prevalent in the Cascadia because of the abundant active shallow faults in the North American plate (Elnashai and Sarno 2008). Megathrust subduction earthquakes, on the other hand, develop in subduction (or convergent) zones where adjacent tectonic plates converge and collide. In the region stretching from Vancouver Island to California along the Pacific coast, the Juan de Fuca and Gorda plates subduct beneath the North American plate creating the Cascadia subduction zone. Geological evidence exists that such zone is capable of generating large-magnitude subduction earthquakes (Atwater et al. 1995; Goldfinger et al. 2012). Subduction earthquakes are scarce but if generated typically produces long-duration earthquakes with large number of load reversal cycles. For this reason, longitudinal bars are more prone to fracture due to low-cycle fatigue during such events. An effective measure of the effect of long-duration ground motions on the low-cycle fatigue performance of rebars in concrete columns is the cumulative damage concept on which, as mentioned earlier, the proposed damage analysis procedure was based (Hancock and Bommer 2006). In this study, two suites of ground motions were compiled, the first contained ten horizontal components of seed ground motion records from shallow crustal earthquakes, and the second contained the same but from megathrust subduction earthquakes. Table 15 gives a summary of the selected records. Ground motion records of crustal earthquakes were extracted from the Pacific Earthquake Engineering Research Center (PEER 2011), whereas those of subduction earthquakes were extracted from Kyoshin Network (K-Net) database. Pulse-type near-field ground motions are beyond the scope of this study, hence were excluded from the selected ground motions. Besides, the effect of vertical acceleration was not accounted for in the analysis presented herein, and hence, the vertical components of the selected ground motions were not considered.

Table 15: Summary Details of the Ground Motion Sets.

Set	Earthquake type	Number of records	Moment magnitude range	R ^a range (km)	PGA ^a range (g)	Duration range (seconds)
1	Crustal	10	6.61-7.40	13-51	0.109-0.568	28.6-61.8
2	Subduction	10	9	152-166	0.800-1.246	390

^aR = distance to the rupture surface; PGA = peak ground acceleration.

5.6 Characteristics of Bridge Columns

Three samples each containing 8 concrete bridge columns with unique combination of values with the upper and lower levels of the variable parameters were generated. Variable parameters considered in the samples were axial load ratio (i.e., ratio of axial load, P , to the product of concrete compressive strength and gross area of the cross section, P_o), longitudinal reinforcement ratio (ρ_l), and spiral reinforcement ratio (ρ_s) with upper and lower level values of 5% and 20%, 1% and 4%, and 0.7% and 1.3%, respectively. The upper and lower levels were set to obtain performance data for well-confined circular bridge columns having typical details of those found in regions of high seismicity in the United States and Canada. The aspect ratio (also known as moment–shear span ratio), which is the ratio of column height to column diameter, was set at 4 for all columns to ensure flexure-dominated behavior. In this study, concrete bridge columns are identified by axial load ratio (P05 or P20), longitudinal reinforcement ratio (L1 or L4), and spiral reinforcement ratio (S07 or S13). Hence, P05L1S07 represents a bridge column subjected to a constant axial load ratio of 5% with longitudinal and spiral reinforcement ratios of 1% and 0.7%, respectively. The columns in the three samples were identical but reinforced with either ASTM A706 Grade 420, ASTM A706 Grade 550, or ASTM A1035 Grade 690. Concrete columns reinforced with ASTM A706 Grade 420 served as control columns when evaluating the low-cycle fatigue performance of HSS bars in their counterparts. This study also examines the hypotheses postulated by Ghannoum and Slavin (2016) and Aldabagh and Alam (2021b) according to which a closer spacing for lateral reinforcement may be beneficial for HSS in plastic hinge regions. Therefore, the low-cycle fatigue of the rebars in the three

samples was evaluated for spacing-to-rebar diameter ratios (i.e., ratio of pitch of spiral, s , to longitudinal bar diameter, d_b) of 4 and 6. The upper level of s/d_b was set to 6 to reflect the *AASHTO Guide Specifications for LRFD Seismic Bridge Design* requirements which limit the maximum spacing for lateral reinforcement in the plastic hinge regions to six longitudinal bar diameters.

Prior to performing the low-cycle fatigue damage analysis, the concrete bridge columns were first analyzed under static pushover loading to determine their effective yield displacements. The effective yield displacements of the concrete bridge columns were obtained by multiplying the ratio of nominal to first yield moments by the first yield displacement. The effective yield drift ratios of concrete bridge columns reinforced with the three types of HSS rebars having s/d_b of 4 are given in Table 16. The s/d_b has little to no effect on the effective yield displacement and consequently only those with s/d_b of 4 are given in Table 16. The effective yield displacement was subsequently employed to determine the displacement ductility demand (μ_d), which is defined as the ratio of maximum absolute value of displacement response to effective yield displacement. As previously mentioned, this study focuses on evaluating the low-cycle fatigue performance of HSS rebars in concrete columns at target μ_d of two, four, and six. To this end, the well-established incremental dynamic analysis (IDA) (Vamvatsikos and Cornell 2004) was adopted. As part of the IDA, the selected ground motions were scaled to seismic intensity levels at which the target displacement ductility demands can be achieved. Following the IDA, the previously described fatigue-based damage model was implemented to predict the deterioration and failure of longitudinal rebars in the concrete bridge columns at target μ_d .

Table 16: Effective Yield drift Ratios (In Percent) of Bridge Columns with s/d_b of 4.

Bridge column	Bar type		
	ASTM A706	ASTM A706	ASTM A1035
	Grade 420	Grade 550	Grade 690
P05L1S07	0.69	0.91	1.43
P20L1S07	0.63	0.88	1.26
P05L4S07	1.02	1.34	2.02
P20L4S07	0.96	1.24	1.82
P05L1S13	0.70	0.93	1.43
P20L1S13	0.64	0.89	1.19
P05L4S13	1.06	1.37	2.06
P20L4S13	0.96	1.26	1.88

5.7 Results of Low-Cycle Fatigue Damage Analysis

The computed damage indices of longitudinal bars for all bridge columns are presented in tables in Appendix B. In those tables, as a recap, damage indices equal to unity indicate bar fracture. To facilitate the comparisons between the low-cycle fatigue performances of the three types of rebars in the bridge columns, a bar fracture index is introduced. The bar fracture index is defined herein as the ratio of the number of observed bar fractures in a sample of bridge columns under a set of ground motions to the product of the number of bridges in the sample and number of records within the set. In this study, the number of bridge columns in each of the three samples was 8 and the number of records in each of the two ground motions sets was 8, hence the divisor in the bar fracture index held a constant value of 80. For instance, in the sample of concrete bridge columns reinforced with ASTM A706 Grade 550 under a set of ground motions from crustal earthquakes, the number of bar fractures was 19 for μ_d of 4 and s/d_b of 6, thereby for such configuration, the associated bar fracture index was $19/80 = 0.24$. Bar fracture index reflects the probability of bar fracture in concrete bridge columns having characteristics similar to those of the sample columns under certain conditions of earthquake type, displacement ductility level, and s/d_b . Bar fracture index versus displacement ductility demand, μ_d , plots for bridge columns reinforced with ASTM A706 Grade 420, ASTM A706 Grade 550, and ASTM A1035 Grade 690 are given in Figure 29.

At μ_d level of 2, bridge columns reinforced with ASTM A706 Grade 420 and ASTM A706 Grade 550 were characterized with bar fracture indices of zero for both crustal and subduction earthquakes irrespective of s/d_b . This indicates that for such configurations, the damage indices in all bars were less than unity, and consequently no bar fractures were recorded. However, this was not the case for bridge columns reinforced with ASTM A1035 Grade 690 rebars which exhibited a bar fracture index greater than zero for the two earthquake types and spacing-to-bar diameter ratios. For crustal earthquakes, the bar fracture indices were 0.04 and 0.13 for s/d_b of 4 and 6, respectively. This implies that under crustal earthquakes, it is unlikely that the ASTM A1035 Grade 690 bars will experience fracture due to low-cycle fatigue in concrete bridge columns with maximum spacing-to-bar diameter ratio of 6. However, for the same type of concrete bridge columns, greater bar fracture indices were observed under subduction earthquakes in comparison to crustal earthquakes (see Figure 29 (c)). This is primarily due to the long duration effect of the ground motions of subduction earthquakes which typically impose greater number of cyclic strain reversals in rebars than those imposed by ground motions of crustal earthquakes. For bridge columns reinforced with ASTM A1035 Grade 690 under subduction earthquakes, bar fracture indices were 0.45 and 0.49 for s/d_b of 4 and 6, respectively. Such bar fracture indices impart significant differences between low-cycle fatigue performance of ASTM A1035 Grade 690 and that of benchmark ASTM A706 Grade 420 under subduction earthquakes regardless of the s/d_b . Based on such observation, it appears that the ASTM A1035 Grade 690 bars are likely to experience fracture in bridge columns subjected to subduction earthquakes even at μ_d level as low as 2.

At μ_d level of 4, because of the larger imposed displacement demands, the bar fracture indices of all bridge columns were greater than those of their counterparts at μ_d level of 2. Control bridge columns reinforced with ASTM 706 Grade 420 steel were characterized with bar fracture indices nearly equal to zero except for one combination where the bridge columns had s/d_b of 6 and were subjected to subduction earthquakes. For such combination, the bar fracture index was 0.15 for bridge columns reinforced with ASTM A706 Grade 420. At the same μ_d level, concrete bridge columns reinforced with ASTM A706 Grade

550 under crustal earthquakes demonstrated comparable low-cycle fatigue performance to that of the benchmark ASTM A706 Grade 420 for s/d_b of 4 and 6 with bar fracture indices of 0.08 and 0.24, respectively. The performance of the same type of rebars in bridge columns under subduction earthquakes was noticeably influenced by s/d_b . At s/d_b of 4, the bar fracture index was 0.39, whereas at s/d_b of 6, the bar fracture index was 0.76 for bridge columns reinforced with ASTM A706 Grade 550 (see Figure 29 (b)). This postulates that in order for ASTM A706 Grade 550 to maintain comparable low-cycle performance to that of the benchmark ASTM A706 Grade 420, spacing-to-bar diameter ratio must be limited to 4 for bridge columns prone to subduction earthquakes. In addition, at the same μ_d level, bridge columns reinforced with ASTM A1035 Grade 690 rebars were characterized by minimum bar fracture index of 0.84. This implies that at μ_d level of 4, irrespective of s/d_b , there is a high chance of ASTM A1035 Grade 690 bar fracture in concrete bridge columns during crustal and subduction earthquakes.

At μ_d level of 6, when compared to μ_d level of 4, a noticeable increase in number of bar fractures, and therefore bar fracture indices, was observed for all bridge columns which, as evident in Figure 29, appeared to be significant only for ASTM A706 Grade 420 and ASTM A706 Grade 550 steel bars. Owing to the superior low-cycle fatigue performance of ASTM A706 Grade 420, concrete bridge columns reinforced with this type of bars exhibited the lowest bar fracture indices when compared to their counterparts at μ_d level of 6. For instance, they had bar fracture indices of 0.08 and 0.23 for s/d_b of 4 and 6, respectively, under crustal earthquakes indicating a relatively low chance of bar fracture due to low-cycle fatigue. For the same type of bridge columns under subduction earthquakes, however, greater bar fracture indices were observed especially for s/d_b of 6 where the bar fracture index reached 0.66, consequently implying that there is a good chance of the benchmark ASTM A706 Grade 420 bar fracture in columns subjected to long-duration records at μ_d level of 6. This observation is consistent with results reported by Mohammed et al. (2017) from shake table tests of flexure-dominated well-confined circular concrete columns under subduction earthquakes. According to Mohammed et al. (2017), bar fractures were observed in concrete columns subjected to μ_d ranging from 5.2 to 7.6 under subduction earthquakes. On the other

hand, at μ_d level of 6, all concrete bridge columns reinforced with HSS bar types were characterized by relatively large bar fracture indices with the minimum value being 0.53. While lower ratios of spacing to bar diameter ratios, s/d_b , were associated with lower bar fracture damage indices for HSS types, they were still insufficient to bring the bar fracture indices to levels comparable to those of the control columns at μ_d level of 6.

In light of the observations above, it appears that up to μ_d level of 4, ASTM A706 Grade 550 rebars have comparable performance to that of ASTM A706 Grade 420 in bridge columns subjected to crustal and subduction earthquakes provided that the latter lower limit of s/d_b is imposed. In addition, ASTM A1035 Grade 690 bars demonstrated fairly adequate low-cycle fatigue performances in bridge columns subjected to both crustal and subduction earthquakes but only if imposed displacements are limited to μ_d of 2. Although bar fracture indices are effective in identifying the configurations in which low-cycle fatigue performances comparable to that of the benchmark ASTM A706 Grade 420 can be achieved, they do not reflect the accumulated damage in the rebars. Although steel rebars might not fracture under certain damaging cycles, their permanent memory stores the damage caused by those cycles, and at any instance in time such memory could be triggered making the rebars more vulnerable to fatigue failure, especially in the case of an earthquake followed by aftershocks. Therefore, damage indices need to be considered in conjunction with bar fracture indices before design recommendations can be made. Damage indices for potential configurations where HSS rebars demonstrated adequate low-cycle fatigue performance are presented and examined next.

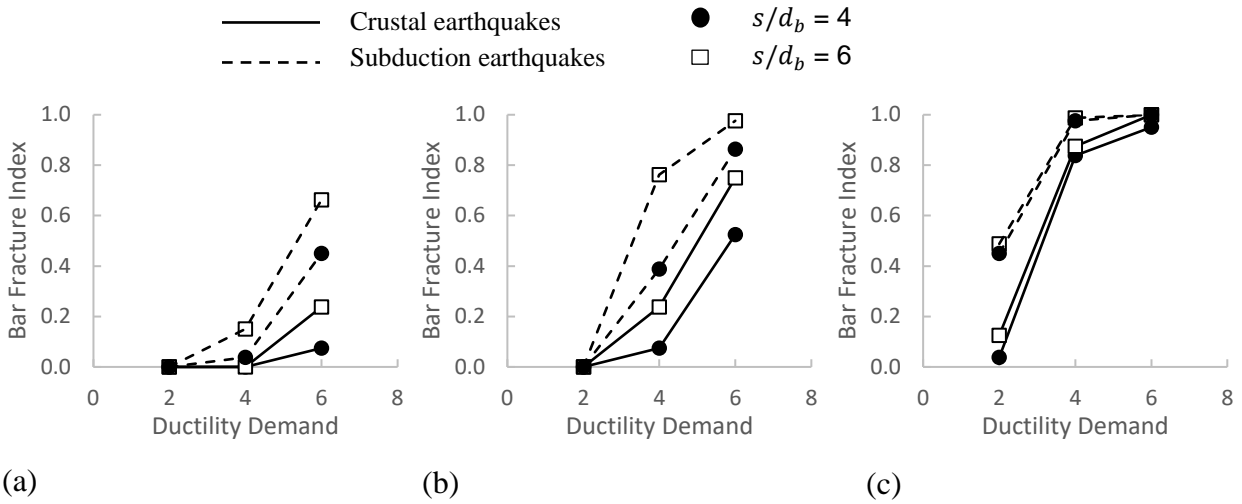


Figure 29: Bar fracture index versus ductility demand for bridge columns reinforced with: (a) ASTM A706 Grade 420; (b) ASTM A706 Grade 550; and (c) ASTM A1035 Grade 690.

5.8 Cumulative Damage

Figures 30 (a) and (b) plot the computed damage indices for bridge columns reinforced with ASTM A706 Grade 550 and subjected to crustal and subduction earthquakes, respectively, at μ_d level of 4. Figures 31 (a) and (b) plot the same but for bridge columns reinforced with ASTM A1035 Grade 690 and subjected to crustal and subduction earthquakes, respectively, at μ_d level of 2. Figs. 30 and 31 differentiate between damage indices computed for s/d_b of 4 and those computed for s/d_b of 6. Horizontal dashed lines representing the average damage indices are also shown in those figures.

As can be seen in Figure 30 (a), the average damage indices in bridge columns reinforced with ASTM A706 Grade 550 bars subjected to crustal earthquakes at μ_d level of 4 were 0.38 and 0.60 for s/d_b of 4 and 6, respectively. The average damage indices in ASTM A706 Grade 420 bars in counterpart control columns were 0.14 and 0.22, respectively. Despite these differences, the average damage indices in ASTM A706 Grade 550 rebars, whether for s/d_b of 4 or 6, indicate that such rebars could still exhibit an adequate reserve fatigue life after being subjected to crustal earthquakes at μ_d level of 4. This, however, does not apply to ASTM A706 Grade 550 rebars subjected to strain reversals generated from subduction

earthquakes. Under subduction earthquakes, the average damage indices in ASTM A706 Grade 550 bars were 0.70 and 0.93 for s/d_b of 4 and 6, respectively, as can be seen in Figure 30 (b). This implies that ASTM A706 Grade 550 are susceptible to bar fracture if subjected to additional strain reversals (e.g., aftershock effects) after a subduction earthquake at μ_d level of 4, especially if s/d_b is equal to 6. The average damage indices in rebars of their counterpart control columns were 0.37 and 0.56 for s/d_b of 4 or 6, respectively, indicating that at μ_d level of 4, even the benchmark ASTM A706 Grade 420 rebars noticeably deteriorated after subduction earthquakes.

According to Figures 31 (a) and (b), the average damage indices in ASTM A1035 Grade 690 bars in bridge columns subjected to subduction earthquakes at μ_d level of 2 were 0.41 and 0.36 for s/d_b of 4 and 6, respectively. The effect of s/d_b on the average damage index was found to be less significant for ASTM A1035 Grade 690 than ASTM A706 Grade 550. This reflects the observations from the proposed fatigue life models. For instance, under ε_a of 0.01, the increase in s/d_b from 4 to 6 results in higher low-cycle fatigue life of ASTM A706 Grade 550 by 187 half-cycles, whereas the same increase in s/d_b results in higher low-cycle fatigue life of ASTM A1035 Grade 690 by 97 cycles. Under conditions of earthquake type and μ_d level identical to those of the computed damage indices presented in Figure 31 (a), the average damage indices in ASTM A706 Grade 420 bars were 0.02 and 0.03 for s/d_b of 4 to 6, respectively. The significant differences between the two types of steel are not only owing to the poorer low-cycle fatigue performance of ASTM A1035 Grade 690 steel but also its higher yield strain when compared to ASTM A706 Grade 420. Because of the higher yield strain of steel, concrete bridge columns reinforced with ASTM A1035 Grade 690 were characterized with higher yield drift, and thereby to achieve the same μ_d level as their counterparts, their ground motions were scaled to greater intensities. Despite the observed differences from the benchmark performances, the reported average damage indices under the conditions considered in Figure 31 (a) were, nonetheless, relatively low, indicating that ASTM A1035 Grade 690 bars exhibit adequate reserve fatigue life after crustal earthquake at μ_d level of 2. On the other hand, at μ_d level of 2, the average damage indices in ASTM A1035 Grade 690 bars in bridge columns subjected to subduction

earthquakes were 0.68 and 0.77 for s/d_b of 4 and 6, respectively. The average damage indices in ASTM 706 Grade 420 in counterpart control columns were 0.05 and 0.1, respectively. The significant differences between the two types can be explained by following the same rationale described earlier when the average damage indices in ASTM A1035 Grade 690 were examined for crustal earthquakes. The reported average damage indices in Figure 31 (b), nonetheless, does indicate a high chance of ASTM A1035 bar fracture if sustained additional strain reversals after a subduction earthquake even at μ_d levels as low as 2.

According to Article 8.4.1 of the *AASHTO Guide Specifications for LRFD Seismic Bridge Design (2014)*, ASTM A706 Grade 550 and ASTM A1035 Grade 690 steel rebars can be used in seismic applications only if demonstrated through testing that their low-cycle fatigue performance is not inferior to normal-strength steel rebars. In review of the reported results, despite their poorer low-cycle fatigue performance, ASTM A706 Grade 550 and ASTM A1035 Grade 690 demonstrated rather adequate performance when compared to that of the benchmark ASTM A706 Grade 420 under certain conditions. From a low-cycle fatigue performance standpoint, up to μ_d level of 4, ASTM A706 Grade 550 steel bars appear to have the potential to be implemented in concrete columns subjected to crustal and subduction earthquakes provided that for the latter the spacing-to-bar diameter ratio is limited to 4. Such limitation on the s/d_b is critical to ensure that ASTM A706 Grade 550 steel bars do not experience significant deterioration, and possibly fracture, in concrete columns subjected to subduction earthquakes at μ_d levels less than 4. ASTM A1035 Grade 690 steel bars, on the other hand, seem to have the potential to be utilized in seismic applications in bridge columns subjected to only crustal earthquakes with maximum μ_d level of 2. While the authors acknowledge the code committees' concerns over the low-cycle fatigue performance of HSS bars, the current requirement of the AASHTO (2014) appears to be overly conservative given the reported observations herein. This study recommends imposing certain limits on the μ_d and s/d_b , such as those proposed above for ASTM A706 Grade 550 and ASTM A1035 Grade 690, for HSS bars rather than completely restricting their use in bridge columns based on a meager low-cycle fatigue life.

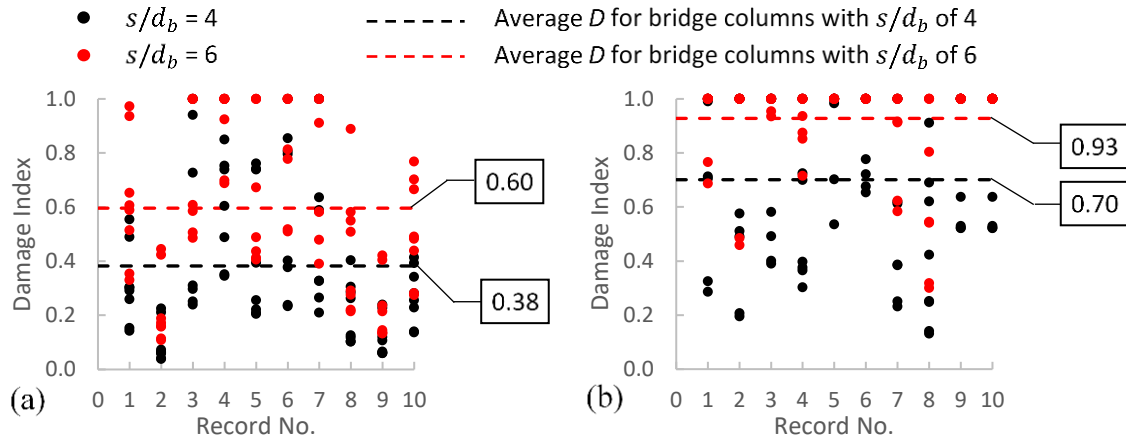


Figure 30: Computed damage indices for rebar in concrete columns reinforced with ASTM A706 Grade 550 and subjected to: (a) crustal earthquakes, and (b) subduction earthquakes at μ_d level of 4.

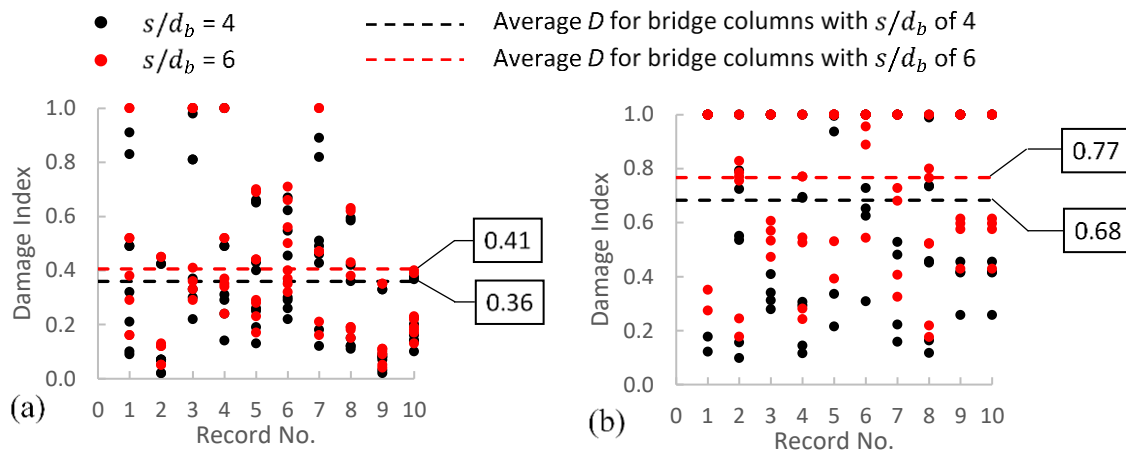


Figure 31: Computed damage indices for rebar in concrete columns reinforced with ASTM A1035 Grade 690 and subjected to: (a) crustal earthquakes, and (b) subduction earthquakes at μ_d level of 2.

5.9 Summary

Design codes restrict the use of certain high-strength steel bar types such as ASTM A706 Grade 550 and ASTM A1035 Grade 690 in seismic application in bridge columns due to their poorer low-cycle fatigue performance in comparison to the conventional ASTM A706 Grade 420. In this study, previously reported fatigue data of ASTM A706 Grade 550 and ASTM A1035 Grade 690 steel bars were utilized as

part of an analytical program to identify conditions under which HSS rebars can achieve adequate performance when compared to that of benchmark ASTM A706 Grade 420 steel bars in concrete bridge columns. A hypothetical sample of well confined circular concrete bridge columns with flexure-dominated behavior and characteristics reflective of those currently in use in regions of high seismicity in North America was assembled. The variables considered within the sample were axial load ratio, and longitudinal and spiral reinforcement ratios. The concrete bridge columns in the sample were alternately reinforced with ASTM A706 Grade 420, ASTM A706 Grade 550, and ASTM A1035 Grade 690 and analyzed under different conditions of displacement ductility level (2, 4, and 6), earthquake type (crustal and subduction earthquakes), and ratio of hoop spacing to longitudinal bar diameter ratio (4 and 6). As part of the numerical analysis, cumulative damage theory was utilized to predict low-cycle fatigue-induced bar deterioration and fracture under certain conditions. Comparisons between the low-cycle fatigue performances of two HSS types and those of conventional steel were made based on the computed bar fracture and accumulated damage indices. Within the limits of the variables investigated in this program the following key observations were made:

- (1) Up to displacement ductility level of 4, ASTM A706 Grade 550 were found to have adequate low-cycle fatigue performance in concrete bridge columns subjected to crustal and subduction earthquakes provided that for the latter, ratio of hoop spacing to longitudinal bar diameter ratio is limited to 4. Such limitation on the spacing-to-bar diameter ratio is critical to provide an additional safety margin against fatigue deterioration and fracture of ASTM A706 Grade 550 steel bars in concrete columns subjected to subduction earthquakes imposing displacement ductility levels up to 4.
- (2) Irrespective of the spacing-to-bar diameter ratio, ASTM A1035 Grade 690 rebars demonstrated adequate low-cycle fatigue performance only for crustal earthquakes and displacement ductility level of 2.

While the authors acknowledge the code committees' concerns over the low-cycle fatigue performance of HSS types such as those considered in this study, the current requirement of the AASHTO appears to be

overly conservative given the reported observations herein. This study recommends imposing certain limits on the μ_d and s/d_b , such as those proposed above for ASTM A706 Grade 550 and ASTM A1035 Grade 690, for HSS bars rather than relying solely on the results of low-cycle fatigue tests to determine their adequacy for seismic applications.

CHAPTER 6: SEISMIC FRAGILITY ASSESSMENT OF BRIDGE PIERS INCORPORATING HIGH-STRENGTH STEEL AND CONCRETE UNDER NEAR-FAULT GROUND MOTIONS

6.1 General

High-strength steel (HSS) reinforcement conforming to the requirements of ASTM A1035 (ASTM 2020b) is being produced in the United States and Canada in two grades, namely, Grade 690 and Grade 830. HSS lacks a distinct yield plateau and therefore, establishing its yield strength (f_y) requires using one of the following methods: (1) the 0.35% extension under load (EUL) method; (2) the 0.5% EUL method; and (3) the 0.2% offset method (most commonly used in practice). In the 0.2% offset method, the yield strength is the stress on the engineering stress-strain curve at its intersection with a line having a slope equal to the modulus of elasticity of steel and starting from the strain of 0.2%. Grade 690 and 830 exhibit a minimum yield strength of 690 and 830 MPa, respectively, based on the 0.2% offset method. The modulus of elasticity of the two grades is 200 GPa, and the tensile strength for Grade 690 and 830 is 1070 and 1100 MPa, respectively (WJE 2008). The stress-strain curve of the ASTM A1035 Grade 690 reinforcing bar used in this study is shown in Figure 32. The use of the aforementioned methods to establish the f_y of ASTM A1035 Grade 690 reinforcing bar is illustrated in Figure 32.

Since HSS exhibits considerably higher strength than conventional Grade 420 steel, it allows for a substantial reduction in the required area of reinforcement resulting in improved concrete placement, particularly in heavily reinforced sections. HSS often balances the increase in material cost by reducing the labor cost, which is a function of the material weight (Thomas et al. 2013). In addition, several researchers have reported that HSS exhibits considerably higher corrosion resistance capabilities compared to conventional steel (Seliem 2007; Darwin et al. 2009; Ji et al. 2005; Clemena and Virmani 2004). The better performance of HSS in corrosion resistance, compared to conventional steel, is primarily due to the higher chromium content. There have been several successful attempts to introduce HSS in bridge decks. Seliem (2007) reported that the use of HSS in concrete bridge decks reduces the amount of required

longitudinal reinforcement by 33% without compromising the load-carrying capacity or altering the serviceability behavior of the bridge deck. In addition, according to Pedro et al. (2018), the use of HSS in steel-concrete bridge decks allows for a reduction of 25 to 30% in the steel weight. Saleem et al. (2011) utilized HSS and ultrahigh-performance concrete to develop an innovative lightweight bridge deck system to replace the open-grid steel decks from moveable bridges. It is clear from the previous examples that HSS can be a promising alternative to conventional steel in bridge decks; however, extending its application to bridge piers requires further attention due to two main reasons. First, bridge piers are usually susceptible to damage during a seismic event, i.e. the location where inelastic deformation is expected to occur. Second, the substantial difference in material properties between conventional steel and HSS may lead to noticeable differences in seismic response (Aldabagh and Alam 2020). While designing reinforced concrete (RC) structural elements against seismic forces, several material properties of reinforcing steel must be carefully examined. These include: (1) minimum yield strength; (2) tensile strength; (3) uniform elongation and total elongation; (4) ratio of tensile strength to yield strength (hereinafter referred to as the yield ratio). Table 17 provides a comparison between the main tensile properties of ASTM A706 Grade 420 and ASTM A1035 Grade 690 and 830. For conventional steel, ASTM A706 (2016) requires that the tensile strength shall not be less than 1.25 times the actual yield strength. This is an important limit since the yield ratio controls the length of the yield region along the axis of the members, and thus contributes directly to the plastic rotation capacity. In ASTM A1035 reinforcement, the yield ratio is normally found to exceed 1.25 if the yield strength is established based on the 0.2% offset method (WJE 2008). However, the elongation, which is another important measure of ductility, of ASTM A1035 reinforcement is lower than that of ASTM A706 reinforcement (Table 17). As a result, due to the uncertainty associated with the ductility of members containing ASTM A1035 Grade 690 and 830 reinforcement, the AASHTO Guide Specifications for LRFD Seismic Bridge Design (AASHTO 2017) limits the use of such reinforcement to members which are expected to remain elastic, i.e. not part of the seismic-force resisting system. The Canadian Highway Bridge Design Code (CHBDC) (CSA 2019b), on the other hand, does not permit the use of ASTM A1035 reinforcing bars in both non-seismic and seismic applications.

Several researchers have investigated the performance of concrete columns reinforced with HSS when subjected to reversed cyclic loading (Restrepo et al. 2006; Rautenberg et al. 2013; Barbosa et al. 2016; Li et al. 2018; and Lim et al. 2017). Concrete columns reinforced with HSS are more flexible than those reinforced with a larger amount of conventional steel. Rautenberg et al. (2013) reported that columns reinforced with HSS reinforcement were characterized by a high drift ratio at yield (1.4-1.7%), which was up to 90% higher than that measured in specimens reinforced with conventional steel. Concrete columns reinforced with HSS were characterized with less ductile response than those reinforced with conventional steel, and hence dissipated less energy (Rautenberg et al. 2013). However, Rautenberg et al. (2013) reported, based on numerical analysis, that multi-story moment RC frame buildings with columns reinforced with HSS are less susceptible to larger drifts when compared to buildings with columns reinforced with conventional steel. Concrete bridge columns reinforced with HSS can attain approximately 4% ultimate drift ratio before failure (Restrepo et al. 2006). Concrete columns reinforced with HSS are capable of achieving resistance, maximum lateral displacement, and curvature ductility comparable to that of columns reinforced with conventional steel (Barbosa et al. 2016).

In addition to HSS, high-strength concrete (HSC) is another high-performance material (HPM) that has been gaining popularity for many years due to its numerous advantages over normal strength concrete (NSC). Since HSC exhibits concrete compressive strength (f'_c) higher than that of NSC, utilizing it in buildings leads to a considerable reduction in the column sizes. This is mostly beneficial in high-rise buildings where the columns in lower stories are larger in size. Besides, HSC has other advantages related to lateral stiffness and axial shortening (Colaco et al. 1985). However, HSC is more brittle than NSC, and therefore, requires additional attention when extending current design code requirements to the design and detailing of HSC columns located in seismically active regions. According to Cusson et al. (1994) and Razvi et al. (1994), increasing the amount of transverse reinforcement is necessary to maintain a constant level of ductility for columns subjected to the same level of axial load. Studies have shown that HSC columns, whose transverse reinforcement is designed as per the ACI confinement requirements, exhibit adequate ductility when subjected to axial loads below 20% of column axial load capacity (Légeron et al.

2000; Azizinamini et al. 1994; and Bayrak et al. 1998). In addition, Paultre et al. (2009) demonstrated that HSC circular columns designed according to the CSA A23.3 requirements are characterized by ductile performance regardless of the yield strength of transverse reinforcement and axial load ratio. HSS and HSC have the potential of replacing current conventional materials in members resisting seismic forces if the design code requirements are met and proper reinforcement detailing is provided (Aldabagh and Alam 2020). However, before introducing design recommendations related to the use of HPMs, it is crucial to evaluate the seismic performance of structures incorporating such materials. The seismic performance of concrete buildings utilizing HPMs such as HSS and HSC has been evaluated numerically by Billah and Alam (2013) and Konstantinidis and Kappos (2003). It was concluded that introducing such materials improved the seismic performance of the buildings by reducing the probability of failure when compared to normal strength materials. However, there is a lack of research works evaluating the seismic vulnerability of bridge piers incorporating HPMs. Therefore, this study aims to perform a fragility-based seismic vulnerability assessment of a bridge pier incorporating different combinations of HSC and HSS under near-fault ground motions. Fragility curves are often effective in expressing the seismic vulnerability since they identify the probability of a structure sustaining a particular level of damage when subjected to certain ground acceleration. In this paper, the design of a bridge pier in Vancouver, British Columbia is initially verified using normal strength materials, i.e. the actual materials used in the construction of the bridge. Then, based on the force-based seismic design procedure prescribed in the CHBDC (CSA 2019b), the bridge pier is redesigned using different combinations of HPMs. The seismic performance of the proposed bridge pier sections is assessed using nonlinear static-pushover and dynamic time history analyses. The findings of this research are expected to reduce the concerns over the seismic performance of bridge piers reinforced with HSS and cast with HSC. In addition, design recommendations for the design of single-column bridge piers are proposed based on the results of the fragility-based seismic assessment. Hence, this research should help relax current restrictions related to the use of HPMs found in the bridge design codes (such as CHBDC and AASHTO), and consequently, allow bridge engineers to make efficient use of their potential benefits.

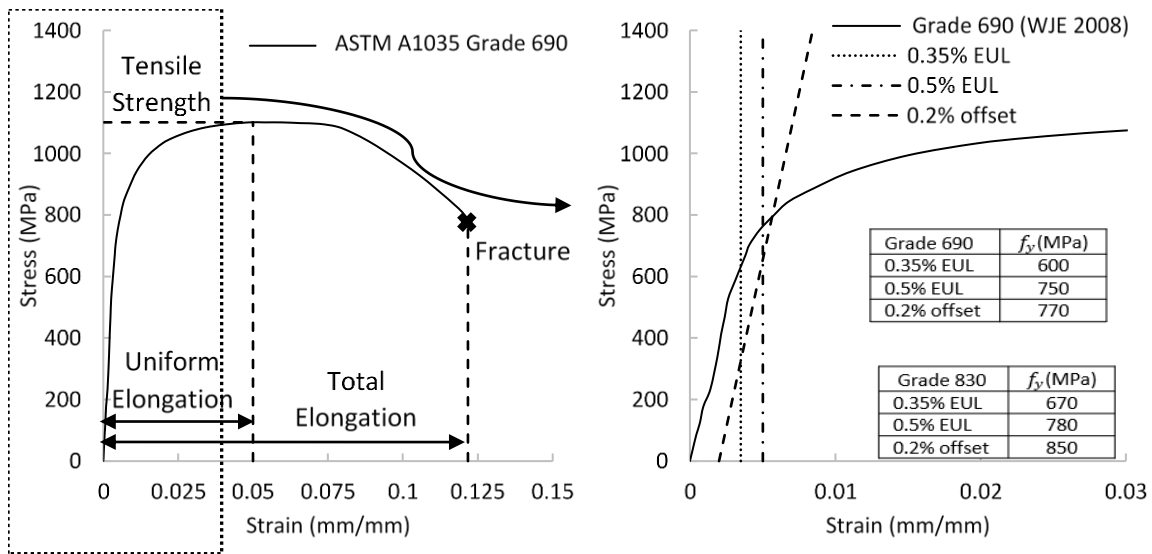


Figure 32: Stress-strain response of ASTM A1035 Grade 690 reinforcing bar.

Table 17: Comparison Between Tensile Properties of ASTM A706 Grade 420 Reinforcement and ASTM A1035 Grade 690 and 830 Reinforcement (ASTM 2016; ASTM 2020b).

Property	ASTM A706 Grade 420	ASTM A1035 Grade 690	ASTM A1035 Grade 830
Yield strength, minimum (MPa)	420	690*	830*
Tensile strength (MPa)	550	1035	1035
Total elongation in 200 mm, minimum			
Bar size:			
10M to 35M (%)	12-14	7	7
45M and 55M (%)	10	6	N.A.

* Based on 0.2% offset method

6.2 Geometry and Design of Prototype Bridge

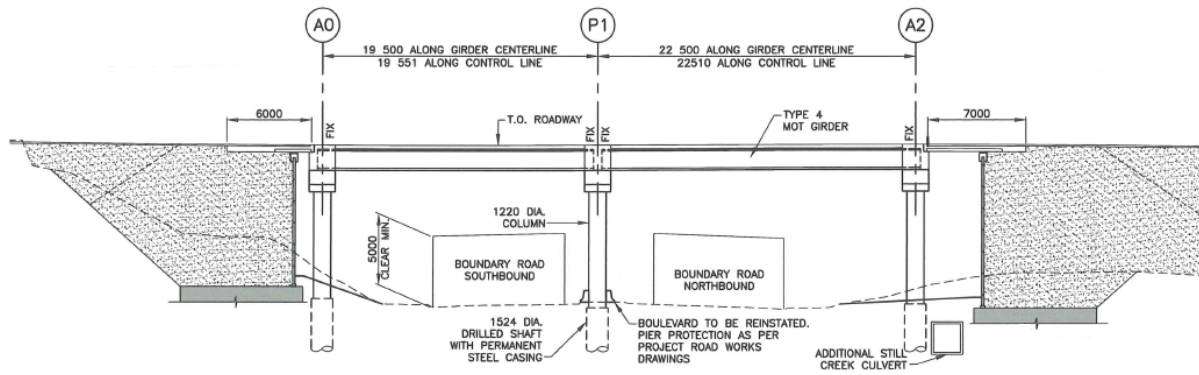
A two-span continuous concrete girder bridge located in Vancouver, British Columbia, Canada was selected for this study. The bridge is representative of the inventory for this particular bridge type of Western Canada. The configuration of the bridge is illustrated in Figure 33. The bridge has two spans, which are 19.5 and 22 m long for a total length of 41.5 m. The width of the bridge deck is 10 m, which is composed of a 235 mm thick composite reinforced concrete deck supported by 3 MOTI Type IV precast

pretensioned I-girders (D202 2006). The deck has a full integral connection at both abutment and pier locations, making the bridge a continuous bridge. The bridge bent consists of a single circular column 1.22 m in diameter and 8.8 m in height. The total superstructure self-weight from the two half spans carried by the pier is 2450 kN. The material properties used in the original design were $f_y = 420$ MPa and $f'_c = 35$ MPa. In the original design, the column reinforcement consists of 22-35M longitudinal reinforcement and a 20M spiral with a pitch of 75 mm in the plastic hinge region. The column is continued to the ground as cast-in-drilled-hole pile shaft with permanent steel casing; however, since the effect of the foundation system on the seismic performance of the bridge is beyond the scope of this study, the foundation is modeled as fixed at the column-shaft interface, as outlined in the subsequent sections. The seismic response of the bridge was studied using a single-degree-of-freedom system (SDOF) model. Hence, the bent of the bridge was represented by a single column with tributary mass from the two adjacent half spans of the superstructure. The spectral accelerations for a probability of exceedance of 2% in 50 years were extracted from the 2015 National Building Code of Canada (NBCC 2015) for the bridge location in Vancouver, British Columbia, and used in the elastic dynamic analysis to compute the design lateral elastic earthquake forces.

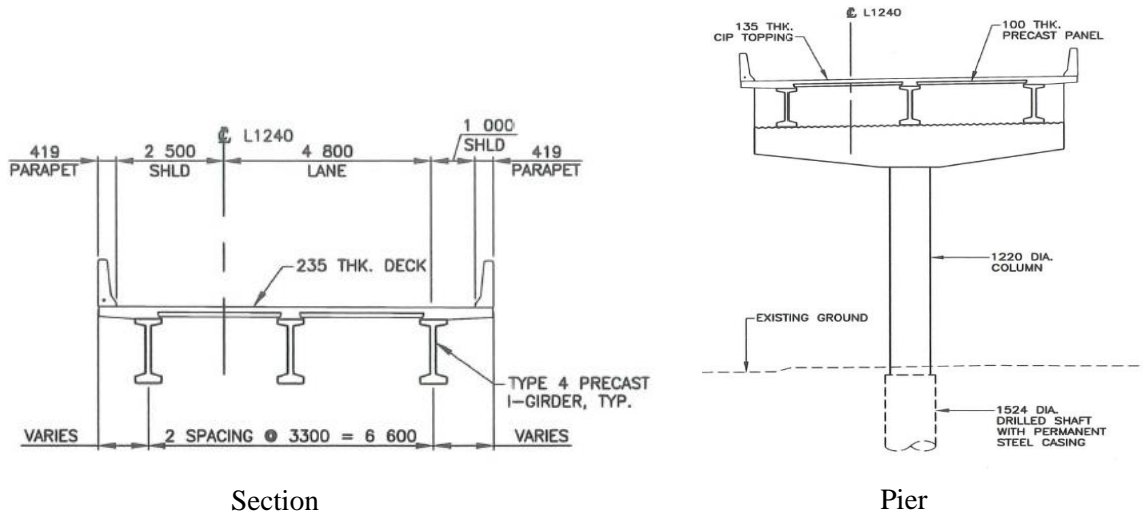
In this study, section diameter of 1220 mm and 914 mm, reinforcement with f_y of 420, 690, and 830 MPa, and concrete with f'_c of 50 and 80 MPa are considered, resulting in a total of 12 different sections. The middle pier of the considered bridge was redesigned using these proposed sections. The force-based design procedure was initially validated by designing the bridge pier using its original section and material properties described earlier. A Response modification factor, R , of 4 and an importance factor, I_E , of 1.5 were assigned in the design of all sections, as prescribed in the CHBDC (CSA 2019b). A thorough review of bent column SLS stress and cracking requirements for non-seismic loads per CHBDC (CSA 2019b) is beyond the scope of this manuscript. However, the seismic performance of the bridge pier at different hazard levels was compared against the performance criteria of the CHBDC (CSA 2019b) as part of the performance-based design framework. The sections were labeled to indicate section diameter,

reinforcement strength, and concrete strength—for example, 1220-420-50 refers to bridge pier section with 1220 mm diameter, 420 MPa reinforcement yield strength, and 50 MPa concrete compressive strength. Table 18 lists these sections, along with the output of the force-based design (design base shear (V), longitudinal reinforcement ratio (ρ_l), and spiral transverse reinforcement ratio (ρ_s)). Axial load ratio, which is defined as the ratio of the applied load (P), to the gross area of section (A_g) multiplied by f'_c , ranged between 2.7% and 7.7% due to the change in diameter, ϕ , and f'_c . The axial load ratios are close to 5% which is the approximate average design axial load ratio of bridge piers in seismic regions (Sritharan et al. 2007). Besides, the aspect ratio, which is the ratio of the height to diameter of the column, was more than 4 for all the sections, ensuring flexure-controlled failure. 1220-420-50 and 914-420-50 sections are considered as the reference sections for bridge piers with diameters of 1220 and 914 mm, respectively. Sections incorporating steel reinforcement and concrete with greater f_y and f'_c , respectively, were characterized by lower longitudinal reinforcement ratios. However, this observation was not clear in sections with a diameter of 1220 mm due to the minimum longitudinal reinforcement requirement (0.8%) set by CHBDC (CSA 2019b) which restricted further reductions in ρ_l in sections reinforced with HSS. In addition, the design of the prototype bridge pier indicates that the increase in yield strength of the reinforcement is more effective than the increase in concrete compressive strength in reducing the required ρ_l . For example, ρ_l of 914-690-50 section is reduced by 51%, whereas ρ_l of 914-420-80 section is reduced by only 8%, when compared to 914-420-50, i.e. the control section. However, the effectiveness of utilizing higher strength reinforcement on ρ_l decreases with the increase in yield strength. For instance, ρ_l of 914-690-50 is less than that of 914-420-50 by 51%, while ρ_l of 914-830-50 is less than that of 914-690-50 by 17%. Therefore, switching from Grade 690 to Grade 830 is not as beneficial as switching from Grade 420 to Grade 690, i.e. from conventional steel to HSS. Also, from Table 18, it can be noted that 914-690-50 requires almost the same ρ_l as that of 1220-420-50, indicating that, with the use of HSS, it is possible to reduce the section diameter without increasing ρ_l . On the other hand, the amount of required transverse reinforcement was influenced by the change in f'_c and f_y . Spiral reinforcement was determined following

clause 4.7.5.2.5, i.e. transverse reinforcement for confinement at plastic hinge regions, of CHBDC (CSA 2019b). The increase in f'_c resulted in increasing the required amount of transverse reinforcement, which is necessary to maintain the same level of ductility as reported by Cusson et al. (1994) and Razvi et al. (1994). Utilizing transverse reinforcement with f_y of 690 and 830 MPa reduced ρ_s by 40% and 50%, respectively.



General Elevation



Section

Pier

Figure 33: Selected bridge configuration (dimensions are in mm) (reproduced with permission from the project team).

Table 18: Summary of the Force-Based Design Results.

Section	\varnothing (mm)	f_y (MPa)	f'_c (MPa)	$P/A_g f'_c$ (%)	V (kN)	ρ_l (%)	ρ_s (%)
1220-420-35*	1220	420	35	6.0	324	1.9	1.5
1220-420-50	1220	420	50	4.3	334	1.9	1.5
1220-420-80	1220	420	80	2.7	343	1.7	2.4
1220-690-50	1220	690	50	4.3	315	1.0	0.9
1220-690-80	1220	690	80	2.7	334	1.0	1.4
1220-830-50	1220	830	50	4.3	315	1.0	0.75
1220-830-80	1220	830	80	2.7	334	1.0	1.2
914-420-50	914	420	50	7.7	238	3.7	1.5
914-420-80	914	420	80	4.8	238	3.4	2.4
914-690-50	914	690	50	7.7	210	1.8	0.9
914-690-80	914	690	80	4.8	219	1.7	1.4
914-830-50	914	830	50	7.7	200	1.5	0.75
914-830-80	914	830	80	4.8	210	1.4	1.2

* Original section of the bridge pier.

6.3 Finite Element Modeling and Model Verification

SeismoStruct (Seismosoft 2018), a finite-element package featuring fiber-based modeling for structural analysis, is used in this study to perform the static pushover and nonlinear dynamic time history analysis. The bridge pier was modeled using inelastic displacement-based elements (DBEs), that approximate the response by enforcing constant axial deformation and linear curvature distribution along the element length. Therefore, when utilizing such elements, the member is often subdivided into members of smaller lengths to achieve higher accuracy, particularly in the plastic hinge region. Figure 34 shows the finite element model of the bridge, along with the discretized section. Rayleigh damping with initial stiffness was used to model the energy dissipation in the bridge pier. To simulate bar-slip rotations, an elastic rotational spring was used at the column end, as shown in Figure 34. The rotational stiffness of the bond-slip springs (K_{SE}) is given by the following equation:

$$K_{SE} = \frac{2M_y}{\phi_y l_{sp}} \quad (55)$$

where M_y is the yield moment of the section, ϕ_y is the corresponding yield curvature, and l_{sp} is effective strain penetration depth at bar yield. l_{sp} is defined as follows (Elwood and Eberhard 2009):

$$l_{sp} = \frac{1}{3.2} \frac{f_y}{\sqrt{f'_c}} d_b \quad (56)$$

where d_b is the diameter of the longitudinal rebar. Menegotto-Pinto steel model (Menegotto and Pinto 1973) was used to model the material properties of the reinforcing steel. In the case of HSS, the model parameters were modified to produce a similar stress-strain relationship to that of HSS. Several researchers have successfully utilized the Menegotto-Pinto steel model to evaluate the seismic behavior of structures incorporating HSS reinforcement (Billah and Alam 2013; Laughery 2016). Nevertheless, the accuracy of the models utilized in this paper was validated using experimental results of concrete columns reinforced with conventional steel and HSS and tested under cyclic loading. Normal-strength concrete material properties were incorporated into the model using Mander et al. (1988) nonlinear concrete model, while the HSC properties were incorporated into the model using Kappos and Konstantinidis (1999). The 2450 kN self-weight of the superstructure is applied on top of the column, as shown in Figure 34. A fixed connection, i.e. all degrees-of-freedom are restrained, is assigned to the column base. The strains in the unconfined concrete and steel reinforcement fibers were measured at the two extreme points of the section to capture the maximum tensile and compression strains in the steel reinforcement and concrete, respectively.

The numerical models described above were validated with experimental results of concrete columns reinforced with conventional steel (Moyer and Kowalsky 2003), and HSS (Restrepo et al. 2006). Table 19 summarizes the main properties of the two columns used in the validation process. The reader may refer to the corresponding research work for additional details on the experimental tests. Figure 35 shows a comparison between the experimental and numerical responses for columns reinforced with conventional steel and HSS. It is observed that for the two specimens, the maximum shear force and displacement are predicted within 10% error and strength decay, stiffness degradation, and energy dissipation are accurately reflected in the models. Therefore, the numerical models developed in this study are valid and capable of capturing the dynamic response of columns incorporating materials of different strengths. It must be noted that in the validation models, the effect of the geometric nonlinearity, i.e. P-delta effect, is excluded since the load-displacement responses presented in the corresponding papers are based

only on loads measured from the horizontal actuators. However, in the subsequent analysis of this paper, the effect of geometric nonlinearity is included in the analysis due to the critical height of the bridge pier where such effect is expected to noticeably contribute to the response.

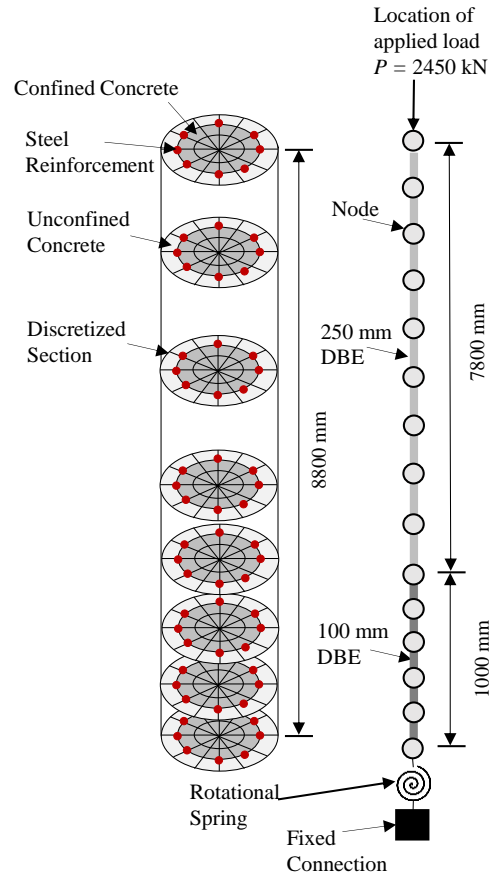


Figure 34: Finite element modeling of the bridge pier.

Table 19: Properties of the Validated Experimental Tests.

Experimental Program	\varnothing (m)	H (m)	f'_c (MPa)	f_y (MPa)	f_{ul} (Mpa)	ε_{su} (%)	f_{yh} (MPa)
Moyer and Kowalsky (2003)	0.457	2.44	32.7	565.4	696.4	-	434.4
Restrepo et al. (2006)	0.914	2.9	56.5	648.1	1067.3	5.2	827.4

Here, \varnothing = diameter of the column; H = column's height; f'_c = nominal concrete compressive strength; f_y = longitudinal reinforcement yield stress; f_{ul} = longitudinal reinforcement ultimate stress; ε_{su} = ultimate steel strain in longitudinal reinforcement; and f_{yh} = transverse spiral yield stress.

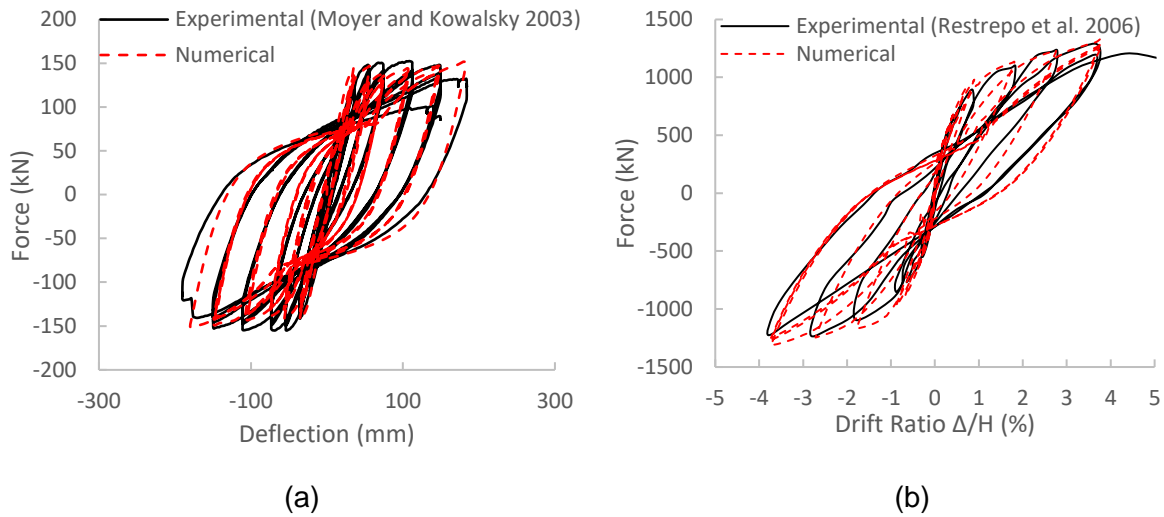


Figure 35: Comparison of experimental and numerical responses of column reinforced with (a) conventional steel, and (b) ASTM A1035 Grade 690 steel.

6.4 Fragility Function Methodology

Fragility curves are critical in the seismic risk assessment of bridges since they describe the level of damage to the bridge components when subjected to different levels of ground shaking. Direct comparison of vulnerability functions or so-called fragility curves of different bridge design alternatives is an effective approach in selecting the optimal bridge design. However, constructing these curves might not be practical (for certain cases) due to the amount of time and effort required to develop them, as will be illustrated in this section. A fragility function represents the conditional probability of meeting or exceeding a given damage state (or performance) for a given ground motion intensity measure. This conditional probability function can be expressed as follows:

$$Fragility = P[LS|IM = y] \quad (57)$$

where LS is the limit state (or performance) or level of damage to the bridge component; IM is the ground motion intensity measure; and y is the realized condition of the chosen ground motion intensity measure.

The realization of the ground motion intensity measure is normally achieved by expressing y in terms of peak ground acceleration or spectral acceleration at the fundamental period. The initial step involves

defining a suite of ground motions representing the geographic area of interest and capturing the uncertainties associated with the magnitude and epicentral distances. Details related to the suite of ground motions selected in this study are presented in the next section. The earthquake ground motion records are scaled to various levels of excitation as part of an incremental dynamic analysis (*IDA*). In the *IDA*, non-linear time history analyses are performed on the bridge model incorporating different levels of excitations of each earthquake record in the selected suite of ground motions to capture the peak structural response of the column. After that, a probabilistic seismic demand model (*PSDM*) is established utilizing regression analysis of peak structural response or so-called engineering demand parameter (*EDP*) and ground intensity measure (*IM*). The study presented herein considers the drift ratio as the *EDP*, and the peak ground acceleration (*PGA*) as the *IM*. The *PGA* has been selected as the *IM* based on the recommendation of Billah et al. (2013) and Padgett et al. (2008). According to Padgett et al. (2008), contrary to former studies that have selected spectral quantities as the most appropriate *IMs*, on the basis of efficiency, practicality, proficiency, sufficiency, and hazard computability, *PGA* was found to be the optimal *IM* for these bridge portfolios. Besides, according to Chen (2020), the optimal intensity measure in probabilistic seismic demand models of tall-pier bridges subjected to near-fault ground motions is *PGA*. A linear regression of the logarithms of the *EDP* and *IM* can be utilized to describe the probabilistic seismic demand model as given in Eq. 58 (Cornell et al. 2002).

$$\ln(EDP) = \ln(a) + b \ln(IM) \quad (58)$$

where *a* and *b* are unknown coefficients which can be determined from the regression analysis. The dispersion of the *EDP* given a specified *IM* ($\beta_{EDP|IM}$) is

$$\beta_{EDP|IM} = \sqrt{\frac{\sum_{i=1}^N (\ln(EDP) - \ln(aIM^b))^2}{N-2}} \quad (59)$$

where *N* is the total number of simulations. The structural capacity often referred to as limit or damage state, is normally established using expert-, experimentally-, and/or analytically-based approaches. In this study, the limit states are extracted from CHBDC (CSA 2019b). The performance criteria for different performance levels (limit states) are given in Table 20. This table provides a general description for each

limit state in terms of serviceability and damage, along with performance criteria specifically applied to concrete structures since the bridge piers analyzed in this study are reinforced concrete columns.

After establishing the *PSDMs* and limit states, the fragility curve, i.e. the conditional probability of entering a *LS* given an *IM* is generated using Eq. 60 (Nielson 2005).

$$P[LS|IM] = \phi \left[\frac{\ln(IM) - \ln(IM_n)}{\beta_{comp}} \right] \quad (60)$$

where $\phi []$ is the standard normal cumulative distribution function; and $\ln(IM_n)$ is the median value of the intensity measure for the selected damage state; and β_{comp} is the dispersion component. The $\ln(IM_n)$ is related to the capacity of the section since it is established based on the capability of the section in meeting the performance criteria presented in Table 20. $\ln(IM_n)$ and β_{comp} can be computed as follows:

$$\ln(IM_n) = \frac{\ln(S_c) - \ln(a)}{b} \quad (61)$$

$$\beta_{comp} = \frac{\sqrt{\beta_{EDP|IM}^2 + \beta_C^2}}{b} \quad (62)$$

where S_c is the median value for the structural capacity defined for the chosen limit state; and β_C is the dispersion value of the chosen limit state; a and b are the coefficients determined from the regression analysis. β_C is computed using Eq. 63.

$$\beta_C = \sqrt{\ln(1 + COV^2)} \quad (63)$$

where COV is the coefficient of variation which is incorporated to account for some degree of uncertainty associated with each limit state. Such uncertainty mainly arises from the variation in material properties and geometry of the structure. The COV is normally assumed to be smaller for minimal and repairable limit states as compared to extensive and probable replacement limit states. In this research, and as recommended by Nielson (2005), the COV for the minimal and repairable limit states is taken as 0.25, while the COV for the extensive and probable replacement limit states is taken as 0.5.

Table 20: Performance Criteria (CSA 2019b).

Service	Damage	Concrete Structures Criteria
Immediate	Minimal damage	$\varepsilon_c \leq 0.006$
Limited	Repairable damage	$\varepsilon_s \leq 0.01$ $\varepsilon_s \leq 0.025$
Service disruption	Extensive damage	$\varepsilon_s \leq 0.05$ $\varepsilon_{cc} \leq 0.8\varepsilon_{cu}$
Life safety	Probable replacement	$\varepsilon_s \leq 0.075$ $\varepsilon_{cc} \leq \varepsilon_{cu}$

Note: ε_c = concrete compressive strain; ε_s = flexural reinforcing steel strain; ε_{cc} = confined concrete strain; and ε_{cu} = ultimate confined concrete strain; d_b = diameter of the flexural reinforcing steel.

6.5 Selection of Ground Motions

A suite of twenty near-fault ground motions having a range of magnitude and *PGA* values representative of medium and strong ground motions is selected. Table 21 presents the main characteristics of the selected ground motions. The *PGA* of the selected ground motions ranges from 0.37g to 1.07g, where g is the gravitational acceleration. All of the selected ground motions are characterized with an epicentral distance less than 10 km, and therefore, are representative of the near-field effects (CSA 2019b). Earthquakes generated in the vicinity of an active fault constitute a primary seismic hazard due to the distinctive features of these earthquakes when compared to the far-fault ones, and thus have received much attention in recent years (Chopra and Chintanapakdee 2001). Near-fault earthquakes normally contain powerful long-period pulses and permanent ground displacements (Somerville 2002). In near-fault earthquakes, high seismic energy from the fault is transmitted to the structure in the form of a single large pulse of motion in the initial phase of the record. Retrofitted bridge bents (Billah et al. 2013) and cable-supported bridges (Soyluk and Karaca 2017) were more vulnerable when subjected to near-fault ground motions than far-fault ground motions. Major earthquakes that have occurred in western Canada in the past 150 years had magnitudes in the range of 5.7-8.6 (Milne et al. 1978). The magnitudes of the selected earthquakes in this study range from 6.7 to 7.4. The two horizontal components of each record are considered. These records were extracted from the Pacific Earthquake Engineering Research (PEER) Center earthquake database (PEER 2011). Before utilizing them in the non-linear time history analysis, the

records were spectrally matched with the uniform hazard design response spectra of Vancouver for a 2% probability of exceedance in 50 years using the wavelets algorithm by Hancock et al. (2006) available on SeismoMatch (Seismosoft 2016). The values in the response spectra are for the firm ground which is classified as soil class C as per the NBCC (2015) and it was assumed to have 5% damping. Figure 36 (a) shows the acceleration response spectra of each original ground motion used in this study along with the mean (μ) and μ plus or minus one standard deviation (σ) acceleration response spectra. Similarly, Figure 36 (b) shows the acceleration response spectra of each spectrally matched ground motion, along with the μ and $\mu \pm \sigma$.

Table 21: Characteristics of the Selected Ground Motion Records.

No.	Earthquake	Year	Magnitude	Station	Epicentral Distance (km)	Closest Distance to the Earthquake Rupture Plane (km)	PGV (cm/sec)	PGA (g)
1	Tabas	1978	7.35	Tabas	1.79	2.05	98.8	0.90
2	Tabas	1978	7.35	Tabas	1.79	2.05	123.4	0.96
3	Loma Prieta	1989	7	Corralitos	0.16	3.85	56.0	0.7
4	Loma Prieta	1989	7	Corralitos	0.16	3.85	47.6	0.46
5	Loma Prieta	1989	7	LGPC	0	3.88	96.1	0.67
6	Loma Prieta	1989	7	LGPC	0	3.88	51.6	0.37
7	C. Mendocino	1992	7.1	Petrolia	0	8.18	49.3	0.63
8	C. Mendocino	1992	7.1	Petrolia	0	8.18	88.5	0.65
9	Landers	1992	7.3	Lucrene	2.19	2.19	133.4	0.69
10	Landers	1992	7.3	Lucrene	2.19	2.19	28.1	0.79
11	Kobe	1995	6.9	KJMA	0.94	0.96	91.1	1.07
12	Kobe	1995	6.9	KJMA	0.94	0.96	76.1	0.56
13	Kobe	1995	6.9	Takatori	1.46	1.47	241.4	0.77
14	Kobe	1995	6.9	Takatori	1.46	1.47	169.0	0.42
15	Northridge	1994	6.7	Rinaldi	0	6.5	148.0	0.87
16	Northridge	1994	6.7	Rinaldi	0	6.5	74.8	0.38
17	Northridge	1994	6.7	Olive View	1.74	5.3	38.8	0.72
18	Northridge	1994	6.7	Olive View	1.74	5.3	64.7	0.58
19	Erzican	1992	6.7	Erzincan	0	4.38	78.2	0.42
20	Erzican	1992	6.7	Erzincan	0	4.38	107.14	0.45

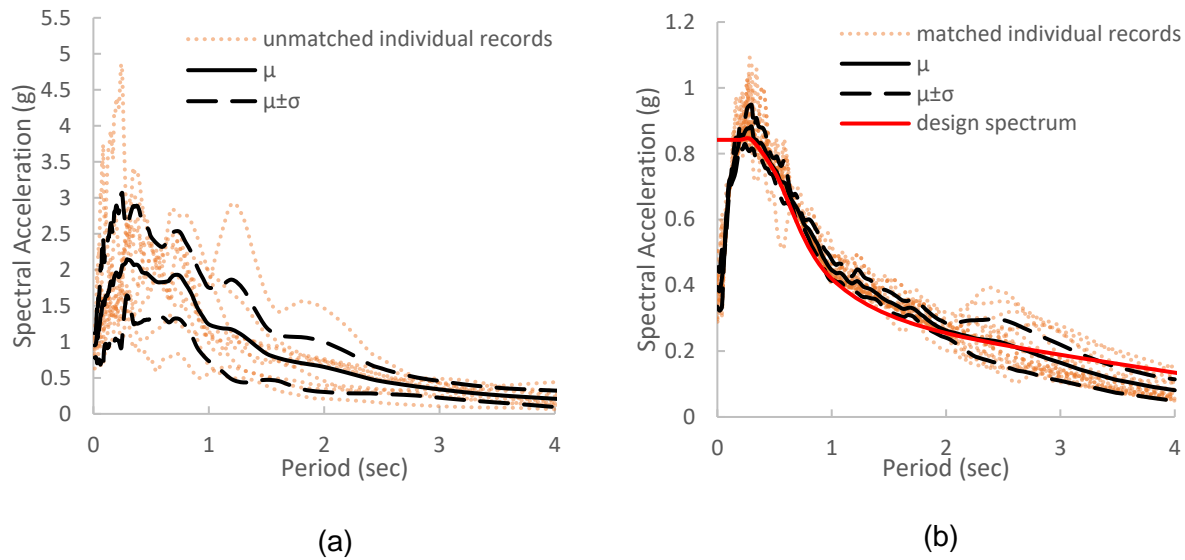


Figure 36: Response spectra, mean response spectra, and mean response spectra \pm one standard deviation of response spectra of (a) original ground motions and (b) spectrally matched ground motions

6.6 Results

6.6.1 Static-push Over Analysis

Static pushover analysis has been performed to assess the performance of the bridge pier sections when subjected to constant gravity load and monotonically increasing lateral displacement pattern of constant shape. Figure 37 illustrates the base shear vs. top displacement plots, i.e. pushover curves, for all the sections. Table 22 provides a summary of the main characteristics including initial stiffness (K_i), maximum load (F_m), ultimate load (F_u), drift ratio at yield (Δ_y/H), drift ratio at ultimate (Δ_u/H), displacement ductility (μ_Δ), curvature at yield (ϕ_y), curvature at ultimate (ϕ_u), curvature ductility (μ_ϕ), and ultimate to displacement demand ratio ($\Delta_u/\Delta_{2\%}$) extracted from the pushover curve for each section. The drift ratio at yield (Δ_y/H) and ultimate (Δ_u/H) are defined as the ratio of lateral top displacement at yield (Δ_y) and ultimate (Δ_u), respectively, to the height of the pier (H). The ultimate displacement to displacement demand ratio ($\Delta_u/\Delta_{2\%}$) is the ratio of Δ_u to the displacement demand at hazard level of 2% probability of exceedance in 50 years. F_m is the maximum recorded load, whereas F_u is the load established

at 10% drop in F_m . In the pushover analysis, bridge piers were subjected to a target drift demand of 9% to determine their ultimate capacity. The ultimate lateral load capacity is taken as the point corresponding to a 10% reduction in strength compared to the peak load as per Elnashai and Sarno (2008). A larger target drift was chosen to ensure that all bridge piers experience a 10% reduction in strength beyond their peak loads. The yield drift is defined as the drift corresponding to the yield point of an equivalent elasto-plastic system with the same energy absorption as the real system (Park 1988). μ_Δ and μ_ϕ are defined as the ratio of displacement and curvature at ultimate, respectively, to the corresponding values at yield. Sections reinforced with steel having higher yield strength and cast with concrete having higher concrete compressive strength attained higher F_m and F_u when compared to the reference section, i.e. section with $f_y = 420$ MPa and $f'_c = 50$ MPa. Section 1220-830-80 attained a F_m of 745 kN which is 30.7% higher than that attained by section 1220-420-50. Sections reinforced with Grade 690 and 830 steel were characterized with higher drift ratio at yield but lower drift ratio at ultimate when compared to sections reinforced with Grade 420 steel. The higher drift ratio at yield in such sections is attributed to the higher strain levels required for Grade 690 and 830 steel to yield when compared to Grade 420 steel. Sections incorporating HSS reinforcement generally are characterized by lower displacement and curvature ductility when compared to the sections reinforced with conventional steel. This is primarily due to the higher load required to yield Grade 690 and 830 steel and the lower ultimate rupture strain when compared to Grade 420 steel. Sections 1220-690-50 and 1220-830-50 are characterized by lower displacement ductility than section 1220-420-50 by 40% and 50%, respectively. Similarly, the curvature ductility in these sections is reduced by approximately the same percentages. Sections with higher concrete compressive strength exhibited less ductile behavior. The displacement ductility of sections with $f'_c = 80$ MPa decreased by 2%-22% when compared to that of sections with $f'_c = 50$ MPa. The ratio of Δ_u to $\Delta_{2\%}$ tends to decrease in sections incorporating HSS, and this is primarily due to the decrease in Δ_u in such sections when compared to sections reinforced with conventional steel. For example, introducing HSS in sections 1220-50-690 and 1220-80-830 reduced $\Delta_u / \Delta_{2\%}$ by 19.1 and 16.7%, respectively, when compared to section 1220-50-420.

In addition, the pushover analysis was utilized to evaluate the ability of the proposed sections in meeting the minimum performance requirements set by CHBDC (CSA 2019b). For lifeline bridges, the bridge must be able to sustain minimal damage for an earthquake return period of 475 and 975; and sustain repairable damage for an earthquake return period of 2475 years. The strain limits associated with each damage level have been presented earlier in this chapter in Table 20. In Figure 37, the vertical lines (from left to right) represent the displacement demand for 10, 5, and 2% seismic ground motion probability of exceedance in 50 years, respectively, and the blue icons on the curves represent the different material strain limits. It should be noted that although the bridge pier sections were designed for only a 2% probability of exceedance in 50 years, the 5% and 10% probability of exceedance in 50 years are included in this section for illustrative purposes. It can be seen from Figure 37 that all sections were able to meet the minimum performance requirements. However, in sections incorporating conventional steel reinforcing bars, a steel strain value of 0.01 was reached at a displacement slightly higher than the displacement demand for a 5% probability of exceedance in 50 years, hence indicating an efficient design. As for sections incorporating HSS reinforcing steel bars, drift demands were significantly lower than those at the onset of their corresponding limit states, indicating an inefficient design. Therefore, if a performance-based design was to be undertaken for these sections, the design must be revised to produce a more efficient design, i.e. section with a smaller diameter or less longitudinal reinforcement.

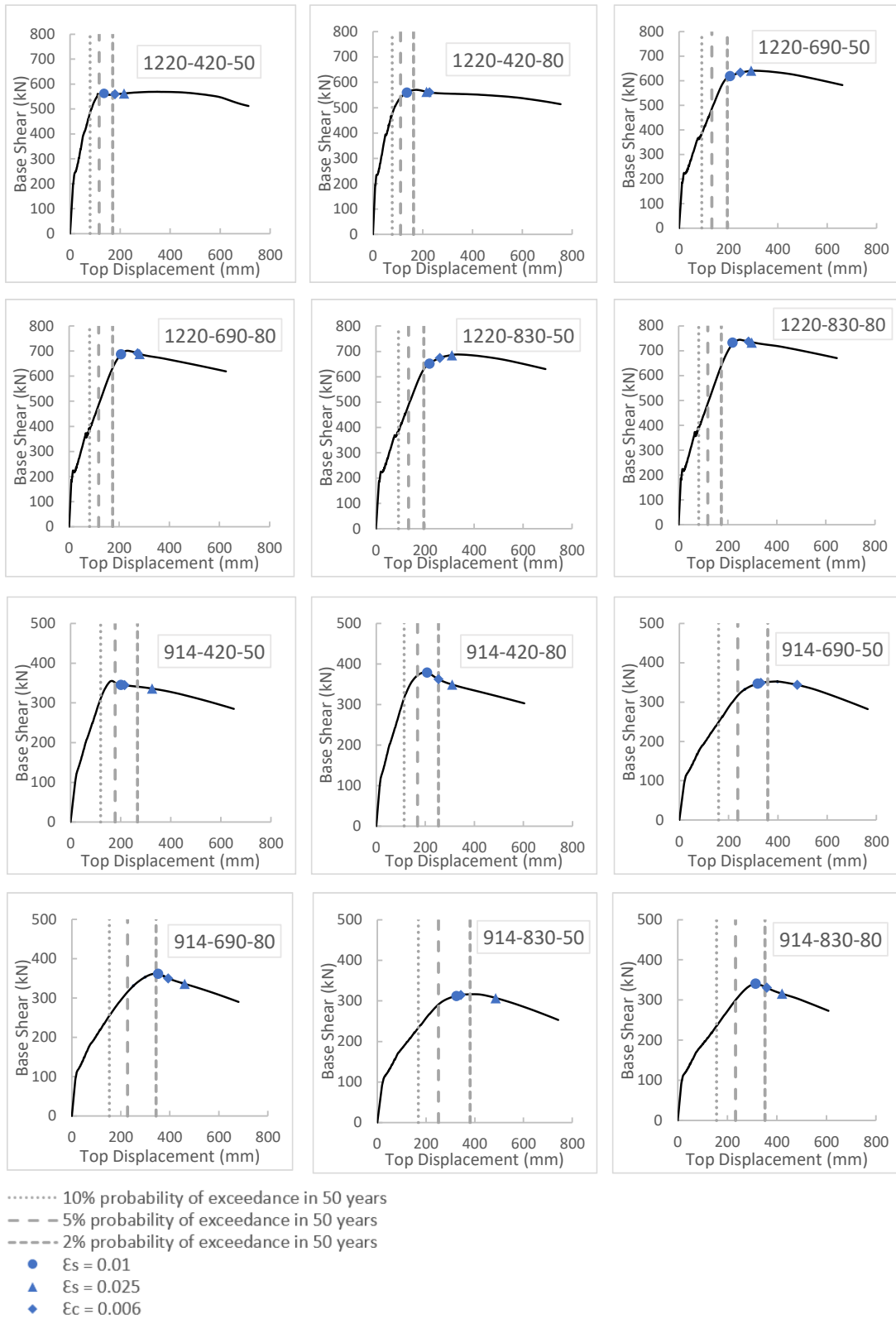


Figure 37: Static pushover curves of all sections.

Table 22: Summary of the Static Pushover Analysis Results.

Section	K_i (kN/mm)	F_m (kN)	F_u (kN)	Δ_y/H (%)	Δ_u/H (%)	μ_Δ	Φ_y ($\times 10^{-6}$ 1/mm)	Φ_u ($\times 10^{-6}$ 1/mm)	μ_ϕ	$\Delta_u/\Delta_{2\%}$ (%)
1220-420-50	16.5	570	512	0.8	8.1	10.6	3.1	94.1	30.8	4.2
1220-420-80	18.3	570	523	0.8	8.0	10.4	2.8	105.6	37.1	4.3
1220-690-50	15.1	641	583	1.2	7.5	6.4	4.6	113.0	24.7	3.4
1220-690-80	16.5	702	631	1.2	6.5	5.5	4.4	96.1	21.9	3.3
1220-830-50	15.3	687	630	1.5	7.9	5.3	5.5	113.3	20.5	3.5
1220-830-80	16.5	745	671	1.4	7.3	5.2	5.2	109.0	20.8	3.7
914-420-50	5.5	355	320	1.2	5.1	4.1	4.3	70.6	16.3	1.7
914-420-80	7.2	380	342	1.2	4.0	3.4	4.2	50.5	12.0	1.4
914-690-50	4.7	353	319	1.9	7.0	3.6	7.0	69.4	9.9	1.7
914-690-80	6.6	365	329	1.8	6.0	3.3	6.7	52.4	7.8	1.5
914-830-50	4.7	317	286	2.2	7.0	3.2	8.4	64.7	7.7	1.6
914-830-80	6.5	341	307	2.2	5.4	2.5	7.8	52.4	6.7	1.3

6.6.2 Seismic Fragility Curves

The fragility curves for all sections generated based on the analytical procedure outlined in an earlier section of this paper are shown in Figure 38. The capacities of the sections corresponding to each damage state were established based on the performance criteria presented in Table 20. For all the sections, the capacities associated with minimal and extensive damage states were governed by the strain in the longitudinal reinforcing steel. The drift ratios corresponding to the four damage states for all the proposed sections are shown in Table 23.

One of the simplest ways of comparing the seismic performance of the sections is to identify the relative change in the median value of the fragility estimate. The percent change in the median values relative to the reference sections is listed in Table 24. For sections with a diameter of 1220 mm, the reference section is 1220-420-50 whereas, for sections with a diameter of 914 mm, the reference section is 914-420-50. A positive percent change in the median indicates a shift in the fragility curve to the right, i.e. less vulnerable section, while a negative percent change in the median value indicates a shift to the left, i.e. more vulnerable section. For each damage state, the section with the largest positive percent difference in the median is the least vulnerable. In Table 24, the section with the largest median improvement for each

damage state is presented in boldface type. Screening of these median value changes for sections with a diameter of 1220 mm indicates that section 1220-830-80 is the least vulnerable for all damage states. As for sections with a diameter of 914 mm, section 914-690-80 is the least vulnerable for the minimal damage state, while section 914-830-50 is the least vulnerable for repairable, extensive, and probable replacement damage states. For minimal and repairable damage states, sections incorporating HSS and HSC are always less vulnerable than the reference section whereas, for extensive and probable replacement damages states, this is not true since some sections are characterized with negative percent change in the median value indicating a more vulnerable section when compared to the reference section. However, it was interesting to observe that all the sections having a negative percent change in the median value, the percent change is relatively small and does not exceed 10%. This appears to be similar to the findings of Billah and Alam (2013) who evaluated the seismic performance of concrete columns in buildings incorporating HPMS. Introducing HSC without altering the grade of steel reinforcement is found to be more effective in sections having a diameter of 1220 mm than sections having a diameter of 914 mm. For example, section 1220-420-80 had a positive percent change in the median value for all damage states, whereas section 914-420-80 had a positive percent change in the median value for only minimal and probable replacement damage states. Based on the previous findings of the fragility assessment, designing bridge piers reinforced with HSS using a response modification factor of 4 yielded sections exhibiting better seismic performance for the minimal and repairable damages states, and comparable seismic performance for extensive and probable replacement damage states when compared to the performance of bridge piers reinforced with conventional steel. Besides, all of the sections incorporating HSS and HSC met the criteria of the performance-based design prescribed in the CHBDC (CSA 2019b). However, in certain sections, especially those with a diameter of 914 mm, displacement ductility capacity was less than 4, making them unsuitable for a force reduction factor of 4. For this reason, further research work is warranted before incorporating the response modification factor into the CHBDC applicable to bridge piers incorporating HPMS to examine a wider range of column diameters, concrete compressive strengths, ground motions, and possibly other bridge bent configurations.

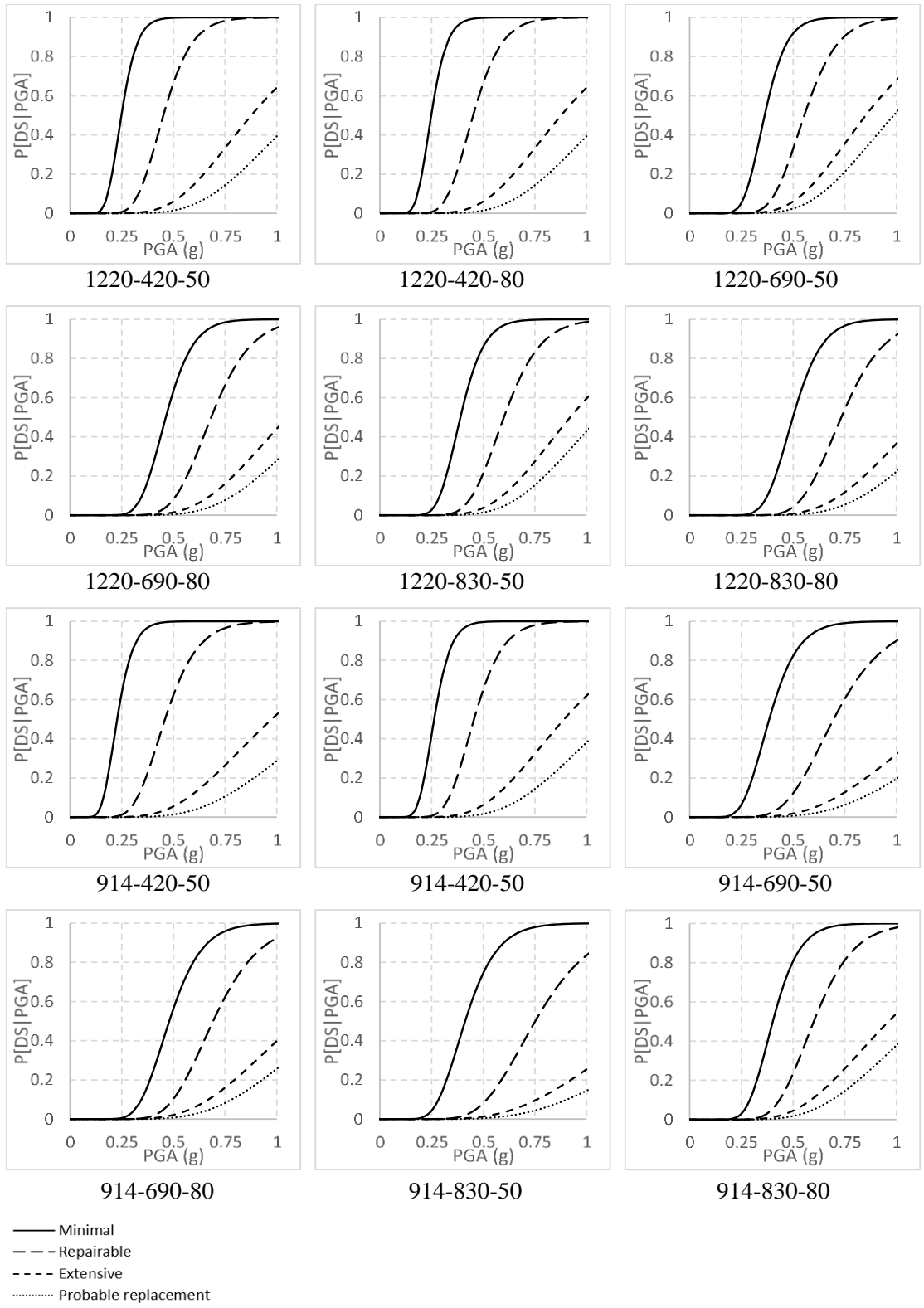


Figure 38: Fragility curves of all sections.

Table 23: Drift Ratio Corresponding to Minimal, Repairable, Extensive, and Probable replacement Damage States.

Section	Damage States			
	Minimal	Repairable	Extensive	Probable Replacement
	Drift Ratio (%)			
1220-420-50	1.5	2.5	4.1	4.9
1220-420-80	1.5	2.4	4.0	4.7
1220-690-50	2.4	3.3	4.8	5.3
1220-690-80	2.4	3.2	4.5	5.0
1220-827-50	2.5	3.5	5.0	5.6
1220-827-80	2.5	3.4	4.7	5.2
914-420-50	2.3	3.7	6.2	7.3
914-420-80	2.4	3.5	5.8	6.8
914-690-50	3.6	5.4	8.0	8.9
914-690-80	4.0	5.2	7.3	8.1
914-827-50	3.7	5.5	8.0	9.0
914-827-80	3.6	4.8	6.8	7.5

Table 24: Percent Difference in Fragility Medians PGA for All Sections Relative to the Reference Sections.

Section	% Difference in median PGA from reference section			
	Minimal	Repairable	Extensive	Probable Replacement
1220-420-50	-	-	-	-
1220-420-80	+16	+12	+10	+9
1220-690-50	+44	+21	-2	-9
1220-690-80	+84	+50	+20	+11
1220-830-50	+58	+32	+5	-3
1220-830-80	+99	+59	+29	+19
914-420-50	-	-	-	-
914-420-80	+14	-0	-10	+3
914-690-50	+66	+51	+23	+36
914-690-80	+109	+51	+10	+19
914-830-50	+79	+64	+34	+47
914-830-80	+74	+31	-4	+3

6.7 Assessment of Members Inelastic Rotation and Ductility Capacity

The applicability of utilizing concentrated plasticity elements with predefined plastic hinge length in predicting the inelastic rotation and ductility capacity of concrete columns incorporating HPMs was assessed. An assessment of members' inelastic rotation and ductility capacity was carried out based on the procedure proposed by Priestley et al. (1996). The procedure requires establishing a bilinear approximation to the moment-curvature relationship for each section. The equivalent yield curvature ϕ_y is measured by extrapolating the line joining the origin and conditions at first yield, to the nominal moment capacity M_n . The moment-curvature relationships for sections having diameters of 1220 and 914 mm are plotted in Figures 39 (a) and (b), respectively. The plastic curvature capacity ϕ_p , which is the difference between the ultimate curvature ϕ_u and the yield curvature ϕ_y , is assumed to be constant over the equivalent plastic hinge length L_p . According to Priestley et al. (1996), L_p may be approximated as

$$L_p = 0.08L + 0.022f_{ye}d_{bl} \geq 0.044f_{ye}d_{bl} \quad (64)$$

where L is the distance from the critical section of the plastic hinge to the point of contraflexure and d_{bl} is the diameter of the longitudinal reinforcement. The plastic rotation θ_p is given as follows:

$$\theta_p = L_p\phi_p \quad (65)$$

The curvature ductility μ_ϕ , as defined earlier, is the ratio of curvature at ultimate to the curvature at yield. The results of the member inelastic rotation and ductility assessment based on Priestley et al. (1996) procedure are summarized in Table 25. According to Table 25, sections reinforced with HSS appear to be significantly less ductile than sections reinforced with conventional steel. The curvature ductility for sections with $f_y = 690$ and 830 MPa and $f'_c = 50$ and 80 MPa ranges from 14.8 to 20.7 with an average value of 17.4, while the curvature ductility for sections with $f_y = 420$ MPa and $f'_c = 50$ or 80 MPa ranges from 28.1 to 33.5 with an average value of 30. Increasing the concrete compressive strength only without altering the reinforcement yield strength has little to no impact on the curvature ductility of the column. Although the curvature ductility values generated based on Priestley's procedure (presented in Table 25) were inconsistent with those generated from the pushover analysis in which distributed plasticity elements

were utilized (presented in Table 22), both led to the same conclusion regarding the effect of introducing HSS and HSC on the ductility of the columns. The differences between ductility capacity measured from the pushover analysis and that computed using Priestley et al. (1996) model are primarily due to the inaccuracy associated with establishing the plastic hinge length for columns reinforced with HSS. According to Restrepo (2006), using the Priestley equation to calculate the plastic hinge length in columns reinforced with HSS underestimates the plastic hinge length measured experimentally by at least 40%. Further future research work is required to re-evaluate the plasticity and strain penetration coefficients in the plastic hinge length equation to improve the accuracy of the equation when being applied to members reinforced with HSS.

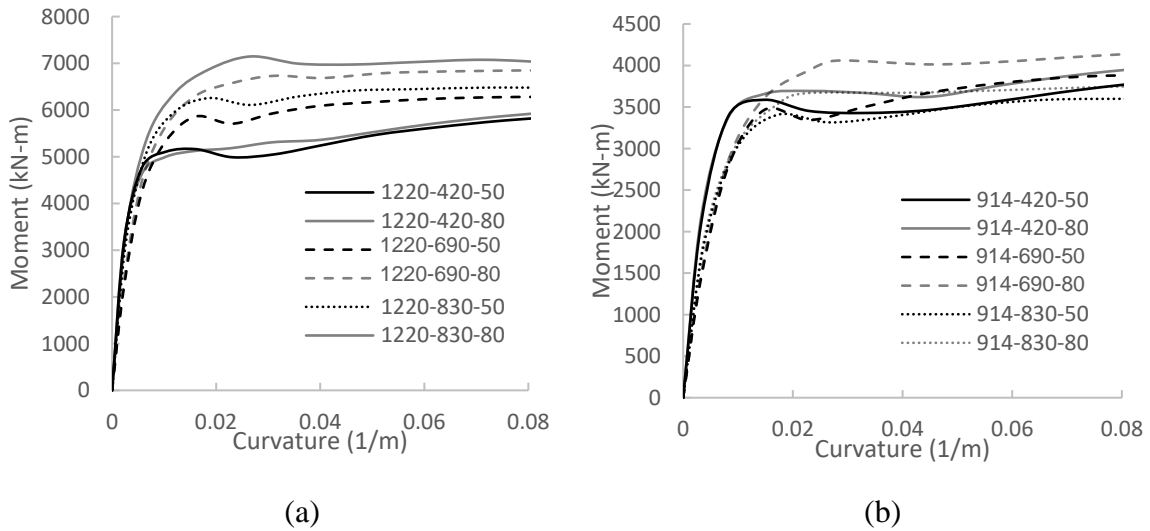


Figure 39: Moment-curvature relationships of bridge pier sections with diameter of (a) 1220 mm and (b) 914 mm.

Table 25: Measured Properties Based on Approach Proposed by Priestley et al. (1996).

Section	Φ_y ($\times 10^{-6}$ 1/mm)	M_n ($\times 10^6$ N-mm)	Φ_u ($\times 10^{-6}$ 1/mm)	M_u ($\times 10^6$ N-mm)	Φ_p ($\times 10^{-6}$ 1/mm)	μ_ϕ	L_p (mm)	θ_p (rad)
1220-420-50	3.0	4900	88.9	5882	85.9	29.6	1018	0.09
1220-420-80	3.1	4950	102.8	6141	99.7	33.5	1018	0.10
1220-690-50	4.3	5700	88.4	6278	84.1	20.7	1086	0.09
1220-690-80	4.3	6400	88.4	6842	84.1	20.5	1086	0.09
1220-830-50	5.5	6200	86.3	6471	80.8	15.8	1162	0.09
1220-830-80	5.2	6800	86.3	7075	81.1	16.5	1162	0.09
914-420-50	4.4	3400	126.6	3885	122.2	28.7	1018	0.12
914-420-80	4.2	3500	117.8	4128	113.6	28.1	1018	0.12
914-690-50	6.9	3600	126.6	3912	119.7	18.3	1086	0.13
914-690-80	6.5	3900	107.8	4184	101.3	16.5	1086	0.11
914-830-50	8.3	3400	123.6	3621	115.3	14.8	1162	0.14
914-830-80	7.8	3600	125.5	3767	117.7	16.0	1162	0.14

6.8 Summary

In this chapter, a coordinated analytical and numerical research program is conducted to evaluate the seismic performance of an existing bridge in Vancouver, British Columbia when different combinations of HSS and HSC are incorporated into its middle pier. The following conclusions are drawn:

1. Bridge piers designed based on the force-based design approach and reinforced with HSS are characterized with less amount of longitudinal and transverse reinforcement steel when compared to those reinforced with conventional steel.
2. Based on the static pushover analysis, columns containing HSS and HSC exhibit higher load capacity, yet less ductility capacity, when compared to columns with $f_y = 420$ MPa and $f'_c = 50$ MPa.
3. Bridge piers incorporating HSS and HSC are less seismically vulnerable than those incorporating normal-strength steel and concrete for minimal and repairable damage states but not extensive and probable replacement damage states.
4. The Priestley et al. (1996) procedure is commonly used to carry out pushover analysis employing the lumped plasticity approach. This procedure was used to assess the effect of HSS on the ductility capacity of members reinforced with HSS. This approach led to similar conclusions as obtained from

the fiber-based pushover procedure using SeismoStruct. However, noticeable discrepancies were observed in the ductility capacity measured from the pushover analysis and that computed using the Priestley et al. (1996) model. One possible reason for such discrepancies could be related to the inadequacy of the plastic hinge length equation proposed by Priestley et al. (1996) when applied to concrete columns longitudinally reinforced with HSS. Future research is deemed warranted to reevaluate the coefficients in Priestley's plastic hinge length equation to improve its accuracy when applied to members reinforced with HSS.

CHAPTER 7: SUMMARY, CONCLUSIONS AND FUTURE WORK

7.1 Summary and Conclusions

The research presented in this dissertation employed a combination of analytical and experimental procedures to assess the seismic performance of bridge columns reinforced with different types of HSS. The overarching objective was to propose design recommendations applicable to concrete bridge columns reinforced with different types of HSS. The specific objectives of this study were to i) develop expressions to predict the drift ratio limit states of concrete bridge columns reinforced with HSS, ii) experimentally evaluate the low-cycle fatigue performance of ASTM A1035 Grade 690, iii) identify conditions under which HSS bars can achieve low-cycle fatigue performance comparable to that of the conventional normal-strength steel in concrete bridge piers, and iv) develop seismic fragility curves for a bridge pier alternately reinforced with HSS and conventional normal-strength steel.

This first part of this study presents the results of a comprehensive analytical program with an overarching objective of proposing simplified expressions to predict drift ratios corresponding to the onset of different damage states for concrete columns reinforced with HSS. Three types of HSS, namely, ASTM A706 Grade 550, ASTM A615 Grade 690, and ASTM A1035 Grade 690, were considered. The accuracy of the fiber-based numerical models in predicting the drift limit states of concrete columns reinforced with HSS was initially verified using available previous experimental data. Full factorial analysis considering upper and lower levels of geometry-, section-, and material-related parameters was carried out. The results of the factorial analysis provided a better understanding of the effect of different parameters on the drift ratio limit states and were critical in limiting the complexity of the proposed simplified expressions since only those with significant contribution were considered. To generate sufficient data to generate the expressions, the Monte Carlo sampling technique was adopted. Three samples each consisting of 1000 unique columns, were generated for the three types of HSS. The columns were subjected to displacement-controlled quasi-static cyclic loading protocols, and the drift ratios at the onset of the damage states were

recorded. The resulting data were first used to establish the drift ratio limit states on a probabilistic basis. Then, the resulting data were processed through a symbolic regression analysis which fitted simplified numerical expressions to the data. The proposed simplified expressions for concrete columns reinforced with ASTM A706 Grade 550 had the highest square of correlation coefficients. This was owing to the lower variability in the mechanical properties of ASTM A706 Grade 550 when compared to ASTM A615 Grade 690 and ASTM A1035 Grade 690. Nevertheless, the proposed simplified expression provided adequate predictions of the drift ratio limits determined from the analyses of the fiber-based models as well as those measured in previous experimental programs. As more experimental data from cyclic tests on concrete columns reinforced with different types of HSS become available, the accuracy of the proposed expressions could be further validated for concrete columns having a wider range of geometrical and material properties. It must be noted that the proposed expressions are only applicable to concrete columns having properties falling within the upper and lower levels of the data on which the proposed expressions were based. The proposed expressions would be mostly useful at preliminary design stages where detailed types of analysis such as nonlinear static pushover are often unnecessary. Besides, since the predictions of the proposed expressions were validated using previous experimental data, they would serve as a benchmark for the bridge engineering community when determining the limit states of concrete columns reinforced with HSS through numerical analyses.

In the second part of this study, ASTM A1035 Grade 690 rebars were tested under monotonic tension and low-cycle fatigue tests to evaluate their adequacy for structural seismic applications. Rebars with diameters of 12.7 and 15.88 mm were tested under monotonic tension to determine their mechanical properties and generate stress-strain relationships. The stress-strain curves were characterized with a linear portion up to a proportional limit followed by a nonlinear relationship up to the tensile strength, hence lacked a well-defined yield point and plateau. ASTM A1035 Grade 690 rebars satisfied the condition that the tensile-to-yield strength ratio exceeds 1.25 which is often prescribed by design codes for steel reinforcing bars used in seismic applications. However, the inelastic tensile strain capacity of ASTM A1035 Grade 690 rebars was approximately one-third that of ASTM A706 Grade 420. In the low-cycle fatigue

tests, sixty-four ASTM A1035 Grade 690 rebar specimens were tested considering the following variables: rebar size, strain amplitude, and buckling length. Rebar size had little to no effect on low-cycle fatigue performance. Increasing the strain amplitude and gripping span generally reduced fatigue life and total energy dissipated. Using fatigue experimental data, constants of existing strain, and energy-based fatigue-life models were calibrated. The results revealed that utilizing previous fatigue life models with constants calibrated using reinforcing steel exhibiting nearly identical mechanical properties to that of ASTM A1035 would lead to inaccurate fatigue life predictions. The effect of inelastic buckling was incorporated into the proposed strain and energy-based fatigue-life models by correlating their constants with a buckling parameter. While utilizing the proposed models, it was found that ASTM A1035 Grade 690 reinforcing bars in reinforced concrete columns subjected to a target displacement ductility of 2 could exhibit sufficient fatigue life provided that center-to-center transverse reinforcement is limited to six longitudinal bar diameters.

In the third part of this study, the previously reported fatigue data of ASTM A706 Grade 550 and ASTM A1035 Grade 690 steel bars were utilized as part of an analytical program to identify conditions under which HSS rebars can achieve adequate performance when compared to that of benchmark ASTM A706 Grade 420 steel bars in concrete bridge columns. A hypothetical sample of well confined circular concrete bridge columns with flexure-dominated behavior and characteristics reflective of those currently in use in regions of high seismicity in North America was assembled. The variables considered within the sample were axial load ratio, and longitudinal and spiral reinforcement ratios. The concrete bridge columns in the sample were alternately reinforced with ASTM A706 Grade 420, ASTM A706 Grade 550, and ASTM A1035 Grade 690 and analyzed under different conditions of displacement ductility level (2, 4, and 6), earthquake type (crustal and subduction earthquakes), and ratio of hoop spacing to longitudinal bar diameter ratio (4 and 6). As part of the numerical analysis, cumulative damage theory was utilized to predict low-cycle fatigue-induced bar deterioration and fracture under certain conditions. Comparisons between the low-cycle fatigue performances of two HSS types and those of conventional steel were made based on the

computed bar fracture and accumulated damage indices. Within the limits of the variables investigated in this program the following key observations were made:

- Up to displacement ductility level of 4, ASTM A706 Grade 550 were found to have adequate low-cycle fatigue performance in concrete bridge columns subjected to crustal and subduction earthquakes provided that for the latter, ratio of hoop spacing to longitudinal bar diameter ratio is limited to 4. Such limitation on the spacing-to-bar diameter ratio is critical to provide an additional safety margin against fatigue deterioration and fracture of ASTM A706 Grade 550 steel bars in concrete columns subjected to subduction earthquakes imposing displacement ductility levels up to 4.
- Irrespective of the spacing-to-bar diameter ratio, ASTM A1035 Grade 690 rebars demonstrated adequate low-cycle fatigue performance only for crustal earthquakes and displacement ductility level of 2.

While the authors acknowledge the code committees' concerns over the low-cycle fatigue performance of HSS types such as those considered in this study, the current requirement of the AASHTO appears to be overly conservative given the reported observations herein. This study recommends imposing certain limits on the μ_d and s/d_b , such as those proposed above for ASTM A706 Grade 550 and ASTM A1035 Grade 690, for HSS bars rather than relying solely on the results of low-cycle fatigue tests to determine their adequacy for seismic applications.

In the last part of this study, a coordinated analytical research program was conducted to evaluate the seismic performance of an existing bridge in Vancouver, British Columbia when different combinations of HSS and HSC are incorporated into its middle pier. The following conclusions are drawn:

- Bridge piers designed based on the force-based design approach and reinforced with HSS are characterized with less amount of longitudinal and transverse reinforcement steel when compared to those reinforced with conventional steel.

- Based on the static pushover analysis, columns containing HSS and HSC exhibit higher load capacity, yet less ductility capacity, when compared to columns with $f_y = 420$ MPa and $f'_c = 50$ MPa.
- Bridge piers incorporating HSS and HSC are less seismically vulnerable than those incorporating normal-strength steel and concrete for minimal and repairable damage states but not extensive and probable replacement damage states.
- The Priestley et al. (1996) procedure is commonly used to carry out pushover analysis employing the lumped plasticity approach. This procedure was used to assess the effect of HSS on the ductility capacity of members reinforced with HSS. This approach led to similar conclusions as obtained from the fiber-based pushover procedure using SeismoStruct. However, noticeable discrepancies were observed in the ductility capacity measured from the pushover analysis and that computed using the Priestley et al. (1996) model. One possible reason for such discrepancies could be related to the inadequacy of the plastic hinge length equation proposed by Priestley et al. (1996) when applied to concrete columns longitudinally reinforced with HSS. Future research is deemed warranted to reevaluate the coefficients in Priestley's plastic hinge length equation to improve its accuracy when applied to members reinforced with HSS.

7.2 Limitations of This Study

The limitations of this study are as follows:

- In this study, only concrete bridge columns with flexure-dominated behavior were considered. Therefore, the findings in this research are not applicable to bridge columns whose geometric and reinforcement details enforce other types of failure modes such as shear and flexure-shear.
- The effect of foundation flexibility on the responses is beyond the scope of this study and consequently was not considered.

- Due to the MTS testing machine capacity, the maximum rebar size tested was 15.88-mm-nominal-diameter rebar which is unlikely to be used as longitudinal reinforcement in concrete bridge columns.
- The proposed low-cycle fatigue models are based on the low-cycle fatigue performance of ASTM A1035 Grade 690 supplied by a single manufacturer. Therefore, the proposed low-cycle fatigue models are not necessarily applicable to ASTM A1035 Grade 690 steel bars supplied by other manufacturers.
- The conclusions drawn from the seismic fragility curves are only applicable to the selected prototype bridge and associated seismic hazard.

7.3 Recommendations for Future Research

The work in the present study could be extended through additional research as follows:

- Expressions for drift limit states of concrete bridge columns with rectangular cross-section need to be also established. Also, expressions applicable to bridge columns susceptible to failure modes other than flexure need to be developed.
- The findings in this study could be verified considering other types of earthquakes and larger database of ground motions.
- Low-cycle fatigue tests could be performed using more realistic bar sizes, i.e. larger than those tested in this study. The results from such tests could be used to evaluate the adequacy of the models proposed herein when larger sizes of ASTM A1035 Grade 690 steel bars are used.
- A more generalized low-cycle fatigue life models could be developed by considering ASTM A1035 Grade 690 rebars supplied by different manufacturers.
- The predictions of the cumulative damage model considered in this study could be further improved by employing a more refined prediction techniques of buckling location and inception such as those considering the effect of the load history.

- The inherent overstrength in the members reinforced with high-strength steel needs to be accounted to ensure that members which are not part of the seismic-force-resisting system remain elastic, i.e. capacity-protected. Therefore, there a need for research work evaluating the overstrength moment capacities of concrete members reinforced with HSS.
- Seismic fragility curves could be developed considering uncertainties in material, geometric, and reinforcement details to draw more generalized conclusions of the seismic vulnerability of concrete bridge columns reinforced with HSS.

BIBLIOGRAPHY

- AASHTO. (2007). *LRFD bridge design specifications*, 4th Ed., AASHTO, Washington, DC.
- AASHTO. (2012). *LRFD bridge design specifications*, 6th Ed., AASHTO, Washington, DC.
- AASHTO. (2014). *Guide specifications for LRFD seismic bridge design*, Washington, DC.
- AASHTO. (2017). *LRFD bridge design specifications*, 8th Ed., AASHTO, Washington, DC.
- Aldabagh, S. and Alam, M. S. (2020). High-strength steel reinforcement (ASTM A1035/A1035M Grade 690): state-of-the-art review. *Journal of Structural Engineering*, 146(8), 03120003.
- Aldabagh, S., Abed, F., and Yehia, S. (2018). Effect of types of concrete on flexural behavior of beams reinforced with high-strength steel bars. *ACI Struct. J.*, 115(2), 351–364.
- Aldabagh, S., and Alam, M. S. (2021a). Drift ratio limit states for circular concrete columns reinforced with different types of high-strength steel. Submitted to *Journal of Bridge Engineering*.
- Aldabagh, S., and Alam, M. S. (2021b). Low-cycle fatigue performance of high-strength steel reinforcing bars considering the effect of inelastic buckling. *Engineering Structures*, 235, 112114.
- American Concrete Institute (ACI) Committee 318. (2008). *Building code requirements for reinforced concrete*. ACI 318-08, Detroit, MI.
- American Concrete Institute (ACI) Committee 318. (2011). *Building code requirements for reinforced concrete*. ACI 318-11, Detroit, MI.
- American Concrete Institute (ACI) Committee 318. (2014). *Building code requirements for reinforced concrete*. ACI 318-14, Detroit, MI.
- American Concrete Institute (ACI) Committee 408. (2003). *Bond and development of straight reinforcing bars in tension*. ACI 408R-03, Detroit, MI.
- American Concrete Institute (ACI) Committee 439.6R. (2019a). *Guide for the use of ASTM A1035/A1035M Type CS Grade 100 (690) steel bars for structural concrete*. ACI 439.6R-19, Detroit, MI.
- American Concrete Institute (ACI) Committee 318. (2019b). *Building code requirements for reinforced concrete*. ACI 318-19, Detroit, MI.

- American Concrete Institute (ACI) Committee 93. (2010). *Design guide for the use of ASTM A1035/A1035M Grade 100 (690) steel bars for structural concrete*. ACI ITG-6R-10, Detroit, MI.
- ASTM. (2016). *Standard Specification for Deformed and Plain Low-Alloy Steel Bars for Concrete Reinforcement*. ASTM A706 / A706M-16, ASTM International, West Conshohocken, PA.
- ASTM. (2017). *Standard Practices for Cycle Counting in Fatigue Analysis*. E1049-85, West Conshohocken, PA.
- ASTM. (2020a). *Standard specification for deformed and plain carbon-steel bars for concrete reinforcement*. ASTM A615-20, West Conshohocken, PA.
- ASTM. (2020b). *Standard Specification for Deformed and Plain, Low-Carbon, Chromium, Steel Bars for Concrete Reinforcement*. ASTM A1035 / A1035M-20, ASTM International, West Conshohocken, PA.
- Atwater, B. F., et al. (1995). Summary of coastal geologic evidence for past great earthquakes at the Cascadia subduction zone. *Earthquake Spectra*, 11(1), 1–18.
- Australian/New Zealand Standard (AS/NZS) committee BD-084. (2001). *Steel reinforcing materials*. AS/NZS 4671:2001, Sydney, Australia, and Wellington, New Zealand.
- Azizinamini, A.; Baum Kuska, S. S.; Brungardt, P.; and Hatfield, E. (1994). Seismic behavior of square high-strength concrete columns. *ACI Structural Journal*, 91(3), 336-345.
- Babazadeh, A., Burgueño, R., and Silva, P. (2015). Use of 3-D finite-element models for predicting intermediate damage limit states in RC bridge columns. *J. Struct. Eng.* 141(10), 04015012.
- Barbosa, A. R., Link, T., and Trejo, D. (2015). Seismic performance of high-strength steel RC bridge columns. *Journal of Bridge Engineering*, 21(2), 04015044.
- Barcley, L., and M. Kowalsky. (2020). Seismic performance of circular concrete columns reinforced with high-strength steel. *J. Struct. Eng.*, 146 (2): 04019198.
- Barr, P. J., and Wixom, K. (2009). Feasibility of using high-strength steel and MMFX rebar in bridge design. *Rep. UTCM 09-09*, Utah Department of Transportation, Salt Lake City, UT.

- Bauschinger, J. (1881). Ueber die Veränderung der elasticitätsgrenze und dea elasticitatemoduls verschiadener metalle. *Zivilingenieur*, 27, 289–348.
- Bayrak, O., and Sheikh, S. A. (1998). Confinement reinforcement design considerations for ductile HSC columns. *Journal of Structural Engineering*, 124(9), 999-1010.
- Bazaez, R. and Dusicka, P. (2016). Cyclic loading for RC bridge columns considering subduction megathrust earthquakes, *Journal of Bridge Engineering*, 21(5), 4016009.
- BC MoTI. (2016). Volume 1 - *Supplement to CHBDC S6-14*, British Columbia Ministry of Transportation and Infrastructure, Victoria, BC.
- Berry, M. P., (2006). Performance Modeling Strategies for Modern Reinforced Concrete Bridge Columns. Ph.D. Thesis, University of Washington, Seattle, WA.
- Berry, M. P., and Eberhard, M. O. (2005). Practical performance model for bar buckling. *Journal of Structural Engineering*, 131(7), 1060-1070.
- Berry, M., Myles, P, and Eberhard, M. (2013). PEER structural performance database. Pacific Earthquake Engineering Research Center, University of California, Berkeley.
- Billah, A. H. M. M., and Alam, M. S. (2013). Seismic fragility assessment of high strength reinforced concrete columns considering parameter uncertainty. *ACI Special Publication*, 293, 1-18.
- Billah, A. H. M. Muntasir, Alam, M. S., and Bhuiyan, M. A. R. (2013). Fragility analysis of retrofitted multicolumn bridge bent subjected to near-fault and far-field ground motion. *Journal of Bridge Engineering*, 18(10), 992-1004.
- Billah, A. H. M. Muntasir, and Kabir, M. A. B. (2020). Development of performance limit states for concrete bridge piers with high strength concrete and high strength steel reinforcement. *Canadian Journal of Civil Engineering*.
- Bischoff, P. H. (2005). Reevaluation of deflection prediction for concrete beams reinforced with steel and fiber reinforced polymer bars. *Journal of Structural Engineering*, 131(5), 752-767.
- Bishaw, B. B. (2016). Effect of high strength materials on the seismic performance of reinforced concrete moment resisting frames. Ph.D. thesis, The University of Utah, Salt Lake City, UT.

- Branson, D. E. (1977). *Deformation of concrete structures*. McGraw-Hill, New York.
- Breña, S. F., Messier, J., and Peterfreund, S. W. (2018). Behavior of straight and T-headed ASTM A1035/A1035M bar splices in flexural members. *ACI Structural Journal*, 115(1), 79-90.
- Brown, J., and Kunnath, S. K. (2004) Low-cycle fatigue failure of reinforcing steel bars, *ACI Materials Journal*, 101(6), 457-466.
- BSDC (Bridge Structures Design Criteria). 2018. *Bridge structures design criteria version 8.1*. Edmonton, Canada: Technical Standards Branch, Alberta Transportation.
- Budek, A. M., Priestley, M. J. N., and Lee, C. O. (2002). Seismic design of columns with high-strength wire and strand as spiral reinforcement. *ACI Structural Journal*, 99(5), 660-670.
- Caifu, Y. (2010) Development of high strength construction rebars. *In Proc., Int. Seminar on Production and Application of High Strength Seismic Grade Rebar Containing Vanadium*. Beijing: Central Iron and Steel Research Institute.
- California Department of Transportation (Caltrans). (2006). *Visual Catalog of Reinforced Concrete Bridge Damage*. Structure Maintenance and Investigations, Caltrans, Sacramento.
- Canadian Standards Association (CSA). (2004). *Design of concrete structures*. CSA A23.3-04, Rexdale, ON.
- Canadian Standards Association (CSA). (2007). *Carbon steel bars for concrete reinforcement*. CSA G30.18. Rexdale, ON: CSA.
- Canadian Standards Association (CSA). (2019a). *Design of concrete structures*. CSA A23.3-19, Rexdale, ON.
- Canadian Standards Association (CSA). (2019b). *Canadian highway bridge design code*. CSA S6-19, Rexdale, ON.
- Casanova, N. M. (2018). Performance of high-strength steel reinforcement in shear friction applications. M.S. Thesis, Oregon State University.

- Chopra, A. K., and Chintanapakdee, C. (2001). Comparing response of SDF systems to near-fault and far-fault earthquake motions in the context of spectral regions. *Earthquake Engineering & Structural Dynamics*, 30(12), 1769-1789.
- Clemena, G. G., and Virmani, Y. P. (2004). Comparing the chloride resistances of reinforcing bars. *ACI Concrete International*, 26(11), 39-49.
- Coffin, Jr, L. F. (1954). A study of the effects of cyclic thermal stresses on a ductile metal. *Trans.*, American Society of Mechanical Engineers, New York, N.Y., 76, 931–950.
- Colaco, J. P. (1985). 75-story Texas Commerce Plaza, Houston-The use of high-strength concrete. High-Strength Concrete, *SP-87*, ACI international, Detroit, MI.
- Collins, A. (1993). *Failure of materials in mechanical design*. 2nd Ed., Ohio State University, Columbus, Ohio.
- Cornell, A. C., Jalayer, F., and Hamburger, R. O. (2002). Probabilistic basis for 2000 SAC federal emergency management agency steel moment frame guidelines. *Journal of Structural Engineering*, 128(4), 526–532.
- Cusson, D., and Paultre, P. (1994). High-strength concrete columns confined by rectangular ties. *Journal of Structural Engineering*, 120(3), 783-804.
- D202. 2006. Bridge Standards & Procedures Manual. Volume 3. British Columbia Ministry of Transportation and Infrastructure, Coquitlam, BC.
- Darwin, D., Browning, J., Nguyen, T. Van, and Locke, C. (2002). *Mechanical and corrosion properties of a high-strength, high chromium reinforcing steel for concrete*. SM Rep. No. 66. Lawrence, KS: Univ. of Kansas Center for Research.
- Darwin, D., Browning, J., O'Reilly, M., Xing, L., and Ji, J. (2007). Critical Chloride Corrosion Threshold of Galvanized Reinforcing Bars. *ACI Materials Journal*, 106(2), 176–183.
- Dejong, S. J., Macdougall, C., and Heffernan, P. J. (2006). Fatigue behavior of MMFX corrosion-resistant reinforcing steel. *In Proc., 7th Int. Conf. on Short and Medium Span Bridges*. New York: Springer.

- Desalegne, A. S., and Lubell, A. S. (2011). Shear behavior of concrete slabs longitudinally reinforced with high-performance steel. *ACI Structural Journal*, 107(2), 228-236.
- Desalegne, A. S., and Lubell, A. S. (2013). Deflection control of concrete slabs longitudinally reinforced with ASTM A1035/A1035M-07 steel. *ACI Structural Journal*, 109(6), 867-878.
- Dhakal, R.P., and Maekawa, K. (2002). Reinforcement stability and fracture of cover concrete in reinforced concrete members. *Journal of Structural Engineering*, 128(10), 1253-1262.
- Dodd, L. and Restrepo-Posada, J. (1995). Model for Predicting Cyclic Behavior of Reinforcing Steel. *J. Struct. Eng.*, 121(3), 433-445.
- Eissa, M., Kandil, A., Hamed, A., Mattar, T., and Ali, O. (2018). Developing high strength-high toughness low carbon steel using combined V-Ti-micro-alloying and different thermo-mechanical treatments. *Key Engineering Materials*, 786, 57-64.
- El-Bahy, A., Kunnath, S. K., Stone, W. C., and Taylor, A. W. Cumulative seismic damage of circular bridge columns: Benchmark and low-cycle fatigue tests. *ACI Structural Journal*, 96(4), 633-641.
- Elnashai, A. S., and Sarno, L. D. (2008). *Fundamentals of earthquake engineering*, Wiley, New York.
- Elwood, K.J., and Eberhard, M.O. (2009). Effective stiffness of reinforced concrete columns. *ACI Structural Journal*, 106(4), 476-484.
- Fahim, A., Dean, A. E., Thomas, M. D. A., and Moffatt, E. G. (2019). Corrosion resistance of chromium-steel and stainless steel reinforcement in concrete. *Materials and Corrosion*, 70(2), 328-344.
- Farshadfar, O. (2017). Performance evaluation of corrosion protection systems for reinforced concrete. Ph.D. thesis, University of Kansas, Lawrence, KS.
- Feng, Y., Kowalsky, M. J., and Nau, J. M. (2015). Finite-element method to predict reinforcing bar buckling in RC structures. *Journal of Structural Engineering*, 141(5), 4014147.
- Filippou, F. C., Popov, E. P., and Bertero, V. V. (1983). *Effects of bond deterioration on hysteretic behavior of reinforced concrete joints*. Report EERC 83-19. Earthquake Engineering Research Center, University of California, Berkeley.

- Frosch, R. J. (1999). Another look at cracking and crack control in reinforced concrete. *ACI Structural Journal*, 96(3), 437-442.
- Gervas'ev, M. A., Sharapova, V. A., and Berdnikov, A. A. (2019). Effect of micro-alloying with boron and niobium on properties of Cr-Mn-Mo steels. *Materials Science Forum*, 946, 3-7.
- Ghannoum, W. M., and Slavin, C. M. (2016). Low-cycle fatigue performance of high-strength steel reinforcing bars. *ACI Materials Journal*, 113(6), 803-814.
- Glucksman, R. (2018). Defining structurally acceptable properties of high-strength steel bars through material testing. M.S. Thesis, Lyles School of Civil Engineering, Purdue University.
- Goldfinger, C., et al. (2012). *Turbidite event history—Methods and implications for Holocene paleoseismicity of the Cascadia subduction zone*. Reston, VA: US Dept. of the Interior, USGS.
- Gong, L., Darwin, D., Browning, J. P., and Carl, L. (2002). *Evaluation of mechanical and corrosion properties of MMFX reinforcing steel for concrete*. SM Rep. No. 70. Lawrence, KS: Univ. of Kansas Center for Research.
- Gong, Y. (2012). Simple rain flow counting algorithm. Retrieved from MATLAB File Exchange, <https://www.mathworks.com/matlabcentral/fileexchange/38834-simple-rain-flow-counting-algorithm>.
- Goodnight, J. C., Feng, y., Kowalsky, M. J., and Nau, J. M. (2015). *The effects of load history and design variables on performance limit states of circular bridge columns, volumes 2: experimental observations*. Report No. 4000(72). Alaska Department of Transportation and Public Facilities, Juneau, AK.
- Goodnight, J. C., Kowalsky, M. J., and Nau, J. M. (2016). Strain limit states for circular RC bridge columns. *Earthquake Spectra*, 32(3), 1627-1652.
- Hancock, J. and Bommer, J. J. (2006). A state-of-knowledge review of the influence of strong-motion duration on structural damage. *Earthquake Spectra*, 22(3), 827-845.

- Hancock, J., Watson-Lamprey, J., Abrahamson, N. A., Bommer, J. J., Markatis, A., McCoyh, E., and Mendis, R. (2006). An improved method of matching response spectra of recorded earthquake ground motion using wavelets. *J. Earthquake Eng.*, 10(1), 67–89.
- Harries, K. A., Shahrooz, B. M., and Soltani, A. (2012a). Flexural crack widths in concrete girders with high-strength reinforcement. *Journal of Bridge Engineering*, 17(5), 804-812.
- Harries, K. A., Shahrooz, B. M., Soltani, A., Reis, J. M., Wells, E. L. (Ward)., Miller, R., and Russell, H. G. (2010). Bond and anchorage of high-strength reinforcing steel. *Transp. Res. Rec.*, 2172(1), 96-102.
- Harries, K. A., Zeno, G., and Shahrooz, B. (2012b). Toward an improved understanding of shear-friction behavior. *ACI Structural Journal*, 109(6), 835-844.
- Hassan, T. K., Mantawy, A., Soliman, J., Sherif, A., and Rizkalla, S. H. (2012). Bond characteristics and shear behavior of concrete beams reinforced with high-strength steel reinforcement. *Advances in Structural Engineering*, 15(2), 303-318.
- Hawileh, R. A., Abdalla, J. A., Oudah, F., and Abdelrahman, K. (2016) Low-cycle fatigue life behaviour of BS 460B and BS B500B steel reinforcing bars. *Fatigue & Fracture of Engineering Materials & Structures*, 33(7), 397-407.
- Hawileh, R., Rahman, A., and Tabatabai, H. (2010). Evaluation of the low-cycle fatigue life in ASTM A706 and A615 grade 60 steel reinforcing bars, *Journal of Materials in Civil Engineering*, 22(1), 65-76.
- Hayter, A. (2012). *Probability and Statistics for Engineers and Scientists*, Duxbury Press.
- Hose, Y. D., and F. Seible. (1999). *Performance Evaluation Database for Concrete Bridge Components and Systems under Simulated Seismic Loads*. Pacific Earthquake Engineering Research Center, Berkeley, Calif.
- Hose, Y., Silva, P., and Seible, F. (2000). Development of a performance evaluation database for concrete bridge components and systems under simulated seismic loads. *Earthquake Spectra*, 16(2), 413-442.

- Hoult, N. A., Sherwood, E. G., Bentz, E. C., and Collins, M. P. (2008). Does the use of FRP reinforcement change the one-way shear behavior of reinforced concrete slabs? *Journal of Composites for Construction*, 12(2), 125-133.
- Hwang, H., Liu, J. B., and Chiu, Y.-H. (2001). *Seismic fragility analysis of highway bridges*. Mid-America Earthquake Center report: project MAEC RR-4. Urbana: MACE.
- Ibarra, L., and Bishaw, B. (2016). High-strength fiber-reinforced concrete beam-columns with high-strength steel. *ACI Structural Journal*, 113(1), 147-156.
- Ji, J., Darwin, D., and Browning, J. P. (2005). *Corrosion resistance of duplex stainless steels and MMFX microcomposite steel for reinforced concrete bridge decks*. SM Rep. No. 80. Lawrence, KS: Univ. of Kansas Center for Research.
- Kahl, S. (2007). *Corrosion resistant alloy steel (MMFX) reinforcing bar in bridge decks*. R-1499. Lansing, MI: Michigan Dept. of Transportation Construction and Technology Division.
- Kappos, A. J., and Konstantinidis, D. (1999). Statistical analysis of confined high strength concrete. *Materials and Structures*, 32(10), 734-748.
- Kashani, M. M., Barmi, A. K., and Malinova, V. S. (2015). Influence of inelastic buckling on low-cycle fatigue degradation of reinforcing bars. *Construction and Building Materials*, 94, 644-655.
- Kashani, M.M. (2014) Seismic performance of corroded RC bridge piers-Development of a multi-mechanical nonlinear fibre beam-column model. Ph.D. thesis, Department of Civil Engineering, University of Bristol.
- Kelly, D. J., Lepage, A., Mar, D., Restrepo, J. I., Sanders, J. C., and Taylor, A. W. (2017). ATC-98 project on seismic design of concrete structures with high-strength reinforcement. *ACI Special Publication SP 313-06*, American Concrete Institute, Farmington Hills, MI.
- K-Net (Kyoshin Network Database). Strong-motion data. <http://www.kyoshin.bosai.go.jp>. (Mar 1, 2021).
- Koh, S. K. and Stephens, R. I. (1991) Mean stress effects on low cycle fatigue for a high strength steel. *Fatigue & Fracture of Engineering Materials & Structures*, 14(4), 413-428.

- Konstantinidis, D., and Kappos, A. (2003). Seismic evaluation of R/C buildings using high performance materials. In *Proceedings of Advanced Materials for Construction of Bridges, Buildings, and Other Structures III*, Davos, Switzerland.
- Kowalsky, M. J. (2000). "Deformation limit states for circular reinforced concrete bridge columns. *Journal of Structural Engineering*, 126(8), 869-878.
- Krawinkler, H., et al. (1983). *Recommendations for experimental studies on the seismic behavior of steel components and materials*. John A. Blume Center Rep. No. 61. Dept. of Civil Engineering, Stanford Univ., Stanford, CA.
- Kunnath, S., El-Bahy, A., Taylor, A., W., and Stone, W. C. (1997). *Cumulative seismic damage of reinforced concrete bridge piers*. NISTIR 6075. National Institute of Standards and Technology, Gaithersburg, MD.
- Laughery, L. (2016). Response of high-strength steel reinforced concrete structures to simulated earthquakes. Ph.D. Dissertation, Purdue University, West Lafayette, IN.
- Lefebvre, D., and Ellyin, F. (1984). Cyclic response and inelastic strain energy in low cycle fatigue, *Int. J. Fatigue*, 6(1), 9-15.
- Légeron, F., and Paultre, P. (2000). Behavior of high-strength concrete columns under cyclic flexure and constant axial load. *ACI Structural Journal*, 97(4), 591-601.
- Lehman, D., Moehle, J., Mahin, S., Calderone, A., and Henry, L. (2004). Experimental evaluation of the seismic performance of reinforced concrete bridge columns. *Journal of Structural Engineering*, 130(6), 869-879.
- Lepage, A., Tavallali, H., Pujol, S., and Rautenberg, J. M. (2012). High-performance steel bars and fibers as concrete reinforcement for seismic-resistant frames. *Advances in Civil Engineering*, 2012, 1-13.
- Lepage, Andrés, Tavallali, H., Pujol, S., and Rautenberg, J. (2008). Towards earthquake-resistant concrete structures with ultra high-strength steel reinforcement. In Proc., *14th World Conf. on Earthquake Engineering*. Beijing: World Conference on Earthquake Engineering.

- Li, Y., Cao, S., and Jing, D. (2018). Concrete columns reinforced with high-strength steel subjected to reversed cycle loading. *ACI Structural Journal*, 115(4), 1037-1048.
- Lim, J., Park, H., and Eom, T. (2017). Cyclic load tests of reinforced concrete columns with high-strength bundled bars. *ACI Structural Journal*, 114(1), 197-207.
- Lorenzo, F., and Laird, C. (1984). A new approach to predicating fatigue life behavior under the action of mean stresses. *Mater. Sci. and Engrg.*, 62(2), 9-15.
- Lu, Y., Gu, X., and Guan, J. (2005). Probabilistic drift limits and performance evaluation of reinforced concrete columns. *J. Earthquake Eng.*, 131(6), 966–978.
- Macchi, G., Pinto, P. E., and Sanpaolesi, L. (1996). Ductility requirements for reinforcement under Eurocodes, *Structural Engineering International*, 6(4), 249-254.
- Mander, J. B., Panthaki, F. D., and Kasalanati, A. (1994). Low-cycle fatigue behavior of reinforcing steel. *J. Mater. Civ. Eng.*, 6(4), 453–468.
- Mander, J. B., Priestley, M. J. N., and Park, R. (1988). Theoretical stress-strain model for confined concrete. *Journal of Structural Engineering*, 114(8), 1804-1826.
- Manson, S. S. (1953). Behavior of materials under conditions of thermal stress. In *Proc., Heat Transfer Symp.*, Univ. of Michigan Engineering Research Institute, Ann Arbor, Mich., 9–75.
- Mast, R. F., Dawood, M., Rizkalla, S. H., and Zia, P. (2008). Flexural strength design of concrete beams reinforced with high-strength steel bars. *ACI Structural Journal*, 105(5), 570-577.
- Mast, R.F. (2006). *Memorandum: behavior of flexural members reinforced with MMFX steel*, 1–15. West Conshohocken, PA: ASTM.
- McKenna, F., Fenves, G. L., and Scott, M. H. (2000). Open System for Earthquake Engineering Simulation. University of California, Berkeley, <http://opensees.berkeley.edu>.
- Menegotto, M., and Pinto, P. E. (1973). Method of analysis for cyclically loaded R.C. plane frames including changes in geometry and nonelastic behavior of elements under combined normal force and bending. Symposium on the Resistance and Ultimate Deformability of Structures Acted on By

- Well-Defined Repeated Loads, International Association for Bridge and Structural Engineering, Zurich, Switzerland, 15–22.
- Milne, W. G., Rogers, G. C., Riddihough, R. P., McMechan G. A., and Hyndman R. D. (1978). Seismicity in western Canada. *Can. J. Earth Sci.*, 15, 1170-1193.
- Miner, M.A. (1945). Cumulative Damage in Fatigue. *Journal of Applied Mechanics*, 3, 159-164.
- Mohammed, M., Sanders, D., and Buckle, I. (2017). Reinforced concrete bridge columns tested under long and short-duration ground motions. In *Proc., 16th World Conf. on Earthquake Engineering*, Santiago, Chile.
- Montgomery, D. C. (2013). *Design and analysis of experiments*, Willey, New York.
- Moyer, M., and Kowalsky, M. (2003). Influence of tension strain on buckling of reinforcement in concrete columns. *ACI Structural Journal*, 100(1), 75-85.
- Muguruma, H., and Watanabe, F. (1990). Ductility improvement of high-strength concrete columns with lateral confinement. In *Proc., 2nd Int. Symp. on High-Strength Concrete, SP-121*, 47–60. Farmington Hills, MI: American Concrete Institute.
- Muguruma, H., Nishiyama, M., Watanabe, F., and Tanaka, H. (1991). Ductile behavior of high-strength concrete columns confined by high-strength transverse reinforcement. In *Proc., Evaluation and Rehabilitation of Concrete Structures and Innovations in Design, SP-128*, 877–891. Farmington Hills, MI: American Concrete Institute.
- Munikrishna, A., Hosny, A., Rizkalla, S., and Zia, P. (2011). Behavior of concrete beams reinforced with ASTM A1035 grade 100 stirrups under shear. *ACI Structural Journal*, 108(1), 34-41.
- National Institute of Standards and Technology (NIST). (2014). *Use of high-strength reinforcement in earthquake-resistant concrete structures*. NIST GCR 14-917-30, Gaithersburg, MD.
- NBCC. (2015). *National building code of Canada*. Institute for Research in Construction, National Research Council of Canada, Ottawa, Ont.
- Nielson, B. G. (2005). Analytical fragility curves for highway bridges in moderate seismic zones. Ph.D. Dissertation, Georgia Institute of Technology, Atlanta, GA.

- Ning, C., and Li, B. (2016). Probabilistic approach for estimating plastic hinge length of reinforced concrete columns. *Journal of Structural Engineering*, 142(3), 04015164.
- NZT. (2018). *New Zealand Bridge Manual*, 3rd ed. Wellington: NZ Transport Agency.
- OpenSees. (2011). The Open System for Earthquake Engineering Simulation, Pacific Earthquake Engineering Research Center (PEER), Univ. of California, Berkeley CA.
- Overby, D., Kowalsky, M., and Seracino, R. (2017). Stress-strain response of A706 grade 80 reinforcing steel. *Construction & Building Materials*, 145, 292-302.
- Pacific Earthquake Engineering Research (PEER). 2011. New ground motion selection procedures and selected motions for the PEER transportation research program. PEER Rep. 2011/03, PEER center, University of California, Berkeley, CA.
- Padgett, J. E., Nielson, B. G., and DesRoches, R. (2008). Selection of optimal intensity measures in probabilistic seismic demand models of highway bridge portfolios. *Earthquake Engineering & Structural Dynamics*, 37(5), 711-725.
- Palmgren, A. G. (1924). Die lebensdauer von kugellagern. *Zeitschrift des Vereines Deutscher Ingenieure (ZVDI)*, 14, 339-341 (in German).
- Pande, C. S., A and Cooper, K. P. (2009). Nanomechanics of Hall–Petch relationship in nanocrystalline materials. *Progress in Materials Science*, 54(6), 689-706.
- Park, R. (1988). Ductility evaluation from laboratory and analytical testing. *In Proceedings of the 9th World Conference on Earthquake Engineering*, Tokyo-Kyoto, Japan, Vol. VIII, 605–616.
- Paulay, T., and Priestley, M. N. J. (1992). *Seismic design of reinforced concrete and masonry buildings*, Willey, New York.
- Paultre, P., Eid, R., Robles, H. I., and Bouaanani, N. (2009). Seismic performance of circular high-strength concrete columns. *ACI Structural Journal*, 106(4), 395-404.
- Pedro, J. J. O., Reis, A. J., and Baptista, C. (2018). High strength steel S690 in highway bridges. *Stahlbau*, 87(6), 555-564.

- PEER (Pacific Earthquake Engineering Research Center) (2011). “PEER ground motion database” (<http://peer.berkeley.edu/nga/>) (Mar. 1, 2021).
- Priestley, M. J. N., and Park, R. (1987). Strength and ductility of concrete bridge columns under seismic loading. *ACI Struct. J.*, 84(1), 61–76.
- Priestley, M. J. N., Seible, F., and Calvi, G. M. (1996). *Seismic design and retrofit of bridges*, Wiley, New York.
- Puranam, A. Y. (2018). Strength and serviceability of concrete elements reinforced with high-strength steel. Ph.D. thesis, Purdue University, West Lafayette, IN.
- Ramberg, W., and Osgood, W. R. (1943). *Description of stress-strain curves by three parameters*. Technical Note No. 902, National Advisory Committee for Aeronautics, Washington, DC.
- Rautenberg, J. M., and Pujol, S. (2013). Numerical estimates of the seismic response of building structures reinforced with high-strength steel. *ACI Special Publication*, 293: 1-10.
- Rautenberg, J. M., S. Pujol, H. Tavallali, and A. Lepage. (2013). Drift capacity of concrete columns reinforced with high-strength steel. *ACI Struct. J.*, 110 (2): 307–318.
- Razvi, S. R., and Saatcioglu, M. (1994). Strength and deformability of confined high-strength concrete columns. *ACI Structural Journal*, 91(6), 678-687.
- Restrepo, J. I., Seible, F., Stephan, B., and Schoettler, M. J. (2006). Seismic testing of bridge columns incorporating high-performance materials. *ACI Structural Journal*, 103(4), 496-504.
- Russell, H. G., Ghosh, S. K., and Saiidi, M. (2011). “Design guide for use of ASTM A1035 high-strength reinforcement in concrete bridge elements, *n.p.*, 1–26.
- Saleem, M. A., Mirmiran, A., Xia, J., and Mackie, K. (2011). Ultra-high-performance concrete bridge deck reinforced with high-strength steel. *ACI Structural Journal*, 108(5), 601-609.
- Salomon, A. L., and Moen, C. D. (2014). *Structural design guidelines for concrete bridge decks reinforced with corrosion-resistant reinforcing bars*. VCTIR 15-R10, Virginia Center for Transportation Innovation and Research, Charlottesville, VA.

- Salomon, A. L., and Moen, C. D. (2017). *Design, installation, and condition assessment of a concrete bridge deck constructed with ASTM A1035 CS No. 4 Bars*. VTRC 17-R16, Virginia Center for Transportation Innovation and Research, Charlottesville, VA.
- Schmidt, M. and Lipson, H. (2013). Eureka (Version 1.24) [Software]. Available from <http://formulize.nutonian.com/>
- Schmidt, M., and Lipson, H. (2009). "Distilling free-form natural laws from experimental data." *Science* (American Association for the Advancement of Science), 324(5923), 81-85. doi:10.1126/science.1165893
- Schoettler, M. J., Restrepo, J. I., Guerrini, G., Duck, D. E., and Carrea, F. (2015). *A full-scale single-column bridge bent tested by shake-table excitation*. PEER Report No. 2015/02. Pacific Earthquake Engineering Research Center, Berkeley, CA.
- Seismosoft. (2016). SeismoMatch- A computer program for an application capable of adjusting earthquake records, through wavelet addition, Available from URL: www.seismosoft.com.
- SeismoSoft. (2018). SeismoStruct-A computer program for static and dynamic nonlinear analysis of framed structures. Available from URL: www.seismosoft.com
- Seliem, H. M. (2007). Behavior of concrete bridges reinforced with high-performance steel reinforcing bars. Ph.D. Dissertation, North Carolina State University, Raleigh, NC.
- Seliem, H. M., Hosny, A., Rizkalla, S., Zia, P., Briggs, M., Miller, S., Darwin, D., Browning, J., Glass, J. M., Hoyt, K., Donnelly, K., and Jirsa, J. O. (2009). Bond characteristics of ASTM A1035 steel reinforcing bars. *ACI Structural Journal*, 106(4), 530-539.
- Shahrooz, B. M., Harries, K. A., Reis, J. M., Wells, E. L., Zeno, G., Miller, R. A., and Russell, H. G. (2017). "Basis of AASHTO specifications for high-strength shear reinforcement." *Journal of Bridge Engineering*, 22(11), 4017090.
- Shahrooz, B. M., Miller, R. A., Harries, K. A., and Russell, H. G. (2011). *Design of concrete structures using high-strength steel reinforcement*. NCHRP Report 679, Transportation Research Board, Washington, DC.

- Shahrooz, B. M., Reis, J. M., Wells, E. L., Miller, R. A., Harries, K. A., and Russell, H. G. (2014). Flexural members with high-strength reinforcement: Behavior and code implications. *Journal of Bridge Engineering*, 19(5), 4014003.
- Sharp, S. R., and Moruza, A. K. (2009). *Field comparison of the installation and cost of placement of epoxy-coated and MMFX 2 steel deck reinforcement: establishing a baseline for future deck monitoring*. VTRC 09-R9. Virginia Transportation Research Council, Charlottesville, VA.
- Shen, L., Soliman, M., Ahmed, S., and Waite, C. (2019). Life-cycle cost analysis of reinforced concrete bridge decks with conventional and corrosion resistant reinforcement. In Vol. 271 of *Proc., MATEC Web of Conf.*, 01009. Les Ulis, France: EDP Sciences.
- Slavin, C. M. (2015). Defining structurally acceptable properties of high-strength steel bars through material testing. M.S. Thesis, University of Texas at Austin.
- Smith, K. N., Watson, P., and Topper, T. H. (1970). A stress-strain function for the fatigue of metals. *J. Mater.*, 5(4), 767-778.
- Sokoli, D. (2018). Fracture of high-strength bars in concrete frame members under earthquake loads. Ph.D. thesis, Department of Civil, Architectural and Environmental Engineering, The University of Texas at Austin.
- Sokoli, D., Limantono, A., and Ghannoum, W. M. (2017). Plasticity spread in columns reinforced with high strength steel. In *Proc., 16th World Conference on Earthquake Engineering*, 16WCEE 2017. Santiago Chile.
- Soltani, A. (2010). Bond and serviceability characterization of concrete reinforced with high strength steel.” Ph.D. thesis, University of Pittsburgh, Pittsburgh, PA.
- Soltani, A., Harries, K. A., and Shahrooz, B. M. (2013). Crack opening behavior of concrete reinforced with high strength reinforcing steel. *International Journal of Concrete Structures and Materials*, 7(4), 253-264.
- Soltani, A., Harries, K. A., Shahrooz, B. M., Russell, H. G., and Miller, R. A. (2012). Fatigue performance of high-strength reinforcing steel. *Journal of Bridge Engineering*, 17(3), 454-461.

- Somerville, P.G. (2002). Characterizing near fault ground motion for the design and evaluation of bridges. *In Proceedings of the 3rd National Conference and Workshop on Bridges and Highways*, Portland.
- Soyluk, K., & Karaca, H. (2017). Near-fault and far-fault ground motion effects on cable-supported bridges. *Procedia Engineering*, 199, 3077-3082.
- Sperry, J., Darwin, D., O'Reilly, M., Lepage, A., Lequesne, R. D., Matamoros, A., Feldman, L. R., Yasso, S., Searle, N., DeRubeis, M., and Ajaam, A. (2018). Conventional and high-strength steel hooked bars: Detailing effects. *ACI Structural Journal*, 115(1), 247-257.
- Sperry, J., Yasso, S., Searle, N., DeRubeis, M., Darwin, D., O'Reilly, M., Matamoros, A., Feldman, L. R., Lepage, A., Lequesne, R. D. and Ajaam, A. (2017). Conventional and high-strength hooked Bars— Part 1: Anchorage tests. *ACI Structural Journal*, 114(1), 255-265.
- Sritharan, S., Suleiman, M. T., and White, D. J. (2007). Effects of seasonal freezing on bridge Column– Foundation–Soil interaction and their implications. *Earthquake Spectra*, 23(1), 199-222.
- Stephan, B., Restrepo, J., and Seible, F. (2008). *Seismic behavior of bridge columns built incorporating MMFX steel*. SSRP-2003/09. University of California, San Diego, La Jolla, CA.
- Sugano, S., Nagashima, T., Kimura, H., Tamura, A., and Ichikawa, A. (1990). Experimental studies on seismic performance of high strength reinforced concrete columns. In *Proc., 2nd Int. Symp. on High-Strength Concrete, SP-121*. Farmington Hills, MI: American Concrete Institute.
- Sumpter, M. S., Rizkalla, S. H., and Zia, P. (2009). Behavior of high-performance steel as shear reinforcement for concrete beams. *ACI Structural Journal*, 106(2), 171-177.
- Thomas, A., Davis, B., Dadi, G. B., and Goodrum, P. M. (2013). Case study on the effect of 690 MPa (100 ksi) steel reinforcement on concrete productivity in buildings. *Journal of Construction Engineering and Management*, 139(11), 4013025.
- To, D. V., Sokoli, D., Ghannoum, W. M., and Moehle J. P. (2021). Seismic performance of tall moment frames with high- strength reinforcement. *ACI Structural Journal*, 118(1), 113-124.
- Tong, X., Wang, D., and Xu, H. (1989). Investigation of cyclic hysteresis energy in fatigue failure process. *Int. J. Fatigue*, 11(5), 353-359.

- Trejo, D., and Pillai, R. G. (2004). Accelerated chloride threshold Testing—Part II: Corrosion-resistant reinforcement. *ACI Materials Journal*, 101(1), 57-64.
- Trejo, D., Link, T. B., and Barbosa, A. R. (2016). Effect of reinforcement grade and ratio on seismic performance of reinforced concrete columns. *ACI Structural Journal*, 113(5), 907-916.
- Tripathi, M. , Dhakal, R. P., Dashti, F., and Massone L. M. (2018). Low-cycle fatigue behaviour of reinforcing bars including the effect of inelastic buckling. *Construction and Building Materials*, 190, 1226-1235.
- Tripathi, M., Dhakal, R.P., and Dashti, F. (2019) Bar buckling in ductile RC walls with different boundary zone detailing: Experimental investigation, *Engineering Structures* 198, 109544.
- Vamvatsikos, D., and Cornell, C. A. (2004). Applied incremental dynamic analysis. *Earthquake Spectra*, 20(2), 523-553.
- Ward, E.L. (2009). Analytical evaluation of structural concrete members with high-strength steel reinforcement. MS thesis, University of Cincinnati, Cincinnati, OH.
- Wiss, Janney, Elstner Associates, Inc. (WJE). (2006). *Corrosion resistance of alternative reinforcing bars: an accelerated test*. WJE No. 2006.0773. Northbrook, IL: WJE.
- Wiss, Janney, Elstner Associates, Inc. (WJE). (2008). *Mechanical properties of ASTM A1035 high strength steel bar reinforcement*. WJE No. 2008.9901.0, Northbrook, IL: WJE.
- Yan, S., Liu, X., Liu, W. J., Lan, H., and Wu, H. (2015). Comparison on mechanical properties and microstructure of a C–Mn–Si steel treated by quenching and partitioning (Q&P) and quenching and tempering (Q&T) processes. *Materials Science & Engineering A*, 620, 58-66.
- Yang, J., Yoon, Y., Cook, W. D., and Mitchell, D. (2011). Punching shear behavior of two-way slabs reinforced with high-strength steel. *ACI Structural Journal*, 107(4), 468-475.
- Zhao, J. and Sritharan, S. (2007). Modeling of strain penetration effects in fiber-based analysis of reinforced concrete structures. *ACI Structural Journal*, 104(2), 133-141.

APPENDICES

Appendix A

Table A.1: Chemical requirements of typical types of reinforcing steel bars.

Element	Bar Type		
	ASTM A1035/A1035M	ASTM A615/A615M	ASTM A706/A706M
	Maximum Content, Percent		
Carbon	0.15-0.30	_*	0.3
Chromium	2.0 to 10.9	-	-
Manganese	1.5	_*	1.5
Nitrogen	0.05	-	-
Phosphorous	0.035	0.06	0.035
Sulfur	0.045	_*	0.045
Silicon	0.5	-	0.5

* Content should be reported but no limit is established.

Table A.2: Properties of the *Concrete01* Constitutive Model Used for Numerical Model Validation.

Experimental Program	Specimen	Concrete Type	Fpc (MPa)	epsc0	Fpcu (MPa)	epsU
Barclay and Kowalsky (2020)	Test 1	Unconfined	-39.8	-0.0020	0.0	-0.0040
		Confined	-55.4	-0.0059	-48.3	-0.0145
Sokoli (2018)	CH100	Unconfined	-35.9	-0.0020	0.0	-0.0040
		Confined	-65.7	-0.0103	-58.3	-0.0305
Restrepo et al. (2006)	Unit 2	Unconfined	-56.6	-0.0020	0.0	-0.0040
		Confined	-76.2	-0.0055	-68.7	-0.0102

Table A.3: Properties of the *ReinforcingSteel* Constitutive Model Used for Numerical Model Validation.

Experimental Program	Specimen	fy (MPa)	fu (MPa)	Es (MPa)	Esh (MPa)	esh	eult
Barclay and Kowalsky (2020)	Test 1	572	758	192281	5768	0.008	0.104
Sokoli (2018)	CH100	689	877	196197	5886	0.008	0.076

Table A.4: Properties of the *Steel02* Constitutive Model Used for Numerical Model Validation.

Experimental Program	Specimen	fy (MPa)	Es (MPa)	b	R0	cR1	cR2
Restrepo et al. (2006)	Unit 2	648.1	193998	0.01	15	0.925	0.15

Table A.5: Properties of the *Bond_SP01* Constitutive Model Used for Numerical Model Validation.

Experimental Program	Specimen	f_y (MPa)	S_y (mm)	f_u (MPa)	S_u (mm)	b	R
Barclay and Kowalsky (2020)	Test 1	572	0.54	758	16.2	0.5	0.5
Sokoli (2018)	CH100	689	0.74	877	22.2	0.5	0.5
Restrepo et al. (2006)	Unit 2	648	0.45	1062	10.0	0.5	0.5

The following symbols are used in Tables A.2 to A.5:

F_{pc} = concrete compressive strength at 28 days;

ϵ_{psc0} = concrete strain at maximum strength;

F_{pcu} = concrete crushing strength;

ϵ_{psU} = concrete strain at crushing strength;

f_y = yield stress in tension;

f_u = ultimate stress in tension;

E_s = Initial elastic tangent;

E_{sh} = tangent at initial strain hardening;

ϵ_{sh} = strain corresponding to initial strain hardening;

ϵ_{ult} = strain at peak stress;

b = strain-hardening ratio;

R_0 = parameter to control the transition from elastic to plastic branches;

cR_1 = parameter to control the transition from elastic to plastic branches;

cR_2 = parameter to control the transition from elastic to plastic branches;

S_y = Rebar slip at member interface under yield stress;

S_u = Rebar slip at the loaded end at the bar fracture strength;

b = Initial hardening ratio in the monotonic slip vs. bar stress response; and

R = Pinching factor for the cyclic slip vs. bar response.

Table A.5: Estimated Distributions Parameters by the Maximum Likelihood (ML) Method.

Type of HSS	Damage States	Probability Distribution	Location	Shape	Scale	Threshold
ASTM A706 Grade 550	DS-1	3-Parameter Weibull	-	2.45931	0.00993	0.0072
	DS-2	3-Parameter Weibull	-	2.6022	0.01213	0.00764
	DS-3	Lognormal	-3.14418	-	0.2917	-
	DS-4 _{cu}	Lognormal	-2.96058	-	0.30206	-
	DS-4 _{sb}	Lognormal	-2.8201	-	0.24099	-
ASTM A615 Grade 690	DS-1	3-Parameter Weibull	-	2.21632	0.01123	0.00819
	DS-2	3-Parameter Weibull	-	2.3477	0.01206	0.00843
	DS-3	Lognormal	-3.14075	-	0.29219	-
	DS-4 _{cu}	Lognormal	-2.95477	-	0.29549	-
	DS-4 _{sb}	Lognormal	-2.70217	-	0.24872	-
ASTM A1035 Grade 690	DS-1	3-Parameter Weibull	-	2.09048	0.01393	0.00889
	DS-2	3-Parameter Weibull	-	2.34013	0.01266	0.00849
	DS-3	Lognormal	-3.28219	-	0.29182	-
	DS-4 _{cu}	Lognormal	-3.08522	-	0.2821	-
	DS-4 _{sb}	Lognormal	-2.57515	-	0.25624	-

Table A.6: Drift Ratio Limit States (in Percent) of Bridge Columns Reinforced with ASTM A706 Grade 550.

Col. No.	L/D	$P/A_g f'_c$	ρ_l	ρ_s	f'_c	f_y	f_u	E	ε_{sh}	ε_u	DS-1	DS-2	DS-3	DS-4 _{cu}	DS-4 _{sb}
1	7.4	0.13	0.010	0.011	594	64.2	777	171225	0.0067	0.0953	1.5	1.8	4.4	5.4	6.0
2	6.3	0.07	0.022	0.008	590	78.6	786	178195	0.0069	0.0947	1.4	2.0	3.4	4.0	5.3
3	9.5	0.11	0.010	0.012	575	71.5	779	200415	0.0083	0.0915	1.7	2.3	5.2	6.3	6.7
4	6.5	0.15	0.040	0.011	642	45.2	790	189113	0.0080	0.0883	1.8	1.7	4.3	5.1	6.8
5	9.8	0.12	0.021	0.007	622	79.1	786	187023	0.0082	0.0979	2.1	2.4	4.1	4.8	6.2
6	9.8	0.13	0.025	0.007	579	42.5	750	198820	0.0077	0.0963	2.2	2.5	5.3	6.3	6.9
7	9.7	0.08	0.014	0.009	606	35.2	782	200945	0.0071	0.0936	2.1	2.6	7.7	9.7	8.2
8	9.6	0.12	0.031	0.013	583	53.1	738	196951	0.0080	0.1045	2.2	2.4	7.0	8.4	9.2
9	4.1	0.10	0.032	0.009	554	61.2	788	196197	0.0077	0.0929	0.9	1.1	2.5	3.0	4.0
10	5.6	0.11	0.035	0.009	537	55.0	799	212762	0.0082	0.0887	1.2	1.4	3.1	3.7	4.7
11	4.9	0.09	0.032	0.011	616	64.2	797	190065	0.0073	0.1008	1.2	1.4	3.5	4.3	5.4
12	4.6	0.18	0.032	0.008	581	37.8	750	196015	0.0076	0.0953	1.2	1.1	2.7	3.3	3.8
13	8.0	0.07	0.035	0.013	550	72.7	782	178978	0.0073	0.0923	1.8	2.3	5.0	6.0	8.9
14	8.1	0.07	0.016	0.011	577	33.6	747	187883	0.0079	0.0941	1.8	2.2	8.3	10.3	8.7
15	9.3	0.10	0.010	0.008	577	63.9	749	172608	0.0083	0.0979	1.8	2.4	4.8	5.8	6.2
16	8.6	0.06	0.036	0.012	608	47.4	761	175456	0.0060	0.0875	2.3	2.5	6.7	8.1	10.2
17	7.6	0.14	0.021	0.012	544	48.1	802	189428	0.0082	0.0954	1.6	1.8	5.2	6.3	6.7
18	7.2	0.19	0.035	0.010	593	47.8	809	191961	0.0077	0.0867	1.8	1.8	3.8	4.5	5.9
19	8.9	0.17	0.031	0.011	591	44.9	799	190529	0.0076	0.0917	2.2	2.2	5.3	6.3	7.7
20	8.0	0.15	0.028	0.010	602	67.5	760	208865	0.0074	0.0958	1.7	1.9	4.0	4.7	5.8
21	6.4	0.15	0.038	0.008	580	33.6	783	207306	0.0073	0.0922	1.6	1.6	3.8	4.6	5.3
22	7.1	0.20	0.034	0.007	589	76.3	771	194483	0.0079	0.0923	1.6	1.6	2.5	2.8	3.9
23	9.8	0.06	0.032	0.011	548	58.9	760	184015	0.0078	0.1038	2.2	2.8	6.3	7.8	9.5
24	4.6	0.10	0.028	0.007	569	61.8	785	191335	0.0077	0.0902	1.0	1.3	2.5	3.0	4.1
25	9.9	0.11	0.036	0.010	590	61.9	739	187885	0.0080	0.1003	2.3	2.6	5.4	6.3	8.0
26	5.4	0.10	0.021	0.012	572	50.5	724	216845	0.0085	0.0958	1.1	1.4	4.3	5.3	5.3
27	9.7	0.17	0.038	0.011	565	37.7	763	192799	0.0065	0.1016	2.4	2.4	6.5	7.9	8.6
28	8.2	0.07	0.019	0.008	583	78.1	713	181453	0.0074	0.0984	1.7	2.1	4.0	4.8	5.9
29	4.5	0.12	0.010	0.010	611	53.7	795	182058	0.0075	0.0904	1.0	1.1	3.5	4.3	4.5
30	4.1	0.19	0.040	0.008	601	59.9	788	201190	0.0069	0.0961	1.0	1.0	1.9	2.2	3.1
31	8.6	0.13	0.021	0.012	583	39.7	773	220462	0.0087	0.0924	1.8	2.1	6.6	8.4	7.7
32	7.5	0.15	0.021	0.012	572	52.1	792	199018	0.0081	0.0927	1.6	1.7	4.8	5.8	6.4
33	9.1	0.15	0.039	0.009	621	72.7	769	193608	0.0082	0.0974	2.2	2.3	4.1	4.6	6.4
34	9.5	0.15	0.017	0.010	563	47.3	773	187340	0.0075	0.0978	2.0	2.2	5.9	7.2	7.3
35	6.9	0.07	0.013	0.011	593	35.7	823	205036	0.0091	0.0954	1.5	2.0	7.4	9.4	7.1
36	6.0	0.05	0.034	0.010	589	55.8	768	186135	0.0077	0.1027	1.5	1.8	4.5	5.5	6.7
37	8.7	0.11	0.018	0.011	591	68.4	797	183463	0.0072	0.0955	1.8	2.2	5.1	6.1	7.1

38	7.1	0.11	0.025	0.009	584	62.5	795	190583	0.0068	0.0915	1.6	1.9	3.9	4.7	5.8
39	9.6	0.17	0.038	0.013	573	51.0	816	202507	0.0072	0.1054	2.2	2.3	6.0	7.3	8.6
40	7.6	0.19	0.027	0.008	612	36.3	731	202230	0.0064	0.1035	1.9	1.8	4.4	5.2	5.2
41	5.2	0.11	0.014	0.010	598	70.3	809	205680	0.0076	0.0939	1.0	1.4	3.2	3.9	4.4
42	6.6	0.05	0.036	0.009	604	30.2	781	193824	0.0075	0.0888	1.7	1.9	5.0	6.1	7.4
43	9.8	0.13	0.026	0.013	567	60.3	700	186362	0.0071	0.0970	2.2	2.4	6.1	7.4	8.6
44	6.3	0.10	0.038	0.007	533	52.2	830	181820	0.0073	0.0971	1.5	1.7	3.3	3.9	5.2
45	9.0	0.18	0.028	0.010	606	50.9	746	200273	0.0074	0.0856	2.1	2.1	4.5	5.3	6.6
46	8.3	0.17	0.019	0.008	579	43.1	780	186081	0.0073	0.0906	1.8	1.9	4.5	5.4	5.9
47	8.0	0.08	0.032	0.009	573	50.4	792	189869	0.0072	0.1007	1.8	2.2	4.9	5.9	7.1
48	4.2	0.08	0.021	0.010	584	48.4	798	196735	0.0079	0.0887	1.0	1.2	3.3	4.1	4.6
49	7.0	0.15	0.014	0.008	624	37.9	806	191462	0.0068	0.0972	1.6	1.7	5.0	6.1	5.5
50	9.6	0.05	0.013	0.007	568	52.4	759	197152	0.0080	0.0981	1.9	2.9	5.8	7.1	6.5
51	4.1	0.09	0.022	0.012	564	73.3	789	202968	0.0070	0.0912	0.9	1.2	3.0	3.6	4.5
52	9.0	0.17	0.011	0.011	561	55.0	765	192109	0.0086	0.0929	1.7	1.8	4.9	5.9	6.0
53	5.9	0.11	0.022	0.011	587	49.7	747	184765	0.0069	0.0987	1.4	1.6	4.6	5.6	6.0
54	7.1	0.05	0.023	0.009	587	59.9	750	199088	0.0083	0.0933	1.5	2.2	4.3	5.2	6.0
55	9.0	0.08	0.038	0.011	597	75.8	795	197811	0.0070	0.0971	2.0	2.5	5.0	5.9	8.0
56	5.0	0.11	0.020	0.011	580	52.0	790	180112	0.0081	0.0853	1.1	1.4	3.6	4.4	5.3
57	9.4	0.17	0.034	0.009	600	62.8	745	196886	0.0070	0.0995	2.2	2.2	4.4	5.0	6.4
58	7.3	0.07	0.017	0.011	591	33.9	815	192760	0.0067	0.0914	1.7	2.1	7.7	9.6	8.4
59	9.5	0.17	0.029	0.009	584	71.3	747	179779	0.0079	0.0941	2.1	2.2	4.1	4.7	6.3
60	9.5	0.16	0.026	0.012	593	63.4	790	201911	0.0081	0.1065	2.0	2.2	5.5	6.4	7.4
61	7.8	0.19	0.032	0.011	592	63.3	778	194567	0.0064	0.0917	1.8	1.8	3.7	4.4	5.9
62	6.5	0.13	0.032	0.010	553	64.0	793	185111	0.0069	0.0897	1.5	1.7	3.5	4.2	5.6
63	7.9	0.12	0.031	0.013	583	55.3	752	190473	0.0080	0.0984	1.8	2.1	5.6	6.7	8.0
64	5.9	0.16	0.022	0.010	617	47.7	815	183181	0.0070	0.0956	1.4	1.5	3.9	4.7	5.4
65	9.4	0.15	0.015	0.012	586	62.7	763	199602	0.0082	0.0951	1.8	2.1	5.3	6.4	6.8
66	6.8	0.11	0.028	0.008	568	32.0	774	201876	0.0063	0.0965	1.6	1.8	4.5	5.4	5.8
67	5.8	0.19	0.013	0.010	622	65.7	826	187946	0.0073	0.0941	1.2	1.2	3.1	3.7	4.5
68	6.8	0.08	0.035	0.009	599	79.4	786	198583	0.0075	0.0969	1.5	2.0	3.5	4.1	5.7
69	9.7	0.07	0.025	0.007	592	32.1	806	197257	0.0074	0.0897	2.3	2.7	6.6	8.1	8.6
70	8.5	0.16	0.013	0.010	586	78.4	762	171088	0.0081	0.0847	1.6	1.7	3.8	4.6	6.2
71	5.8	0.13	0.020	0.008	594	38.7	783	193012	0.0074	0.0967	1.4	1.5	4.0	4.8	4.9
72	6.3	0.12	0.025	0.013	571	38.6	743	179626	0.0076	0.0978	1.6	1.7	5.7	6.9	7.2
73	4.9	0.06	0.016	0.011	595	53.9	786	183534	0.0076	0.0963	1.1	1.6	4.3	5.3	5.3
74	9.7	0.17	0.020	0.012	573	37.5	764	185317	0.0067	0.0971	2.3	2.3	7.5	9.1	9.0
75	7.4	0.14	0.016	0.009	620	30.9	777	199637	0.0085	0.0942	1.7	1.8	6.1	7.5	6.4
76	5.1	0.19	0.014	0.007	578	39.0	742	181495	0.0075	0.0872	1.1	1.1	2.8	3.4	3.6
77	8.9	0.18	0.040	0.011	577	75.5	748	192604	0.0080	0.0972	2.0	2.0	3.9	4.5	6.5
78	9.7	0.14	0.025	0.009	597	47.5	777	194496	0.0073	0.0870	2.2	2.4	5.5	6.5	7.7

79	8.4	0.11	0.038	0.010	549	74.7	806	203014	0.0070	0.1037	1.8	2.2	4.1	4.8	6.2
80	8.3	0.10	0.020	0.009	627	77.5	782	202725	0.0072	0.0991	1.7	2.2	4.2	5.0	6.0
81	9.2	0.15	0.019	0.010	585	58.3	777	197113	0.0072	0.0974	1.9	2.1	5.0	6.0	6.5
82	7.0	0.12	0.027	0.008	613	74.5	786	205790	0.0069	0.0957	1.5	1.8	3.4	4.0	5.2
83	7.5	0.09	0.018	0.010	603	58.6	787	204777	0.0074	0.1034	1.6	2.0	4.9	5.9	6.0
84	6.0	0.15	0.027	0.011	575	57.6	747	204979	0.0081	0.1026	1.3	1.4	3.8	4.4	5.1
85	9.9	0.18	0.012	0.011	588	39.0	771	205677	0.0063	0.1044	2.0	2.1	7.1	8.6	7.0
86	10.0	0.11	0.036	0.013	589	68.1	799	197021	0.0064	0.0995	2.3	2.6	6.0	7.1	9.2
87	8.3	0.10	0.034	0.011	550	45.3	778	198606	0.0070	0.0918	1.9	2.2	5.4	6.6	8.0
88	9.4	0.18	0.032	0.008	616	46.7	792	189476	0.0073	0.0851	2.4	2.3	4.6	5.3	6.8
89	9.7	0.18	0.037	0.011	602	44.7	755	188512	0.0069	0.0932	2.5	2.4	5.9	7.0	8.6
90	7.4	0.13	0.034	0.011	586	68.8	807	188375	0.0078	0.0865	1.7	1.9	3.9	4.6	6.6
91	4.6	0.06	0.021	0.011	599	51.7	757	188348	0.0071	0.0992	1.1	1.4	4.1	5.0	5.2
92	6.5	0.05	0.014	0.011	611	75.2	768	206059	0.0074	0.0930	1.3	2.1	4.7	5.7	5.7
93	7.3	0.08	0.012	0.011	557	65.6	807	199583	0.0068	0.0953	1.3	2.0	4.6	5.7	5.7
94	8.4	0.11	0.017	0.011	561	78.0	784	183324	0.0075	0.1065	1.6	2.1	4.6	5.5	6.5
95	6.7	0.05	0.011	0.013	561	42.9	784	180734	0.0080	0.0918	1.4	2.1	7.5	9.7	7.4
96	6.6	0.11	0.016	0.009	604	68.8	770	198099	0.0074	0.1018	1.3	1.8	3.9	4.7	5.2
97	7.6	0.19	0.037	0.012	545	37.6	809	188625	0.0071	0.0893	1.9	1.8	4.8	5.9	7.0
98	8.5	0.11	0.012	0.008	595	46.9	807	193756	0.0070	0.0851	1.7	2.0	4.9	6.0	6.1
99	5.2	0.12	0.034	0.008	599	78.8	752	189488	0.0072	0.0977	1.2	1.4	2.5	2.9	4.1
100	7.4	0.14	0.023	0.008	581	49.3	725	185428	0.0069	0.0934	1.7	1.9	4.1	4.8	5.5

Table A.6: Drift Ratio Limit States (in Percent) of Bridge Columns Reinforced with ASTM A615 Grade 690.

Col. No.	L/D	$P/A_g f'_c$	ρ_l	ρ_s	f_y	f'_c	f_u	E	ε_{sh}	ε_u	DS-1	DS-2	DS-3	DS-4 _{cu}	DS-4 _{sb}
1	5.1	0.19	0.011	0.007	674	55.9	881	222438	0.0086	0.0781	1.0	1.1	2.4	3.0	3.4
2	4.4	0.20	0.014	0.009	649	70.6	850	180743	0.0087	0.0843	0.9	0.9	2.0	2.4	3.4
3	4.5	0.20	0.012	0.009	674	54.0	866	223241	0.0092	0.0828	0.9	0.9	2.6	3.2	3.5
4	4.5	0.16	0.035	0.007	674	70.1	912	207586	0.0077	0.0837	1.1	1.1	2.0	2.3	3.5
5	4.8	0.18	0.021	0.009	682	72.0	753	212745	0.0079	0.0827	1.1	1.1	2.2	2.7	3.7
6	4.3	0.18	0.036	0.008	673	59.9	883	198782	0.0081	0.0938	1.1	1.1	2.2	2.6	3.7
7	4.6	0.17	0.026	0.007	628	64.0	970	179989	0.0077	0.0793	1.1	1.2	2.1	2.5	3.7
8	5.2	0.17	0.013	0.007	694	48.7	935	223274	0.0078	0.0835	1.1	1.2	2.9	3.5	3.7
9	4.2	0.17	0.010	0.008	674	39.9	907	204743	0.0079	0.0817	1.0	1.0	3.1	3.8	3.7
10	4.2	0.17	0.022	0.008	707	50.3	828	215719	0.0054	0.0550	1.0	1.1	2.0	2.5	3.8
11	5.1	0.19	0.022	0.009	708	70.5	819	236216	0.0069	0.0757	1.1	1.2	2.3	2.8	3.8
12	4.5	0.17	0.028	0.008	702	37.8	814	221773	0.0084	0.0824	1.2	1.1	2.7	3.2	3.8
13	4.8	0.19	0.024	0.008	725	71.6	816	197563	0.0082	0.0790	1.2	1.2	2.2	2.6	3.8
14	4.4	0.10	0.015	0.007	687	67.2	903	217183	0.0087	0.1096	1.0	1.3	3.0	3.6	3.8
15	4.0	0.14	0.011	0.010	628	51.6	813	208131	0.0086	0.0790	0.9	1.0	2.9	3.6	3.9
16	4.1	0.08	0.014	0.007	726	79.7	971	208285	0.0091	0.0825	0.9	1.4	2.5	3.1	4.0
17	4.8	0.16	0.038	0.008	667	70.6	929	197508	0.0083	0.0818	1.2	1.3	2.2	2.5	4.0
18	4.7	0.12	0.012	0.007	687	43.5	775	213614	0.0078	0.0812	1.1	1.3	3.2	3.9	4.0
19	5.5	0.15	0.013	0.008	689	70.4	908	217195	0.0081	0.0872	1.1	1.3	2.7	3.3	4.0
20	4.8	0.17	0.026	0.008	726	71.0	830	218463	0.0088	0.0657	1.1	1.2	2.1	2.6	4.0
21	4.0	0.18	0.040	0.009	686	44.2	894	199665	0.0085	0.0930	1.2	1.1	2.5	3.1	4.0
22	5.8	0.18	0.013	0.008	716	77.5	928	204518	0.0085	0.0853	1.2	1.3	2.6	3.1	4.0
23	5.8	0.17	0.013	0.007	673	77.2	946	186053	0.0085	0.0807	1.2	1.3	2.4	2.9	4.0
24	5.1	0.17	0.035	0.009	658	63.3	885	234371	0.0082	0.0605	1.2	1.2	2.1	2.6	4.1
25	4.1	0.17	0.020	0.011	664	68.2	956	203875	0.0089	0.0699	0.9	1.0	2.2	2.7	4.1
26	5.2	0.18	0.019	0.010	691	73.5	889	228092	0.0082	0.0824	1.1	1.2	2.6	3.1	4.1
27	4.9	0.17	0.018	0.008	750	75.9	857	188381	0.0084	0.0768	1.2	1.2	2.3	2.8	4.1
28	4.6	0.17	0.015	0.010	616	72.7	782	183179	0.0095	0.0894	1.0	1.1	2.6	3.1	4.1
29	4.1	0.17	0.021	0.008	742	32.4	1001	199803	0.0078	0.0691	1.2	1.1	2.7	3.3	4.2
30	4.5	0.09	0.011	0.008	727	57.0	810	202280	0.0085	0.0905	1.0	1.4	3.3	4.1	4.2
31	5.7	0.19	0.012	0.009	666	78.5	809	188069	0.0087	0.0880	1.1	1.2	2.6	3.1	4.2
32	5.0	0.20	0.027	0.010	644	50.1	864	226502	0.0083	0.0759	1.2	1.2	2.7	3.3	4.2
33	5.3	0.18	0.014	0.009	703	60.9	1022	205620	0.0079	0.0930	1.2	1.2	3.1	3.7	4.2
34	4.0	0.15	0.036	0.008	727	46.9	851	199216	0.0085	0.0783	1.2	1.1	2.4	2.9	4.2
35	4.8	0.09	0.024	0.008	665	56.7	913	238016	0.0095	0.0743	1.1	1.4	2.7	3.3	4.3
36	5.3	0.19	0.013	0.007	729	34.9	877	196811	0.0083	0.0773	1.4	1.3	3.4	4.0	4.3
37	4.1	0.16	0.021	0.010	734	67.9	875	197795	0.0075	0.0795	1.0	1.0	2.5	3.0	4.3

38	5.1	0.05	0.011	0.008	672	71.0	870	221240	0.0076	0.0723	1.0	1.8	3.3	3.9	4.3
39	4.0	0.16	0.034	0.010	665	72.0	821	189510	0.0075	0.0767	1.0	1.0	2.1	2.6	4.3
40	4.1	0.08	0.025	0.010	652	77.4	889	227761	0.0100	0.0741	0.9	1.3	2.4	3.0	4.3
41	5.0	0.17	0.036	0.009	670	58.8	961	210928	0.0084	0.0837	1.3	1.3	2.5	3.0	4.3
42	5.0	0.18	0.025	0.009	738	74.9	880	209948	0.0081	0.0807	1.2	1.2	2.5	2.9	4.3
43	6.9	0.18	0.020	0.007	656	73.7	962	214547	0.0069	0.0599	1.4	1.5	2.3	2.9	4.3
44	4.3	0.20	0.036	0.009	737	53.7	861	187911	0.0078	0.0843	1.3	1.1	2.5	3.0	4.3
45	4.5	0.13	0.038	0.009	671	57.7	797	212574	0.0078	0.0732	1.2	1.2	2.4	2.8	4.3
46	7.0	0.19	0.021	0.008	696	77.9	738	218053	0.0070	0.0671	1.5	1.5	2.5	3.0	4.3
47	4.5	0.16	0.033	0.010	686	66.1	1008	216327	0.0096	0.0662	1.1	1.1	2.2	2.7	4.4
48	6.1	0.17	0.014	0.008	725	65.3	783	223513	0.0066	0.0904	1.3	1.4	3.2	3.9	4.4
49	4.7	0.16	0.019	0.010	647	53.9	918	199190	0.0083	0.0875	1.1	1.1	3.1	3.7	4.4
50	4.4	0.17	0.038	0.009	753	66.5	803	201206	0.0086	0.0685	1.2	1.2	2.2	2.6	4.4
51	4.2	0.07	0.016	0.007	697	44.5	954	206753	0.0086	0.0862	1.0	1.3	3.3	4.1	4.4
52	5.5	0.17	0.025	0.007	717	35.1	737	211146	0.0084	0.0870	1.5	1.4	3.4	4.1	4.4
53	4.1	0.09	0.034	0.008	701	71.3	906	207417	0.0100	0.0768	1.1	1.2	2.3	2.8	4.4
54	4.8	0.15	0.025	0.009	669	49.0	830	206624	0.0065	0.0829	1.2	1.2	2.9	3.5	4.4
55	4.8	0.20	0.016	0.009	727	50.1	830	189769	0.0063	0.0871	1.3	1.1	3.1	3.7	4.4
56	6.1	0.17	0.038	0.007	673	61.9	1001	221553	0.0076	0.0697	1.5	1.5	2.5	2.9	4.4
57	4.9	0.08	0.012	0.008	697	79.9	917	199401	0.0116	0.0848	1.1	1.5	3.0	3.6	4.5
58	4.5	0.17	0.039	0.010	634	50.1	897	199857	0.0095	0.0792	1.2	1.2	2.5	3.0	4.5
59	4.6	0.12	0.017	0.008	701	75.8	887	184419	0.0087	0.0764	1.1	1.3	2.5	3.1	4.5
60	4.4	0.08	0.031	0.007	684	71.1	800	177730	0.0080	0.0813	1.2	1.4	2.4	2.9	4.5
61	4.3	0.12	0.025	0.010	628	50.8	958	211640	0.0075	0.0879	1.0	1.2	3.1	3.7	4.5
62	5.0	0.10	0.011	0.009	696	47.2	937	226608	0.0082	0.0802	1.1	1.4	3.7	4.6	4.5
63	5.6	0.13	0.022	0.007	685	69.2	856	196973	0.0074	0.0863	1.3	1.5	2.8	3.4	4.5
64	4.9	0.14	0.015	0.009	702	59.1	899	198469	0.0083	0.0771	1.1	1.3	2.9	3.6	4.5
65	4.9	0.08	0.011	0.007	743	52.6	875	209290	0.0072	0.0725	1.2	1.5	3.2	4.0	4.5
66	4.9	0.10	0.036	0.008	693	59.5	920	223672	0.0075	0.0830	1.2	1.4	2.7	3.2	4.5
67	9.0	0.18	0.016	0.007	655	74.3	785	235700	0.0087	0.0821	1.7	1.9	3.1	3.7	4.6
68	5.2	0.09	0.017	0.009	647	57.9	712	208211	0.0080	0.0892	1.1	1.5	3.5	4.2	4.6
69	4.5	0.16	0.031	0.008	740	47.4	862	184485	0.0070	0.0872	1.4	1.2	2.9	3.4	4.6
70	4.7	0.12	0.037	0.008	721	73.0	908	204354	0.0078	0.0884	1.2	1.3	2.6	3.1	4.6
71	4.0	0.17	0.021	0.011	751	70.1	945	201467	0.0064	0.0703	1.0	1.0	2.4	3.0	4.6
72	5.3	0.17	0.022	0.008	693	44.8	869	186512	0.0084	0.0784	1.4	1.4	3.0	3.6	4.6
73	4.9	0.15	0.014	0.011	666	63.6	977	201761	0.0093	0.0904	1.1	1.2	3.3	4.0	4.6
74	5.3	0.11	0.012	0.009	690	70.5	831	205214	0.0079	0.0809	1.1	1.5	3.1	3.8	4.6
75	6.0	0.15	0.010	0.007	747	69.8	800	178101	0.0105	0.0802	1.3	1.4	2.9	3.5	4.6
76	4.9	0.15	0.038	0.007	740	41.5	903	219091	0.0081	0.0679	1.4	1.3	2.6	3.1	4.6
77	4.3	0.11	0.033	0.008	698	52.3	880	189558	0.0083	0.0966	1.2	1.2	3.0	3.5	4.6
78	4.6	0.20	0.030	0.011	755	74.0	978	213113	0.0067	0.1017	1.2	1.1	2.8	3.3	4.6

79	5.3	0.17	0.038	0.008	691	52.8	1047	200992	0.0084	0.0796	1.5	1.4	2.7	3.1	4.7
80	4.1	0.06	0.029	0.008	762	69.0	835	206143	0.0094	0.0796	1.1	1.4	2.7	3.3	4.7
81	4.7	0.09	0.033	0.008	617	60.1	806	197597	0.0085	0.0752	1.1	1.4	2.6	3.1	4.7
82	4.8	0.07	0.013	0.008	760	66.9	879	199697	0.0090	0.0849	1.2	1.6	3.3	4.1	4.7
83	4.2	0.05	0.036	0.008	704	72.6	845	196341	0.0086	0.0904	1.1	1.4	2.7	3.2	4.7
84	4.3	0.11	0.019	0.010	655	49.7	827	193813	0.0105	0.0659	1.0	1.2	2.8	3.5	4.7
85	4.6	0.14	0.022	0.011	649	51.8	1031	209221	0.0058	0.0810	1.1	1.1	3.1	3.8	4.7
86	4.6	0.12	0.013	0.009	652	35.6	918	192482	0.0101	0.0682	1.1	1.2	3.4	4.2	4.7
87	4.3	0.17	0.032	0.011	707	58.8	1004	200266	0.0079	0.0840	1.2	1.1	2.7	3.2	4.7
88	4.1	0.13	0.016	0.010	694	34.6	974	195134	0.0073	0.0935	1.1	1.1	4.1	5.0	4.8
89	4.7	0.19	0.034	0.012	723	71.1	772	214277	0.0091	0.0789	1.2	1.2	2.6	3.1	4.8
90	4.5	0.08	0.011	0.011	668	61.2	861	202973	0.0077	0.0709	1.0	1.4	3.3	4.2	4.8
91	5.6	0.16	0.040	0.007	685	34.3	819	206507	0.0090	0.0813	1.6	1.5	3.1	3.7	4.8
92	5.6	0.18	0.018	0.009	687	57.4	1003	206288	0.0076	0.0779	1.3	1.3	3.1	3.7	4.8
93	5.2	0.15	0.011	0.008	819	61.8	932	201224	0.0073	0.0791	1.2	1.3	3.3	4.0	4.8
94	4.5	0.10	0.030	0.009	706	30.4	725	210719	0.0087	0.0903	1.3	1.3	3.7	4.4	4.8
95	5.8	0.20	0.010	0.012	624	59.4	916	201567	0.0082	0.0736	1.1	1.1	3.1	3.9	4.8
96	4.6	0.14	0.029	0.010	733	66.9	904	212236	0.0080	0.0819	1.2	1.2	2.8	3.4	4.8
97	5.5	0.12	0.013	0.009	662	74.2	866	201318	0.0081	0.0829	1.1	1.5	3.2	3.9	4.8
98	8.2	0.19	0.017	0.008	675	68.5	894	239592	0.0100	0.0717	1.6	1.7	3.2	3.8	4.8
99	5.1	0.07	0.024	0.007	662	63.6	885	192044	0.0088	0.0871	1.2	1.6	3.0	3.7	4.8
100	4.7	0.15	0.010	0.010	615	36.6	891	180045	0.0093	0.0762	1.1	1.1	3.8	4.8	4.8

Table A.7: Drift Ratio Limit States (in Percent) of Bridge Columns Reinforced with ASTM A1035 Grade 690.

Col. No.	L/D	$P/A_g f'_c$	ρ_l	ρ_s	f_y	f'_c	E	ε_u	DS-1	DS-2	DS-3	DS-4 _{cu}	DS-4 _{sb}
1	9.7	0.16	0.038	0.011	850	68.9	192455	0.0483	3.1	2.7	4.9	5.8	10.9
2	5.6	0.13	0.023	0.012	767	34.5	194548	0.0502	1.7	1.6	3.9	4.8	7.3
3	4.3	0.10	0.037	0.008	939	60.0	196517	0.0454	1.5	1.3	2.3	2.8	5.5
4	4.6	0.15	0.034	0.012	649	74.9	191213	0.0502	1.1	1.2	2.1	2.6	5.1
5	6.3	0.19	0.012	0.007	922	54.6	179063	0.0464	1.9	1.4	3.0	3.8	6.2
6	9.4	0.18	0.013	0.009	792	58.0	202832	0.0467	2.1	2.1	3.8	4.8	7.5
7	8.5	0.08	0.010	0.009	884	76.6	194485	0.0582	2.1	2.4	4.5	5.5	7.4
8	5.9	0.09	0.021	0.007	848	79.5	192257	0.0503	1.6	1.8	2.7	3.3	5.7
9	5.2	0.19	0.029	0.013	946	74.5	191936	0.0424	1.8	1.3	2.8	3.4	7.8
10	5.0	0.12	0.016	0.008	856	50.2	205861	0.0606	1.4	1.4	3.1	3.8	5.2
11	7.9	0.12	0.016	0.012	938	53.7	162222	0.0464	2.8	2.3	5.5	6.7	11.6
12	5.3	0.12	0.025	0.013	895	67.8	175248	0.0468	1.7	1.5	3.3	4.1	8.2
13	5.1	0.18	0.019	0.009	911	40.7	194083	0.0442	1.8	1.3	3.0	3.6	6.0
14	9.9	0.11	0.015	0.010	841	63.4	197826	0.0471	2.5	2.7	4.8	5.9	9.4
15	8.3	0.16	0.034	0.010	838	38.2	210265	0.0514	2.8	2.4	4.7	5.5	8.6
16	4.5	0.16	0.037	0.011	786	46.1	209985	0.0532	1.4	1.2	2.5	3.0	5.2
17	9.4	0.07	0.012	0.012	924	72.8	183422	0.0466	2.6	3.0	5.5	6.9	11.2
18	6.9	0.18	0.034	0.008	957	64.1	190301	0.0514	2.6	1.9	3.5	4.1	7.2
19	4.0	0.17	0.027	0.012	910	57.3	175550	0.0463	1.5	1.1	2.5	3.1	6.6
20	4.2	0.08	0.014	0.012	740	64.5	187064	0.0591	1.1	1.4	3.1	4.0	5.6
21	4.2	0.12	0.023	0.007	905	48.3	190363	0.0412	1.4	1.3	2.3	2.8	5.2
22	9.1	0.11	0.020	0.012	859	53.9	191788	0.0504	2.6	2.6	5.7	6.9	10.8
23	4.6	0.09	0.032	0.012	750	62.1	188264	0.0510	1.3	1.4	2.8	3.4	6.4
24	9.0	0.19	0.026	0.011	910	49.5	184670	0.0521	3.3	2.4	5.4	6.4	10.7
25	6.3	0.12	0.037	0.011	838	70.3	175650	0.0482	2.1	1.9	3.5	4.2	8.4
26	7.6	0.13	0.029	0.008	808	35.5	169948	0.0475	2.8	2.3	4.4	5.1	8.4
27	6.6	0.07	0.016	0.010	858	61.0	199964	0.0514	1.8	2.1	4.0	5.0	7.6
28	8.6	0.16	0.026	0.011	878	76.5	181480	0.0451	2.6	2.3	4.2	5.2	10.1
29	6.0	0.17	0.014	0.008	982	66.5	195306	0.0485	1.7	1.5	3.0	3.8	6.3
30	5.7	0.12	0.015	0.009	856	33.2	164935	0.0444	2.0	1.7	4.0	4.9	7.5
31	7.9	0.12	0.025	0.010	935	47.6	200442	0.0502	2.7	2.3	5.1	6.1	9.7
32	7.5	0.20	0.020	0.007	816	52.7	200768	0.0500	2.1	1.8	3.3	4.0	6.2
33	8.5	0.06	0.032	0.007	754	53.6	186405	0.0529	2.4	2.7	4.3	5.2	8.4
34	9.5	0.13	0.020	0.012	892	52.0	185741	0.0507	3.0	2.6	6.3	7.6	12.1
35	9.3	0.11	0.011	0.010	725	42.4	189733	0.0528	2.2	2.5	5.4	6.7	8.6
36	7.9	0.09	0.013	0.013	829	71.5	173522	0.0525	2.1	2.4	4.7	5.9	9.6
37	7.6	0.06	0.013	0.010	860	57.1	233514	0.0492	1.8	2.4	4.5	5.7	7.3

38	6.5	0.18	0.031	0.011	767	49.4	201389	0.0547	2.0	1.7	3.5	4.2	6.9
39	4.3	0.16	0.022	0.012	820	64.6	179560	0.0540	1.3	1.1	2.6	3.3	6.0
40	7.2	0.07	0.025	0.008	937	79.8	195232	0.0486	2.2	2.4	3.7	4.4	7.9
41	9.0	0.14	0.024	0.011	775	73.6	193376	0.0580	2.3	2.4	4.5	5.5	8.9
42	4.0	0.19	0.020	0.012	838	72.5	226232	0.0476	1.0	0.9	2.0	2.6	4.9
43	6.9	0.16	0.017	0.009	859	35.0	212989	0.0461	2.1	1.9	4.0	4.9	7.0
44	5.2	0.10	0.018	0.008	753	54.6	206672	0.0506	1.3	1.5	2.7	3.4	5.0
45	8.5	0.12	0.016	0.009	891	42.2	193697	0.0541	2.6	2.4	5.7	6.9	9.3
46	5.0	0.15	0.035	0.009	800	33.7	195423	0.0514	1.8	1.5	2.9	3.5	5.8
47	7.1	0.13	0.016	0.011	910	69.0	167458	0.0478	2.1	1.9	4.2	5.2	9.6
48	4.9	0.13	0.025	0.012	826	33.4	200395	0.0532	1.7	1.4	3.6	4.4	6.8
49	9.0	0.12	0.019	0.010	804	57.1	208058	0.0371	2.3	2.5	4.0	5.0	8.9
50	4.6	0.12	0.021	0.013	866	71.6	179307	0.0473	1.4	1.3	2.9	3.7	7.2
51	7.6	0.15	0.037	0.011	875	37.7	210450	0.0476	2.7	2.2	4.4	5.3	9.0
52	9.1	0.11	0.034	0.010	962	62.3	179220	0.0492	3.4	2.8	5.5	6.5	11.7
53	9.8	0.12	0.018	0.012	864	67.0	186121	0.0513	2.7	2.7	5.7	7.0	11.5
54	7.9	0.05	0.016	0.011	697	44.9	195667	0.0457	1.9	2.5	4.6	5.7	8.2
55	9.0	0.08	0.037	0.009	657	33.4	206536	0.0420	2.4	2.5	4.1	4.9	8.3
56	9.9	0.07	0.019	0.012	826	69.8	218149	0.0501	2.4	3.0	5.3	6.6	10.3
57	7.7	0.08	0.033	0.009	854	59.0	205831	0.0576	2.3	2.4	4.3	5.2	8.2
58	8.2	0.11	0.011	0.013	960	73.0	197450	0.0557	2.1	2.2	5.1	6.5	9.9
59	6.8	0.10	0.027	0.009	973	34.1	187409	0.0444	2.8	2.1	4.5	5.3	9.1
60	7.6	0.16	0.036	0.012	886	73.8	175774	0.0496	2.7	2.1	4.2	5.0	10.1
61	9.7	0.17	0.015	0.011	866	35.1	202585	0.0597	3.1	2.5	7.0	8.4	10.2
62	8.9	0.06	0.016	0.012	791	47.2	176490	0.0584	2.5	2.8	6.8	8.4	10.9
63	7.4	0.20	0.018	0.010	637	41.1	172010	0.0521	1.9	1.7	3.6	4.4	6.5
64	9.4	0.19	0.011	0.009	832	57.0	202753	0.0454	2.2	2.0	4.0	5.0	7.8
65	5.6	0.19	0.039	0.008	893	76.5	189415	0.0577	1.9	1.5	2.7	3.2	6.0
66	4.4	0.11	0.021	0.009	649	41.4	173324	0.0442	1.2	1.3	2.4	3.1	5.1
67	8.8	0.19	0.019	0.009	735	63.1	206113	0.0441	2.1	2.0	3.4	4.3	7.2
68	5.5	0.13	0.027	0.009	820	45.8	200774	0.0486	1.7	1.6	3.1	3.7	6.2
69	5.8	0.10	0.033	0.009	726	37.6	191757	0.0562	1.8	1.7	3.5	4.1	6.5
70	7.4	0.07	0.028	0.008	785	67.3	192868	0.0610	2.0	2.3	3.9	4.7	7.3
71	8.1	0.06	0.021	0.011	888	73.3	203885	0.0458	2.3	2.6	4.5	5.6	9.6
72	6.6	0.14	0.016	0.010	784	55.1	195839	0.0443	1.7	1.7	3.3	4.2	6.9
73	7.9	0.19	0.040	0.010	936	31.1	177746	0.0468	3.6	2.3	5.2	5.9	10.2
74	6.5	0.18	0.023	0.010	676	50.6	182694	0.0546	1.7	1.6	3.2	3.9	6.2
75	4.7	0.17	0.028	0.009	735	36.2	184991	0.0408	1.5	1.3	2.4	2.9	5.3
76	6.6	0.14	0.018	0.010	827	31.1	198778	0.0582	2.1	1.8	4.8	5.8	7.3
77	6.4	0.08	0.013	0.012	799	58.3	167871	0.0379	1.8	2.0	3.5	4.4	8.4
78	4.1	0.19	0.020	0.009	790	73.3	191500	0.0379	1.1	1.0	1.6	2.1	4.6

79	9.4	0.05	0.037	0.012	790	76.2	193960	0.0532	2.6	3.0	5.1	6.1	10.9
80	6.8	0.16	0.030	0.008	756	40.7	215713	0.0507	2.0	1.8	3.2	3.8	5.8
81	4.9	0.16	0.027	0.007	912	32.2	205073	0.0417	1.8	1.4	2.7	3.1	5.4
82	4.0	0.08	0.022	0.007	919	31.8	206517	0.0443	1.4	1.3	2.7	3.2	5.2
83	6.0	0.12	0.039	0.012	787	48.2	184693	0.0468	2.0	1.8	3.5	4.2	8.0
84	6.3	0.16	0.021	0.007	702	58.2	182758	0.0584	1.6	1.6	2.8	3.4	5.2
85	6.9	0.11	0.027	0.012	913	65.7	197211	0.0422	2.2	2.0	4.0	4.9	9.5
86	6.3	0.20	0.022	0.012	815	45.1	173506	0.0515	2.2	1.6	3.9	4.7	7.9
87	5.4	0.17	0.014	0.008	793	45.8	173174	0.0483	1.6	1.4	2.9	3.6	5.6
88	8.8	0.16	0.022	0.012	777	44.6	188619	0.0497	2.7	2.3	5.2	6.3	9.8
89	5.3	0.12	0.034	0.010	943	48.1	193661	0.0549	2.0	1.6	3.5	4.1	7.1
90	5.9	0.15	0.026	0.010	940	72.4	181042	0.0600	2.0	1.6	3.5	4.2	7.4
91	6.1	0.15	0.038	0.011	894	79.4	173347	0.0482	2.2	1.7	3.3	4.0	8.5
92	4.8	0.12	0.014	0.011	765	50.2	183746	0.0455	1.3	1.3	2.9	3.7	6.0
93	10.0	0.08	0.036	0.008	812	34.6	200389	0.0506	3.3	3.1	5.5	6.3	10.0
94	5.1	0.08	0.020	0.009	848	66.4	199892	0.0442	1.4	1.6	2.7	3.3	5.8
95	8.1	0.19	0.033	0.012	779	66.0	206594	0.0535	2.3	2.1	4.0	4.8	8.3
96	7.4	0.13	0.037	0.008	998	33.0	181667	0.0556	3.4	2.3	5.2	6.0	9.6
97	8.5	0.17	0.030	0.009	907	44.3	196597	0.0542	3.1	2.4	5.0	5.9	9.3
98	8.5	0.18	0.026	0.008	900	60.6	193768	0.0407	2.8	2.2	3.7	4.5	8.2
99	7.6	0.11	0.023	0.011	974	55.7	187118	0.0491	2.7	2.3	5.1	6.1	10.4
100	6.7	0.14	0.017	0.012	751	51.2	181404	0.0425	1.8	1.7	3.7	4.6	8.1

Appendix B

Table B.1: Properties of the *Concrete01* Constitutive Model Used for Numerical Model Validation.

Experimental Program	Specimen	Concrete Type	F _{pc} (MPa)	eps _{c0}	F _{pcu} (MPa)	eps _U
Goodnight et al. (2015)	Test 15	Unconfined	-49.9	-0.002	0	-0.004
		Confined	-59.9	-0.004	-38.0	-0.014
Barcley and Kowalsky (2020)	Test 3	Unconfined	-47.0	-0.002	0	-0.004
		Confined	-59.1	-0.005	-43.8	-0.014
Restrepo et al. (2006)	Unit 2	Unconfined	-56.5	-0.002	0	-0.004
		Confined	-73.8	-0.005	-66.0	-0.009

Table B.2: Properties of the *ReinforcingSteel* Constitutive Model Used for Numerical Model Validation.

Experimental Program	Specimen	f _y (MPa)	f _u (MPa)	E _s (MPa)	E _{sh} (MPa)	esh	eult
Goodnight et al. (2015)	Test 15	469.5	653.6	200000	5998	0.015	0.133
Barcley and Kowalsky (2020)	Test 3	572.3	758.4	192281	5768	0.008	0.104

Table B.3: Properties of the *Steel02* Constitutive Model Used for Numerical Model Validation.

Experimental Program	Specimen	f _y (MPa)	E _s (MPa)	b	R0	cR1	cR2
Restrepo et al. (2006)	Unit 2	689.5	193998	0.05	15	0.925	0.15

Table B.4: Properties of the *Bond_SP01* Constitutive Model Used for Numerical Model Validation.

Experimental Program	Specimen	f _y (MPa)	S _y (mm)	f _u (MPa)	S _u (mm)	b	R
Goodnight et al. (2015)	Test 15	469.5	0.432	653.6	12.8	0.5	0.5
Barcley and Kowalsky (2020)	Test 3	572.3	0.508	758.4	15.0	0.5	0.5
Restrepo et al. (2006)	Unit 2	689.5	0.467	1172.1	14.0	0.5	0.5

The following symbols are used in Tables B.1 to B.4:

F_{pc} = concrete compressive strength at 28 days;

ϵ_{sc0} = concrete strain at maximum strength;

F_{pcu} = concrete crushing strength;

ϵ_{sU} = concrete strain at crushing strength;

f_y = yield stress in tension;

f_u = ultimate stress in tension;

E_s = Initial elastic tangent;

E_{sh} = tangent at initial strain hardening;

ϵ_{sh} = strain corresponding to initial strain hardening;

ϵ_{ult} = strain at peak stress;

b = strain-hardening ratio;

R_0 = parameter to control the transition from elastic to plastic branches;

cR_1 = parameter to control the transition from elastic to plastic branches;

cR_2 = parameter to control the transition from elastic to plastic branches;

S_y = Rebar slip at member interface under yield stress;

S_u = Rebar slip at the loaded end at the bar fracture strength;

b = Initial hardening ratio in the monotonic slip vs. bar stress response; and

R = Pinching factor for the cyclic slip vs. bar response.

Table B.5: Computed Damage Indices for Bridge Columns Reinforced with ASTM A706 Grade 420 Steel Bars and Subjected to Ground Motions from Crustal Earthquakes at Target Displacement Ductility Level of 2.

Bridge Column	Bar Slenderness Ratio	Record No.									
		1	2	3	4	5	6	7	8	9	10
P05L1S07	4	0.01	0.00	0.01	0.01	0.01	0.01	0.01	0.01	0.00	0.01
P20L1S07		0.03	0.00	0.03	0.03	0.01	0.04	0.02	0.01	0.00	0.01
P05L4S07		0.03	0.02	0.03	0.02	0.03	0.02	0.02	0.02	0.01	0.01
P20L4S07		0.02	0.01	0.02	0.05	0.02	0.02	0.03	0.01	0.00	0.01
P05L1S13		0.01	0.00	0.01	0.01	0.01	0.02	0.02	0.01	0.00	0.01
P20L1S13		0.03	0.00	0.03	0.03	0.01	0.03	0.02	0.01	0.00	0.01
P05L4S13		0.03	0.02	0.03	0.02	0.03	0.02	0.02	0.02	0.02	0.01
P20L4S13		0.02	0.01	0.02	0.04	0.02	0.01	0.02	0.01	0.00	0.01
P05L1S07	6	0.02	0.01	0.02	0.02	0.02	0.03	0.03	0.02	0.01	0.01
P20L1S07		0.06	0.01	0.05	0.06	0.03	0.07	0.03	0.03	0.01	0.02
P05L4S07		0.05	0.04	0.05	0.04	0.06	0.04	0.04	0.04	0.02	0.02
P20L4S07		0.03	0.01	0.04	0.08	0.04	0.03	0.05	0.02	0.01	0.02
P05L1S13		0.02	0.01	0.02	0.02	0.02	0.04	0.03	0.02	0.01	0.01
P20L1S13		0.06	0.01	0.05	0.05	0.03	0.06	0.03	0.03	0.01	0.02
P05L4S13		0.05	0.04	0.06	0.04	0.06	0.04	0.04	0.04	0.03	0.03
P20L4S13		0.03	0.01	0.03	0.07	0.03	0.03	0.04	0.02	0.01	0.02

Table B.6: Computed Damage Indices for Bridge Columns Reinforced with ASTM A706 Grade 420 Steel Bars and Subjected to Ground Motions from Crustal Earthquakes at Target Displacement Ductility Level of 4.

Bridge Column	Bar Slenderness Ratio	Record No.									
		1	2	3	4	5	6	7	8	9	10
P05L1S07	4	0.04	0.02	0.10	0.11	0.07	0.08	0.11	0.04	0.02	0.05
P20L1S07		0.14	0.02	0.13	0.28	0.11	0.18	0.20	0.05	0.03	0.13
P05L4S07		0.11	0.08	0.30	0.25	0.26	0.25	0.36	0.10	0.08	0.13
P20L4S07		0.18	0.03	0.30	0.53	0.20	0.50	0.19	0.12	0.03	0.07
P05L1S13		0.03	0.02	0.11	0.11	0.07	0.09	0.11	0.04	0.02	0.05
P20L1S13		0.13	0.02	0.13	0.24	0.10	0.15	0.11	0.05	0.03	0.11
P05L4S13		0.12	0.09	0.33	0.27	0.27	0.29	0.37	0.12	0.09	0.15
P20L4S13		0.21	0.03	0.23	0.29	0.12	0.27	0.19	0.09	0.03	0.08
P05L1S07	6	0.08	0.04	0.16	0.18	0.12	0.14	0.17	0.07	0.04	0.08
P20L1S07		0.24	0.03	0.21	0.43	0.18	0.29	0.36	0.09	0.05	0.20
P05L4S07		0.18	0.13	0.44	0.36	0.37	0.37	0.51	0.17	0.13	0.20
P20L4S07		0.29	0.05	0.52	0.92	0.37	0.89	0.33	0.23	0.05	0.14
P05L1S13		0.06	0.04	0.17	0.19	0.12	0.15	0.17	0.07	0.04	0.08
P20L1S13		0.21	0.03	0.20	0.37	0.15	0.25	0.16	0.08	0.05	0.18
P05L4S13		0.19	0.14	0.47	0.38	0.38	0.42	0.52	0.18	0.14	0.22
P20L4S13		0.32	0.05	0.35	0.44	0.19	0.41	0.28	0.15	0.05	0.12

Table B.7: Computed Damage Indices for Bridge Columns Reinforced with ASTM A706 Grade 420 Steel Bars and Subjected to Ground Motions from Crustal Earthquakes at Target Displacement Ductility Level of 6.

Bridge Column	Bar Slenderness Ratio	Record No.									
		1	2	3	4	5	6	7	8	9	10
P05L1S07	4	0.38	0.05	0.32	0.33	0.21	0.41	0.32	0.11	0.05	0.13
P20L1S07		0.37	0.04	0.29	0.80	0.37	0.77	0.54	0.09	0.08	0.59
P05L4S07		0.50	0.16	1.00	0.86	0.88	0.90	1.00	0.24	0.19	0.41
P20L4S07		0.69	0.12	0.70	1.00	0.70	0.99	0.62	0.28	0.25	0.79
P05L1S13		0.38	0.05	0.35	0.34	0.21	0.38	0.32	0.12	0.05	0.14
P20L1S13		0.23	0.05	0.22	0.54	0.31	0.57	0.41	0.11	0.08	0.28
P05L4S13		0.33	0.19	1.00	0.77	0.68	0.75	1.00	0.25	0.21	0.38
P20L4S13		0.39	0.06	0.53	1.00	0.64	0.97	0.43	0.30	0.15	0.81
P05L1S07	6	0.55	0.09	0.48	0.49	0.30	0.60	0.44	0.18	0.08	0.20
P20L1S07		0.56	0.07	0.49	1.00	0.63	1.00	0.83	0.17	0.12	0.94
P05L4S07		0.91	0.25	1.00	1.00	1.00	1.00	1.00	0.39	0.27	0.63
P20L4S07		1.00	0.28	1.00	1.00	1.00	1.00	0.90	0.47	0.42	1.00
P05L1S13		0.55	0.09	0.51	0.50	0.31	0.56	0.44	0.19	0.08	0.20
P20L1S13		0.36	0.09	0.33	0.76	0.50	0.96	0.66	0.17	0.12	0.40
P05L4S13		0.48	0.28	1.00	1.00	0.86	0.99	1.00	0.37	0.29	0.50
P20L4S13		0.57	0.11	0.83	1.00	0.96	1.00	0.63	0.50	0.21	1.00

Table B.8: Computed Damage Indices for Bridge Columns Reinforced with ASTM A706 Grade 420 Steel Bars and Subjected to Ground Motions from Subduction Earthquakes at Target Displacement Ductility Level of 2.

Bridge Column	Bar Slenderness Ratio	Record No.									
		1	2	3	4	5	6	7	8	9	10
P05L1S07	4	0.04	0.02	0.02	0.03	0.04	0.05	0.02	0.01	0.02	0.02
P20L1S07		0.03	0.03	0.04	0.02	0.06	0.06	0.04	0.01	0.04	0.04
P05L4S07		0.09	0.08	0.11	0.07	0.12	0.08	0.06	0.04	0.09	0.09
P20L4S07		0.07	0.03	0.02	0.02	0.12	0.08	0.03	0.02	0.05	0.05
P05L1S13		0.04	0.03	0.02	0.03	0.05	0.06	0.02	0.02	0.02	0.02
P20L1S13		0.03	0.03	0.03	0.01	0.05	0.06	0.04	0.01	0.04	0.04
P05L4S13		0.05	0.09	0.12	0.08	0.13	0.09	0.06	0.04	0.10	0.10
P20L4S13		0.07	0.03	0.02	0.02	0.11	0.07	0.03	0.02	0.04	0.04
P05L1S07	6	0.08	0.05	0.04	0.06	0.09	0.11	0.04	0.02	0.05	0.05
P20L1S07		0.07	0.06	0.08	0.04	0.11	0.12	0.08	0.03	0.08	0.08
P05L4S07		0.18	0.16	0.20	0.14	0.23	0.14	0.11	0.07	0.17	0.17
P20L4S07		0.13	0.07	0.04	0.04	0.22	0.16	0.07	0.04	0.09	0.09
P05L1S13		0.09	0.06	0.04	0.06	0.10	0.13	0.05	0.03	0.05	0.05
P20L1S13		0.06	0.06	0.07	0.03	0.11	0.11	0.08	0.02	0.08	0.08
P05L4S13		0.09	0.17	0.23	0.16	0.25	0.17	0.12	0.07	0.19	0.19
P20L4S13		0.13	0.07	0.04	0.04	0.20	0.14	0.06	0.04	0.08	0.08

Table B.9: Computed Damage Indices for Bridge Columns Reinforced with ASTM A706 Grade 420 Steel Bars and Subjected to Ground Motions from Subduction Earthquakes at Target Displacement Ductility Level of 4.

Bridge Column	Bar Slenderness Ratio	Record No.									
		1	2	3	4	5	6	7	8	9	10
P05L1S07	4	0.26	0.17	0.13	0.10	0.29	0.24	0.15	0.10	0.18	0.18
P20L1S07		0.18	0.18	0.30	0.22	0.33	0.44	0.14	0.08	0.37	0.37
P05L4S07		0.65	0.38	0.66	0.47	0.68	1.00	0.49	0.20	0.54	0.54
P20L4S07		0.83	0.44	0.98	0.49	1.00	0.51	0.25	0.14	0.85	0.85
P05L1S13		0.26	0.17	0.13	0.10	0.31	0.24	0.15	0.10	0.18	0.18
P20L1S13		0.14	0.09	0.25	0.10	0.28	0.40	0.12	0.07	0.30	0.30
P05L4S13		0.68	0.41	0.72	0.51	0.74	1.00	0.52	0.18	0.57	0.57
P20L4S13		0.39	0.23	0.49	0.25	0.54	0.49	0.24	0.14	0.54	0.54
P05L1S07	6	0.45	0.29	0.23	0.19	0.50	0.42	0.27	0.16	0.31	0.31
P20L1S07		0.31	0.41	0.48	0.37	0.54	0.71	0.24	0.13	0.59	0.59
P05L4S07		0.99	0.61	1.00	0.76	1.00	1.00	0.77	0.31	0.81	0.81
P20L4S07		1.00	0.88	1.00	0.98	1.00	0.83	0.41	0.23	1.00	1.00
P05L1S13		0.45	0.30	0.23	0.19	0.52	0.41	0.27	0.17	0.31	0.31
P20L1S13		0.25	0.16	0.40	0.19	0.46	0.65	0.22	0.12	0.49	0.49
P05L4S13		1.00	0.66	1.00	0.81	1.00	1.00	0.81	0.27	0.85	0.85
P20L4S13		0.63	0.38	0.76	0.41	0.85	0.79	0.39	0.23	0.82	0.82

Table B.10: Computed Damage Indices for Bridge Columns Reinforced with ASTM A706 Grade 420 Steel Bars and Subjected to Ground Motions from Subduction Earthquakes at Target Displacement Ductility Level of 6.

Bridge Column	Bar Slenderness Ratio	Record No.									
		1	2	3	4	5	6	7	8	9	10
P05L1S07	4	0.73	0.50	0.43	0.59	0.87	0.70	0.36	0.22	0.47	0.47
P20L1S07		0.40	0.61	1.00	0.69	1.00	1.00	0.29	0.27	1.00	1.00
P05L4S07		1.00	1.00	1.00	1.00	1.00	1.00	1.00	0.91	1.00	1.00
P20L4S07		1.00	0.88	1.00	1.00	1.00	1.00	0.65	0.55	1.00	1.00
P05L1S13		0.74	0.53	0.43	0.59	0.89	0.71	0.37	0.22	0.49	0.49
P20L1S13		0.43	0.30	0.69	0.36	0.81	0.75	0.27	0.15	0.54	0.54
P05L4S13		1.00	1.00	1.00	1.00	1.00	1.00	1.00	0.80	1.00	1.00
P20L4S13		1.00	0.68	1.00	0.92	1.00	1.00	0.48	0.32	1.00	1.00
P05L1S07	6	1.00	0.77	0.69	0.92	1.00	1.00	0.58	0.34	0.72	0.72
P20L1S07		0.66	1.00	1.00	1.00	1.00	1.00	0.46	0.52	1.00	1.00
P05L4S07		1.00	1.00	1.00	1.00	1.00	1.00	1.00	1.00	1.00	1.00
P20L4S07		1.00	1.00	1.00	1.00	1.00	1.00	1.00	0.93	1.00	1.00
P05L1S13		1.00	0.81	0.69	0.91	1.00	1.00	0.59	0.34	0.75	0.75
P20L1S13		0.67	0.47	1.00	0.57	1.00	1.00	0.43	0.23	0.82	0.82
P05L4S13		1.00	1.00	1.00	1.00	1.00	1.00	1.00	1.00	1.00	1.00
P20L4S13		1.00	1.00	1.00	1.00	1.00	1.00	0.75	0.47	1.00	1.00

Table B.11: Computed Damage Indices for Bridge Columns Reinforced with ASTM A706 Grade 550 Steel Bars and Subjected to Ground Motions from Crustal Earthquakes at Target Displacement Ductility Level of 2.

Bridge Column	Bar Slenderness Ratio	Record No.									
		1	2	3	4	5	6	7	8	9	10
P05L1S07	4	0.02	0.01	0.03	0.03	0.03	0.05	0.05	0.02	0.01	0.02
P20L1S07		0.06	0.01	0.05	0.05	0.03	0.06	0.03	0.03	0.01	0.02
P05L4S07		0.06	0.05	0.09	0.05	0.08	0.06	0.07	0.06	0.04	0.04
P20L4S07		0.11	0.01	0.06	0.11	0.05	0.04	0.07	0.03	0.01	0.03
P05L1S13		0.02	0.01	0.04	0.03	0.03	0.05	0.05	0.02	0.01	0.02
P20L1S13		0.05	0.01	0.05	0.05	0.03	0.06	0.03	0.03	0.01	0.02
P05L4S13		0.06	0.05	0.10	0.05	0.08	0.06	0.08	0.06	0.04	0.04
P20L4S13		0.09	0.01	0.07	0.11	0.05	0.04	0.06	0.04	0.01	0.03
P05L1S07	6	0.06	0.05	0.10	0.10	0.08	0.14	0.14	0.08	0.04	0.06
P20L1S07		0.17	0.03	0.14	0.15	0.09	0.17	0.09	0.08	0.02	0.05
P05L4S07		0.19	0.14	0.22	0.14	0.21	0.16	0.17	0.15	0.10	0.10
P20L4S07		0.27	0.05	0.16	0.29	0.13	0.11	0.16	0.10	0.03	0.08
P05L1S13		0.06	0.05	0.12	0.10	0.08	0.14	0.15	0.08	0.04	0.06
P20L1S13		0.15	0.03	0.15	0.14	0.09	0.17	0.09	0.08	0.02	0.05
P05L4S13		0.18	0.14	0.25	0.14	0.21	0.16	0.19	0.17	0.10	0.11
P20L4S13		0.23	0.05	0.18	0.28	0.13	0.11	0.15	0.11	0.03	0.08

Table B.12: Computed Damage Indices for Bridge Columns Reinforced with ASTM A706 Grade 550 Steel Bars and Subjected to Ground Motions from Crustal Earthquakes at Target Displacement Ductility Level of 4.

Bridge Column	Bar Slenderness Ratio	Record No.									
		1	2	3	4	5	6	7	8	9	10
P05L1S07	4	0.14	0.06	0.30	0.35	0.20	0.23	0.33	0.12	0.06	0.14
P20L1S07		0.30	0.04	0.25	0.60	0.26	0.38	0.26	0.10	0.06	0.26
P05L4S07		0.29	0.21	1.00	0.74	0.74	0.80	1.00	0.29	0.23	0.39
P20L4S07		0.49	0.06	0.94	1.00	0.76	1.00	0.64	0.40	0.11	0.34
P05L1S13		0.15	0.06	0.31	0.35	0.21	0.24	0.33	0.13	0.06	0.14
P20L1S13		0.26	0.04	0.24	0.49	0.22	0.40	0.21	0.10	0.07	0.23
P05L4S13		0.30	0.23	1.00	0.75	0.74	0.86	1.00	0.31	0.24	0.41
P20L4S13		0.55	0.07	0.73	0.85	0.39	0.81	0.59	0.26	0.12	0.28
P05L1S07	6	0.33	0.16	0.59	0.69	0.41	0.51	0.58	0.28	0.13	0.28
P20L1S07		0.65	0.11	0.51	1.00	0.49	0.78	0.48	0.22	0.14	0.48
P05L4S07		0.59	0.42	1.00	1.00	1.00	1.00	1.00	0.55	0.40	0.67
P20L4S07		0.94	0.17	1.00	1.00	1.00	1.00	1.00	0.89	0.21	0.77
P05L1S13		0.35	0.16	0.61	0.70	0.41	0.52	0.58	0.29	0.13	0.28
P20L1S13		0.52	0.11	0.49	0.92	0.44	0.81	0.39	0.21	0.14	0.44
P05L4S13		0.61	0.45	1.00	1.00	1.00	1.00	1.00	0.58	0.42	0.70
P20L4S13		0.97	0.19	1.00	1.00	0.67	1.00	0.91	0.51	0.24	0.49

Table B.13: Computed Damage Indices for Bridge Columns Reinforced with ASTM A706 Grade 550 Steel Bars and Subjected to Ground Motions from Crustal Earthquakes at Target Displacement Ductility Level of 6.

Bridge Column	Bar Slenderness Ratio	Record No.									
		1	2	3	4	5	6	7	8	9	10
P05L1S07	4	1.00	0.14	1.00	1.00	0.65	1.00	1.00	0.36	0.14	0.42
P20L1S07		0.83	0.09	0.72	1.00	0.91	1.00	1.00	0.23	0.16	1.00
P05L4S07		1.00	0.90	1.00	1.00	1.00	1.00	1.00	0.76	0.80	1.00
P20L4S07		1.00	0.57	1.00	1.00	1.00	1.00	1.00	0.88	0.89	1.00
P05L1S13		1.00	0.15	1.00	1.00	0.64	1.00	0.98	0.38	0.15	0.42
P20L1S13		1.00	0.19	1.00	1.00	1.00	1.00	1.00	0.98	0.48	1.00
P05L4S13		1.00	0.51	1.00	1.00	1.00	1.00	1.00	0.71	0.61	1.00
P20L4S13		0.56	0.11	0.47	1.00	0.67	0.91	0.68	0.24	0.17	0.62
P05L1S07	6	1.00	0.30	1.00	1.00	1.00	1.00	1.00	0.68	0.26	0.66
P20L1S07		1.00	0.22	1.00	1.00	1.00	1.00	1.00	0.51	0.30	1.00
P05L4S07		1.00	1.00	1.00	1.00	1.00	1.00	1.00	1.00	1.00	1.00
P20L4S07		1.00	1.00	1.00	1.00	1.00	1.00	1.00	1.00	1.00	1.00
P05L1S13		1.00	0.32	1.00	1.00	1.00	1.00	1.00	0.71	0.27	0.66
P20L1S13		0.92	0.27	0.83	1.00	1.00	1.00	1.00	0.42	0.32	1.00
P05L4S13		1.00	0.88	1.00	1.00	1.00	1.00	1.00	1.00	0.89	1.00
P20L4S13		1.00	0.42	1.00	1.00	1.00	1.00	1.00	1.00	0.76	1.00

Table B.14: Computed Damage Indices for Bridge Columns Reinforced with ASTM A706 Grade 550 Steel Bars and Subjected to Ground Motions from Subduction Earthquakes at Target Displacement Ductility Level of 2.

Bridge Column	Bar Slenderness Ratio	Record No.									
		1	2	3	4	5	6	7	8	9	10
P05L1S07	4	0.13	0.08	0.07	0.07	0.12	0.15	0.08	0.05	0.06	0.06
P20L1S07		0.05	0.05	0.07	0.03	0.09	0.12	0.07	0.02	0.06	0.06
P05L4S07		0.28	0.23	0.31	0.24	0.33	0.25	0.16	0.10	0.26	0.26
P20L4S07		0.22	0.08	0.08	0.11	0.32	0.22	0.09	0.06	0.16	0.16
P05L1S13		0.13	0.09	0.07	0.07	0.12	0.15	0.08	0.06	0.07	0.07
P20L1S13		0.05	0.04	0.09	0.04	0.09	0.12	0.07	0.02	0.07	0.07
P05L4S13		0.28	0.24	0.31	0.23	0.34	0.28	0.16	0.10	0.26	0.26
P20L4S13		0.22	0.09	0.10	0.09	0.29	0.17	0.08	0.06	0.15	0.15
P05L1S07	6	0.39	0.27	0.24	0.23	0.38	0.46	0.25	0.15	0.21	0.21
P20L1S07		0.18	0.15	0.23	0.11	0.30	0.36	0.23	0.07	0.21	0.21
P05L4S07		0.72	0.63	0.80	0.65	0.84	0.65	0.43	0.24	0.64	0.64
P20L4S07		0.59	0.26	0.24	0.30	0.81	0.61	0.26	0.17	0.42	0.42
P05L1S13		0.40	0.29	0.24	0.24	0.38	0.46	0.25	0.17	0.22	0.22
P20L1S13		0.17	0.14	0.28	0.12	0.27	0.36	0.22	0.06	0.22	0.22
P05L4S13		0.73	0.64	0.82	0.62	0.87	0.71	0.45	0.24	0.65	0.65
P20L4S13		0.60	0.27	0.31	0.26	0.74	0.50	0.25	0.16	0.39	0.39

Table B.15: Computed Damage Indices for Bridge Columns Reinforced with ASTM A706 Grade 550 Steel Bars and Subjected to Ground Motions from Subduction Earthquakes at Target Displacement Ductility Level of 4.

Bridge Column	Bar Slenderness Ratio	Record No.									
		1	2	3	4	5	6	7	8	9	10
P05L1S07	4	0.71	0.49	0.39	0.37	0.98	0.65	0.39	0.25	0.52	0.52
P20L1S07		0.33	0.21	0.58	0.38	0.70	0.78	0.25	0.14	0.64	0.64
P05L4S07		1.00	1.00	1.00	1.00	1.00	1.00	1.00	0.62	1.00	1.00
P20L4S07		1.00	1.00	1.00	0.70	1.00	1.00	0.61	0.91	1.00	1.00
P05L1S13		0.70	0.51	0.40	0.40	1.00	0.68	0.38	0.25	0.52	0.52
P20L1S13		0.29	0.20	0.49	0.30	0.54	0.72	0.23	0.13	0.53	0.53
P05L4S13		1.00	1.00	1.00	1.00	1.00	1.00	1.00	0.69	1.00	1.00
P20L4S13		0.99	0.58	1.00	0.72	1.00	1.00	0.62	0.42	1.00	1.00
P05L1S07	6	1.00	1.00	0.93	0.87	1.00	1.00	0.92	0.55	1.00	1.00
P20L1S07		0.77	0.49	1.00	0.85	1.00	1.00	0.62	0.32	1.00	1.00
P05L4S07		1.00	1.00	1.00	1.00	1.00	1.00	1.00	1.00	1.00	1.00
P20L4S07		1.00	1.00	1.00	1.00	1.00	1.00	1.00	1.00	1.00	1.00
P05L1S13		1.00	1.00	0.95	0.94	1.00	1.00	0.91	0.54	1.00	1.00
P20L1S13		0.69	0.46	1.00	0.72	1.00	1.00	0.58	0.30	1.00	1.00
P05L4S13		1.00	1.00	1.00	1.00	1.00	1.00	1.00	1.00	1.00	1.00
P20L4S13		1.00	1.00	1.00	1.00	1.00	1.00	1.00	0.80	1.00	1.00

Table B.16: Computed Damage Indices for Bridge Columns Reinforced with ASTM A706 Grade 550 Steel Bars and Subjected to Ground Motions from Subduction Earthquakes at Target Displacement Ductility Level of 6.

Bridge Column	Bar Slenderness Ratio	Record No.									
		1	2	3	4	5	6	7	8	9	10
P05L1S07	4	1.00	1.00	1.00	1.00	1.00	1.00	1.00	0.64	1.00	1.00
P20L1S07		1.00	1.00	1.00	1.00	1.00	1.00	0.57	0.77	1.00	1.00
P05L4S07		1.00	1.00	1.00	1.00	1.00	1.00	1.00	1.00	1.00	1.00
P20L4S07		1.00	1.00	1.00	1.00	1.00	1.00	1.00	1.00	1.00	1.00
P05L1S13		1.00	1.00	1.00	1.00	1.00	1.00	1.00	0.64	1.00	1.00
P20L1S13		0.89	0.92	1.00	0.71	1.00	1.00	0.58	0.29	1.00	1.00
P05L4S13		1.00	1.00	1.00	1.00	1.00	1.00	1.00	1.00	1.00	1.00
P20L4S13		0.18	1.00	1.00	1.00	1.00	1.00	1.00	0.89	1.00	1.00
P05L1S07	6	1.00	1.00	1.00	1.00	1.00	1.00	1.00	1.00	1.00	1.00
P20L1S07		1.00	1.00	1.00	1.00	1.00	1.00	1.00	1.00	1.00	1.00
P05L4S07		1.00	1.00	1.00	1.00	1.00	1.00	1.00	1.00	1.00	1.00
P20L4S07		1.00	1.00	1.00	1.00	1.00	1.00	1.00	1.00	1.00	1.00
P05L1S13		1.00	1.00	1.00	1.00	1.00	1.00	1.00	1.00	1.00	1.00
P20L1S13		1.00	1.00	1.00	1.00	1.00	1.00	1.00	0.59	1.00	1.00
P05L4S13		1.00	1.00	1.00	1.00	1.00	1.00	1.00	1.00	1.00	1.00
P20L4S13		0.36	1.00	1.00	1.00	1.00	1.00	1.00	1.00	1.00	1.00

Table B.17: Computed Damage Indices for Bridge Columns Reinforced with ASTM A1035 Grade 690 Steel Bars and Subjected to Ground Motions from Crustal Earthquakes at Target Displacement Ductility Level of 2.

Bridge Column	Bar Slenderness Ratio	Record No.									
		1	2	3	4	5	6	7	8	9	10
P05L1S07	4	0.10	0.07	0.33	0.31	0.26	0.29	0.49	0.12	0.08	0.14
P20L1S07		0.32	0.02	0.37	0.24	0.19	0.30	0.18	0.15	0.03	0.16
P05L4S07		0.49	0.42	0.81	0.49	0.66	0.62	0.82	0.58	0.33	0.37
P20L4S07		0.91	0.07	0.98	1.00	0.40	0.46	0.43	0.36	0.08	0.20
P05L1S13		0.09	0.07	0.30	0.29	0.25	0.26	0.51	0.12	0.07	0.14
P20L1S13		0.21	0.02	0.22	0.14	0.13	0.22	0.12	0.11	0.02	0.10
P05L4S13		0.49	0.42	0.81	0.49	0.65	0.67	0.89	0.59	0.33	0.38
P20L4S13		0.83	0.07	1.00	1.00	0.43	0.55	0.46	0.42	0.09	0.22
P05L1S07	6	0.16	0.12	0.36	0.37	0.29	0.37	0.47	0.19	0.11	0.18
P20L1S07		0.38	0.05	0.41	0.34	0.23	0.40	0.21	0.18	0.05	0.19
P05L4S07		0.52	0.45	1.00	0.52	0.70	0.66	1.00	0.62	0.35	0.39
P20L4S07		1.00	0.12	1.00	1.00	0.44	0.50	0.47	0.38	0.09	0.22
P05L1S13		0.16	0.12	0.33	0.35	0.28	0.35	0.47	0.19	0.11	0.17
P20L1S13		0.29	0.05	0.29	0.24	0.17	0.32	0.16	0.15	0.04	0.13
P05L4S13		0.52	0.45	1.00	0.52	0.69	0.71	1.00	0.63	0.35	0.40
P20L4S13		1.00	0.13	1.00	1.00	0.44	0.56	0.47	0.43	0.10	0.23

Table B.18: Computed Damage Indices for Bridge Columns Reinforced with ASTM A1035 Grade 690 Steel Bars and Subjected to Ground Motions from Crustal Earthquakes at Target Displacement Ductility Level of 4.

Bridge Column	Bar Slenderness Ratio	Record No.									
		1	2	3	4	5	6	7	8	9	10
P05L1S07	4	1.00	0.53	1.00	1.00	1.00	1.00	1.00	1.00	0.47	1.00
P20L1S07		1.00	0.33	1.00	1.00	1.00	1.00	1.00	1.00	0.61	1.00
P05L4S07		1.00	1.00	1.00	1.00	1.00	1.00	1.00	1.00	1.00	1.00
P20L4S07		1.00	0.86	1.00	1.00	1.00	1.00	1.00	1.00	1.00	1.00
P05L1S13		1.00	0.52	1.00	1.00	1.00	1.00	1.00	1.00	0.46	1.00
P20L1S13		1.00	0.31	1.00	1.00	1.00	1.00	0.97	0.53	0.45	1.00
P05L4S13		1.00	1.00	1.00	1.00	1.00	1.00	1.00	1.00	1.00	1.00
P20L4S13		1.00	0.72	1.00	1.00	1.00	1.00	1.00	1.00	1.00	1.00
P05L1S07	6	1.00	0.69	1.00	1.00	1.00	1.00	1.00	1.00	0.81	1.00
P20L1S07		1.00	0.33	1.00	1.00	1.00	1.00	1.00	1.00	0.80	1.00
P05L4S07		1.00	1.00	1.00	1.00	1.00	1.00	1.00	1.00	1.00	1.00
P20L4S07		1.00	0.94	1.00	1.00	1.00	1.00	1.00	1.00	1.00	1.00
P05L1S13		1.00	0.68	1.00	1.00	1.00	1.00	1.00	1.00	0.79	1.00
P20L1S13		1.00	0.33	1.00	1.00	1.00	1.00	1.00	0.89	0.68	1.00
P05L4S13		1.00	1.00	1.00	1.00	1.00	1.00	1.00	1.00	1.00	1.00
P20L4S13		1.00	1.00	1.00	1.00	1.00	1.00	1.00	1.00	1.00	1.00

Table B.19: Computed Damage Indices for Bridge Columns Reinforced with ASTM A1035 Grade 690 Steel Bars and Subjected to Ground Motions from Crustal Earthquakes at Target Displacement Ductility Level of 6.

Bridge Column	Bar Slenderness Ratio	Record No.									
		1	2	3	4	5	6	7	8	9	10
P05L1S07	4	1.00	1.00	1.00	1.00	1.00	1.00	1.00	1.00	1.00	1.00
P20L1S07		1.00	0.80	1.00	1.00	1.00	1.00	1.00	1.00	1.00	0.98
P05L4S07		1.00	1.00	1.00	1.00	1.00	1.00	1.00	1.00	1.00	1.00
P20L4S07		1.00	1.00	1.00	1.00	1.00	1.00	1.00	1.00	1.00	1.00
P05L1S13		1.00	1.00	1.00	1.00	1.00	1.00	1.00	1.00	1.00	1.00
P20L1S13		1.00	0.76	1.00	1.00	1.00	1.00	1.00	1.00	1.00	0.93
P05L4S13		1.00	1.00	1.00	1.00	1.00	1.00	1.00	1.00	1.00	1.00
P20L4S13		1.00	1.00	1.00	1.00	1.00	1.00	1.00	1.00	1.00	1.00
P05L1S07	6	1.00	1.00	1.00	1.00	1.00	1.00	1.00	1.00	1.00	1.00
P20L1S07		1.00	1.00	1.00	1.00	1.00	1.00	1.00	1.00	1.00	1.00
P05L4S07		1.00	1.00	1.00	1.00	1.00	1.00	1.00	1.00	1.00	1.00
P20L4S07		1.00	1.00	1.00	1.00	1.00	1.00	1.00	1.00	1.00	1.00
P05L1S13		1.00	1.00	1.00	1.00	1.00	1.00	1.00	1.00	1.00	1.00
P20L1S13		1.00	1.00	1.00	1.00	1.00	1.00	1.00	1.00	1.00	1.00
P05L4S13		1.00	1.00	1.00	1.00	1.00	1.00	1.00	1.00	1.00	1.00
P20L4S13		1.00	1.00	1.00	1.00	1.00	1.00	1.00	1.00	1.00	1.00

Table B.20: Computed Damage Indices for Bridge Columns Reinforced with ASTM A1035 Grade 690 Steel Bars and Subjected to Ground Motions from Subduction Earthquakes at Target Displacement Ductility Level of 2.

Bridge Column	Bar Slenderness Ratio	Record No.									
		1	2	3	4	5	6	7	8	9	10
P05L1S07	4	1.00	0.55	0.34	0.31	1.00	0.73	0.53	0.46	0.46	0.46
P20L1S07		0.18	0.16	0.41	0.14	0.34	0.62	0.22	0.16	0.42	0.42
P05L4S07		1.00	1.00	1.00	1.00	1.00	1.00	1.00	1.00	1.00	1.00
P20L4S07		1.00	0.72	1.00	0.69	1.00	1.00	1.00	0.74	1.00	1.00
P05L1S13		1.00	0.54	0.31	0.29	0.94	0.65	0.48	0.45	0.41	0.41
P20L1S13		0.12	0.10	0.28	0.12	0.22	0.31	0.16	0.12	0.26	0.26
P05L4S13		1.00	1.00	1.00	1.00	1.00	1.00	1.00	0.99	1.00	1.00
P20L4S13		1.00	0.79	1.00	0.69	1.00	1.00	1.00	0.73	1.00	1.00
P05L1S07	6	1.00	0.77	0.57	0.54	1.00	1.00	0.73	0.52	0.61	0.61
P20L1S07		0.35	0.25	0.61	0.28	0.53	0.89	0.41	0.22	0.60	0.60
P05L4S07		1.00	1.00	1.00	1.00	1.00	1.00	1.00	1.00	1.00	1.00
P20L4S07		1.00	0.79	1.00	0.77	1.00	1.00	1.00	0.80	1.00	1.00
P05L1S13		1.00	0.76	0.53	0.53	1.00	0.96	0.68	0.52	0.58	0.58
P20L1S13		0.27	0.18	0.47	0.24	0.39	0.54	0.33	0.18	0.43	0.43
P05L4S13		1.00	1.00	1.00	1.00	1.00	1.00	1.00	1.00	1.00	1.00
P20L4S13		1.00	0.83	1.00	0.77	1.00	1.00	1.00	0.77	1.00	1.00

Table B.21: Computed Damage Indices for Bridge Columns Reinforced with ASTM A1035 Grade 690 Steel Bars and Subjected to Ground Motions from Subduction Earthquakes at Target Displacement Ductility Level of 4.

Bridge Column	Bar Slenderness Ratio	Record No.										
		1	2	3	4	5	6	7	8	9	10	
P05L1S07	4	1.00	1.00	1.00	1.00	1.00	1.00	1.00	1.00	1.00	1.00	
P20L1S07		1.00	1.00	1.00	1.00	1.00	1.00	1.00	1.00	0.83	1.00	1.00
P05L4S07		1.00	1.00	1.00	1.00	1.00	1.00	1.00	1.00	1.00	1.00	1.00
P20L4S07		1.00	1.00	1.00	1.00	1.00	1.00	1.00	1.00	1.00	1.00	1.00
P05L1S13		1.00	1.00	1.00	1.00	1.00	1.00	1.00	1.00	1.00	1.00	1.00
P20L1S13		1.00	1.00	1.00	1.00	1.00	1.00	1.00	1.00	0.71	1.00	1.00
P05L4S13		1.00	1.00	1.00	1.00	1.00	1.00	1.00	1.00	1.00	1.00	1.00
P20L4S13		1.00	1.00	1.00	1.00	1.00	1.00	1.00	1.00	1.00	1.00	1.00
P05L1S07	6	1.00	1.00	1.00	1.00	1.00	1.00	1.00	1.00	1.00	1.00	
P20L1S07		1.00	1.00	1.00	1.00	1.00	1.00	1.00	1.00	1.00	1.00	1.00
P05L4S07		1.00	1.00	1.00	1.00	1.00	1.00	1.00	1.00	1.00	1.00	1.00
P20L4S07		1.00	1.00	1.00	1.00	1.00	1.00	1.00	1.00	1.00	1.00	1.00
P05L1S13		1.00	1.00	1.00	1.00	1.00	1.00	1.00	1.00	1.00	1.00	1.00
P20L1S13		1.00	1.00	1.00	1.00	1.00	1.00	1.00	1.00	0.99	1.00	1.00
P05L4S13		1.00	1.00	1.00	1.00	1.00	1.00	1.00	1.00	1.00	1.00	1.00
P20L4S13		1.00	1.00	1.00	1.00	1.00	1.00	1.00	1.00	1.00	1.00	1.00

Table B.22: Computed Damage Indices for Bridge Columns Reinforced with ASTM A1035 Grade 690 Steel Bars and Subjected to Ground Motions from Subduction Earthquakes at Target Displacement Ductility Level of 6.

Bridge Column	Bar Slenderness Ratio	Record No.										
		1	2	3	4	5	6	7	8	9	10	
P05L1S07	4	1.00	1.00	1.00	1.00	1.00	1.00	1.00	1.00	1.00	1.00	
P20L1S07		1.00	1.00	1.00	1.00	1.00	1.00	1.00	1.00	1.00	1.00	1.00
P05L4S07		1.00	1.00	1.00	1.00	1.00	1.00	1.00	1.00	1.00	1.00	1.00
P20L4S07		1.00	1.00	1.00	1.00	1.00	1.00	1.00	1.00	1.00	1.00	1.00
P05L1S13		1.00	1.00	1.00	1.00	1.00	1.00	1.00	1.00	1.00	1.00	1.00
P20L1S13		1.00	1.00	1.00	1.00	1.00	1.00	1.00	1.00	1.00	1.00	1.00
P05L4S13		1.00	1.00	1.00	1.00	1.00	1.00	1.00	1.00	1.00	1.00	1.00
P20L4S13		1.00	1.00	1.00	1.00	1.00	1.00	1.00	1.00	1.00	1.00	1.00
P05L1S07	6	1.00	1.00	1.00	1.00	1.00	1.00	1.00	1.00	1.00	1.00	
P20L1S07		1.00	1.00	1.00	1.00	1.00	1.00	1.00	1.00	1.00	1.00	1.00
P05L4S07		1.00	1.00	1.00	1.00	1.00	1.00	1.00	1.00	1.00	1.00	1.00
P20L4S07		1.00	1.00	1.00	1.00	1.00	1.00	1.00	1.00	1.00	1.00	1.00
P05L1S13		1.00	1.00	1.00	1.00	1.00	1.00	1.00	1.00	1.00	1.00	1.00
P20L1S13		1.00	1.00	1.00	1.00	1.00	1.00	1.00	1.00	1.00	1.00	1.00
P05L4S13		1.00	1.00	1.00	1.00	1.00	1.00	1.00	1.00	1.00	1.00	1.00
P20L4S13		1.00	1.00	1.00	1.00	1.00	1.00	1.00	1.00	1.00	1.00	1.00